Electropreconcentration in nanofluidic devices : predict and experimentally demonstrate stacking/focusing regimes

Fatima Flores Galicia

Fatima Flores Galicia. Electropreconcentration in nanofluidic devices : predict and experimentally demonstrate stacking/focusing regimes. Biological Physics [physics.bio-ph]. Université Paris-Saclay, 2021. English. NNT : 2021UPAST140 . tel-03628365

Electropréconcentration dans des dispositifs nanofluidiques : prédire et démontrer expérimentalement les régimes focalisants

Electropreconcentration in nanofluidic devices: predict and experimentally demonstrate stacking/focusing regimes

Thèse de doctorat de l'Université Paris-Saclay

École doctorale n° 575, electrical, optical bio: physics and engineering (EOBE)
Spécialité de doctorat: Electronique et Optoélectronique, Nano et Microtechnologies
Unité de recherche: Université Paris-Saclay, CNRS, Centre de Nanosciences et de Nanotechnologies, 91120, Palaiseau, France
Référent: : Faculté des sciences d'Orsay

Thèse présentée et soutenue à Paris-Saclay, le 17 décembre 2021, par

Fatima FLORES GALICIA

Composition du jury

Claude Fermon Directeur de Recherche SPEC CEA/Saclay (UMR3680), ST Aubin	Président
Pierre Joseph Chargé de recherche LAAS-CNRS (UPR8001), Toulouse	Rapporteur et Examinateur
Vincent Senez Directeur de Recherche IEMN (UMR8640), Lille	Rapporteur et Examinateur
Catherine Perrin Professeur- Université de Montpellier IBMM (UMR5247), Montpellier	Examinatrice

Direction de la thèse

Anne-Marie Haghiri Directeur de Recherche CNRS (C2N-UMR9001), Palaiseau	Directrice de thèse
Antoine Pallandre Professeur - Université Paris-Saclay CNRS (ICP-UMR8000), Orsay	Co-directeur de thèse

Thèse de doctorat

NNT: 2021UPAST140

Résumé

Dans le domaine de bioanalyse, la séparation et la détection d'analytes à de très faibles concentrations sont nécessaires afin de diagnostiquer précocement des maladies difficiles à traiter ou de détecter des agents biochimiques nocifs pouvant entraîner un danger, pour ne citer que quelques exemples. Les progrès des technologies de fabrication ont été à la base du développement de dispositifs bioanalytiques micro et nanofluidiques. Différents méthodes basées sur l'électrocinétique ont été introduites pour concentrer des échantillons dans des systèmes nanofluidiques. Dans cette thèse, nous approfondissons l'étude de l'électropréconcentration des analytes basée sur la polarisation de la concentration ionique (ICP en anglais).

Typiquement, l'ICP est induite à travers des nanocanaux ou des membranes qui jouent le rôle de filtres sélectifs d'ions entre les microcanaux. Introduisons le cas d'un nanocanal chargé négativement qui a été intégré à l'intérieur d'un microcanal rempli d'un électrolyte de fond. Dans les régimes de faible force ionique, à des échelles nanométriques, la double couche électrique (EDL en anglais) occupe une partie importante à travers le canal nanofluidique. Les deux doubles couches électriques face à face dans le nanocanal sont insuffisantes pour filtrer complètement le champ électrique provenant de la surface interfaciale. Ainsi, puisque les espèces co-ioniques (Cl^- pour l'électrolyte de fond KCl) sont électrostatiquement exclues dans une certaine mesure du nanocanal, seuls les contre-ions (K^+ pour l'électrolyte de fond KCl) peuvent être transportés à travers le nanocanal. Pour maintenir l'électroneutralité, la concentration des contre-ions doit être supérieure à celle des co-ions à l'intérieur du nanocanal, déclenchant ainsi un comportement sélectif des ions.

Sous l'influence d'un champ électrique appliqué, l'exclusion de charge décrite précédemment et la compétition ou l'addition entre le flux électroosmotique (EOF) et la migration électrophorétique (EP) conduit à un transport ionique déséquilibré entre les espèces anioniques et cationiques d'une solution d'électrolyte à travers l'interface micro/nanocanal. Le transport des contre-ions est favorisé du côté anodique au côté cathodique du nanocanal alors que les co-ions sont exclus du passage le long du nanocanal du côté cathodique au côté anodique. Ce mécanisme crée une asymétrie dans la concentration en espèces ioniques provoquant une zone d'enrichissement en ions du côté cathodique du nanocanal et une zone d'appauvrissement en ions du côté anionique du nanocanal. Le résultat est ainsi une « polarisation » de la distribution de concentration, dans laquelle les ions de l'électrolyte de fond sont épuisés d'un côté du nanocanal et s'accumulent de l'autre. Cet effet d'enrichissement-exclusion est appelé effet ICP.

L'objectif de cette thèse est d'étudier la préconcentration d'analytes modèles par effet ICP dans une puce intégrant plusieurs micro/nano/microcanaux avec des nanocanaux « verticaux ». L'incorporation de plusieurs nanocanaux de largeurs et de longueurs différentes permet d'étudier

ce phénomène multiparamétrique en une seule expérience. Pour résumer, ce travail est divisé en deux parties importantes, la première partie comprend un modèle bidimensionnel pour étudier l'ICP et la préconcentration d'analytes ioniques à l'intérieur d'un simple nanocanal qui relie deux microcanaux considérés comme des réservoirs à l'aide du logiciel COMSOL Multiphysics®; et la deuxième partie fournir une description détaillé étape par étape d' un nouveau protocole pour la fabrication de puces Hard-PDMS/verre (h-PDMS/verre) et montre des résultats expérimentaux d'electropréconcentration dans ces puces mixtes en utilisant différentes molécules modèles: la fluorescéine, l'ovalbumine et l'ADN de l'hépatite C.

Simulations numériques

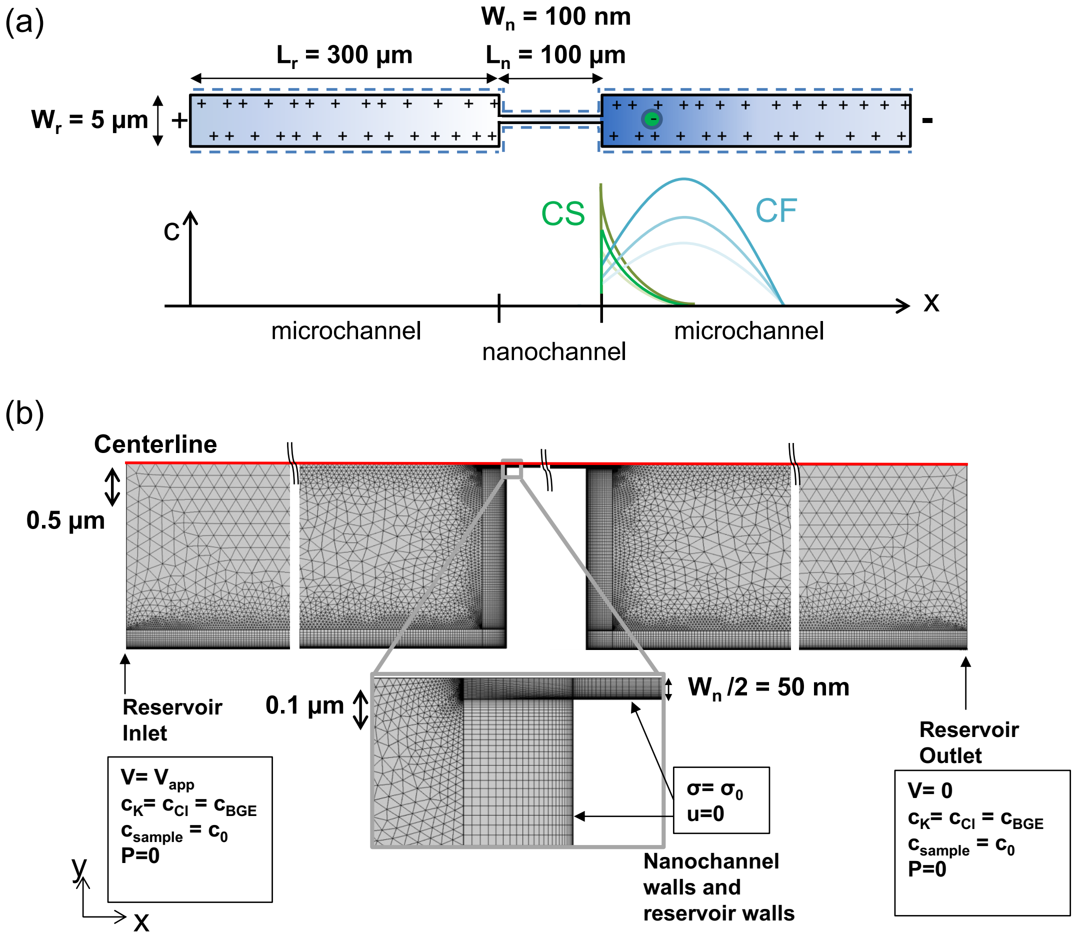

Figure 1: (a) Représentation schématique du dispositif « micro/nano/micro » avec des dimensions typiques et la variation des profils de concentration d'analyte anionique évoluant via l'effet ICP. (b) Maillage et conditions limites utilisées pour les simulations numériques. Les dimensions en x ne sont pas à l'échelle et représentent quatre segments de la structure totale. En raison de la symétrie axiale de la structure (voir (a)) et pour rendre les simulations plus efficaces, une condition de symétrie est imposée le long de la ligne médiane des canaux.

Des simulations numériques ont été réalisées à l'aide de COMSOL© v5.6. La géométrie du système utilisé est présentée sur la figure 1 (a). Elle est composée d'un nanocanal qui relie deux microcanaux considérés comme des réservoirs. Les réservoirs ont une longueur L_r de 300 µm et une largeur W_r de 5 µm. Le nanocanal de 100 µm de long a une largeur W_n de 100 nm. Ici, on considère les ions de l'électrolyte de fond et des analytes anioniques. Le chlorure de potassium (KCl) a été choisi comme électrolyte de fond et la mobilité électrophorétique de l'analyte anionique a été varié en changeant le coefficient de diffusion dans la plage $0,1\text{x}10^{-9}\text{m}^2/\text{s}$ - $2\text{x}10^{-9}\text{m}^2/\text{s}$ (avec D= $0.42\text{x}10^{-9}\text{m}^2/\text{s}$ représentant la Fluorescéine, par exemple). La concentration initiale de l'electrolyte c_{BGE} est variée entre 50 µM et 1 mM, alors que les valeurs de densité de charge de surface imposées σ_s allaient de - 0,1 mC/m^2 et -2,5 mC/m^2, dans les plages de charge de surface rapportées du polydiméthylsiloxane (PDMS) et verre. Le maillage a été construit de telle sorte que des domaines près des parois chargées soient utilisés pour résoudre les doubles couches électriques. La taille de ces domaines de contrôle change en fonction de la concentration initiale de l'électrolyte de fond, s'assurant que les régions près des parois et dans les nanocanaux ont un maillage suffisamment fin par rapport aux éléments du reste du réservoir. Pour rendre les simulations plus efficaces, nous avons exploité la symétrie intrinsèque de la ligne centrale de la géométrie et modélisé seulement la moitié de la structure (cf. figure 1 (b)).

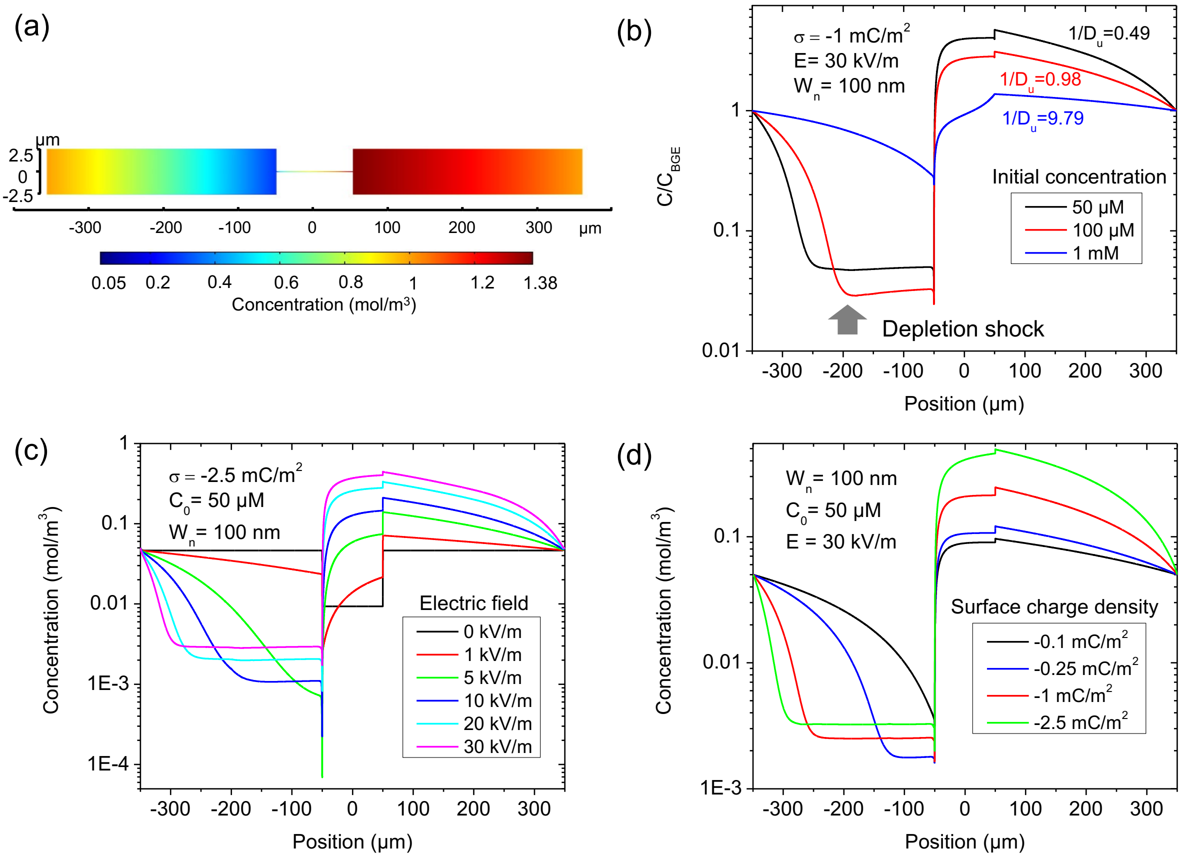

Figure 2: Effets de la polarisation de la concentration ionique (ICP) dans une solution de KCl: (a) une vue 2D typique du profil de concentration pour les ions chlorure à c_{BGE}= 1 mM, et (b) profils de concentration de Cl^- obtenus le long la ligne médiane de la structure micro/nanocanal en fonction du c_{BGE} (50 µM, 100 µM et 1 mM) avec le champ électrique fixé à 30 kV/m. La densité de charge de surface σ_s et la largeur de nanocanal W_n sont respectivement fixés à -1 mC/m^2 et 100 nm. (c) Visualisation de la transition de l'ICP sans propagation à la propagation lorsque le champ électrique appliqué augmente (avec σ_s = -2,5 mC/m^2) et (d) comme la densité de charge de surface est variait de -0,1 mC/m^2 à -2,5 mC/m^2 (avec c_{BGE} = 50 µM et E=30 kV/m).

Une façon simple d'étudier comment les effets ICP varient est de comparer les profils de concentration de co-ions Cl^- dans la structure et de surveiller l'évolution de l'épuisement et les zones d'enrichissement dans chaque réservoir. Commençons donc par examiner la diffusion d'ions chlorure de l'électrolyte de fond à l'intérieur d'un nanocanal de 100 nm de large. Figure 2 (a) et figure 2 (b) montrent respectivement une vue 2D caractéristique de la distribution de la concentration en co-ions Cl^- et des profils de concentration normalisés en régime permanent pour une densité de charge de surface σ_s = -1 mC/m^2. La figure 2 (b) décrit l'épuisement et l'enrichissement caractéristiques de l'ICP à l'entrée et à la sortie du nanocanal. Lorsque les effets de l'ICP sont relativement plus faibles, ces zones d'enrichissement et d'appauvrissement sont en grande partie confinées aux interfaces microcanaux-nanocanaux. Comme les charges de surface gouvernent les effets de transport elles deviennent plus importantes; cependant, la zone d'épuisement peut se propager vers l'extérieur vers la limite du réservoir du microcanal. Ces interfaces d'épuisement qui se propagent (également appelés chocs) peuvent finalement parcourir une distance allant jusqu'à plusieurs centaines de microns à partir du nanocanal dans notre système modélisé, en fonction de la concentration de l'électrolyte de fond c_{BGE}.

A faible c_{BGE} = 50 µM, (courbe noire de la figure 2 (b)), une large zone de déplétion propageante peut être observée dans le réservoir anodique, avec une interface située à environ 200 µm de l'entrée du nanocanal. Pour une concentration modérée c_{BGE} = 100 µM (profil rouge sur la figure 2 (b)), la zone de déplétion ne se propage pas aussi loin, atteignant plutôt une distance de 150 µm de l'entrée du nanocanal, mais la zone peut être appauvrie dans une plus grande mesure que pour c_{BGE} = 50 µM car le plus petit gradient de concentration, entre cet emplacement et la concentration fixée (comme conditions aux limites), limite la diffusion dans la zone appauvrie en ions. Enfin, à c_{BGE} = 1 mM plus élevé (profil bleu sur la figure 2 (b)), l'épuisement est limité et confiné à la jonction du canal, même sous un champ électrique élevé de 30 kV/m. Du côté cathodique du nanocanal, l'enrichissement se produit dans une certaine mesure pour toutes les concentrations initiales.

La figure 2 (c) met en évidence le rôle du champ électrique sur l'effet ICP pour un cas typique (W_n = 100 nm) à faible c_{BGE} = 50 µM et densité de charge de surface σ_s = -2,5 mC/m^2, correspondant à peu près à une surface en verre et un pH de la solution de 6,5. À des champs électriques relativement faibles (< 5 kV/m), des zones d'accumulation et des zones de déplétion apparaissent aux extrémités du nanocanal, et à environ 5 kV/m, la zone de déplétion commence à se propager à partir de la jonction du canal. En augmentant le champ appliqué à 10 kV/m, il se produit un effet ICP propageant avec une interface située à environ 125 µm de l' entrée du nanocanal. Augmenter encore le champ à 30 kV/m conduit à une zone d'épuisement plus étendue et plus d' accumulation à l'interface opposée. Le champ électrique appliqué a un impact aussi important sur l'ICP que la concentration de l'électrolyte de fond, et ne provoque la propagation que lorsqu'il est assez élevé. La figure 2 (d) montre l'influence de la densité de charge de surface σ_s sur l'exclusion co-ionique de charge et l'ICP résultant pour c_{BGE} = 50 µM et un champ électrique de E = 30 kV/m. En augmentant l'amplitude de la densité de charge de surface de -0,1 mC/m^2 à -2,5 mC/m^2 multiplie par cinq l'enrichissement dans le réservoir cathodique, tandis que le début de l'ICP propageant se produit entre -0,1 mC/m^2 et -0,25 mC/m^2 dans ces conditions.

Nous étudions après comment les analytes dilués (valence z = -2 et $c_{\mathrm{analyte}} = c_0 = 10^{-9}$ M), avec des mobilités différentes, peuvent se concentrer dans les conditions étudiées précédemment (c_{BGE} = 50 µM, Wn = 100 nm et E = 30 kV/m - courbe verte sur la figure 2 (d)). La figure 3 présente l'évolution des profils de concentration normalisés d'un analyte dilué transporté à travers un nanocanal de 100 nm de large, avec deux densités de charge de surface différentes (-1 mC/m^2 et - 2,5 mC/m^2) pour une gamme de mobilités d'échantillon.

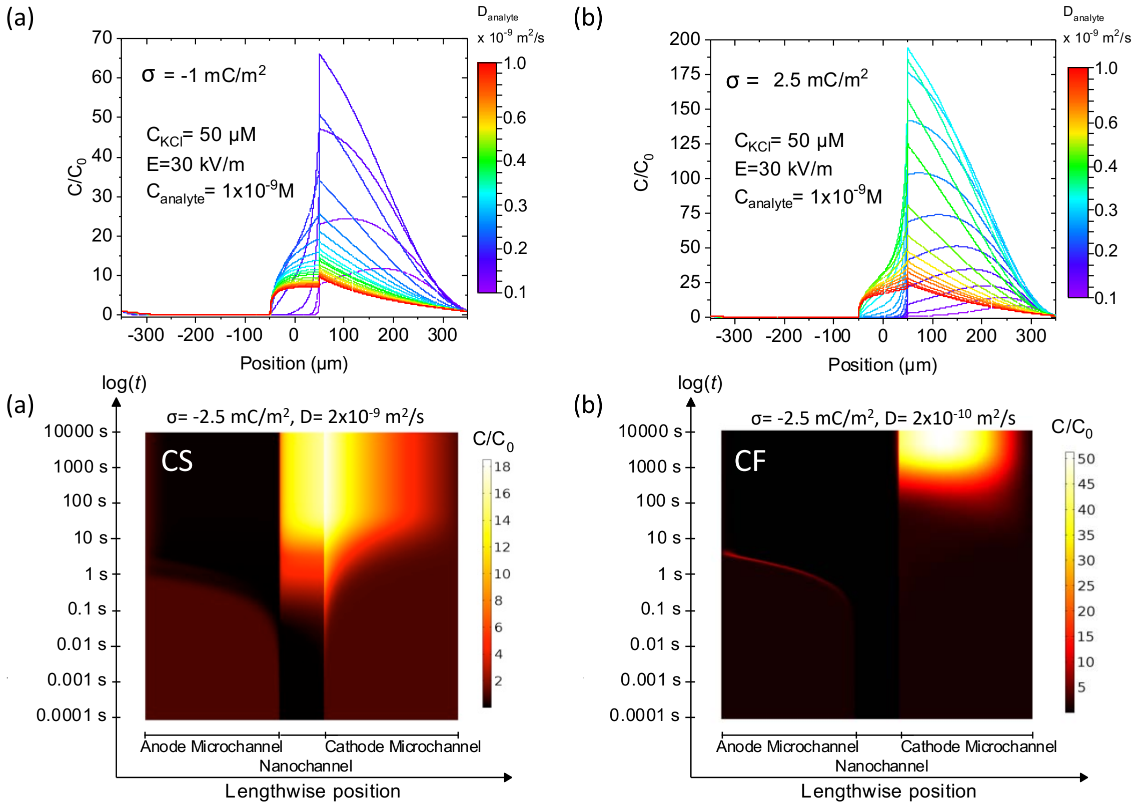

Figure 3: Évolution des profils de concentration normalisés avec des analytes de diffusivité différente pour deux densités de charge surfacique, a) -1 mC/m^2. et b) -2,5 mC/m^2. Pour les deux figures, la concentration initial de l'électrolyte de fond est de 50 µM, la concentration initiale de l'analyte est de 1x10^{-9} M et le champ électrique est de 30 kV/m. L'évolution spatio-temporelle des profils de concentration sur la ligne centrale normalisés est montrée via des tracés d'extrusion temporelle pour deux analytes avec des coefficients de diffusion de c) 2x10^{-9} m^2/s et d) 2x10^{-10} m^2/s et une densité de charge surfacique de -2,5 mC/m^2.

Sur la figure 3 (a), correspondant à une densité de charge surfacique de -1 mC/m^2, on constate une accumulation à la sortie du nanocanal dans un procédé appelé empilement cathodique (CS) pour la plupart des analytes avec des mobilités dans la plage illustrée. Ici, tous les ions analytes anioniques capables de passer l'exclusion électrocinétique à l'interface de transition de la double couche électrique sont encore capables de traverser le canal vers le réservoir anodique. Ainsi, une concentration significative d'ions de l'échantillon est toujours visible dans le nanocanal. Comme le coefficient de diffusion de l'analyte diminue, l'augmentation de la concentration à l'entrée du nanocanal augmente à mesure que l'échantillon a plus de difficulté à entrer et finalement à être transporté par le canal. Au-delà d'une valeur critique de mobilité, l'échantillon n'est plus en mesure de migrer à travers le canal et sera plutôt conduit à un point commun de vitesse nulle des deux côtés de l'interface. Ce phénomène de focalisation cathodique (CF) fournit le taux le plus élevé d'enrichissement de l'analyte lorsque l'emplacement de mise au point coïncide avec l'interface microcanal-nanocanal. Cependant, pour les échantillons à plus faible mobilité, le gradient de champ électrique associé aux zones d'accumulation-appauvrissement provoque que l'emplacement de focalisation s'éloigne de l'interface sélective de charge à travers du microcanal, conduisant à un effet d'amélioration plus faible. Pour une densité de charge surfacique de -2,5 mC/m^2, la figure 3 (b) prédit la focalisation cathodique (CF) maximale pour les analytes avec une diffusivité d'environ $0,35 \mathrm{x} 10^{-9}$ m^2/s.

Pour étudier plus à fond les mécanismes CS et CF, nous résolvons le problème spatio-temporel de l'effet ICP de l'électrolyte de fond et de l'analyte en implémentant une discrétisation logarithmique en temps. Cela nous permet de partir d'une condition d'équilibre des doubles couches électriques et distributions de concentration avant d'introduire très rapidement un champ appliqué et observer l'évolution de la dynamique de transport électrocinétique sur une période prolongée jusqu'à un état stationnaire. Les figures 3 (c) et 3 (d) illustrent une extrusion temporelle logarithmique de la concentration de l'échantillon sur la ligne centrale pour analytes avec des diffusivités de $0,2 \mathrm{x} 10^{-9}$ m^2/s et $2 \mathrm{x} 10^{-9}$ m^2/s. Les profils sont colorés et empilés verticalement pour créer un axe de position horizontal et un axe de log (temps) vertical. Comme l'échantillon avec coefficient de diffusion $2 \mathrm{x} 10^{-9}$ m^2/s a essentiellement la même diffusivité que les ions KCl, la dynamique de l'effect ICP de ces échantillons reflètent ceux des distributions évolutives des ions BGE qui régissent l'écoulement du fluide et les champs électriques. On observe que la région d'épuisement croît linéairement dans le temps, car le front d'épuisement se propage de l'interface du canal à sa position d'état stable ultime environ 250 µm de l'entrée du nanocanal. La région d'accumulation croît également linéairement dans le temps, bien que à un rythme plus lent que la zone d'épuisement rapide, ce qui génère un champ électrique local important et subit par la suite une vitesse de propagation de front plus élevée. Pour un échantillon moins mobile avec une diffusivité de $0,2 \mathrm{x} 10^{-9}$ m^2/s, la figure 3 (d) prédit que la préconcentration se manifestera dans les deux microcanaux, bien qu'à des échelles de temps différentes. Comme la distribution de la concentration de l'électrolyte de fond évolue en raison de l'ICP, le transport des ions de l'échantillon sera considérablement influencé par le front d'épuisement qui se propage.

En analysant la dynamique spatio-temporelle pour des échantillons de mobilité variable, on peut identifier les régimes utiles pour la préconcentration et régler la conception et/ou les conditions de fonctionnement d'un système pour maximiser la concentration d'un analyte donné. La figure 3 montre que, si un front de préconcentration est souhaité, le plus grand niveau d'enrichissement sera obtenu pour un CF à l'interface microcanal-nanocanal.

Résultats expérimentaux

Fabrication du moule et des puces en h-PDMS/verre

Les expériences d'electropéconcentration ont été réalisés sur puces mixtes hard-PDMS/verre à l'aide d'un moule de 2 pouces. Sur la figure 4, une photo du moule en silicium contenant quatre motifs de type "H". Les images à droite montrent le zoom de la partie centrale d'un motif qui incorpore cinq nanocanaux de 100 µm de long avec différentes largeurs variant de 250 nm à 450 nm (figure 4 B) et une image SEM d'un seul nanocanal (figure 4 C). Les principales étapes de fabrication du moule sont illustrées dans la figure 4 D.

Les étapes de fabrication des puces h-PDMS/verre sont présentées à la figure 5 et décrites comme suit :

1. Tout d'abord, du polydiméthylsiloxane dur (h-PDMS) est déposé par centrifugation sur le moule. Ensuite, le PDMS est directement appliqué par centrifugation sur la couche liquide

de h-PDMS.

2. Une fois le PDMS réticulé, le moule et une lame de verre sont activés par traitement plasma.
3. La lame de verre est mise en contact avec le moule et collée grâce à une couche de PDMS liquide.
4. Les résidus de PDMS entourant la lame de verre sont nettoyés sur le moule.
5. Dans une étape suivante, la lame de verre contenant le motif est détachée du moule.
6. La puce h-PDMS et une lamelle en verre avec des réservoirs percés sont activés avec un plasma et ensuite mis en contact pour coller la puce PDMS.
7. Pour l'injection de liquide, un bloc de PDMS (précédemment percé) est collé à la puce par un traitement plasma.
8. Enfin, des connecteurs fluidiques qui incluent les électrodes sont introduits dans le h-PDMS/verre puce pour injecter les solutions.

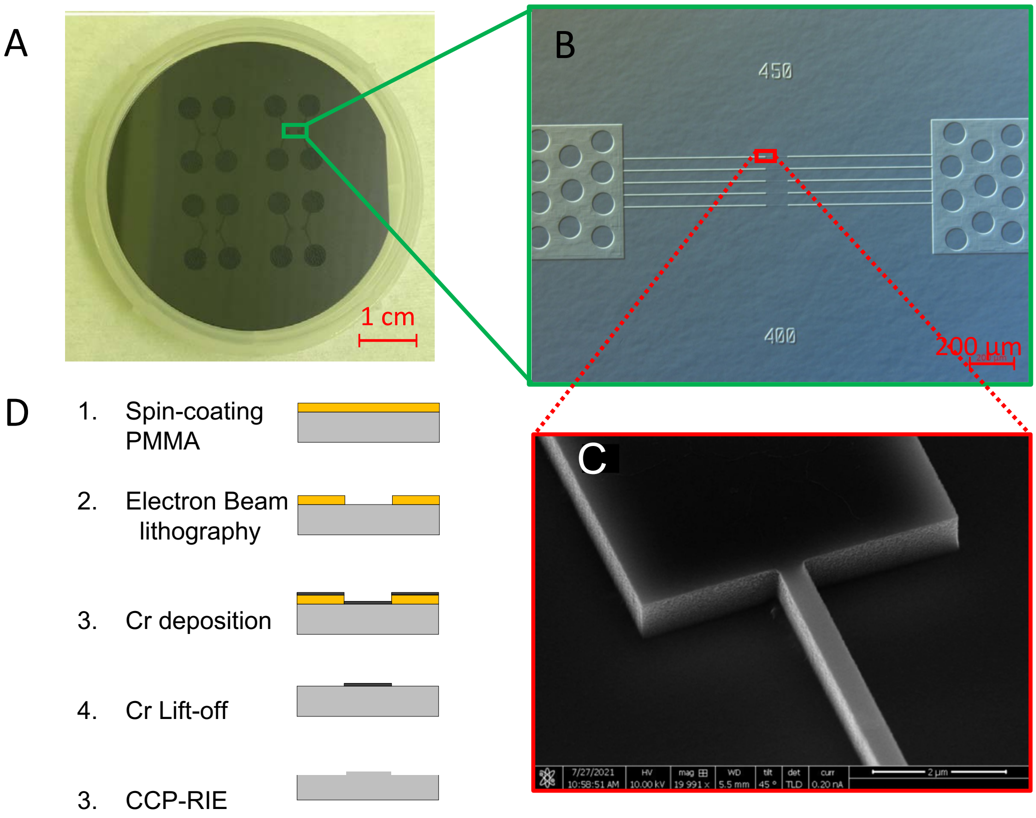

Figure 4: A) Moule en silicium avec zoom correspondant à la partie centrale d'une puce (B) et une photo MEB du nanocanal (C). En (D) une illustration des principales étapes de fabrication du moule.

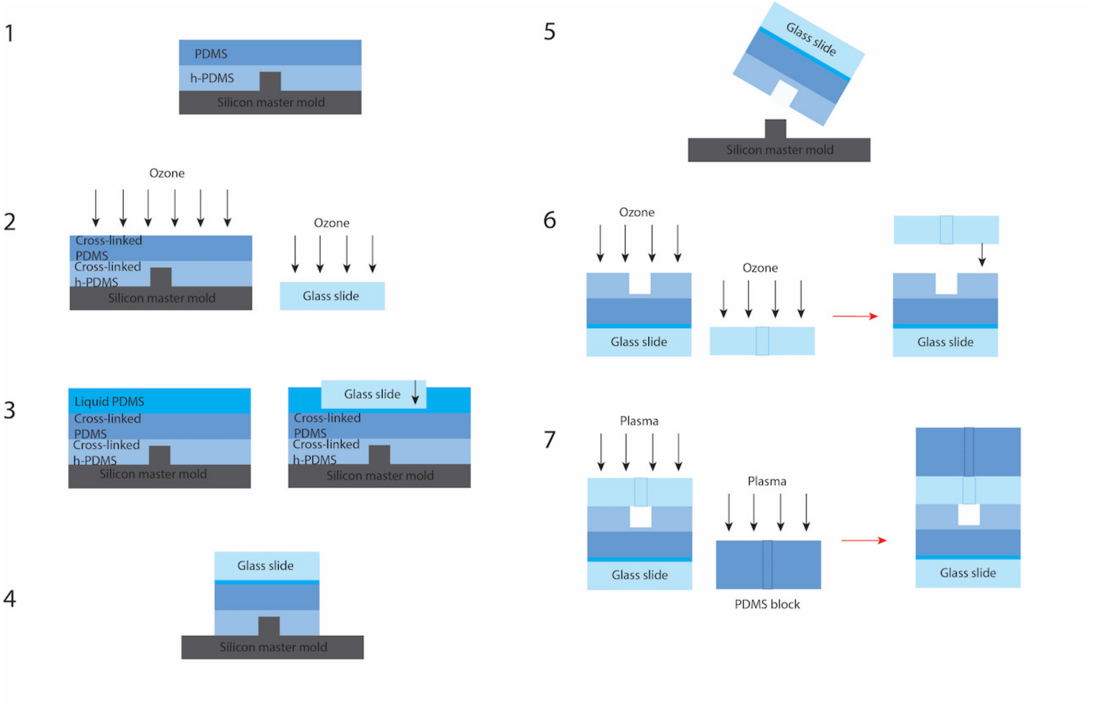

Figure 5: Procédé de fabrication de puces h-PDMS/verre.

Electropreconcentration de la fluorescéine

Nous présentons sur la figure 6 la préconcentration de la fluorescéine 10 µM dans une solution de NaCl 10 µM dans une puce h-PDMS/verre. Dans ce cas, la puce que nous avons utilisée intègre une quinzaine de nanocanaux avec différentes longueurs et largeurs. La figure 6 B présente l'image en fluorescence mesurée après 600 secondes d'électro-préconcentration. On observe uniquement le spot de préconcentration dans le dernier nanocanal de 100 µm de 450 nm de large (rectangle vert - longueur L=100 µm). Les nanocanaux plus étroits ne produisent pas de spots visibles pour ce temps de 600 secondes. La position des nanocanaux de 100 µm de long est indiquée par les lignes verticaux rouges en pointillé. Dans la figure 6 C, le nanocanal (indiqué par une barre grise) et certaines parties de l'anode et les réservoirs cathodiques sont analysés. Les profils d'empilement cathodique (CS) sont visibles dans tous les cas conformément à la théorie. Lorsque le champ électrique passe de 80 V/cm à 100 V/cm, le facteur de préconcentration augmente considérablement sans contre-pression (électropréconcentration classique à ΔP = 0 bar). J'ai aussi mené des expériences en appliquant une contre-pression ΔP, appliquée du réservoir cathodique vers le réservoir anodique [1]. En appliquant cette contre-pression ΔP = 0,2 bar, on obtient des valeurs de préconcentration de 40 et 50, respectivement. Si la contre-pression est augmentée à ΔP = 0,4 les profils CS réduisent leur valeur de facteur de préconcentration. De plus, les profils CS semblent plus étendus au long du réservoir cathodique à 80 V/cm que ceux à 100 V/cm. L'électropréconcentration dans les puces h-PDMS/verre nécessite des champs électriques élevés (80 V/cm et 100 V/cm) comparativement à des puces similaires fabriquées tout en verre [2].

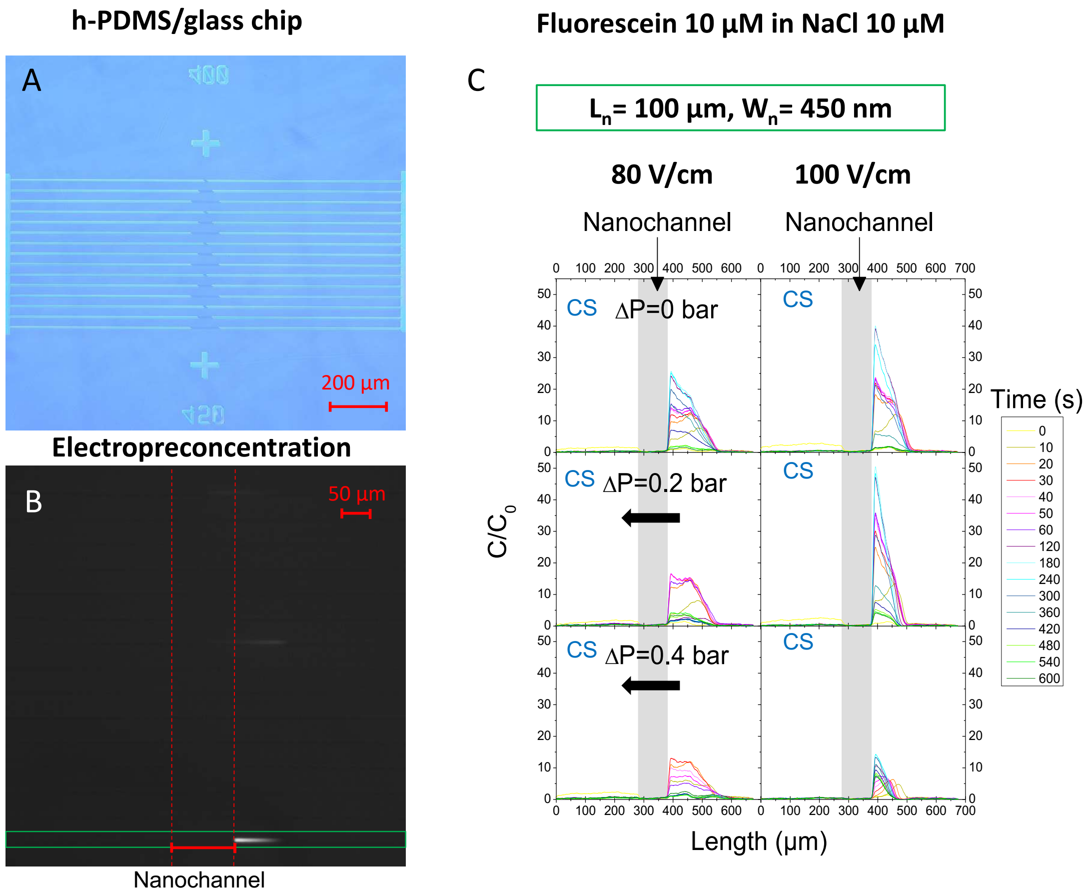

Figure 6: A) Image de la puce h-PDMS/verre utilisée pour l'expérience. B) Image de préconcentration de la fluorescéine après 600 s. C) Profils normalisés d'électropréconcentration de la fluorescéine dans NaCl pour différentes pressions et champs électriques.

Electropreconcentration de l'ovalbumine

Pour les expériences avec l'ovalbumine marquée Texas Red 10 M, nous avons utilisé NaCl comme électrolyte de fond avec une concentration de 10 µM. La puce h-PDMS/verre intègre quinze nanocanaux présentés dans la figure 7 A. L'image de préconcentration de l'ovalbumine après 600 s est montrée sur la figure 7 B où nous avons observé différents fronts de préconcentration à l'entrée des nanocanaux. Le nanocanal de 250 nm de large est encadré avec un rectangle violet et le nanocanal de 400 nm de large est encadré d'un rectangle rouge. Ce sont ces deux largeurs de nanocanaux qui produisent des spots analysables. Dans cette image, nous indiquons la position des nanocanaux de 100 µm de long avec des lignes pointillées parallèles rouges.

La préconcentration à l'intérieur des canaux h-PDMS/verre apparaît au niveau du réservoir anodique (à gauche de la barre grise) lors de l'application d'un champ électrique de 80 V/cm, comme indiqué dans la figure 7 C. Comme prévu par la théorie, les profils d'empilement anodique (AS) apparaissent pour un nanocanal de W_n = 250 nm pour différentes pressions de l'anode vers la cathode (ΔP = 0, ΔP = 0,4 et ΔP=0,8) et avec un facteur de préconcentration supérieur à 250. Si la largeur du nanocanal est augmentée à 400 nm, des profils d'empilement anodique (AS) apparaissent à l'entrée anodique du nanocanal avec un facteur de préconcentration supérieur à 325. Le cas de 400 nm et ΔP=0,4 bar semblent être un profil AF propageant mais cela reste à vérifier car au moment de ces expériences, le protocole de nanostructuration n'était pas optimal. Il est possible que ce nanocanal de 400 nm ait un défaut de fabrication. Ces résultats confirment que les canaux plus larges (jusqu'à 400 nm de large) fonctionnent expérimentalement.

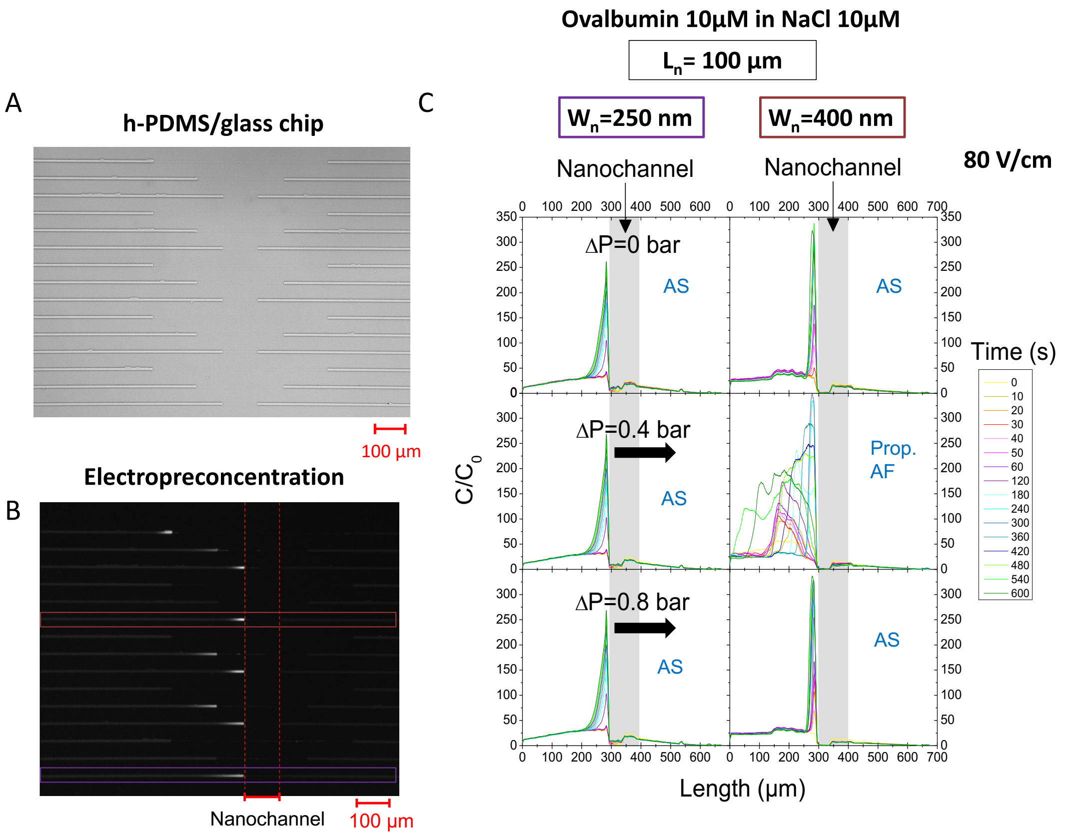

Figure 7: A) Image de la puce h-PDMS/verre utilisée pour l'expérience. B) Image de préconcentration d'ovalbumine après 600 s. C) Profils normalisés d'électropréconcentration de l'ovalbumine dans NaCl pour différentes pressions et champs électriques.

Electropreconcentration de l'ADN

Nous montrons sur la figure 8 A une image de la puce h-PDMS/verre utilisé pour les expériences avec l'ADN de l'hépatite C. Nous présentons une photo de préconcentration de l'ADN après 60 s. Nous avons réalisé des expériences d'électro-préconcentration classique ($\Delta P = 0$) et avec contre-pression ΔP du réservoir anodique vers le réservoir cathodique.

Comme précédemment, la position du nanocanal est indiquée par la ligne verticale rouge en pointillée et le canal d'intérêt est encadré d'un rectangle vert (figure 8 B). La figure 8 C présente les profils de préconcentration dans un nanocanal de 250 µm de long et 350 nm de large (position indiquée par la barre grise). Lorsqu'on applique une pression extérieure $\Delta P =$ 0,8 de l'anode à la cathode, un profil de focalisation anodique (AF) stable est obtenu, comme attendu par la théorie [3], avec un faible facteur de préconcentration de 4. Lorsque le champ électrique augmente jusqu'à 100 V/cm, un profil de focalisation anodique propageant apparaît et un facteur de préconcentration plus élevé de 20 est obtenu. Ce sont ces paramètres 80 V/m et $\Delta P =$ 0,8 bar qui sont les paramètres optimaux permettant d'obtenir un régime AF stable au cours du temps. Les profils sous haute pression ΔP=1 bar conduisent à un profil de focalisation anodique propageant à un champ électrique de 80 V/cm qui est stabilisé à une tension élevée appliquée de 100 V/cm. En effet, ce dernier profil commence par une focalisation anodique (AF) propageant et, après 120 secondes, il reste stable avec un facteur de préconcentration d'environ 13. L'ensemble de nos expériences menées avec l'ADN montre qu'une longueur de 250 µm du nanocanal est préférable à une longueur classique de 100 µm, ce qui est en accord avec la théorie de l'effet ICP.

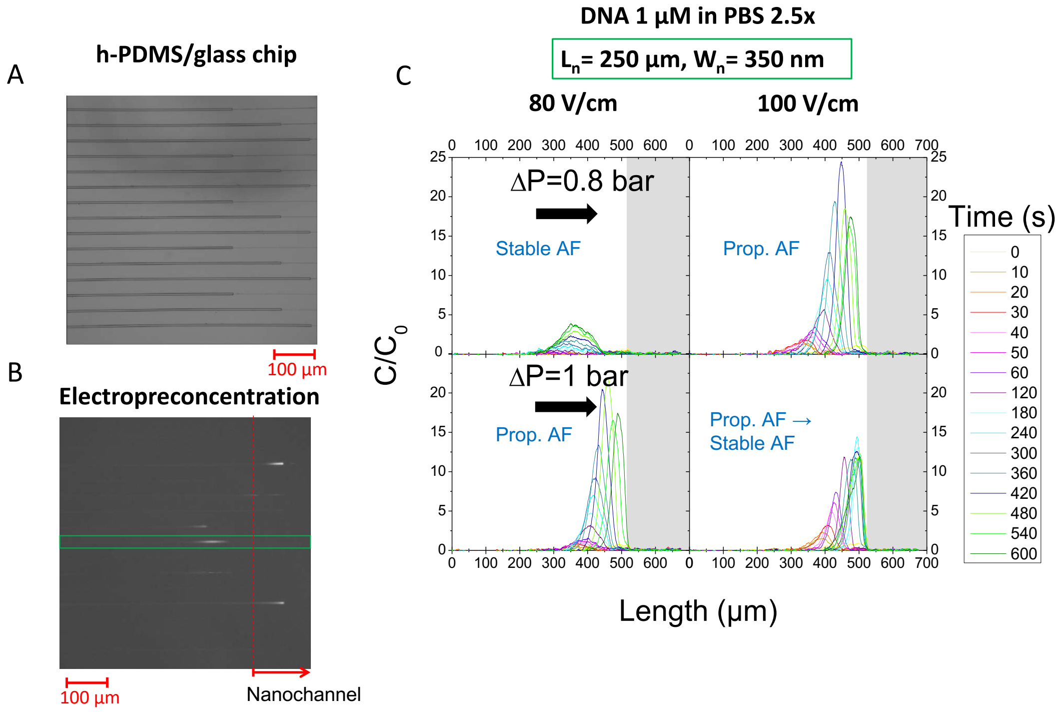

Figure 8: A) Image de la puce h-PDMS/verre utilisée pour l'expérience. B) Image de préconcentration de l'ADN après 60 s. D)Profils d'électropréconcentration normalisés de l'ADN dans du PBS 2,5x à l'intérieur d'un nanocanal de 250 µm de long et 350 nm de largeur à deux champs électriques et pressions différents.

Acknowledgments

I would first like to thank all members of my dissertation committee: M. Pierre Joseph and M. Vincent Senez who accepted to be rapporteurs of my manuscript and who gave me advice to improve my work; M. Claude Fermon and Mme. Catherine Perrin who accepted to be examiners and judged my work.

I would like to express my genuine gratitude to my supervisors Anne-Marie Haghiri-Gosnet and Antoine Pallandre not only for their time and patience, but for all the advice and support during my doctoral studies. Your feedback pushed me to sharpen my thinking and brought my work to a higher level. Thank you for all the contributions to my development as a scientist.

My sincere thanks also to the cleanroom engineers, Dominique Decanini, Edmond Cambril, Laurent Couraud, David Bouville, Abdou Harouri and Christophe Dupuis who helped me in the fabrication of the chips and gave me so much useful advice.

I would like also express my deep appreciation to all the members of the BIOSYS team. Specially to Isabelle, Bernard, Jean, Mery, François-Damien, Choayb, Julie, Claire, Martina Freisa and Sasa.

Finally, but not least, I would like to thank my parents and my brother for their unconditional love and support.

Contents

Chapter 1

Introduction

1.1 Micro and Nanofluidics

Microfluidics studies fluid behaviors in miniaturized systems with at least one dimension smaller than 100 µm. The origins of microfluidics are based on established disciplines to develop micro-analytical tools for biological and chemical applications [4]. The first analytical application of microfluidics was presented by Terry *et al.* [5] in 1979. Now considered as the first Lab-on-a-chip (LOC), they describe a microscale gas chromatography system fabricated with photolithography and etching techniques to identify peaks associated to a component from a mixture. One decade later, at the beginning of the 1990s, Manz *et al.* [6] introduce the concept of miniaturized total analysis systems (µTAS). These systems integrate all functions for analysis: sampling, injection, separation and detection. Advances in microfluidics since the creation of the transistor until the 3D printing devices have been developed in the last years [7].

Nanofluidics is a field that refers to the study of flows in nanometer-scale systems. It was introduced as an analogue of microfluidics. Even if nanofluidic phenomena were already studied for more than a century in diverse disciplines [8], nanofluidics name appears in the nineties. In recent decades, advances in fabrication of nanofluidic devices help the development of this field. Applications include water-energy technologies [9], detection and biological and chemical analyses such as analyzing DNA, metabolites, cells or viruses [10], desalination [11] or nanofluidic circuitry [12].

Miniaturized fluidic devices offers many advantages compared to conventional fluidic platforms. Due to the smaller dimensions, reaction times are faster. In effect, as the characteristic dimensions of a system are decreased, the diffusion time is shortened for any given molecule, leading to quicker reaction times in the system. Additionally, micro and nanofluidic systems consume less sample and reagents due to their reduced size. At the micrometric and nanometric scale, the fluid physics is different from the macroscopic scales allowing the exploration of unique features. Surface tension effects become predominant compared to volume effects; capillary forces also begin to dominate gravitational forces [13]. Microfluidics and Nanofluidics offer the possibility of integration of many components into one compact device and higher sensitivity [14].

1.2 Electrokinetic effects at the liquid-solid interface

1.2.1 The electrical double layer (EDL):

An aqueous solution in contact with a solid surface acquires specific electric charges at the liquid-solid interface that mainly arise from the adsorption or dissociation of surface groups. Due to the fixed surface charge at the solid interface an oppositely charged region of counterions is developed in the liquid to maintain the electroneutrality of the solid-liquid interface. This screening region is known as the electrical double layer (EDL) because ideally it consists of opposite charges, some of which are bound while others are mobile.

Hermann von Helmholtz proposed the earliest model describing the EDL in 1850. His model states that free counterions in the solution are attracted by the charged interface and co-ions are repelled due to Columbic forces. Then, ions redistribute in a parallel plane called the Helmholtz plane (figure 1.1 A), situated a distance from the surface, to balance the charge on the solid-liquid interface. Helmholtz model laid the foundation for describing the solid-liquid interaction, but it was not realistic since it did not consider the thermal motion of the counterions and adsorption.

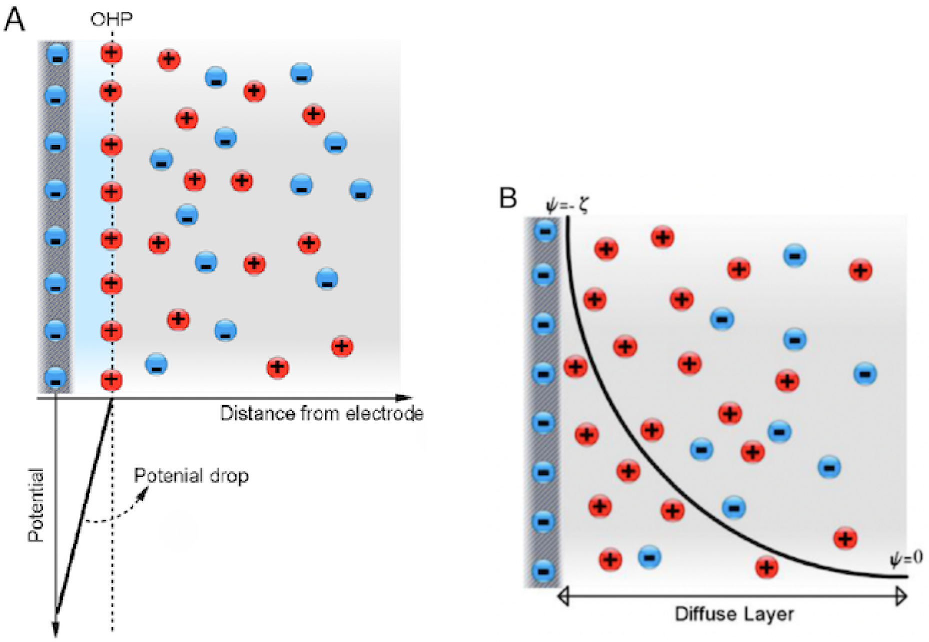

Figure 1.1: (A) Illustration of Helmholtz EDL model, where the surface is negatively charged, and positive ions (counterions) are attracted to the Helmholtz plane. (B) Schematic of the Gouy-Chapman model, the electric potential to drop exponentially normal to the surface [15].

Later, the idea of a diffuse layer was introduced by Louis Georges Gouy and David Leonard Chapman, independently. The resulting model was named **the Gouy-Chapman model** which predicted that counterions are not rigidly attached to the surface, rather they will spread out in space forming a diffuse layer. The counterions in this layer feel the local electrostatic potential from the charged solid-liquid interface and follow the Boltzmann distribution,

$$c_i = c_{i,\infty}\ exp\left(\frac{z_i e\psi}{k_B T}\right) \tag{1.1}$$

where c_i, $c_{i,\infty}$, z_i, k_B, and T represent the i$^{\text{th}}$ ionic concentration, the bulk ion concentration, the ionic valence, Boltzmann constant, and the absolute temperature of the solution, respectively. The model predicted the electric potential to drop exponentially normal to the charged plane (figure 1.1 B). However, the assumption that ionic species are point charges do not accurately represent the reality since the distributed ionic concentration was predicted to be infinitely large at highly charged solid–liquid interfaces.

To overcome the limitations of both models, Otto Stern proposed a combination of **the Helmholtz and Gouy-Chapman models** through a two layers composed EDL. The first one an immobile layer of hydrated ions and the second one a diffuse layer. The Gouy-Chapman-Stern model states that the electric potential has a linear variation from the solid surface to a Stern plane potential. The boundary layer that limits the region where ions are immobile (Stern layer) and beyond where ions are assumed to be mobile point charges (diffuse layer) is the slip plane with electric potential equal to the zeta potential ζ (figure 1.2). The zeta potential is an important parameter that governs EDL composition and coupled effects such as electroosmotic flow (see next section).

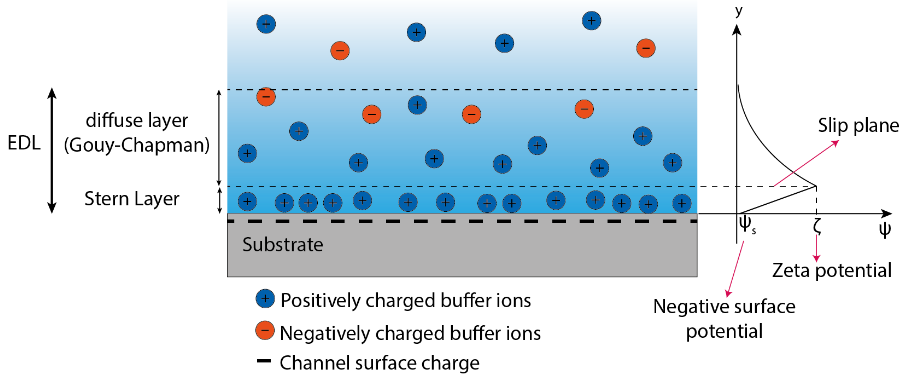

Figure 1.2: Schematic of Gouy-Chapman-Stern model of the solid-liquid interface for a negative charged channel and the corresponding potential distribution.

Theories of Helmholtz, Gouy, Chapman and Stern provide an understanding of the surface charge at the solid–liquid interface. Nevertheless, they were still deficient in some aspects such as overlook chemical reactions on the solid–liquid interface and the solution pH effect. In addition, both the surface charge and zeta potential cannot be calculated considering the pH of the solution and the concentration of ions.

It took 50 years until Davis *et al.* [16] proposed a detail surface model which assume that Stern layer comprises two layers as part of the immobile layer. This third model called the electrical triple layer (ETL) is illustrated in figure 1.3. This triple layer still exhibits the two main layers: a mobile layer, called the diffuse layer and a compact layer called the Stern layer. However, in this model, the Stern layer is divided in two planes: the inner Helmholtz plane that bears the potential ψ_i and the outer Helmholtz plane with potential ψ_d, where co-ions and counterions are adsorbed to the surface. The slip plane or shear surface is an imaginary plane separating ions that are in immobile at the surface from those that are mobile in solution. The potential at this plane is called zeta potential (ζ) and is dependent on the pH and the ionic strength of the solution.

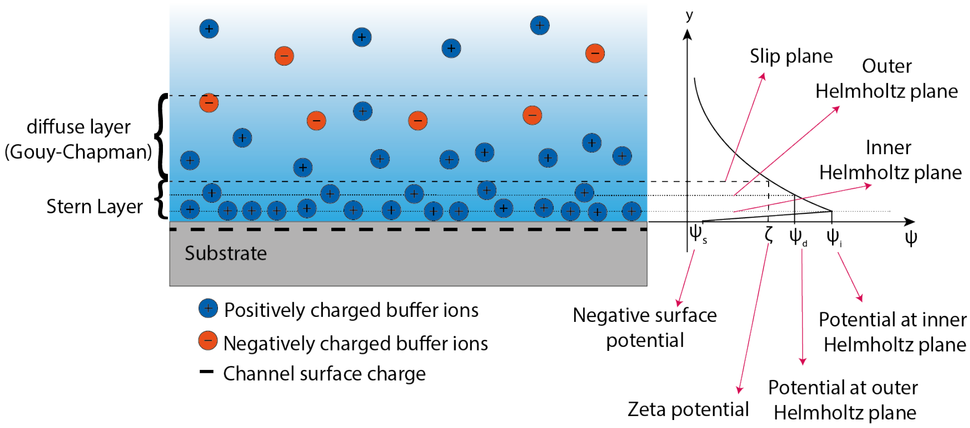

Figure 1.3: ETL model of the solid-liquid interface for a channel with negative surface potential ψ_s with the corresponding potential distribution.

Because in this work we do not consider all the chemical reactions at the solid–liquid interface and the impact of the pH of the solutions, **the simpler conventional Gouy-Chapman-Stern model** was estimated to be sufficient for the description of our nanofluidic devices. One should note that the more complex electrical triple layer model was developed for nanofluidic transistors, devices with integrated metallic gates. In this PhD work, no modification of the zeta potential by such integrated material was done.

The EDL thickness is characterized by the Debye length λ_D and can be calculated by:

$$\lambda_D = \sqrt{\frac{\epsilon RT}{2F^2 c_0}} \tag{1.2}$$

where, ϵ is the dielectric constant, R is the gas constant, T is the temperature, F is the Faraday's constant and c_0 is the ionic strength of the electrolyte. The Debye length changes as function of the electrolyte concentration, and not as function of the zeta potential. Indeed, the lower the ionic strength, the greater the thickness of the diffuse layer as presented in the next Table 1.1. For ionic strength lower than 10^{-4} M, the Debye length can reach several tens of nanometers. This range of ionic strength corresponds to the one of interest for specific electrokinetic effects in nanofluidics.

In nanometers domains, in sub-200nm wide nanochannel for example, the EDL generated at opposite walls can overlap at very low ionic forces. This fact leads to a virtual exclusion of the co-ions in the nanochannels which will be describe later.

KCl concentration (M)	**Debye length λ_D (nm)**
1	0.3
10^{-1}	1.0
10^{-2}	3.1
10^{-3}	9.6
10^{-4}	30.5
10^{-5}	96.3

Table 1.1: Debye length values at different concentration. From [17].

1.2.2 Electroosmosis

Electroosmosis is a non-equilibrium effect where a bulk flow called electroosmotic flow (EOF) is generated by an applied external electric field across capillaries or microchannels filled with an electrolyte solution. Figure 1.4 illustrates a negative charged microchannel. In the bulk region, beyond the diffuse layer, the electrostatic potential arising from the wall charge is zero. Indeed, local attractive or repulsive forces on ions are non-existent due to the EDL which acts as an electrostatic screening of the wall charge. At the Stern and the diffuse layers, the potential distribution decays exponentially.

When applying an external electric field, net ionic charges in the EDLs migrate along the tangential field due to Coulombic forces carrying the fluid with it by viscous drag. Coulombic forces act only in the EDL, where there is an imbalance between anionic and cationic ions, causing the electroosmotic flow. The velocity profile is equal to zero at the slip plane and becomes uniform in the bulk region.

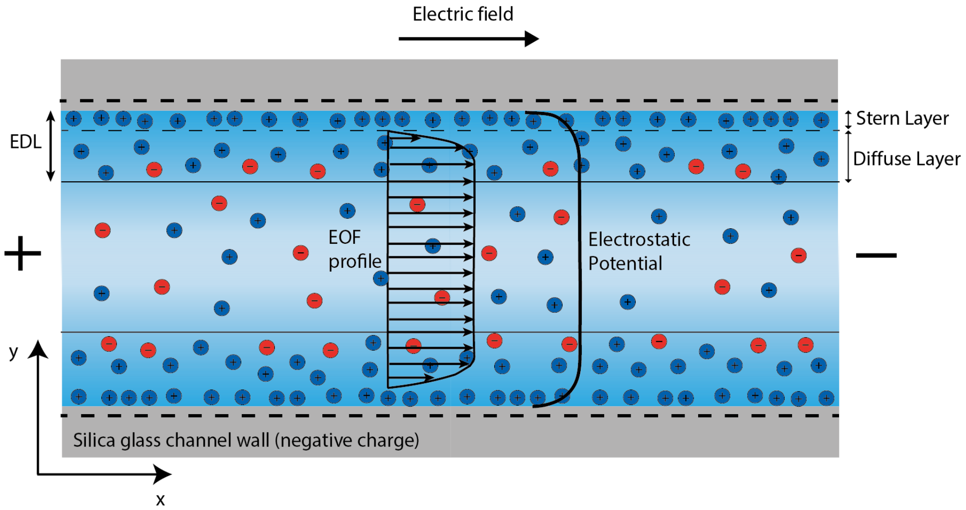

Figure 1.4: Electroosmosis in a microchannel.

The velocity of the EOF is linearly proportional to the applied electric field and depends on the zeta potential, the material of the microchannel and the solution in contact with the microchannel wall. First described by Smoluchowski and considering that EDL is thin in comparison with the microchannel height, it is given by:

$$\overrightarrow{\nu}_{EOF} = -\frac{\epsilon_0 \epsilon_r \zeta \overrightarrow{E}}{\eta} \tag{1.3}$$

where E is the electric field, ϵ_0 the permittivity of free space, ϵ_r the dielectric permittivity, ζ is the zeta potential and η is the dynamic viscosity of the fluid. From this equation, the electroosmotic mobility is:

$$\mu_{EOF} = -\frac{\epsilon_0 \epsilon_r \zeta}{\eta} \tag{1.4}$$

1.2.3 Electrophoresis

Electrophoresis describes the migration and separation of charged ions under an electric field. If a charged analyte is injected in a microchannel containing an electrolyte solution, the analyte migrates under the influence of the electric field. The migration depends on the charge and mobility of the analyte and is called electrophoretic flow (EP). Electrophoretic conditions are also characterized by the chemical nature of the ions, ionic strength, pH value or viscosity, to name a few, of the electrolyte solution where analytes move.

The velocity of the EP is given by:

$$\overrightarrow{\nu}_{EP} = \mu_{EP} \overrightarrow{E} \tag{1.5}$$

where μ_{EP} is the electrophoretic mobility and E is the electric field. As the electrophoretic mobility is dependent on the thickness of the electrical double layer it can be divided into categories of thin and thick EDLs. For an EDL that is thin compared to the molecular radius, electrophoresis is the converse of electroosmosis and it is given by the Helmholtz-Smoluchowski limit,

$$\mu_{EP} = \frac{\epsilon_0 \epsilon_r \zeta}{\eta} \tag{1.6}$$

where ϵ_0 the permittivity of free space, ϵ_r the dielectric permittivity, ζ is the zeta potential and η is the dynamic viscosity of the fluid. On the other hand, for a thick EDL, the force acting on the molecule is the difference between the drag and Coulomb forces, leading to:

$$\mu_{EP} = \frac{q}{f} = \frac{q}{6\pi\eta r} \tag{1.7}$$

where f is the friction coefficient, q is the charge of the analyte, η is the viscosity of the liquid and r is the mean radius of the molecule.

Here, therefore, for a negative charged analyte it exists a competition between the electroosmotic flow and the electrophoretic flow which oppose or in some cases add each other. The velocity of the analyte is then given by the relation:

$$\overrightarrow{\nu} = \overrightarrow{\nu}_{EOF} + \overrightarrow{\nu}_{EP} = (\mu_{EOF} + \mu_{EP})\overrightarrow{E} \tag{1.8}$$

Thus, analytes can be separated and detected thanks to the difference in mobility and/ or charge from solutions containing several analytes. In this thesis we focus on nanofluidic chips where it is possible to create local focal points where the analyte preconcentrate over time under specific experimental conditions (electroosmotic flow and electrophoretic flow are perfectly balanced). This separation/detection technique is known as electropreconcentration by ion concentration polarization (ICP) of the background electrolyte (BGE) solution.

1.3 Ion Concentration Polarization (ICP) effect

In the field of bioanalysis, the separation and the detection of analytes a very low concentrations are necessary in order to earlier diagnose hard-to-treat diseases or to detect harmful biochemical agents that can cause a danger, to give few examples. Advances in fabrication technologies have been the base for the development of bioanalytical micro and nanofluidic devices. Electrokinetic-based methods such as field-amplified sample stacking (FASS) [18–20], ion concentration polarization (called ICP) [3, 21–27], isotachophoresis [28], isoelectric focusing [29–31], concentration gradient focusing [32] and other methods have been introduced for concentrating samples in nanofluidic systems. In this thesis we go in depth in the study of ICP-based focusing electropreconcentration.

Typically, ICP is induced across nanochannels or membranes that play the role of ion-selective filters between microchannels. In previous section we have described the EDL in a conventional microchannel. To better understand ICP effect, let us introduce the case of a negative charged nanochannel that has been integrated inside a microchannel (figure 1.5). In low ionic strength regimes, at nanometric scales, the EDL occupies an important portion across the nanofluidic channel. The two face-to-face electric double layers (EDLs) in the nanochannel are insufficient to fully screen the electric field arising from the interfacial surface. Thus, since co-ionic species (Cl^- for KCl BGE) are electrostatically excluded to some extent from the nanochannel, only counterions (K^+ for KCl BGE) can be transported through the nanochannel. Indeed, to maintain the electroneutrality, the concentration of counterions must be bigger than that of co-ions inside the nanochannel, thus triggering an ion-selective behavior. The electric potential even at the center of the nanochannel is influenced by the surface charge and is not equal to the bulk potential.

Under the influence of an applied electric field, the previously described charge exclusion and the competition or addition between electroosmotic flow (EOF) and electrophoretic migration (EP) lead to unbalanced ionic transport between anionic and cationic species of an electrolyte solution across the microscale-nanoscale interface. Transport of counterions is favored from the anodic to the cathodic side of the nanochannel whereas the co-ions are excluded from passing along the nanochannel from the cathodic to anodic side. This mechanism creates an asymmetry in the ionic species concentration causing an ion enrichment zone at the cathodic side of the

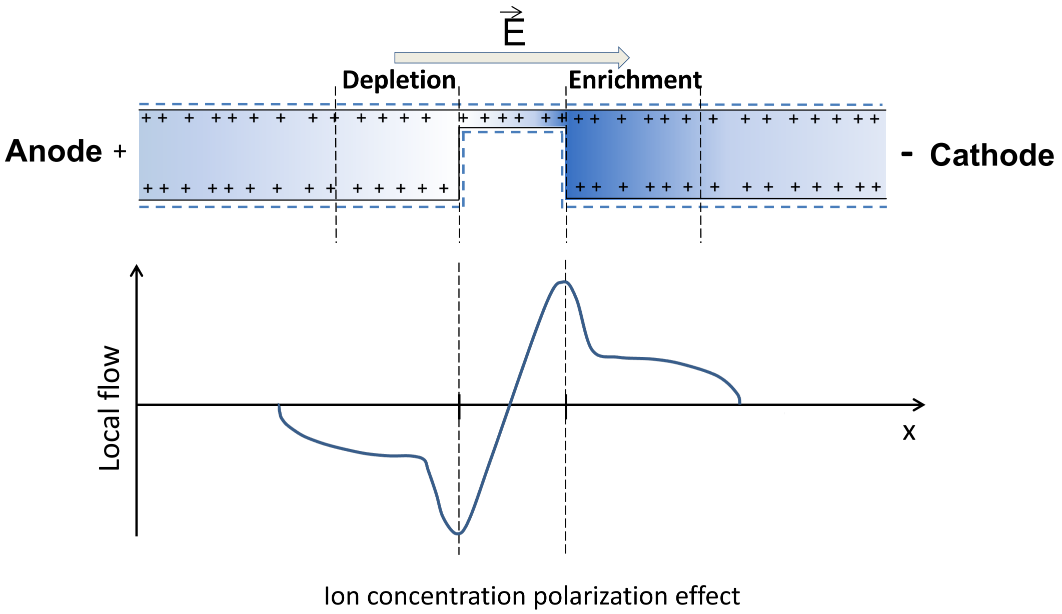

Figure 1.5: Enrichment and depletion zones in a micro/nano/microfluidic device known as Ion concentration polarization effect.

nanochannel and an ion depletion zone at the anionic side of the nanochannel. **The result is thus a "polarization" of the concentration distribution, in which background electrolyte ions are depleted on one side of the nanochannel and accumulate at the other** [25, 33]. This enrichment-exclusion effect is called **ICP effect**.

Assuming that we introduce a negative charged analyte, the electroosmotic flow drives the bulk solution (counterions, co-ions and negative charged analyte) toward the cathode. In contrast, electrophoretic flow drives co-ions and negative charged analyte toward to the opposite direction, the anode. The balance of these two flows lead to preconcentrate the analyte at certain location of the fluidic channel (figure 1.6). By controlling this competition of forces, it is possible to create a stable focal point where the analyte is preconcentrated. In this work, we have integrated several nanochannels as presented in figure 1.5 in a single chip to study the role of the width and length of the nanochannel in the electropreconcentration.

Even if many experimental research has been done, few theoretical works describe the ICP effect and the electropreconcentration process.

1.3.1 The first analytical approach by Mani, Zangle and Santiago:

Mani *et al.* [25, 34] and Zangle *et al.* [24] in the American team of Prof. Santiago were the first to propose a general analytical theory describing ICP mechanisms. They have shown that ICP of the BGE is mainly governed by two key parameters:

1. The inverse Dukhin number $1/\mathrm{D_u}$, which describes the ratio of bulk conductivity G_{bulk} to surface conductance G_σ:

$$\frac{1}{D_u} = \frac{G_{bulk}}{G_\sigma} \tag{1.9}$$

Defined by:

$$c^*_{0,r}h^*_n = \left(\frac{\nu_1 z_1 - \nu_2 z_2}{-2\nu_1\sigma}\right) F h_n c_{0,r} \tag{1.10}$$

where ν_1 and ν_2 are the mobilities of the positive and negative species, z_1 and z_2 the valences of the positive and negative species, F is the Faraday's constant, h_n is the nanochannel height, $c_{0,r}$ is the BGE reservoir concentration and σ is the wall charge. Note that this parameter $c^*_{0,r}h^*_n$ is therefore the product of the normalized concentration $c^*_{0,r}$ and the normalized height of the nanochannel over the Debye length $h^*_n = h_n/\lambda_D$.

2. The velocity of the co-ion non-dimensionalized by the electroosmotic velocity, defined by:

$$\nu^*_2 = \frac{\nu_2 z_2 F \eta}{\zeta_n \epsilon} \tag{1.11}$$

where ζ_n is the zeta potential uniform along the structure, ϵ is permittivity and η is the viscosity.

They also noticed that ICP depends primarily on the inverse Dukhin number and not on the ratio of channel size to Debye length, even if this ratio was often mentioned as a key parameter. Similarly, the term “overlapped EDLs” that corresponds to a ratio of order unity should not be used, since ICP effects can be observed for systems with ratio of channel size to Debye length larger than 10 [24].

The ICP generates zones of enrichment of BGE (cathodic reservoir) and zones of depletion of BGE (anodic reservoir) with high and low conductivities. These conductivity gradients and the corresponding gradients of local electromigration of analytes produce a stacking/focusing phenomenon where the analyte can locate and thus concentrate. Zangle *et al.* distinguish two interfaces between the depletion (or enrichment) zone and the reservoir called the depletion shock and the enrichment shock, respectively, and two interfaces corresponding to the entrance and exit of the nanochannel. Those 4 interfaces where the analyte can locate are shown in the figure 1.6.

Studying ICP effect supposes then to calculate the ratio of bulk conductivity to surface conductivity $1/\mathrm{D_u}$ and the normalized velocity of co-ion ν^*_2. In the Table 1.2 we report the values of ζ_n, $1/\mathrm{D_u}$ and ν^*_2 for a 100 nm-width-nanochannel at different concentrations for two different surface charge densities and considering KCl as background electrolyte.

At higher values of surface conductivity $1/\mathrm{D_u} >> 1$ and low ν^*_2 values, the analyte will stack at the entrance of the nanochannel in a regime called non propagating ICP. Such stacking could not be used for real applications of preconcentration since the analyte is confined in the vicinity of the nanochannel. Depending on the analyte electrophoretic mobility, one would observe a cathodic stacking regime, called **CS**, at the nanochannel output in the cathodic microchannel reservoir (see Fig. 1.6 B at right), or an anodic stacking regime, called AS, at the nanochannel input in the anodic micro-reservoir (see Fig. 1.6 B at left). In Table 1.2, we observe this behavior at high BGE ionic strength, namely 1 mM.

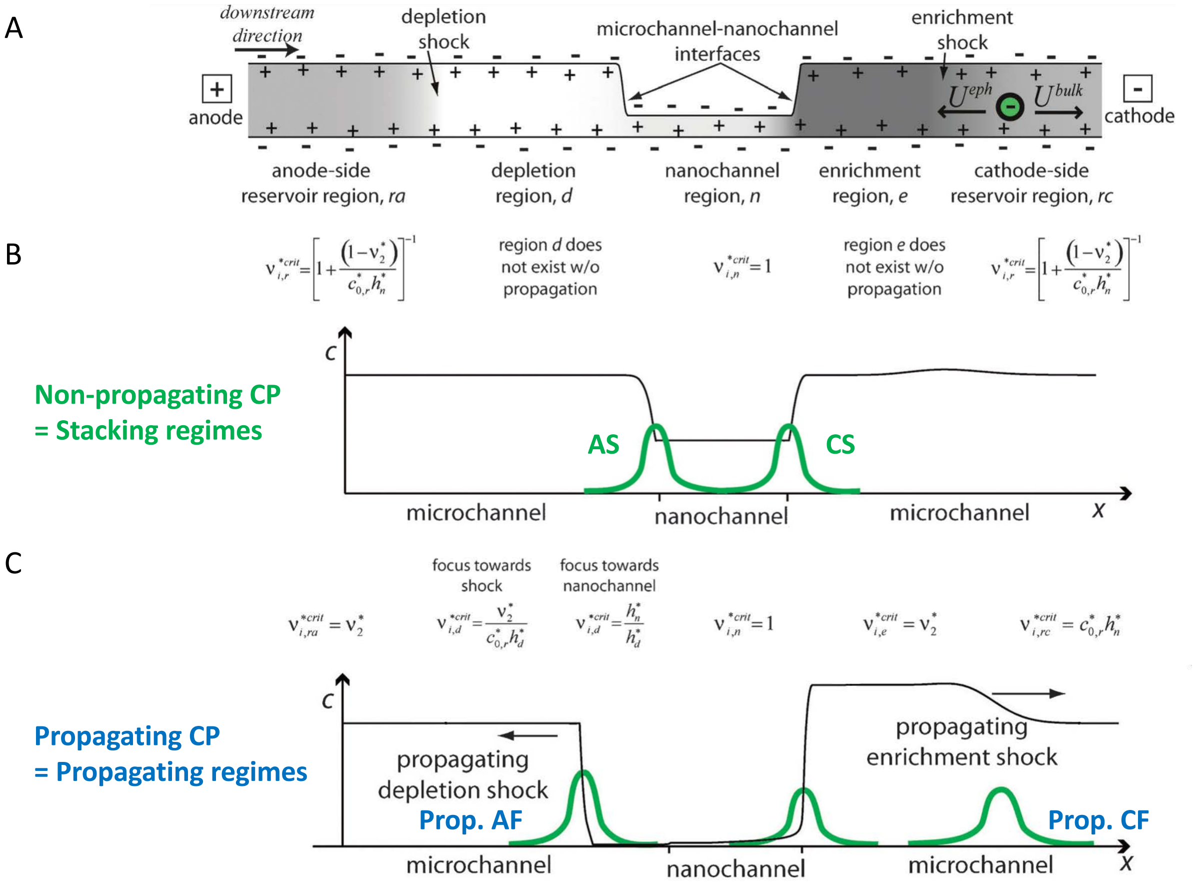

Figure 1.6: A) Schematic presenting a typical microchannel–nanochannel–microchannel layout with enrichment and depletion of the background electrolyte shown as a greyscale map (darker regions correspond to enrichment). B) Non-propagating ICP case. The black curve shows computed BGE concentration and green peaks represent possible stacking zones at the entrance/exit of the nanochannel for a low concentration anionic analyte. C) Propagating ICP case. The black curve also shows computed BGE concentration and green peaks show two possible focusing locations and one stacking location for analyte anions. Equations at the top of B) and C) are the critical values of ν_i^* for anionic analytes. Adapted from [24].

$\sigma = -1$ mC/m^2				$\sigma = -2.5$ mC/m^2			
Concentration BGE	ζ_n	**1/D$_u$**	ν_2^*	**Concentration BGE**	ζ_n	**1/D$_u$**	ν_2^*
10 µM	-86.7 mV	0.098	1.285	10 µM	-132 mV	0.039	0.844
50 µM	-51.4 mV	0.490	2.167	50 µM	-92 mV	0.195	1.211
100 µM	-39 mV	0.980	2.857	100 µM	-75.7 mV	0.391	1.472
1 mM	-13.4 mV	9.790	8.314	1 mM	-31.8 mV	3.912	3.503

Table 1.2: The zeta potential ζ_n, the inverse Dukhin number $1/\mathrm{D_u}$ and the velocity of the coion ν_2^* values considering a surface charge density of σ= -1 mC/m^2 (at left) and σ= -2.5 mC/m^2 (at right).

On the other hand, at low values of surface conductivity ($1/\mathrm{D_u} << 1$), the analyte will stack or focus somewhere along the enrichment shock in the cathodic reservoir or focus at the interface of the depletion zone in the anionic reservoir (see Fig.1.6 C) called propagating ICP.

An anionic analyte, such as fluorescein, diluted at low BGE concentration (down to 10 µM), will concentrate in the cathodic reservoir in an electrophoretically dominated regime. For fluorescein with $\nu^*_{ifluo} = 0.75$ at low concentration ($c_{\text{fluorescein}} = 10$ µM and $\mu_{\text{EP}} = -3.6\text{x}10^{-8}\text{m}^2\text{V}^{-1}\text{s}^{-1}$ [35]), the condition predicted by Zangle *et al.* [24]:

$\nu^{*crit}_{i,e} = \nu^*_2$ (in the cathodic enrichment zone) $> \nu^*_{ianalyte} > \nu^{*crit}_{i,rc} = 1/D_u$ (in the cathodic reservoir) is always respected, predicting stacking of fluorescein at the enrichment shock interface in the cathodic reservoir (see Fig.1.6 C – prop. CF).

To conclude here, the pioneer work of Santiago's team based on a very serious and complete analytical study was able to predict the two stacking regimes (CS and AS) at the two nanochannel input and output interfaces, and the propagating regimes at both depletion and enrichment interfaces inside the microchannels. However, this analytical study was unable to predict some experimental observations of stable AF and CF regimes at those interfaces inside the microchannels [36, 37]. In this context and at the same period around 2008, the theoretical work of A. Plecis based on 1D simulations should be reported and explained.

1.3.2 The 1D simulation approach by Plecis:

Plecis *et al.* [3] proposed a one-dimensional model based on a finite element calculation procedure to describe ion exclusion mechanisms using a straight microchannel integrating a 50 nm thick horizontal nanochannel. They studied the evolution of the apparent zeta potential (ζ_{app}) as function of the ionic strength of the background electrolyte defined as:
$\zeta_{\text{app}}(\text{x}) = \text{a}_{1,\text{m/n}}\left(1 - \tanh\left(\frac{-\log(\lambda(\text{x}))}{\text{a}_{2,\text{m/n}}} + \text{a}_{3,\text{m/n}}\right)\right)$ where m and n correspond to parameters in the micro or nanochannel and $\lambda(x)$ is the Debye length. At ionic strengths lower than 10^{-4} M, the apparent zeta potential remains constant in a nanochannel (very different in comparison with a microchannel) causing a constant permeability. This study also demonstrated the existence of four preconcentration regimes: the two stacking regimes at the entrance or exit of the nanochannel, called Anodic Stacking (AS) and Cathodic Stacking (CS), respectively, as previously observed by Mani and Zangle in their analytical study; but also two focusing regimes where preconcentration appears at hundreds of microns from the nanochannel, called Anodic Counter Gradient Focusing (ACGF) and Cathodic Counter Gradient Focusing (CCGF), respectively (see figure 1.9). For simplicity, these last two terms are replaced by Anodic Focusing (AF) and Cathodic Focusing (CF) along this thesis.

According to Plecis *et al.*, the variation of the electrophoretic flow along the structure can be explained by: i) a sharp increase of the potential caused by the exclusion-enrichment effect at nanochannel entrances; ii) a smooth decrease (increase) of the electrophoretic flux in the cathodic (anodic) microchannels when the molecules try to cross the nanochannel due to the increase (decrease) of the ionic concentration at the cathodic (anodic) side of the nanochannel, caused by the ICP effect.

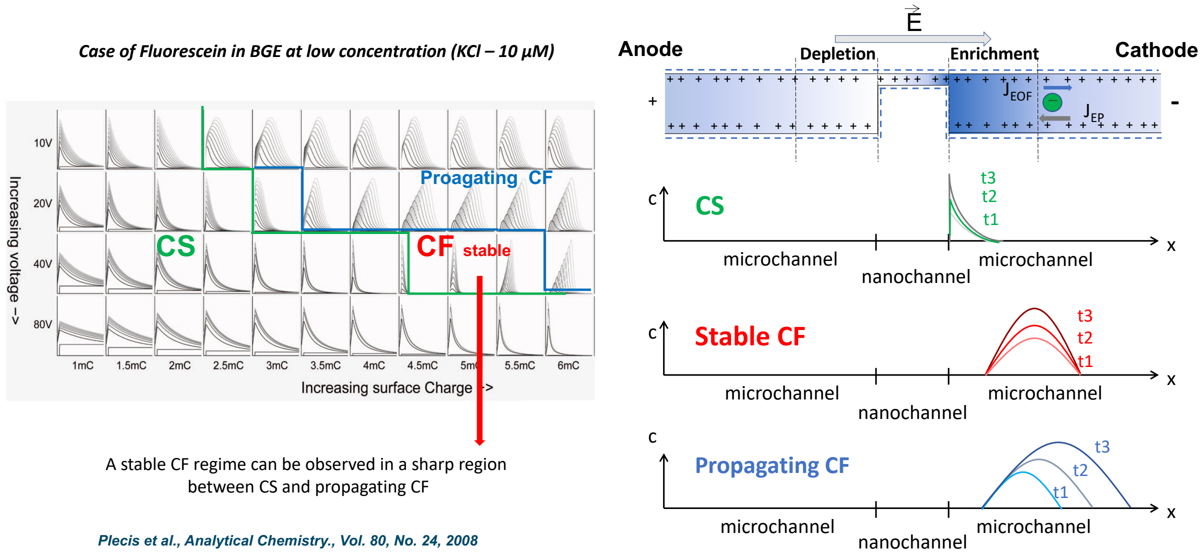
Case of Fluorescein in BGE at low concentration (KCl – 10 µM)

A stable CF regime can be observed in a sharp region between CS and propagating CF

Plecis et al., Analytical Chemistry., Vol. 80, No. 24, 2008

Figure 1.7: (right) 1D Simulations of a fast analyte, Fluorescein, diluted in KCl at low ionic strength. A stable CF focal regime can be observed between CS and propagating CF regimes. (left) Schematic representation of the three modes inside the nanochannel. Adapted from [3].

Let us discuss what happens for an anionic analyte, such as fluorescein diluted in a BGE of very **low concentration** (down to 10 µM). Fluorescein will concentrate in the cathodic reservoir in an electrophoretically dominated regime. Such a very low ionic strength with high surface charge promotes a cathodic concentration profile unstable over time that corresponds to the propagating CP of the BGE [24]. Plecis' simulations also showed that it was possible to obtain a stable focal point CF in a transition region of net surface charge, between the regime of the propagating CF at high surface charge and the regime CS located at the entrance of the nanochannel with a low surface charge. Figure 1.7 right gives some simulations obtained at different electric field and surface charge values and evidences the obtention of a stable CF. However, since the range of parameters (surface charge and electric field) for obtaining this stable CF point is too narrow, few experiments have been reported. To mention one, Hluskou *et al.* [36] have experimentally reported concentration of negatively charged BSA, with a dynamic characteristic of co-ionic species stacking on the enrichment shock, associated to a concentration factor of 100 after 200 seconds.

At **higher moderate BGE concentration**, the situation is different since the four regimes can be observed. The influence of the electrophoretic mobility of molecules on their preconcentration was also studied by Plecis *et al.*, taking 10 mM as ionic strength and applying a voltage difference varied from 10 to 200 V. It was found that fast molecules ($7.1\text{x}10^{-8}\text{m}^2\cdot\text{s}^{-1}\cdot\text{V}^{-1}$ and $5.4\text{x}10^{-8}\text{m}^2\cdot\text{s}^{-1}\cdot\text{V}^{-1}$) preconcentrate at the cathodic side of the nanochannel while slower molecules ($1\text{x}10^{-8}\text{m}^2\cdot\text{s}^{-1}\cdot\text{V}^{-1}$ and $0.54\text{x}10^{-8}\text{m}^2\cdot\text{s}^{-1}\cdot\text{V}^{-1}$) are accumulated at the anodic side since they are transported from this side (figure 1.8).

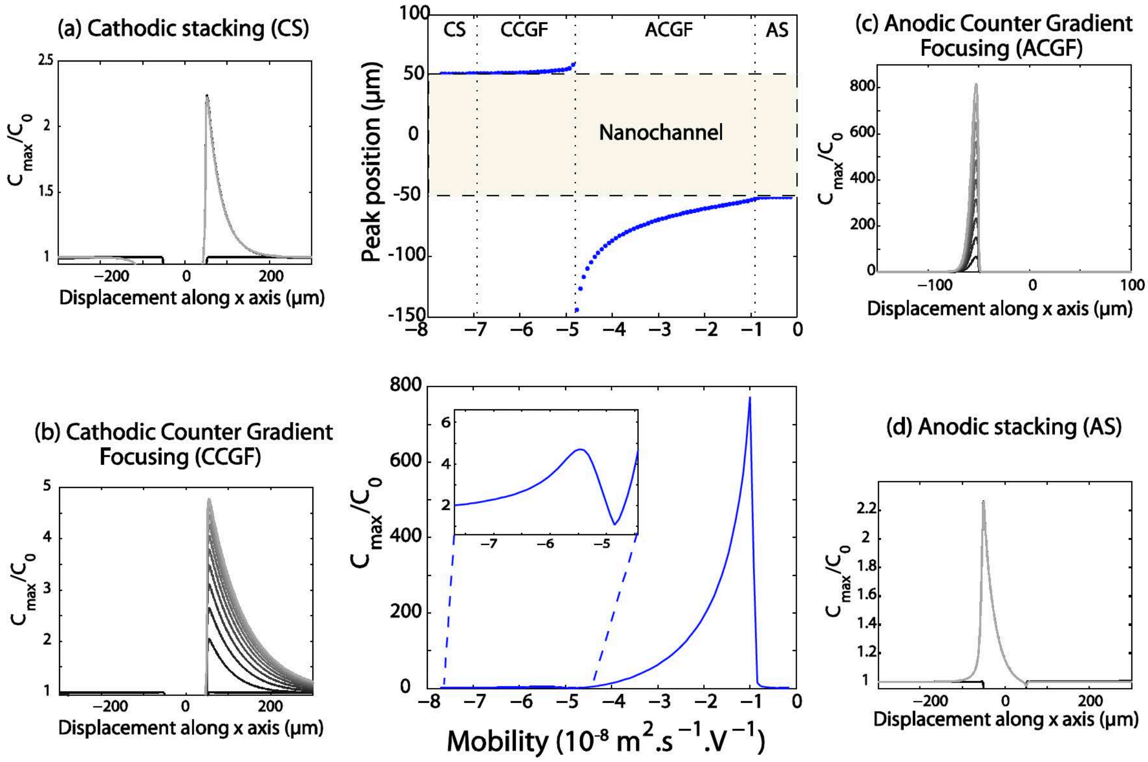

Figure 1.8: Preconcentration profiles corresponding to electrophoretic mobilities (a) $7.1\text{x}10^{-8}\mathrm{m}^2\cdot\mathrm{s}^{-1}\cdot\mathrm{V}^{-1}$, (b) $5.4\text{x}10^{-8}\mathrm{m}^2\cdot\mathrm{s}^{-1}\cdot\mathrm{V}^{-1}$, (c) $1\text{x}10^{-8}\mathrm{m}^2\cdot\mathrm{s}^{-1}\cdot\mathrm{V}^{-1}$ and (d) $0.54\text{x}10^{-8}\mathrm{m}^2\cdot\mathrm{s}^{-1}\cdot\mathrm{V}^{-1}$. In the center, preconcentration peak location and maximum preconcentration rate after one minute as function of the mobility. From [3].

Figure 1.9 summarizes the preconcentration regimes for a negative charge analyte proposed by Zangle *et al.* (CS and propagating CF) and by Plecis *et al.* (stable CF) for a very low ionic strength of BGE such as 10 µM that promotes cathodic regimes.

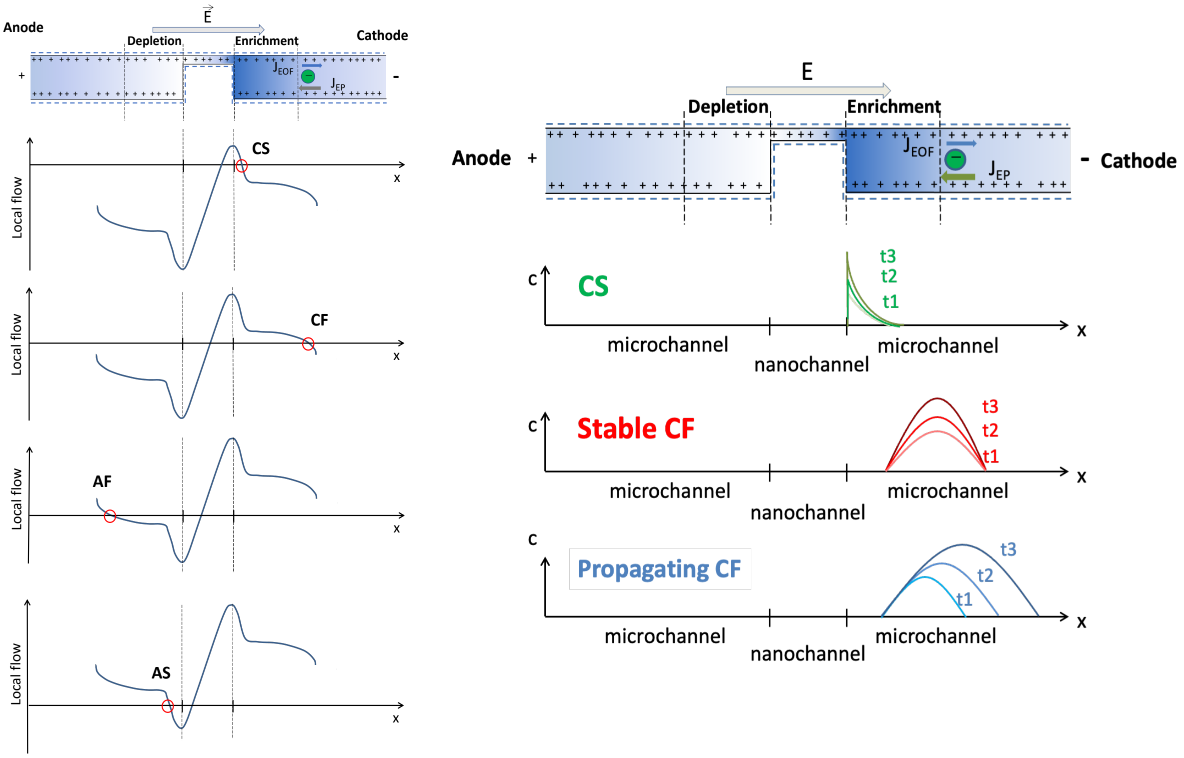

Figure 1.9: (left) Flow profiles proposed by Plecis *et al.* describing the four preconcentration regimes in a micro/nano/microfluidic structure. According with the total liquid flow, the analytes concentrate at certain position of the microchannel. Faster analytes will stack or focus at the cathodic reservoir and heavy analytes will stack or focus at the anodic reservoir [38]. (right) Preconcentration regimes proposed in the analytical model of Zangle *et al.* and in the 1D simulations of Plecis *et al.*

Classic electropreconcentration leads to 4 preconcentration regimes:

- "Cathodic stacking (CS)” regime: the analyte is accumulated at the exit of the nanochannel in the cathodic reservoir. Here, the electrophoretic flow dominates the electroosmotic flow, and this regime is observed for analytes having very high electrophoretic mobility.
- "Cathodic focusing (CF)” regime: the analyte is preconcentrated around 100 µm far from the exit of the nanochannel in the cathode reservoir, at the enrichment interface. The analyte has a slightly lower electrophoretic mobility than in the case of CS.
- "Anodic focusing (AF)" regime: the analyte is focused about 100 µm from the entrance of the nanochannel at the depletion interface in the anode reservoir. The electrophoretic mobility of the analyte is low, and the electroosmotic flow dominates over the electrophoretic flow.
- "Anodic Stacking (AS)" regime: the electropreconcentration takes place at the entrance of the nanochannel. In this case the electrophoretic mobility is very low compared to the electroosmotic velocity.

The stacking/focusing of the analyte at one of these four possible focal points depends on the competition between the electroosmotic and the electrophoretic flows in the analyte flow profile imposed by the ICP effect. In addition, the geometry of the nanochannel (length, width and height), and the chosen background saline solution have an important role. As discussed previously, cathodic regimes will be obtained for low molecular weight and highly charged molecules, while anodic regimes will be those where large molecules with high molecular weight and weakly charged are more likely to be observed.

Numerical simulations have been an important tool to study ICP in the last years. Theoretical works like those of Plecis *et al.* and Zangle *et al.* show the complexity of the physical phenomena that govern the ICP effect and all its processes. This exhibits the need of strong multiphysics coupling, especially for geometries at the nanometric scale where phenomena at the solid-liquid interface become very important. For example, Wang *et al.* [39] studied ion transport of background electrolytes and analytes in a 1 µm long and 50 nm thick nanochannel when applying an external hydrodynamic force thought CFD-ACE+ (ESI-CFD, Inc.) simulation software. Han *et al.* [40, 41] have proposed novel designs of nanochannel structure to analyze the impact in the negative ion concentration of the background electrolyte using COMSOL Multiphysics® software. Liu *et al.* [42] have studied the mechanism for ion transport through micro-nanochannel interfaces for desalination and micromixing, whereas Gong *et al.* [43] have presented numerical simulations of a new microfluidic system based ICP for purification purposes. Simulations in simple channel were also developed by Dubsky *et al.* [44] to investigate ICP of DNA molecule as a plug of immobilized anion. Some multiphysics simulations include the study of membranes to model the ICP effect [45, 46] or the impact of the geometry configuration in the process [47, 48]. Mostly studies use Poisson-Nernst-Planck and Navier-Stokes coupled transport equations to predict ionic fluxes in specific configurations. Chapter 2 of this thesis will enter in more details about these equations and the electrokinetic phenomena, also, it will describe all the 2D numerical simulations realized along my PhD.

1.4 State-of-the-art: preconcentrators based on ICP effect

ICP was first visualized by Pu *et al.* in 2004, since they experimentally demonstrated the ion-enrichment and ion-depletion effects using fluorescein (negatively charged) or rhodamine 6G (positively charged) in a buffer solution. Experiments were performed in a device integrating eight nanochannels connected to two U-shaped microchannels (figure 1.10 A). Both analytes were observed to preconcentrate at the cathodic side; the left-hand side of each image in figure 1.10 B. In this same figure, row 1 illustrates the temporal evolution of fluorescence intensities using fluorescein 30 µM in a sodium tetraborate buffer (pH=8) and row 2 indicates the temporal evolution of fluorescence intensities of rhodamine 6G 10 µM in a 100 µM phosphate buffer (pH=7). The phenomenon of enrichment and depletion was qualitatively interpreted as a result of the extended overlap of the electrical double layer [21]. These experimental observations are important since they are the first electropreconcentration experiments with fluorescein.

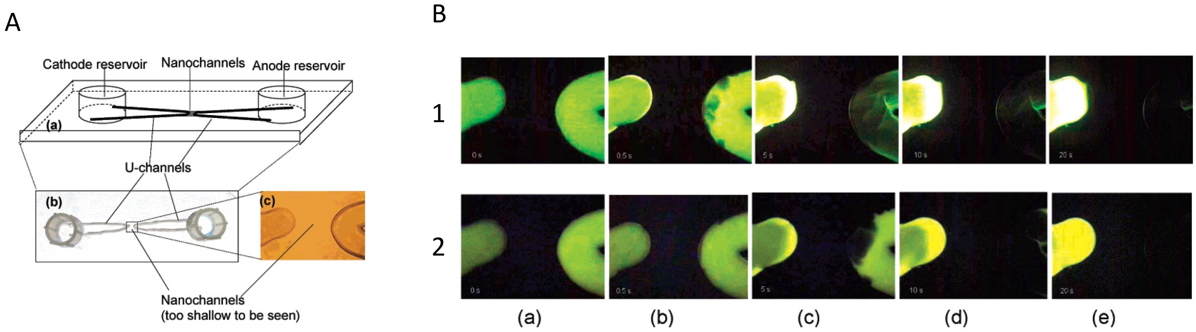

Figure 1.10: (A) Schematic diagram of the device used by Pu *et al.* with two large U-channels connected by 8 nanochannels. (B) The five images in each row respectively represented the fluorescence intensities of fluorescein 30 µM (row 1) and rhodamine 6G 10 µM (row 2) in the two U-channels before any voltage was applied (a), and after a voltage of 1000 V was applied for 0.5 s (b), 5 s (c), 10 s (d), and 20 s (e) [21].

In 2005, Wang *et al.* developed a preconcentration device using a nanochannel as selective membrane. The device was fabricated in silicon by standard photolithography and etching techniques and bonded by a Pyrex wafer. In order to have an accumulation of biomolecules upstream of the depletion zone as shown in figure 1.11 A.2, two separated electric fields E_n and E_T were applied. The normal field is used to generate the ion-depletion region and the tangential field is used to generate the electroosmotic flow to bring the molecules into the trapped region from the reservoir. The temporal evolution of green fluorescent protein is showed in figure 1.11 B, after the injection of the sample and after 25 minutes and 100 minutes, respectively. Concentration factors as high as $10^6 - 10^8$ were obtained after several hours, showing a useful concentration/separation method with applications in bioanalysis [49].

In the same year, Plecis *et al.* studied the exclusion of co-ions and enrichment of counterions in a negative charged Pyrex horizontal nanoslit at low ionic strength (figure 1.11 C). They put in evidence the existence of an electrostatic barrier at the interfaces between the microchannels and the 50 nm-thick-nanoslit. By modulating the thickness of the double layer through the ionic strength of the solution, they measured the permeability of the nanoslit. Their results showed that counterions could pass easily through the nanoslit in comparison with co-ions (figure 1.11 D) [33].

The group of Kim *et al.* presented a PDMS-glass protein preconcentration and separation device in 2006 (figure 1.11 E). By filling the top microchannel with a PBS buffer solution and the bottom channel with a 10 nM FITC-labeled BSA in PBS buffer solution and applying voltages at ports 1-5 (V_1, V_2 = ground, V_3, V_4 = 200 V, and port 5 is left floating), they observed that negatively charged proteins concentrate at the anode side. Enrichment factors of about $10^3 - 10^6$-fold protein were obtained after 30 minutes of preconcentration. Some fluorescent images recorded at different preconcentration times are showed in figure 1.11 F. Then by switching the direction of the electric field, parallel to the thin-walled section, it was also possible to separate two different concentrated proteins [50].

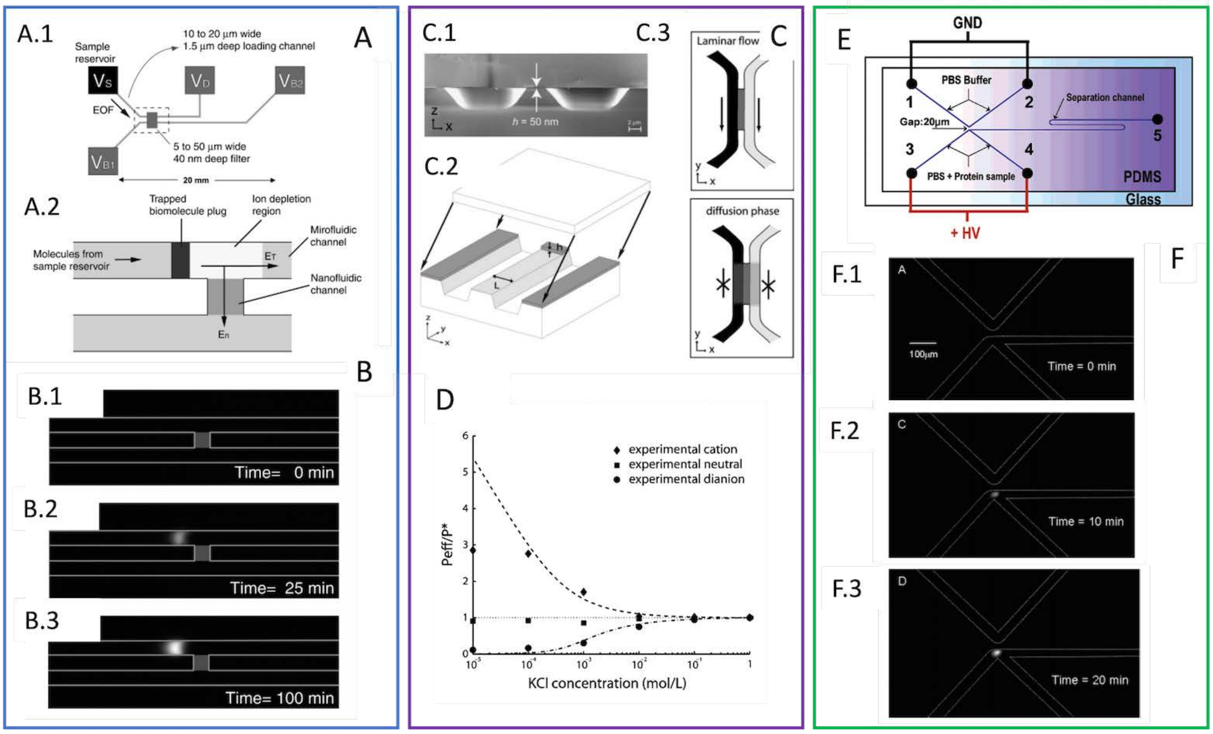

Figure 1.11: (A) Preconcentration device proposed by Wang *et al.* (B) Images of preconcentration evolution of 33 pM green fluorescent protein (GFP). (B.1) Directly after loading the sample into the device. (B.2) After applying V_S = 10 V, V_D= 5 V, and V_{B1} = V_{B2} = 0 V for 25 min. (B.3) After 100 min with the same potential values as (B.2). (C) Geometrical description of a 50 nm-height-nanoslit fabricated by Plecis *et al.* and top view of two experimental conditions: laminar flow and diffusion of fluorescent dyes from one microchannel to the other. (D) Variation of the relative permeability of a 3 µm long nanoslit versus ionic strength for different probe charges. (E) Protein concentration and separation device constructed by Kim *et al.* and electrical description for concentration process. (F) Time sequence images of FITC-labeled BSA, taken before electric field is applied (F.1) and after applying V_1, V_2= ground and V_3, V_4 = 200 V while port 5 is float for 10 min (F.2) and 20 min (F.3), respectively.

During the past decades, several types of nanofluidic preconcentrators based on ICP have been developed to improve their performances. Devices include the fabrication of planar [51] or vertical [52] nanochannels, the fabrication of nanoslits in a substrate as silicon or glass [50, 53, 54], or the integration of nanoporous ion-selective membranes within the microfluidic structure such as Nafion (DuPont, USA) [22, 26, 55, 56] or even gels [36, 57]. In addition, the microfluidic paper-based analytical devices (µPADs) have been received extensive attentions in last years for preconcentration and separation of analytes [26, 58, 59]. More recently, nanofluidic crystals (NCs) provide an alternative method for construction of micro/nanofluidic systems as showed by Choi *et al.* [60]. They first demonstrated that NCs are ICP-generating materials and later they explained the mechanism of ICP in this kind of structures [61].

Figure 1.12 A shows the configuration of the microplatform proposed by Choi *et al.* and the working principle of the ICP phenomena in this device. A shallow channel connecting two deep channels is fully filled with self-assembled homogeneous nanoparticles. The nano-interstices formed in these closed-packed nanoparticles serve as the pores of ion-selective membranes at low ionic strength. When a DC voltage is applied in the case of a cation exchange, positive ions can transport into the perm-selective nanochannel network membrane (NCNM), but negative ions are expelled from the NCNM at the anodic side. As the DC voltage increases, the ion current increases with a fixed diffusion length and bulk concentration. Therefore, the system responds by decreasing the local ion concentration on the anodic side of the membrane (known as the ion-depletion phenomenon). Figure 1.12 B show fluorescence images of ion depletion region when varying the width of the shallow channel.

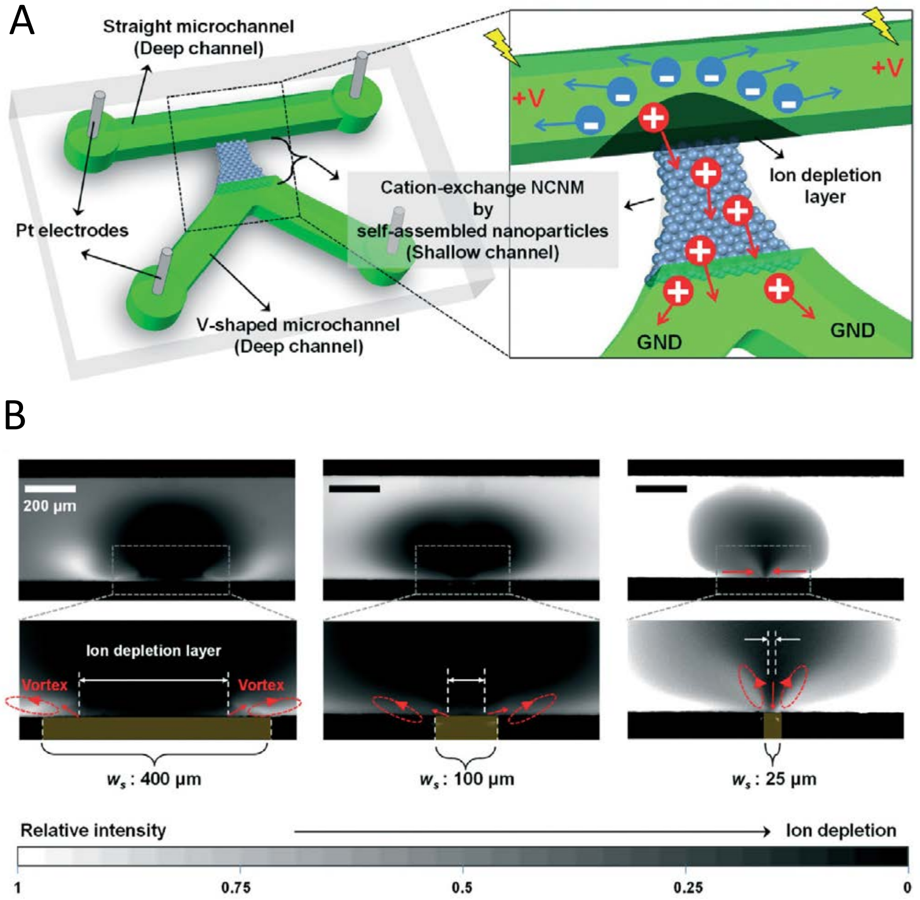

Figure 1.12: (A)Illustration of the microplatform and the working principle of the ICP phenomenon proposed by Choi *et al.* (B) Fluorescence images of the ion depletion region and the corner vortices at each side wall of the NCNM as a function of the width of the shallow channel [61].

The design of ICP devices was also studied to better evaluate their performance. Son *et al.* categorized the design of devices introducing the original H-shape, dual gates, U-shape and one-channel devices [62]. Gholinejad *et al.* recently discussed the operation of the same four devices adding more designs as the X-shaped, O-shaped or Y-shaped devices (figure 1.13) [23]. There are two main variations related to the application of the voltage: a single gate and dual gates, with one or several nanojunctions (nanochannels or ion selective membranes) connecting two microchannels. The simple gated system consists of applying a voltage (V_H and V_L) on the anodic side of the microchannel while the cathodic side of the microchannel is grounded (V_G). If voltages V_H and V_L are equal, the electric field through the nanojunction generates the ICP effect that has been used as preconcentration mechanism. On the other hand, in a dual gated system (1.13 (c)), the depletion at the anodic side can be used as a trapping system. Indeed, by applying a voltage difference $V_H > V_L$ at the anodic side, a tangential electric field is generated along the microchannel. This would generate an electroosmotic flow to bring the target molecules into the region, where they will be trapped by the ICP maintained by the perm-selective current through the junction. However, the dual gates design still have limitation of complex electrical connections. An alternative of the tangential field is an external pressure-driven flow at one end of the microchannel, which corresponds to the mechanism that we use in this work.

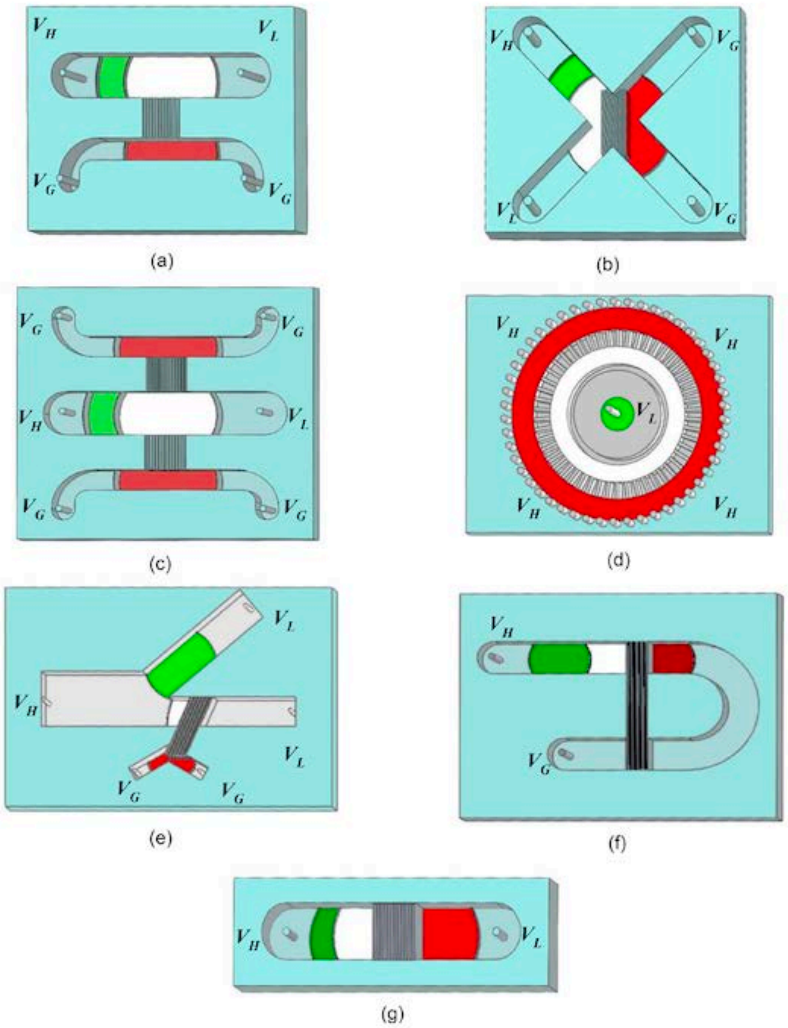

Figure 1.13: Schematic illustrations of the preconcentration device in (a) H-shaped, (b) X-shaped, (c) dual-gate channel, (d) O-shaped, (e) Y-shaped, (f) U-shaped and (g) single channel. V_H and V_L are the applied electric potentials of high and low to induce a tangential electric field and V_G indicate the ground. White, red and green regions refer to ion depletion zone, ion enrichment zone and preconcentrated molecules, respectively. Obtained from [23].

During her PhD in the group, Louër *et al.* [53] proposed a new preconcentration method in which a hydrodynamic pressure is added to both electroosmotic and electrophoretic contributions to control the location of the preconcentration frontline [53]. In figure 1.14 explains how such hydrodynamic pressure allows varying the flow of the analyte inside the micro-nano-micro (MNM) structure. The black curve indicates the classical preconcentration of an analyte when an electric field is applied, as explained previously in the ICP effect description. If a positive pressure is applied (from the anode to the cathode) the flow profile in the diagram moves up giving as a result two anodic regimes which depend on the applied pressure. An AF preconcentration regime is obtained when the addition of the electroosmotic flow and the additional pressure is stronger than the electrophoretic flow $\mathrm{J_{EP}} < \mathrm{J_{EOF}} + \mathrm{J_{P}}$ (red curve) and a AS preconcentration regime appears when the electrophoretic flow is significantly reduced in comparison with the sum of the electroosmotic flow and the additional pressure $\mathrm{J_{EP}} << \mathrm{J_{EOF}} + \mathrm{J_{P}}$ (purple curve). On the other hand, if a negative pressure is applied (from the cathode to the anode) the profile moves down resulting in two cathodic regimes. A CS preconcentration regime appears when the addition of the electrophoretic flow and the additional pressure is stronger than the electroosmotic flow $\mathrm{J_{EP}} + \mathrm{J_{P}} >> \mathrm{J_{EOF}}$ (green curve) and a CF profile when the sum of the electrophoretic flow and the additional pressure is low with respect to the electroosmotic flow $\mathrm{J_{EP}} + \mathrm{J_{P}} > \mathrm{J_{EOF}}$ (blue curve). This additional hydrodynamic flow then moves the position of the focal point depending on the direction of the applied pressure. With this pressure-assisted protocol for BSA (Bovine Serum Albumin) electropreconcentration, Louër *et al.* [53] have shown that depending on this hydrodynamic pressure, the preconcentration location can be chosen, either in the cathodic side or in the anodic one. They proved for the first time that both anodic focusing (AF) and cathodic focusing (CF) regimes can be reached in the same structures.

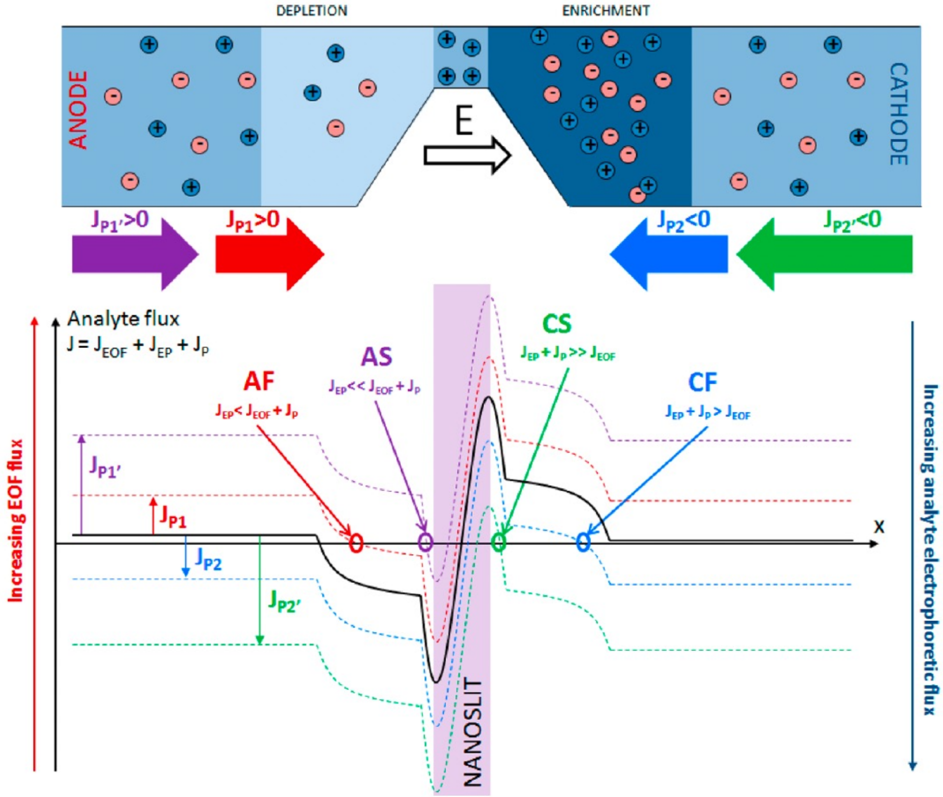

Figure 1.14: Mechanism of pressure-assisted preconcentration. From [53].

Parallelization of microchannels is another alternative to improve the capacity of ICP devices to preconcentrate and thus enhance the detection of molecules. Figure 1.15 shows some examples of devices including series of channels, developed by the group of Han at MIT. In Fig. 1.15 A, using a dual-gated system, up to five assays could be performed simultaneously in a multiplexed format, enabling assay parallelization for high-throughput immunoassay [63]. An example of a parallel concentration device using 16 straight microchannels to detect target molecules was also demonstrated by this team as it can be observed in Fig. 1.15 B [64]. The anode and the cathode are integrated into a straight microchannel with one inlet and one outlet. Finally, in Fig. 1.15 C, a multiplexing device with 16 channels capable of achieving approximately 4000-fold enrichment factor after 30 minutes operation [65].

One of the last works of Han's group is presented in figure 1.16. They used massively paralleled and hierarchically cascaded nanofluidic concentrators as biomolecule enrichment technique. This technique called hierarchical nanofluidic molecular enrichment system (HOLMES) is developed for amplification-free molecular diagnostics. HOLMES uses three stages containing parallel microchannels and one last stage with a single microchannel. In each stage, a nanochannel network (Nafion) bridges the parallel microchannels and side buffer channels at the bottom. When a stage is activated a tangential electric field (ET) is induced along the microchannels, and a normal electric field (EN) is induced along the Nafion, creating an ion depletion zones with significantly amplified electric fields near the micro-nanochannel junctions. Biomolecules concentrated in massive parallel microchannels are released and reconcentrated into the second stage. This process is repeated stage by stage until biomolecules are reconcentrated into the single microchannel in the final stage. Through reconcentration, the concentration performance is dramatically increased. This device can achieve billion-fold enrichment of both nucleic acids and proteins within 30 minutes [66].

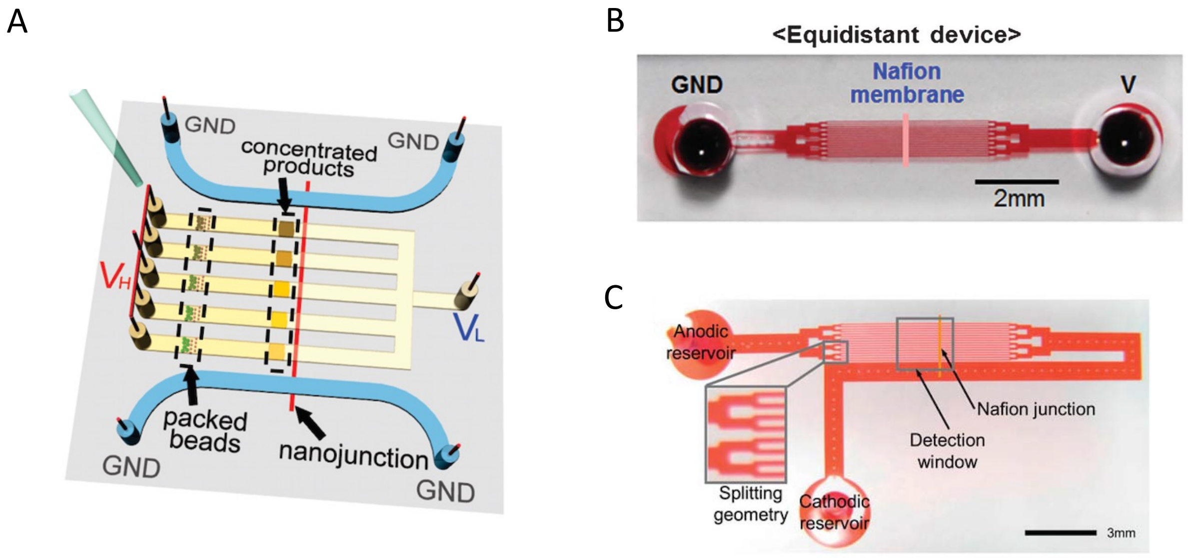

Figure 1.15: ICP devices including parallel channels. (A) Dual-gated device grouping five parallel channels. From [63]. (B) Single channel devices integrating 16 microchannels. From [64]. (C) U-shaped devices including 16 channels. From [65].

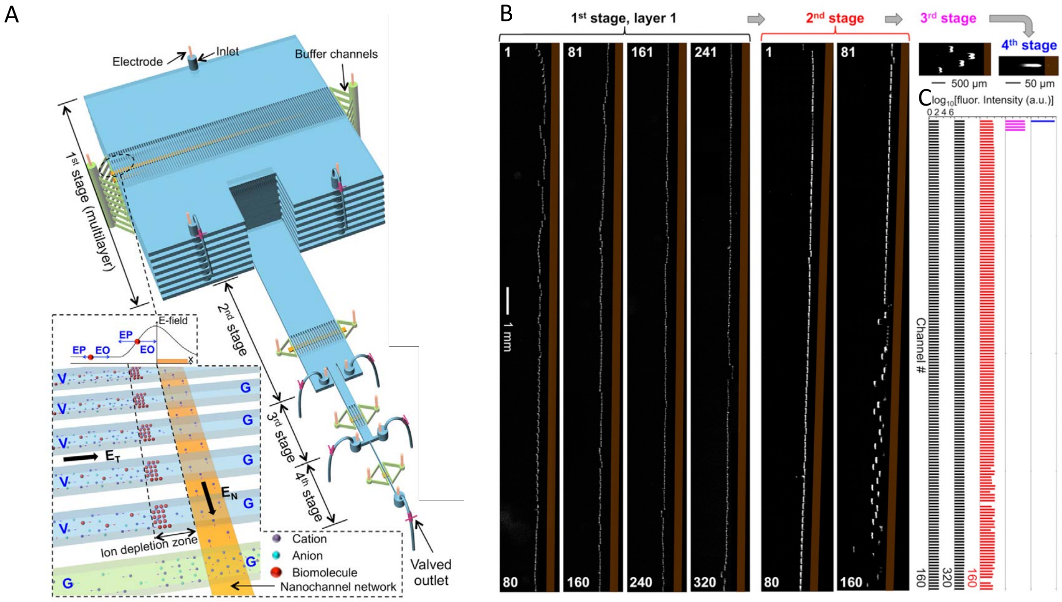

Figure 1.16: (A) Schematic of HOLMES with hierarchical multistages. (B) Fluorescence images of the ssDNA concentration plugs in the parallel microchannels of different stages. (C) The fluorescence intensities of the concentration plugs in individual microchannels of different stages, which increase stage by stage logarithmically. From [66].

To conclude this part, we present the Table 1.3 which summarizes the state-of-the-art in this field either by theoretical studies or by experimental results.

Reference	**Year**	**Type of article**	**Contribution**	**Enrichment factor**
Pu *et al.* [21]	2004	Experimental	First electropreconcentration experiments	$5x10^2$-fold concentration
Wang *et al.* [49]	2005	Experimental	Nanochannel as selective membrane	$10^6 - 10^8$-fold concentration
Plecis *et al.* [33]	2005	Experimental	Study of exclusion-enrichment effect	10^2-fold concentration
Kim *et al.* [50]	2006	Experimental	Preconcentration and separation device	$10^3 - 10^6$-fold concentration
Plecis *et al.* [3]	2008	Simulations	Proposed four electropreconcentration regimes	-
Mani *et al.* [25]	2009	Theoretical	First theoretical work on ICP effect	-
Wang *et al.* [39]	2009	Simulations	ICP simulations with an external pressure	-
Zangle *et al.* [24]	2010	Theoretical	Propagating ICP and non-propagating ICP regimes	-
Louër *et al.* [53]	2013	Experimental	Counter-pressure to stabilize preconcentration fronts	$3x10^2$-fold concentration
Choi *et al.* [61]	2015	Experimental	ICP effect using nanofluidic crystals	Not mentioned
Ouyang *et al.* [37]	2018	Experimental	Enrichment of nucleic acids in human serum	enrichment factor > 4800
Ouyang *et al.* [66]	2019	Experimental	Hierarchical nanofluidic molecular enrichment system	billion-fold enrichment
Gong *et al.* [43]	2019	Simulations	ICP for purification purposes	-
Gholinejad *et al.* [23]	2020	Simulations	Multiphysics ICP study	-
Han *et al.* [40, 41]	2020	Simulations	Study of ICP effect in different geometries	-
Liu *et al.* [42]	2020	Simulations	ICP for desalination and micromixing	-

Table 1.3: Important experimental and theoretical articles studying ion concentration polarization effect.

1.5 Overview of the thesis

The objective of this thesis is to study the preconcentration of model analytes by ICP effect in a chip that integrates series of micro/nano/microchannels with “vertical” nanochannels. It is of importance to note that conventional nanofluidic devices more often integrate a large horizontal nanochannel, such as a nanoslit, between two micro-reservoirs. Such micro/nano/microfluidic (MNM) device is easier to fabricate since the horizontal nanoslit is obtained using a perfectly controlled etching process of the bottom wafer (more often glass wafer). If the nanofabrication of the MNM structures with vertical nanochannels imposes the use of a high-resolution lithography technique, the new designs proposed here with series of MNM structures in parallel allows to study the role of the width and the length of the nanochannel on the location of the focal points. To our knowledge, no studies have investigated the role of the width of the vertical nanochannel on the location of the preconcentration frontline at the interfaces of the depletion and enrichment zones, as function of the mobility of the anionic analyte. Indeed, incorporating multiple nanochannels with different widths and lengths allows to study this multiparametric phenomenon in one single experiment.

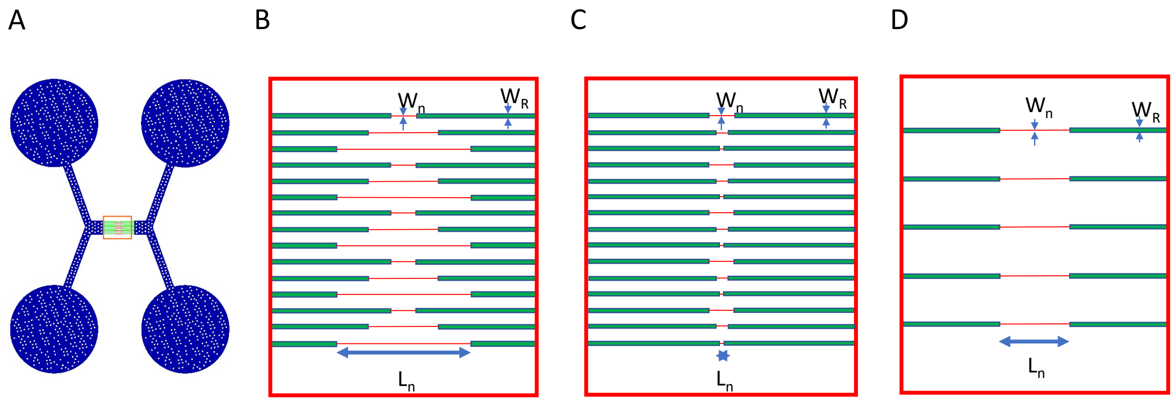

250 nm < W_n < 450 nm
100 μm < L_n < 500 μm
W_R= 5 μm

250 nm < W_n < 450 nm
10 μm < L_n < 100 μm
W_R= 5 μm

250 nm < W_n < 450 nm
L_n = 100 μm
W_R= 5 μm

Figure 1.17: Schema of the fluidic chip with three different designs.

Figure 1.17 A presents a schema of the top view of the fluidic chip incorporating parallel nanochannels at the center represented in red. Blue microchannels correspond to reservoirs where the sample is injected, and intermediate green reservoirs correspond to the microchannels where fluorescent fronts are observed. Blue reservoirs have pillars that avoid the collapse of microchannels. Three different configurations of nanochannels have been investigated. The first design (figure 1.17 B) integrates fifteen vertical and parallel nanochannels in the center part, with a nanochannel width (Wn) ranging from 250 nm to 450 nm. The length of the nanochannel (Ln) is varied from 100 µm to 250 µm and 500 µm. For example, the first three nanochannels (top part of figure 1.17 B) are 250 nm-wide and their lengths Ln are 100 µm, 250 µm and 500 µm, respectively. Then, this configuration is repeated for each value of Wn until 450 nm with steps of 50 nm and with the same three lengths. The second design (figure 1.17 C) conforms fifteen vertical and parallel nanochannels with width Wn varying from 250 nm to 450 nm. The main difference compared to the first design is the shorter length Ln of nanochannels that is 100 µm, 50 µm and 10 µm, respectively. Also, for this design, different widths are arranged randomly to change the fluidic resistance. Finally, the third design (figure 1.17 D) is simpler.

There are five parallel nanochannels with same length Ln = 100 µm and width Wn varying from 250 nm to 450 nm accommodated randomly. This design was proposed for a direct comparison between theoretical simulations and experiments.

The whole PhD manuscript is organized as follow:

In the first chapter, the electrical double layer models and basic concepts of electropreconcentration by ion concentration polarization are introduced. Important theoretical works that explain the ion concentration polarization effect and preconcentration regimes of analytes are presented in detail. Then, as part of the state of art, experimental works involving concentration and separation of analytes by ICP in different kind of devices are reported. Some numerical simulations that have been done to understand ICP mechanisms are also included to put in evidence the applications of this multiparametric phenomenon.

Chapter 2 presents 2D COMSOL® simulations based on the Poisson-Nernst-Planck equations coupled with the Navier-Stokes equation to investigate ICP and electropreconcentration phenomena in a micro/nano/microfluidic structure integrating a 100 µm-long nanochannel. In a first part, the electrokinetic theory in nanochannels is explained and a briefly description of the software operation is introduced. After a general description, the limitations of the first models are described and the last model for our ICP simulations is presented. We study the ion concentration distribution of the background electrolyte as function of the initial concentration, the electric field and the surface charge density. Then, using these results, we study the role of the analyte mobility and its preconcentration inside the structure predicting CS and CF preconcentration regimes. To go further, the temporal study of two kinds of analytes is also reported.

Chapter 3 details the experimental aspects to carry out the electropreconcentration experiments going from the bench to the process of all data to visualize the results. We give in a first part a description of the optical, microfluidic and electronic parts, then we present the experimental protocol and finally the MATLAB® programs to perform the experiments and data treatment is described. A complete spectrophotometric characterization of fluorescein sodium and ovalbumin marked Texas Red, two model molecules that we used, is included. Absorption and emission spectra at different concentrations for both molecules are reported as part of the optimization of the experimental bench. Also, a general description to obtain these spectra is presented.

Chapter 4 begins with the description of the fabrication process of both glass chips and hard-PDMS/glass chips. As the majority of experiments are carried out in hard-PDMS/glass we briefly present the fabrication of glass chips. However, we explain in detail the fabrication of a silicon master mold after the optimization of the etching process, and we demonstrate that this master mold permits the fabrication of hard-PDMS/glass chips that integrate several series of nanochannels. The second part of Chapter 4 describes, electropreconcentration experiments and results using different analytes including fluorescein, ovalbumin and DNA, as model molecules. I discuss in this part the role of the different configurations of the nanochannels with main parameters W_n and L_n. We observed that fluorescein is preconcentrated at the cathodic reservoir in both kind of chips, however the counter-pressure in glass chips permits the stabilization of the preconcentration front. As expected, ovalbumin and DNA are preconcentrated at the anodic reservoir in hard-PDMS/glass chips.

Finally, the last chapter gives the conclusion that summarizes the main results obtained along this work. Perspectives of this work are also presented, and a new design originated from recent 2D COMSOL® simulations is proposed. This new design based on several parallel nanochannels in the same MNM structure seems very promising to increase the enrichment factor for CF preconcentration regimes.

Chapter 2

Theoretical calculations

Numerical simulation is an excellent tool to optimize devices that involve different physical parameters such as ICP in a micro/nano/microfluidic structure. They provide strong multiphysics coupling allowing the comprehension of complex processes. At the same time, by improving fundamental understanding of this processes, researchers can optimize existing technologies or create novel platforms for lab-on-a-chip applications.

In this chapter we present a two-dimensional model to study ICP and preconcentration of ionic analytes inside a simple vertical nanochannel that connects two microchannels considered as reservoirs using COMSOL Multiphysics® software. The first section begins with the background electrokinetic theory in nanochannels. The second section gives an overview of initial models to simulate the ICP effect in short geometries (L_n =10 µm). Although, these models laid the basis for numerical simulations they did not show accordance with the theory. Then, we describe a last 2D model which confirms 1D simulations done by Plecis *et al.* [3]. We explain the model geometry, the construction of the mesh, the physics equations and the boundary conditions. Finally, we show the results of ICP simulations when varying the initial concentration of the background electrolyte, the applied electric field and the surface charge density of walls in a 100 µm-long-nanochannel for the BGE solution and the analytes.

2.1 Electrokinetic theory in nanochannels

Electrokinetic phenomena must be considered when describing ion transport through nanochannels. The three main equations are: (1) the Poisson equation, (2) the Nernst-Planck equation and (3) the Navier-Stokes equation. These equations are used to describe ion transport within a nanochannel under the influence of advection, diffusion, and electromigration [17].

In most nanofluidic systems an aqueous electrolyte is confined in channels. In this case, we need to study ionic concentration and potentials that affect transport phenomena from the wall transferring into the solution.

Since nanochannels are long and thin, we assume that variations of the potential in the axial direction (along the main axis Ln of the nanochannel) are much smaller than in transverse direction (along the width Wn of the nanochannel), and that concentration variation in the transverse direction at any axial position follows the Boltzmann distribution. With these assumptions, the Poisson equation that relates the mean-field electrostatic potential ϕ to the charge density of mobile ions ρ_e in a medium with dielectric permittivity ϵ_r and ϵ_0 the permittivity of free space, is given by:

$$\nabla^2 \phi = -\frac{\rho_e}{\epsilon_0 \epsilon_r} \tag{2.1}$$

For species i, the Boltzmann distribution is:

$$c_i = c_{i,\infty}\ exp\left(\frac{z_i e \phi}{k_B T}\right) \tag{2.2}$$

where c_i is the local concentration of species i, $c_{i,\infty}$ the bulk concentration, z_i is the ion valence, e the elementary charge, k_B the Boltzmann constant and T is the absolute temperature. Equation 2.2 permits to determinate the electrostatic potential from the Boltzmann distribution once the local concentration is known. The charge density ρ_e in equation 2.1 should consider the sum of all N ionic species present in the solution as:

$$\rho_e = F \sum_{i=1}^{N} z_i c_i \tag{2.3}$$

where F is the Faraday constant. Therefore, from equations 2.1 and 2.3 we obtain the Poisson equation:

$$\nabla^2 \phi = -\frac{F}{\epsilon_0 \epsilon_r} \sum_{i=1}^{N} z_i c_i \tag{2.4}$$

It is also important to consider species transport in nanofluidic systems. Ionic transport is classically described by the Nernst-Planck equation:

$$\frac{\partial c_i}{\partial t} = -\nabla \cdot [u c_i - D_i \nabla c_i - \mu_i z_i F c_i \nabla \phi] \tag{2.5}$$

The molar flux of the ith species J_i is given by:

$$J_i = u c_i - D_i \nabla c_i - \mu_i z_i F c_i \nabla \phi \tag{2.6}$$

where, c_i, μ_i, z_i and D_i are the molar ion concentration, electrophoresis mobility, the ion valence and the diffusion coefficient of each specie, and u is the fluid velocity vector. The terms on the right-hand side of Eq. 2.6 represent the contributions of ion transport due to advection, diffusion and electromigration of ions in the nanochannel. Ion mobilities are obtained from the

Nernst-Einstein equation $\mu_i = \frac{D_i}{RT}$ where R is the universal gas constant and T is the solution temperature.

Finally, the fluid velocity is obtained using the Navier-Stokes equations which represent the equations of motion. Here, the incompressible Navier-Stokes equation with electrical force $(-\rho_e \nabla\phi)$ and the continuity equation are:

$$\begin{aligned} \eta\nabla^2 u - \nabla p - \rho_e \nabla\phi = 0 \\ \nabla \cdot u = 0 \end{aligned} \tag{2.7}$$

where u, P and η are the fluid velocity, the pressure within the fluid and the dynamic viscosity of the fluid, respectively. Equation 2.7 has three different terms that correspond to three different forces acting on any volume element inside the nanochannel. Friction forces (first term), mechanical forces due to internal generated pressure gradient (second term) and body forces that appears because of the polarization of the EDL (third term).

Here, the Poisson equation (Eq. 2.4) is used to resolve the mean-field electrostatic potential ϕ, the Nernst-Planck equation (Eq. 2.5) is applied to determine the ion concentration distributions and the Navier-Stokes equation and continuity equation (Eq. 2.7) are used to solve for the fluid flow. All equations are coupled to study the ion transport within a simple two-dimensional micro/nano/microfluidic structure using COMSOL Multiphysics® software. The background electrolyte solution is modeled as two ionic species of opposite charge and we use a third charged ionic component as the sample.

2.2 COMSOL Multiphysics®

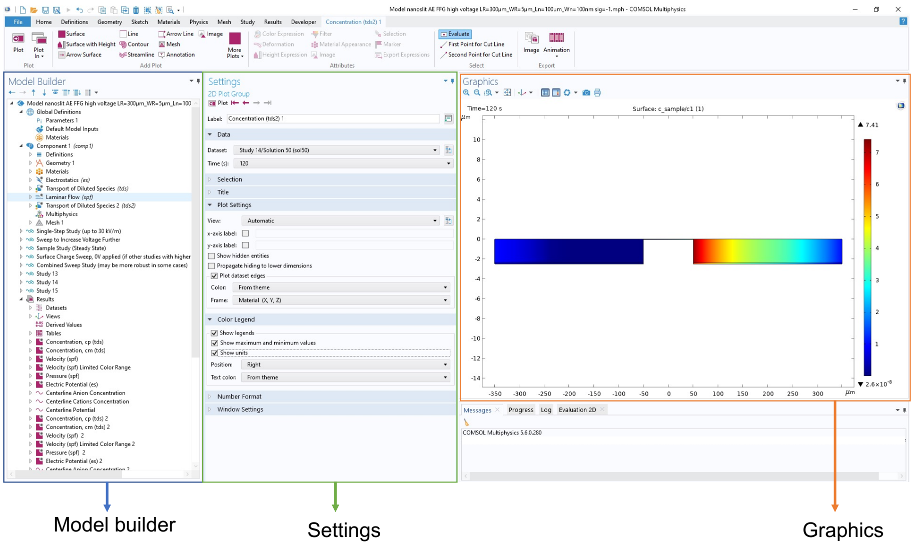

Model nanoslit AE FFG high voltage LR=300µm_WR=5µm_Ln=100µm_Wn=100nm sig=-1.mph - COMSOL Multiphysics

- Model nanoslit AE FFG high voltage LR=300µm_WR=5µm_Ln=100
  - Global Definitions
    - Parameters 1
    - Default Model Inputs
    - Materials
  - Component 1 *(comp1)*
    - Definitions
    - Geometry 1
    - Materials
    - Electrostatics *(es)*
    - Transport of Diluted Species *(tds)*
    - Laminar Flow *(spf)*
    - Transport of Diluted Species 2 *(tds2)*
    - Multiphysics
    - Mesh 1
  - Single-Step Study (up to 30 kV/m)
  - Sweep to Increase Voltage Further
  - Sample Study (Steady State)
  - Surface Charge Sweep, 0V applied (if other studies with higher
  - Combined Sweep Study (may be more robust in some cases)
  - Study 13
  - Study 14
  - Study 15
  - Results
    - Datasets
    - Views
    - Derived Values
    - Tables
    - Concentration, cp (tds)
    - Concentration, cm (tds)
    - Velocity (spf)
    - Velocity (spf) Limited Color Range
    - Pressure (spf)
    - Electric Potential (es)
    - Centerline Anion Concentration
    - Centerline Cations Concentration
    - Centerline Potential
    - Concentration, cp (tds) 2
    - Concentration, cm (tds) 2
    - Velocity (spf) 2
    - Velocity (spf) Limited Color Range 2
    - Pressure (spf) 2
    - Electric Potential (es) 2

Label: Concentration (tds2) 1

Data
Dataset: Study 14/Solution 50 (sol50)
Time (s): 120

Selection
Title

Plot Settings
View: Automatic
x-axis label: ☐
y-axis label: ☐
☐ Show hidden entities
☐ Propagate hiding to lower dimensions
☑ Plot dataset edges
Color: From theme
Frame: Material (X, Y, Z)

Color Legend
☑ Show legends
☑ Show maximum and minimum values
☑ Show units
Position: Right
Text color: From theme

Number Format
Window Settings

COMSOL Multiphysics 5.6.0.280

Figure 2.1: COMSOL multiphysics® GUI where there are three main sections. The model builder section includes parameters, the geometry, physics interfaces, the mesh, the solver and the results. The settings section depends on the element chosen from the model builder section and gives further details of chosen option. Finally, the graphics section permits the visualization of the geometry and results.

COMSOL Multiphysics® is a modeling software that solves Partial Differential Equations (PDE) using Finite Element Method (FEM). As the name states, it can be used for multiphysics modeling. COMSOL incorporates a diverse range of physics included in different interfaces contained in modules. Through a graphical user interface (GUI) (figure 2.1), the user can add the physics equations, create the model geometry, define the parameters and variables, set the boundary conditions, construct the mesh for the geometry, derive a solution and visualize the results. Figure 2.2 summarizes the important steps in the construction of a model. The choice of interfaces, boundary conditions and mesh determinate the convergence of the model and accuracy of results.

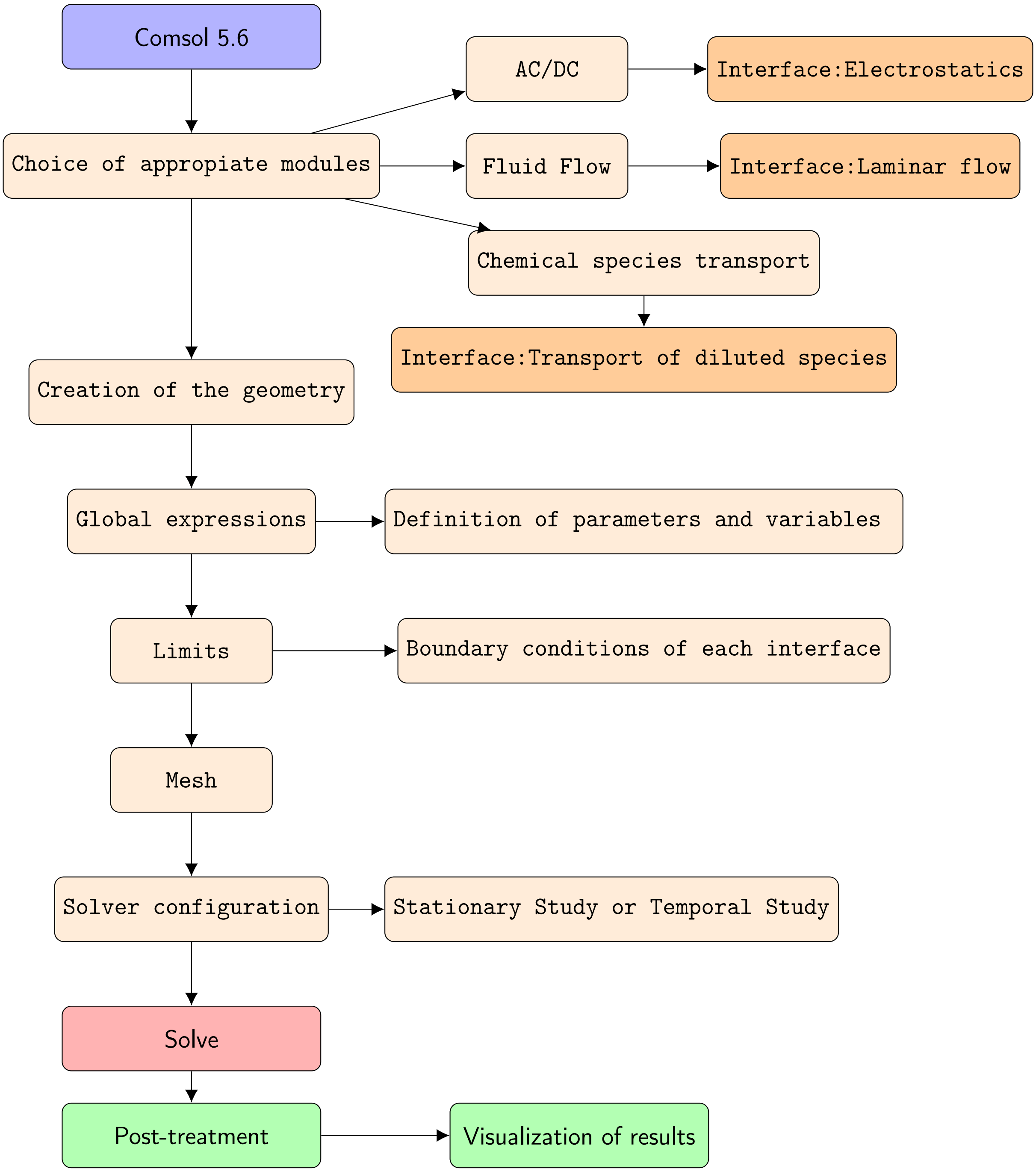

Figure 2.2: Modeling diagram using COMSOL 5.6.

2.3 Model I

The first model is presented in figure 2.3. This simple model geometry consists of a nanochannel that connects two microchannels considered as reservoirs. Letters L and W indicate the length and the width, respectively and subscripts n and r indicate nanochannel and reservoirs. The nanochannel has a length L_n of 10 µm and a width W_n ranging from 50 nm to 200 nm. It is situated between two reservoirs with length L_r ranging from 5 µm to 50 µm and both microchannels are 3 µm width (W_r). Note that we started with this simple short geometry to reduce computation time and to familiarize ourselves with the software.

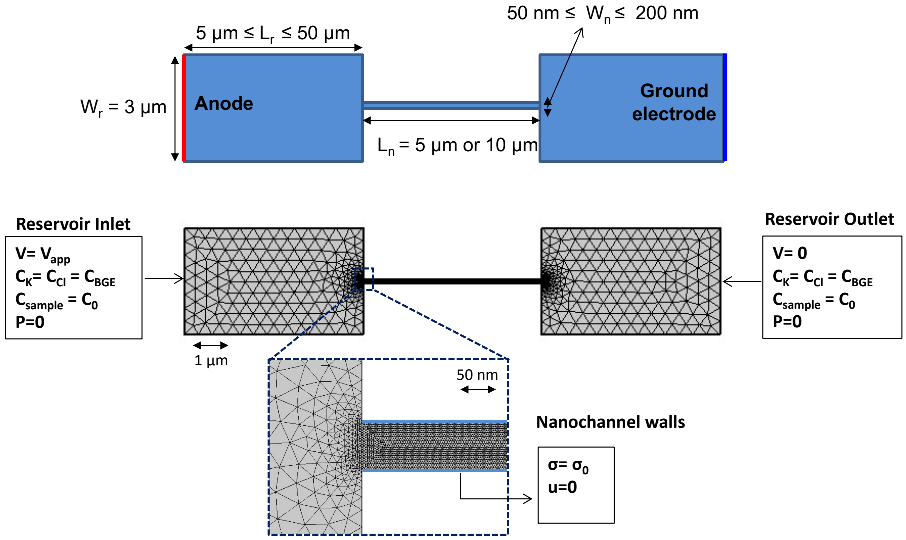

Figure 2.3: Schematic of geometry and the mesh used for model I with corresponding boundary conditions.

As previously mentioned, the ICP effect is studied through the coupled Poisson, Nernst-Planck and Navier-Stokes equations. For model I, these equations are applied, using the Electrostatics, the Laminar flow and the Transport of Diluted Species interfaces, respectively.

The Electrostatics interface solves for the electrostatic potential trough the Poisson's equation $-\nabla \cdot (\epsilon_0 \epsilon_r \nabla \phi) = \rho_e$. As boundary conditions for the interface, a positive voltage is applied at the left side boundary of the left reservoir (in red in figure 2.3) and the right-side boundary of the right reservoir is grounded (in blue dark in figure 2.3). Then, a constant surface charge density $\sigma_0 = -2.5$ mC/m^2, which corresponds approximately to the surface charge density of glass [67] is set as boundary condition at nanochannel walls.

The Laminar flow interface enables to simulate the behavior of fluids solving from the incompressible Navier-Stokes equation. The left side of the left reservoir is considered as the inlet boundary and the right side of the right reservoir is considered as the outlet boundary. A no-slip boundary condition is set to micro and nanochannel walls and no pressure is applied at both inlet and outlet boundaries.

The Transport of Diluted Species interface allows simulating ionic concentration distributions using the Nernst-Planck equation. A constant bulk ionic concentration $c = c_{BGE}$ and a constant concentration of analyte $c = c_0$ are set at inlet and outlet boundaries. The walls of the nanochannel and the reservoirs are assumed to be impermeable for mass transfer $(u = 0)$. The

BGE ionic species and sample species are simulated together in a single interface.

For this model we employed two multiphysics couplings implemented by COMSOL. The first one to use the electrostatic potential calculated by the electrostatics interface in the transport of diluted species interface and the second one to couple the surface charge density from the transport of diluted species interface with the electrostatics interface.

A physics-controlled mesh using fine triangular elements along the nanochannel and coarse triangular elements for the reservoirs was tested (figure 2.3). To study ion transport, a temporal study was used to solve all variables at the same time in the coupled model. An important number of simulations were made using short nanochannel and short reservoirs. Due to the multiparametric nature of the model, the aim was to test different parameters as: initial concentration of both BGE ions and sample ions, the applied voltage, the width of the nanochannel and later the length of the nanochannel and reservoirs. Figure 2.4 shows an example of the temporal study of Cl^- concentration and sample concentration for a 10 µm-long and 100 nm-wide nanochannel with 30 µm-long reservoirs. In Fig. 2.4 a, the depletion at the anodic reservoir is visible but the enrichment inside the nanochannel is higher than inside the cathodic reservoir. On the other hand, in Fig.2.4 b, the concentration profile of fluorescein presents preconcentration at the center of the nanochannel which was not in accordance with the expected results.

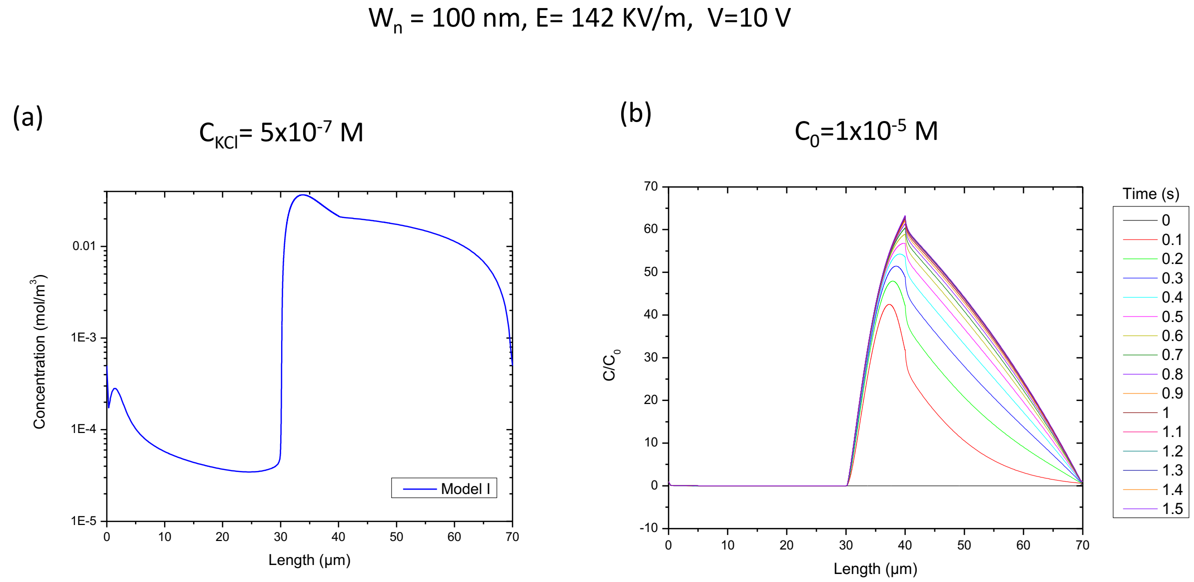

Figure 2.4: Model I: (a) Cl^- concentration profile inside a 10 µm-long and 100 nm-wide nanochannel. (b) Normalized concentration profiles of fluorescein with initial concentration $1x10^{-5}$ M.

We realized that only limited number of initial concentrations for both BGE ions and sample ions could be simulated. Indeed, the Debye length changes as function of the initial concentration of the BGE, then gradients within the electrical double layer were not correctly solved or it was not possible to solve them because elements composing the mesh remain constant. Then, the application of a surface charge density only at the nanochannels walls was generating the concentration of the sample at the center of the nanochannel. For these reasons, a second model was tested.

2.4 Model II

Figure 2.5 shows the geometry and two meshes tested for model II. The geometry is essentially the same as that used in model I with important addition of rectangular domains at the micro and nanochannel walls that represent the EDL. A nanochannel with a length L_n of 10 µm and a width W_n of 50 nm is situated between two reservoirs with length L_r ranging from 10 µm to 30 µm and both microchannels have width W_r= 3 µm. This model integrates the COMSOL interfaces: Coefficient Form PDE, Creeping Flow and Transport of Diluted Species, with same boundary conditions as model I. The Electrostatics interface was replaced by the Coefficient Form PDE interface and the Laminar flow interface was replaced by the Creeping Flow. The idea of changing the interfaces was to solve the model in a different way and to study the differences in results. The Coefficient Form PDE interface provides a general interface to solve many well-known PDEs by specifying coefficients for the derivatives of different orders [68]. In the general equation $-\nabla \cdot (c\nabla u) = f$, c was set equal to $\epsilon_0\epsilon_r$, u was set as ϕ, and f= ρ_e, giving the Poisson's equation ($-\nabla \cdot (\epsilon_0\epsilon_r\nabla\phi) = \rho_e$). On the other hand, the Creeping Flow interface can be used for simulating fluid flows at very low Reynolds numbers for which the inertial term in the Navier-Stokes equations can be neglected. Creeping flow, also referred to as Stokes flow, occurs in systems with small geometrical length scales (for example, in microfluidics and MEMS devices) [69].

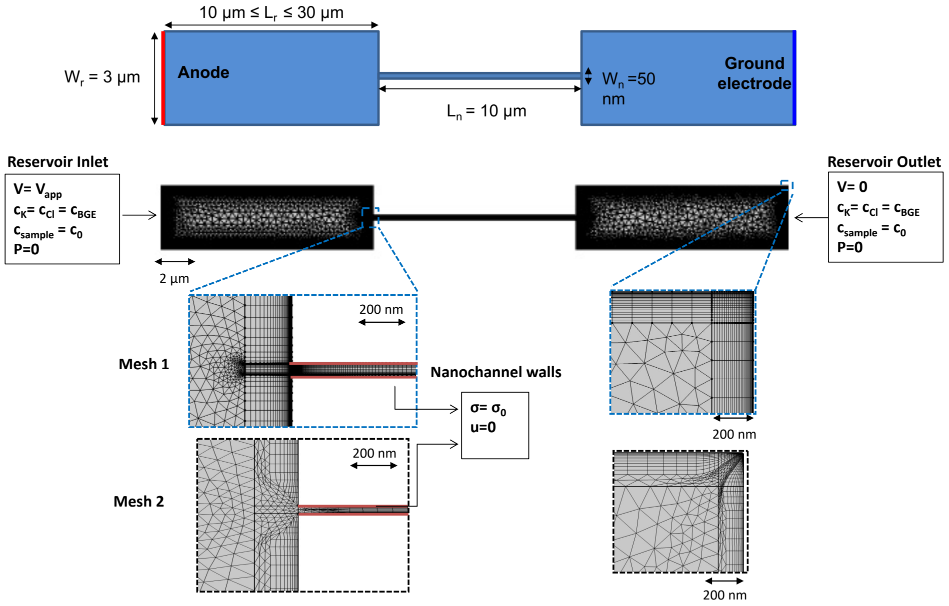

Figure 2.5: Schematic of geometry and two meshes tested for model II with corresponding boundary conditions.

From model I it was seen that gradients in the EDL must be solved when studying the ICP effect. Based on simulations done by Eden et al. [70], we construct a mesh combining mapped elements and triangular elements. Regions near reservoirs walls and all the nanochannel are finely meshed to study transport within the electrical double layer. The rest reservoirs regions are meshed with triangular elements (see figure 2.5 Mesh 1).

From results using Mesh 1, we notice that imposing a potential along all the left side boundary of the left reservoir cause sudden changes in the potential in rectangular corners. This fact did not pose a problem when solving the Poisson equation through the Coefficient Form PDE interface but rather when solving the physics Creeping Flow in the electrical force term, giving problems of convergence of the simulations. The more we refine the mesh, the more this problem increases. For this reason, a second mesh (see figure 2.5 Mesh 2) with rounded corners was constructed using boundaries layers. This option permits to build a mesh with a fine and dense distribution of elements in normal direction along specific boundaries when having rounded corners. To avoid the sudden changes in the potential, rounded corners were tested at the left and right side of the reservoirs where the potential and ground are imposed. Mesh 2 allowed to simulate concentration of electrolyte ions on the order of 1x10^{-8} M and not beyond this value. Figure 2.6 shows images of the solved electrical force term with rectangular (right) and rounded (left) corners, respectively, where the sudden negative value is observed.

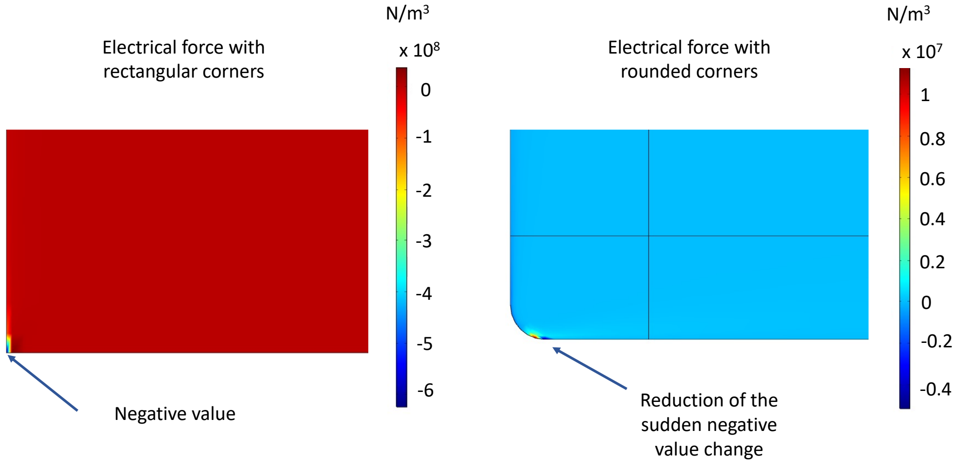

Figure 2.6: Schematic of geometry and two meshes tested for model II with corresponding boundary conditions.

Even if gradients within EDL in reservoirs were correctly meshed the nanochannel was not. In addition, the construction of the mesh with rounded corners without boundary layers was very difficult. This model was then not deeply studied but it was very useful to realize that boundary conditions are very important in the model. Then the construction of the third model was made using mesh 1 with appropriate both boundary conditions and COMSOL interfaces.

2.5 Model III

Previous two models I and II have shown that parameters for the simulation, concerning the choice of boundary conditions, the construction of the mesh and interfaces, are crucial and determinant for the convergence of simulations. In this section, the model III is explained in detail.

2.5.1 Geometry

Figure 2.7 illustrates the model geometry. The length of the nanochannel L_n ranges between 10 µm and 100 µm and the width of the nanochannel W_n ranges between 50 nm and 200 nm. The reservoirs have a length L_r between 5 µm and 300 µm and a width W_r between 3 µm and 5 µm. Note that these values of lengths and widths are closer to experimental geometries.

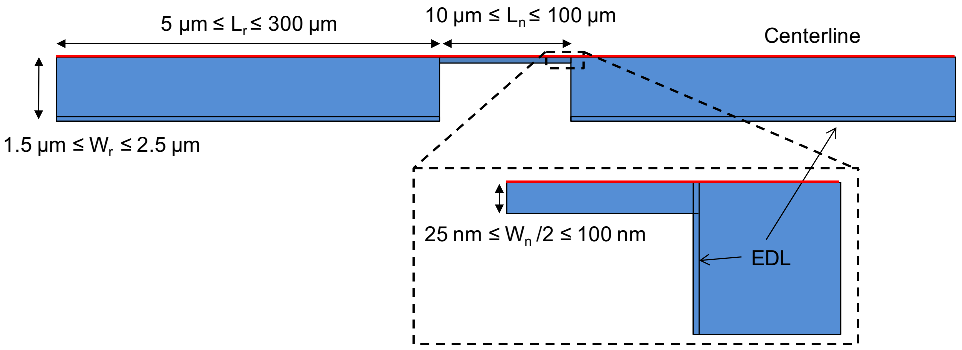

Figure 2.7: Geometry used for simulations with model III. The red line indicates the centerline of the geometry which is an axis of symmetry. Inset shows the thin rectangles in black that indicate the EDL.

It is known that the main principle of FEM is to divide domains into many small, discrete elements and apply the differential equations to each element to solve the system. For this reason, if geometry dimensions become bigger the solving time becomes longer. Therefore, to render simulations more efficient, and taking advantages of symmetric boundary conditions, only the half of the structure is calculated. The symmetry is set at the centerline. Here, the EDL is indicated by the thin rectangles surrounding the reservoirs in the geometry and they are going to change in thickness depending on the initial concentration of electrolyte ions. This is later discussed in the construction mesh part.

2.5.2 Physics interfaces and boundary conditions

To model electroosmotic flow and the electrical double layer, COMSOL suggests using the next interfaces [71]:

1. Electrostatics
2. Transport of Diluted Species
3. Laminar Flow

Unlike the Coefficient Form PDE interface, Electrostatics interface solves the Poisson equation and the electric field through the gradient of the potential. On the other hand, the Laminar Flow interface is adapted to solve the electroosmotic flow.

Electrostatics

The electrostatics physics contains the Poisson equation (Eq. 2.8) to resolve the electrostatic potential ϕ along the micro/nano/microfluidic structure. This interface sums up the contributions of anions and cations to obtain the space charge density and the concentration of ions is obtained through the Transport of Diluted Species interface. The electric field is calculated from the gradients of the potential field (Eq. 2.9).

$$\nabla^2 \phi = -\frac{\rho_e}{\epsilon_0 \epsilon_r} \tag{2.8}$$

$$E = -\nabla \phi \tag{2.9}$$

In the simulations (cf. figure 2.8), the potential ϕ is equal to an applied potential at the left boundary of the inlet reservoir (red) and grounded at the right boundary of the outlet reservoir (blue). It is important to specify that the applied voltage and ground does not include the left side of the EDL and the right side of the EDL respectively to avoid sudden gradients in these regions and then convergence problems. A common surface charge boundary condition is used at the negatively charged walls of both nanochannel and reservoirs to define the normal displacement field component at the edge of the EDL diffuse layer.

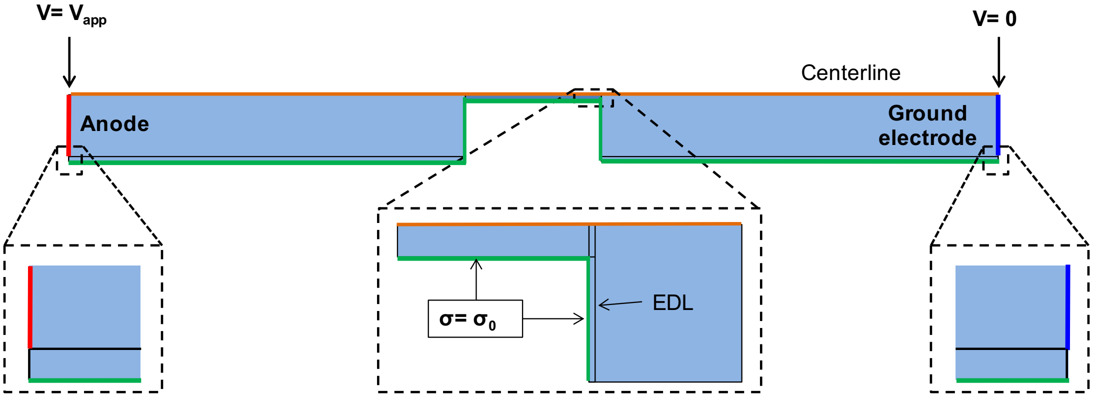

Figure 2.8: Boundary conditions for the Electrostatics interface. The red line at the left inlet reservoir indicates the applied voltage V_{app}, the blue line at the right outlet reservoir refers to the ground and the green line surrounding the nanochannel and reservoirs walls represents the surface charge density.

Transport of Diluted Species

The Transport of Diluted Species interface solves for the ion concentration distributions, through the Nernst-Planck equation (Eq. 2.10), to study the mass transport of diluted species in mixtures. The interface simulates species transport due to diffusion, migration and advection. Therefore, it exists a coupling with the Electrostatic interface that computes the electric field and a coupling with the Laminar Flow interface that computes the fluid flow.

$$\frac{\partial c_i}{\partial t} = -\nabla \cdot [u c_i - D_i \nabla c_i - \mu_i z_i F c_i \nabla \phi] \tag{2.10}$$

As boundary conditions for the simulations (see figure 2.9), c_+ the cation concentration and c_- the anion concentration is equal to the initial concentration of the bulk background electrolyte

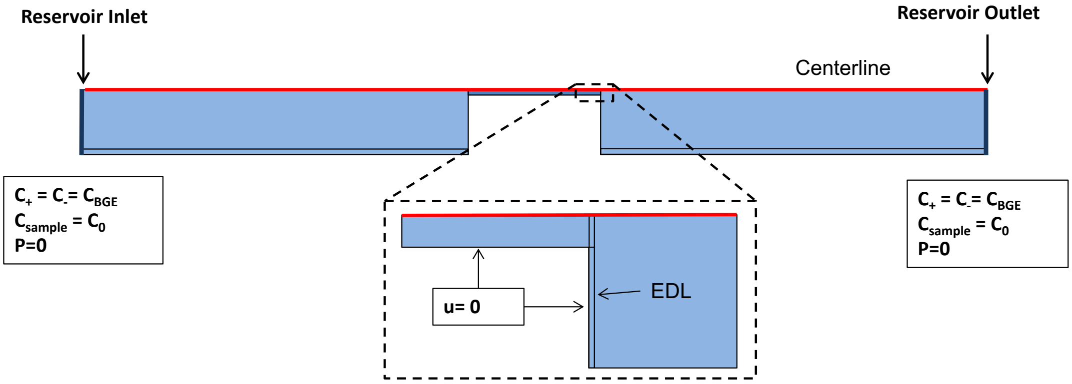

Figure 2.9: Boundary conditions for the Transport of Diluted Species interface. The left inlet and right outlet boundaries in blue navy have equal initial concentrations and no pressure is applied.

c_{BGE} and c_{sample} the sample species concentration is equal to an initial concentration c_0 at the inlet and outlet reservoirs. No pressure is applied at inlet and outlet reservoirs.

The Transport of Diluted Species interface is twice used in the model III, the first one simulates electrolyte ions and the second one simulates sample ion species. Indeed, we suppose that the initial concentration of the sample is lower compared to the initial concentration of the electrolyte, so the charge density of the sample is negligible. This assumption allows solving for electrolyte ions and sampling ions separately which saves time of simulations.

Laminar Flow

Here, the Laminar Flow interface models moving fluids using the incompressible Navier-Stokes equation with volume force $(-\rho_e \nabla \phi)$ and the continuity equation (Eq. 2.11) solving for the velocity field and the pressure. The volume force is computed by the Electrostatics interface.

$$\begin{aligned} \eta \nabla^2 u - \nabla p - \rho_e \nabla \phi = 0 \\ \nabla \cdot u = 0 \end{aligned} \tag{2.11}$$

As boundary conditions for this interface, a no-slip condition u=0 is applied at the nanochannel and reservoir walls. This condition is suggested by F. Schlegel [71] when the width of EDL is comparable to the geometrical width scale, which is the case of this study.

A symmetry condition is imposed along the centerline. Then, left inlet and right outlet boundaries are considered as open boundaries. In real experiments it is difficult to have flow in only one direction, therefore open boundaries act as boundaries that let flows in both directions.

2.5.3 Mesh

The mesh is manually constructed with a combination of mapped elements and triangular elements to resolve gradients within the EDLs surrounding the charged nanochannel and reservoir

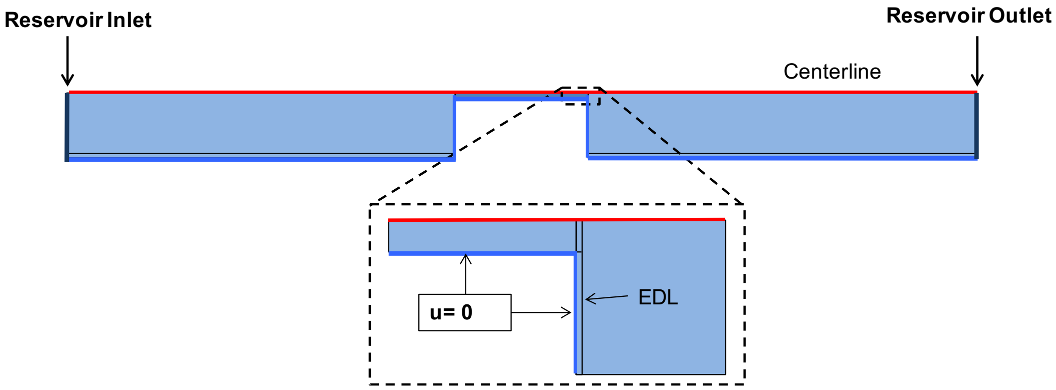

Figure 2.10: Boundary conditions for the Laminar Flow interface. The left inlet and right outlet boundaries in blue navy are open boundaries. A no-slip condition is applied along the nanochannel and reservoirs walls to solve flow in the EDL.

walls (figure 2.11). One of the most important parameters in the construction of the mesh is the width of the EDL. It is known that the Debye length serves as a measure of the EDL thickness and depends mostly on ionic strength. Increasing ionic strength reduces Debye length and makes the EDL thinner. For this reason, EDL was parametrized as function of the initial concentration of the background electrolyte through the Debye length. For the simulations, the width of the EDL is set between 5 to 7 times the Debye length depending on the concentration.

COMSOL offers the possibility to sweep different concentrations in one single study through a Parametric Sweep. This tool is useful when we want that the dimensions of the geometry model vary as function of a parameter, and which is the case of the width of the EDL or the number of elements inside the nanochannel when changing the width W_n.

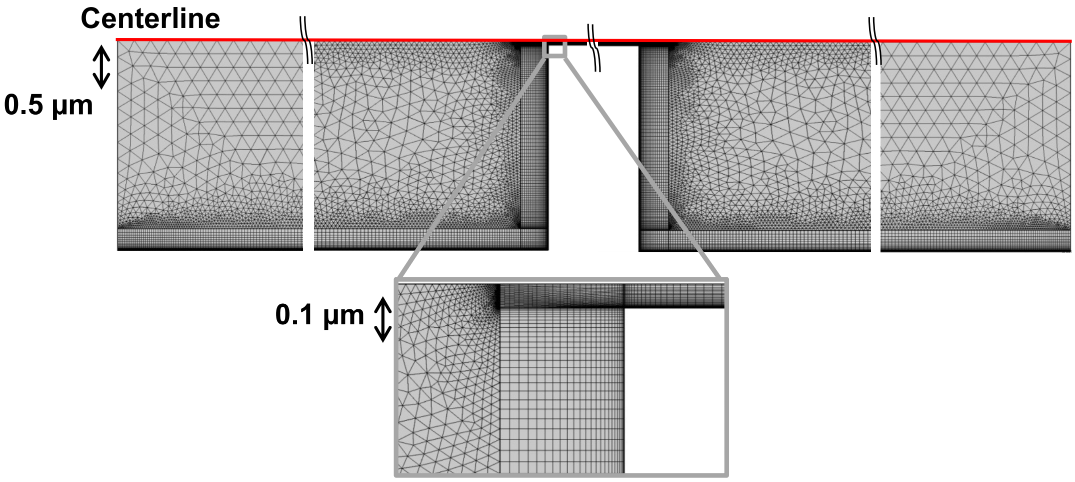

Figure 2.11: COMSOL mesh. The EDL and the nanochannel were meshed with mapped elements and the reservoirs were meshed with triangular elements.

Simulations are first solved for the final steady state transport conditions in the background electrolyte and then using these results, the sample species are separately solved through a temporal study. For both studies, an auxiliary sweep is used to vary the applied electric field and the diffusion constant of species. Figure 2.12 shows the COMSOL GUI corresponding to the window that we used to indicate different solvers and the respective parameters. It is important to emphasize that this model was the result of many improvements. As we set a surface charge boundary condition it is important to correctly choose it, taking into account the initial electrolyte concentration. Surface charge density is chosen using the theory of Hughes et al. [72], but ignoring the dielectric polarization. These surface chemistry equilibrium model considers the concentration of the electrolyte solution, pH, chemical equilibrium constants, Stern layer properties and it applies only for monovalent electrolytes. The surface charge density is a function of the electrolyte solution, therefore for an initial concentration with given pH it is possible to estimate the theoretical surface charge density and the zeta potential. As the pH of the electrolyte solution increases, the surface charge density and the zeta potential become more negative. For all the simulations we consider KCl as BGE and different analytes.

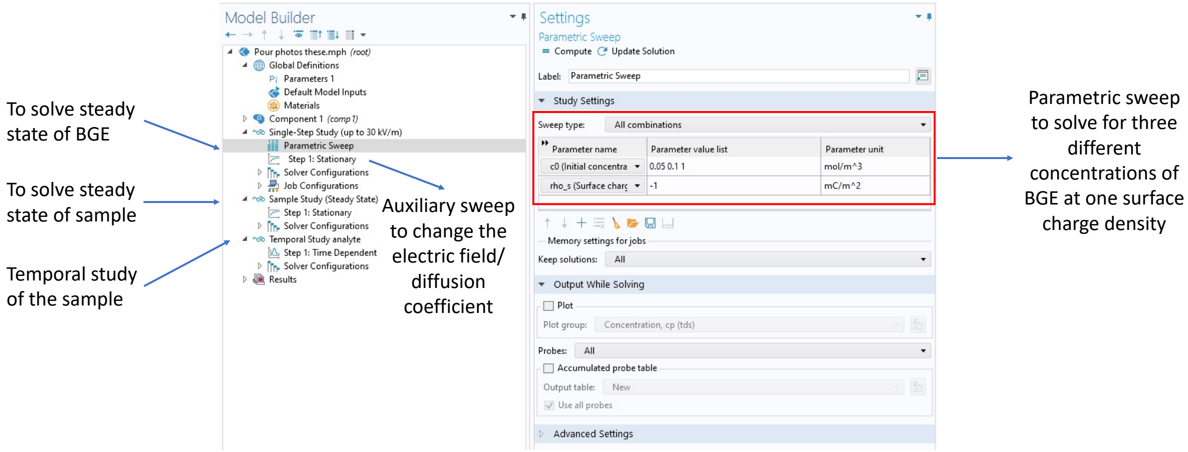

To solve steady state of BGE

To solve steady state of sample

Temporal study of the sample

Auxiliary sweep to change the electric field/ diffusion coefficient

Parametric sweep to solve for three different concentrations of BGE at one surface charge density

Label: Parametric Sweep

Sweep type: All combinations

Parameter name	Parameter value list	Parameter unit
c0 (Initial concentra	0.05 0.1 1	mol/m^3
rho_s (Surface charg	-1	mC/m^2

Memory settings for jobs

Keep solutions: All

☐ Plot

Plot group: Concentration, cp (tds)

Probes: All

☐ Accumulated probe table

Output table: New

☑ Use all probes

Figure 2.12: Model builder and settings windows indicating the different solvers used for the construction of in model III in COMSOL.

2.6 Model III: study of ICP effect in a 100 µm-long-nanochannel

To study ICP effects, we analyze the concentration profiles of chloride ions inside a 100 µm-long nanochannel and 300 µm-long reservoirs. We study the evolution of the depletion and enrichment zones as function of the BGE initial concentration, the applied electric field, the surface charge density and the nanochannel width. Then, we investigate the evolution of different sample preconcentration profiles under the same BGE conditions. All simulations are obtained using Model III described in previous section.

2.6.1 Role of the BGE initial concentration and the electric field

The characteristic 2D depth-average view of Cl ion concentration applying an electric field of 30 kV/m is showed in figure 2.13 (a). The view corresponds to continuous blue curve of figure 2.13 (b) for an initial concentration of 50 µM.

Figures 2.13 (b) presents the steady state concentration profiles of chloride ions along the centerline of the micro/nano/microfluidic structure indicating the ICP depletion and enrichment

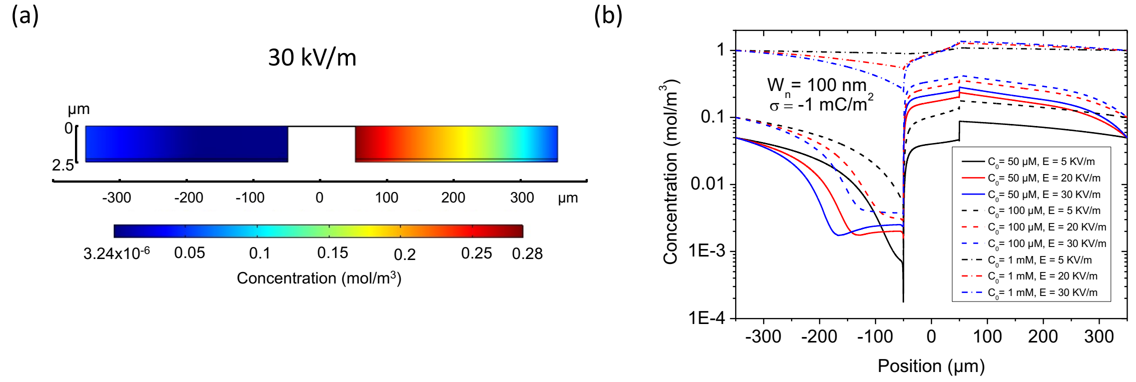

Figure 2.13: (a) Ion Concentration Polarization (ICP) effect of KCl as BGE with (a) top-view of 2D concentration simulation for chloride ions with initial concentration C_0= 50 µM. (b) Cl^- concentration profiles obtained along the centerline of the micro/nanochannel structure as function of the initial concentration (50 µM, 100 µM and 1mM) with the electric field ranging from 5 kV/m to 30 kV/m. The surface charge density σ_s and the nanochannel width W_n are fixed respectively at -1 mC/m^2 and 100 nm.

at the entrance and exit of the nanochannel. The depletion and enrichment shocks are located several hundred of microns from the nanochannel and their value depends on both initial concentration c_{BGE} and electric field E. The plots group three series of curves for different initial concentration and for different applied electric field.

The first group of profiles (bottom continuous curves of figure 2.13 (b)) corresponds to c_{BGE} = 50 µM. At low electric field 5 kV/m, the depletion shock appears near the entrance of the nanochannel. At larger field E $\geq$ 20 kV/m (red continuous curve in figure 2.13 (b)) a large depletion region can be observed in the anodic reservoir with an interface located at around 80 µm from nanochannel entrance. We observe that increasing the field up to 30 kV/m produces a 35 µm-shift of the location of this depletion peak. The enrichment zone interface in the cathodic reservoir is less visible on the profiles of figure 2.13 (b) but more visible on the 2D top view of figure 2.13 (a) with an interface located far from the channel at around 200 µm. This low concentration c_{BGE} =50 µM is thus shown to produce large depletion ICP effect, in agreement with previous observations either analytically by Santiago's work or by 1D simulations by Plecis.

The second group of profiles (middle dashed curves of figure 2.13 (b)) has a moderate initial concentration c_{BGE} =100 µM. Here, the depletion becomes less visible at the entrance of the nanochannel for all electric fields between 1 kV/m to 30 kV/m.

The third group of profiles (top chain curves of figure 2.13 (b)) corresponds to c_{BGE} = 1 mM. The depletion shock is very narrow even at high electric field 20 kV/m and 30 kV/m. On the cathode side of the nanochannel, enrichment occurs for all initial concentrations for electric fields above 5 kV/m.

2.6.2 Role of the surface charge and nanochannel width

After studying the impact of BGE initial concentration and the electric field on ICP effect, we take the case of low initial concentration c_{BGE} = 50 µM and high electric field E = 30 kV/m. As these conditions are showed to produce high depletion/enrichment, we used them to investigate the role of the surface charge density and the nanochannel width (figure 2.14).

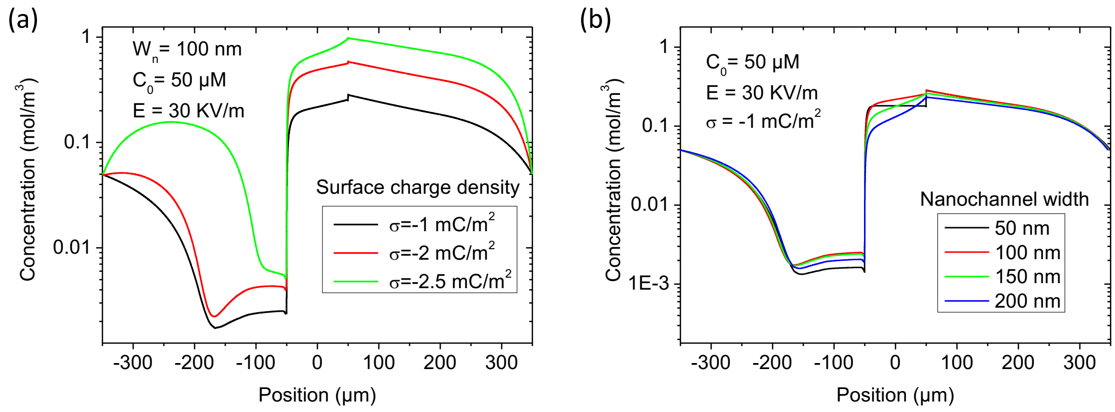

Figure 2.14: Study of how the depletion zone can be affected by (a) the surface charge density σ_s and (b) the nanochannel width $\mathrm{W_n}$.

The role of the surface charge density σ_s on ICP effect is demonstrated in figure 2.14 (a). A depletion zone with an interface located at 125 µm from the nanochannel entrance is observed at $\sigma_\mathrm{s} = -1$ mC/m^2 (case of PDMS material). For glass surface charge density $\sigma_\mathrm{s} = -2.5$ mC/m^2, a reduced depletion zone of around 100 µm is noted. This shows that the smaller the surface charge density σ_s, the larger is the depletion zone. These results are not fully consistent with previous 1D simulations [3] which demonstrated that ICP effect enhances when increasing the absolute value of the surface charge density. However, we continue the simulations with this Model III.

Figure 2.14 (b) exhibits the influence of the nanochannel width $\mathrm{W_n}$ on ICP effect. Here, we consider a surface charge density $\sigma_\mathrm{s} = -1$ mC/m^2 since ICP effect was demonstrated to be stronger. For $\mathrm{W_n}$ = 50 nm, the concentration of ions remains constant along the nanochannel. As the width of the nanochannel increases from 100 nm to 200 nm, the depletion along the nanochannel is perceptible. Another result concerns the depletion interface in the anodic reservoir that is shown to be very stable with no shift for all $\mathrm{W_n}$ values in the range 50 nm to 200 nm. This confirms that it exists an important difference between theory which shows that ICP effect is stronger in thin nanochannels and the simulations.

2.6.3 Role of the analyte mobility

In this section we investigate how diluted anionic analytes with valence z = -2, initial concentration $\mathrm{c_{analyte}} = 10^{-9}$M and with different diffusivity will concentrate in the cathodic reservoir. We use specific conditions for BGE ions studied in the previous section ($\mathrm{c_{BGE}}$= 50 µM, $\mathrm{W_n}$ = 100 nm, $\sigma_\mathrm{s} = -1$ mC/m^2 and E= 30 kV/m corresponding to the dark curve of figure 2.14 (a)).

The evolution of concentration profiles of diluted analytes is is presented in figure 2.15. Concentration profiles of fluorescein with diffusion coefficient value of D = 0.485x10^{-9}m^2/s are depicted in figure 2.15 (a). Fluorescein presents a cathodic stacking (CS) profile at the exit

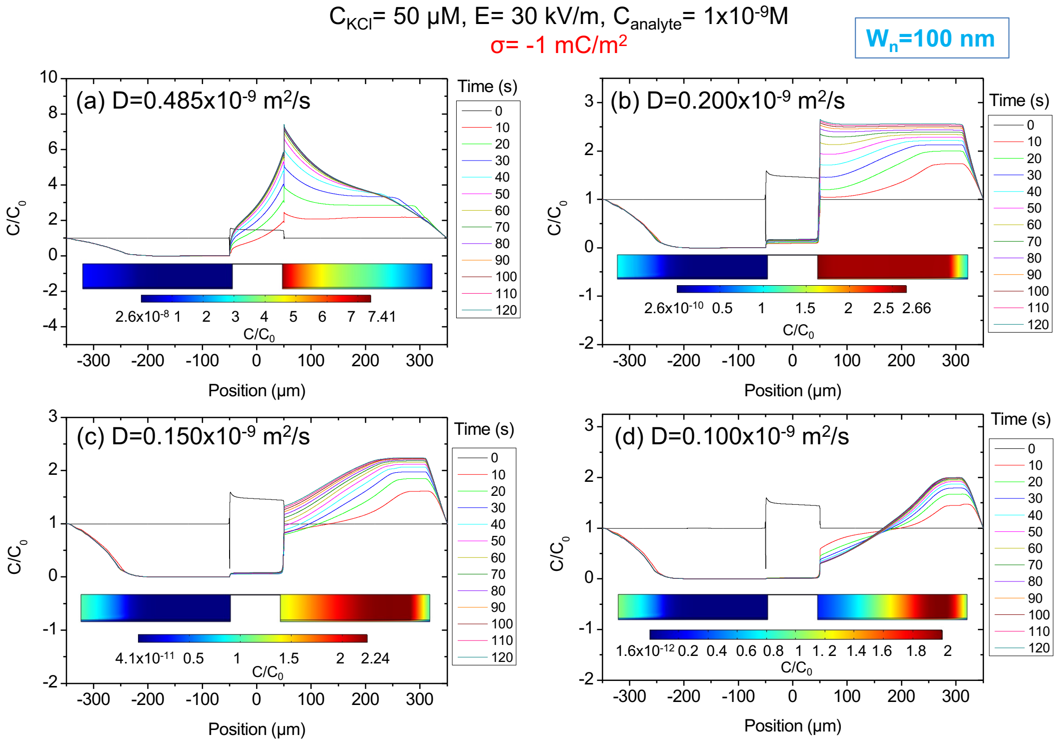

Figure 2.15: Temporal concentration profiles along the centerline of an analyte diluted at 1x10^{-9}M under E=30 kV/m. The diffusion coefficients D are (a) 0.485x10^{-9}m^2/s (fluorescein), (b) 0.200x10^{-9}m^2/s, (c) 0.150x10^{-9}m^2/s and (d) 0.100x10^{-9}m^2/s. The insets give the corresponding 2D sample concentration profile normalized to its initial concentration that allows direct visualization of enrichment factor. All the simulations were done in a 100 nm-wide nanochannel.

of the nanochannel where a maximum of the concentration is observed. This is thanks to its high mobility (3.6x10^{-8}m$^2\cdot$ V$^{-1}\cdot$ s^{-1} [73]). Indeed, the electrophoretic migration surpasses the counter-electroosmotic flow causing that preconcentration takes place at the cathodic side of the nanochannel. When electrophoretic velocity is decreased, the maximum concentration peak slowly moves toward the cathode that corresponds to the CF regime [2].

The behavior of the analyte with diffusivity of about D = 0.200x10^{-9}m^2/s is show in figure 2.15 (b). Here, an "extended" cathodic focusing (CF) profile appears since it spreads-out along the whole cathodic reservoir from the nanochannel to the reservoir outlet. Note also the sudden decrease of the concentration near the right boundary of the outlet reservoir due to the imposed initial conditions.

As long as the diffusivity is more reduced to D = 0.150x10^{-9}m^2/s (figure 2.15 (c)) and D = 0.1x10^{-9}m^2/s (figure 2.15 (d)), a cathodic focusing (CF) profile similarly as the one observed in conventional horizontal nanoslits [2, 3] is obtained. Analyzing the evolution as function of time of both the peak location d$_{\mathrm{max}}$ and its corresponding concentration c$_{\mathrm{max}}$ appears also of great interest. The location of the maximum focal preconcentration shifts towards the right boundary of the outlet reservoir as shown in figure 2.15 (d).

Figure 2.16 groups the normalized concentrations of the BGE ions and the analyte (in this case fluorescein) considering $\sigma_s = -1$ mC/m^2 and E= 30 kV/m. The black curve corresponds to the chloride ions where we observe the enrichment-depletion effect described before. The red curve indicates the distribution of potassium ions, here, the concentration inside the nanochannel is higher than the cathode reservoir as expected. Finally, we show that under these BGE conditions it is possible to concentrate the fluorescein at the exit of the nanochannel after 120 s as indicated by the blue curve. Here, we obtain an unexpected depletion at the anode reservoir that can be explained by the use of a non-conservative form of the Nernst-Planck equation.

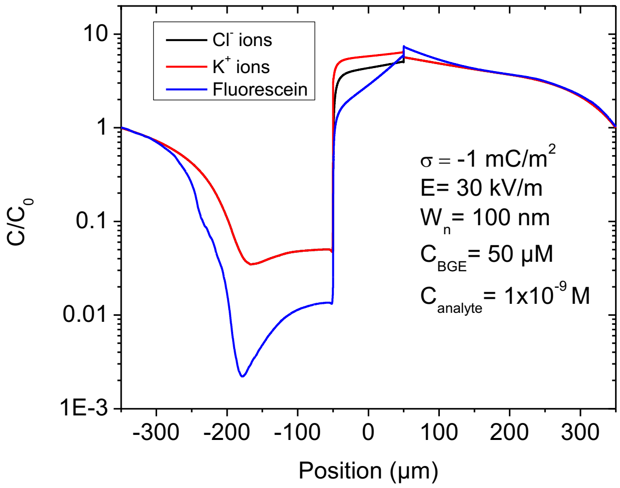

Figure 2.16: Normalized concentration distributions of chloride ions, potassium ions and the analyte (fluorescein).

In a first time, results for different analytes obtained with model III (figure 2.15) seem to be close to the experimental results since preconcentration at different zones of the cathode reservoir are observed, however, upon inspection, curves at t=0 s do not make physical sense. In effect, the concentration inside the nanochannel is higher that the concentration at the reservoir when starting the simulations which is not possible in real.

This evidences some inconsistencies for our model III. After discussions with A. Eden from the University of California, we saw that the problem came from an advanced parameter in the transport of diluted species interface, called non-conservative form. In fact, simulations must be carried out using the conservative form of the Nernst-Planck equation since we are simulating shocks. The non-conservative form generates extra terms in the discretization of the differential equation and then results are far from the theory. For this reason, we created another model that we called Model III B by introducing this little but important change on conservative form in Model III. A step-by-step tutorial is presented in Annex A to help anyone with basic knowledge in COMSOL to reproduce this model.

2.7 Model III B: study of ICP effect in a 100 µm-long-nanochannel

Here, we present the numerical results obtained with model III B. For all simulations, similarly as in previous section, we consider a 100 µm-long nanochannel with 300 µm-long reservoirs.

2.7.1 Studying ICP effects of the BGE as function of initial concentration, electric field and surface charge density

One simple way to study how ICP effects vary as a function of $1/D_u$ is to compare the Cl co-ion concentration profiles in the structure and monitor the manifestation and evolution of depletion and the enrichment zones in each reservoir. We begin by examining the drift-diffusion of BGE chloride ions inside a 100-nm-wide nanochannel.

Figures 2.17 (a) and 2.17 (b) respectively show a characteristic 2D depth-averaged view of the co-ion concentration and the steady state normalized concentration profiles for a surface charge density $\sigma_S = -1$ mC/m^2, showing the characteristic ICP depletion and enrichment at the entrance and exit of the nanochannel. When ICP effects are relatively weaker (e.g., at higher electrolyte concentrations and/or lower surface charge densities), these enrichment and depletion zones are largely confined to the microchannel-nanochannel interfaces, with diffusion flows from the far boundaries capable of balancing the limited enrichment/exclusion effects [25]. As these surface-charge-governed transport effects become more prominent, however, the depletion zone can propagate outward towards the microchannel reservoir boundary. These propagating depletion interfaces (also referred to as shocks) can ultimately travel a distance of up to several hundred of microns from the nanochannel in our modeled system, depending on the bulk BGE concentration c_{BGE}.

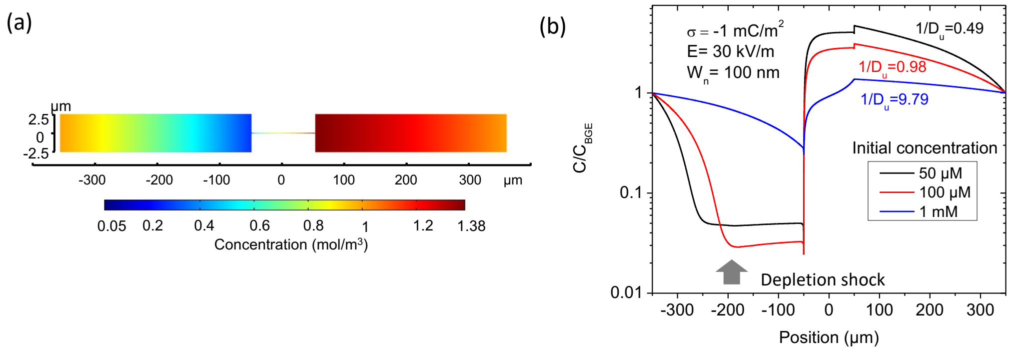

Figure 2.17: Ion concentration polarization (ICP) effects in KCl solution: (a) a typical 2D depth-averaged concentration profile for chloride ions at $c_{BGE} = 1$ mM, and (b) Cl- concentration profiles obtained along the centerline of the micro/nanochannel structure as function of c_{BGE} (50 μM, 100 μM and 1mM) with the electric field fixed at 30 kV/m. The surface charge density σ_S and the nanochannel width Wn are respectively fixed at -1 mC/m^2 and 100 nm.

At low c_{BGE}, and thus low $1/D_u$ ($1/D_u = 0.49$ for c_{BGE}= 50 μM and $\sigma_S = -1$ mC/m^2 – black curve in figure 2.17 (b)), a large propagating depletion region can be observed in the anodic reservoir, with an interface located at around 200 μm from the nanochannel entrance. For a concentration c_{BGE} = 100 μM (corresponding to moderate $1/D_u$ =0.98 – red profile in figure 2.17 (b)), the depletion zone doesn't propagate as far, instead reaching a distance of 150 μm from the nanochannel entrance, but the zone can be depleted to a greater extent than for c_{BGE} = 50 μM because the smaller concentration gradient between this location and the fixed-concentration boundary limits diffusion into the ion-depleted zone. Finally, at higher c_{BGE} and thus higher $1/D_u$ (c_{BGE} = 1 mM and $1/D_u$ =9.79 – blue profile in figure 2.17 (b)), the depletion is limited and confined to the channel junction, even at a high electric field strength of 30 kV/m. On the cathode side of the nanochannel, enrichment occurs to some extent for all initial concentrations. These simulations confirm that lower $1/D_u$ values yield stronger ICP depletion/enrichment effects, in agreement with the theoretical model proposed by Mani *et al.* [25] and Zangle *et al.* [24].

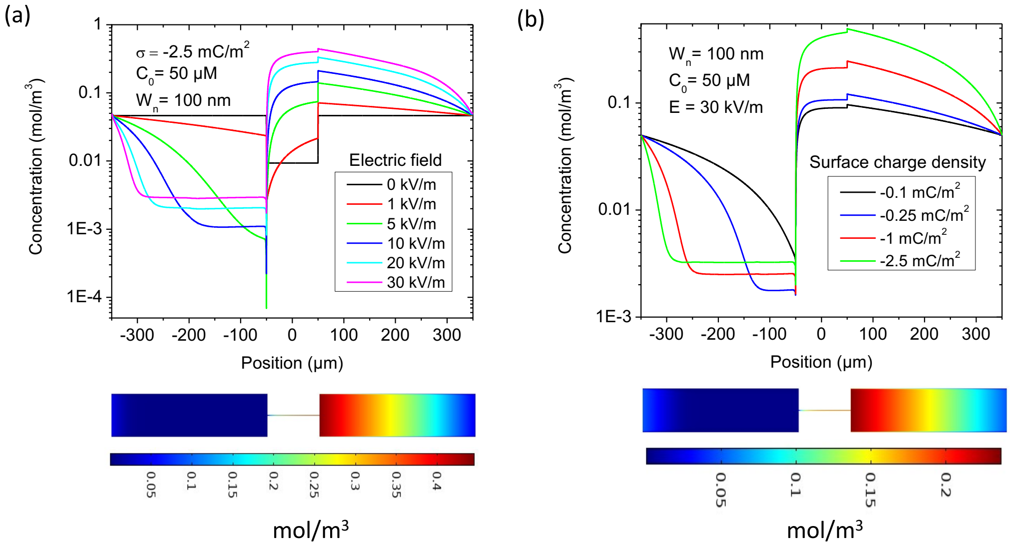

Figure 2.18: (a) Visualization of the transition from non-propagating to propagating ICP as the applied electric field is increased (with $\sigma_S = -2.5$ mC/m^2) with a 2D view of Cl ion concentration at 30 kV/m and (b) as the surface charge density is varied from -1 mC/m^2 to $\sigma_S = -2.5$ mC/m^2 (with $c_{BGE} = 50$ µM and E=30 kV/m) with a 2D view of Cl ion concentration at $\sigma_S = -1$ mC/m^2.

Figure 2.18 (a) evidences the role of the electric field on ICP effects for a typical case (Wn = 100 nm) at low c_{BGE} = 50µM and surface charge density $\sigma_S = -2.5$ mC/m^2, roughly corresponding to a glass surface and a solution pH of 6.5. At relatively low electric fields (< 5 kV/m) accumulation and depletion zones appear at the ends of the nanochannel, and at around 5 kV/m the depletion zone begins to propagate from the channel junction. Increasing the applied field to 10 kV/m produces propagating ICP with an interface located approximately 125 µm from the nanochannel entrance. Further increasing the field to 30 kV/m leads to an extended depletion zone and higher accumulation at the opposite interface. Even at a fixed $1/D_u$ value, the applied electric field has a similarly large impact on ICP as BGE concentration, and only causes propagation when high enough. Figure 2.18 (b) exhibits the influence of the surface charge density σ_S on co-ionic charge exclusion and the resulting ICP for c_{BGE} = 50 µM and an electric field of E= 30 kV/m. Increasing the surface charge density magnitude from -0.1 mC/m^2 to -2.5 mC/m^2 (i.e., going from $1/D_u = 4.891$ to $1/D_u = 0.195$) enhances the enrichment in the cathodic reservoir by five-fold, while the onset of propagating CP occurs between -0.1 mC/m^2 and -0.25 mC/m^2 under these conditions. Clearly, both a sufficiently high electric field and low $1/D_u$ value are necessary to generate strong propagating ICP effects in this single-channel configuration.

Finally, we show the normalized concentration distribution of the BGE ions and the analyte (fluorescein) using model IIIB. If we compare figure 2.16 with figure 2.19 we see that the unexpected depletion is not present when we employ this last model.

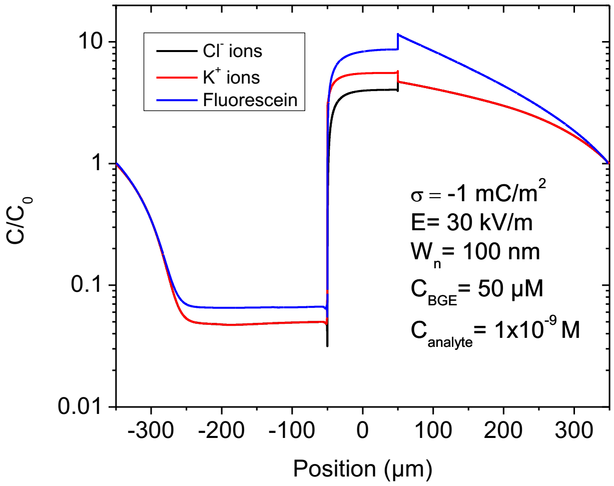

Figure 2.19: Normalized concentration distributions of chloride ions, potassium ions and the analyte (fluorescein) using model IIIB.

2.7.2 Localization of the preconcentration frontline as function of the analyte mobility

Here, we investigate how diluted dianionic analytes (valence z = -2 and $c_{\text{analyte}} = c_0 = 10^{-9}$M) with different mobilities concentrate under the conditions studied in the previous section (c_{BGE}= 50 µM, Wn = 100 nm and E = 30 kV/m - green curve in figure 2.18 (b)).

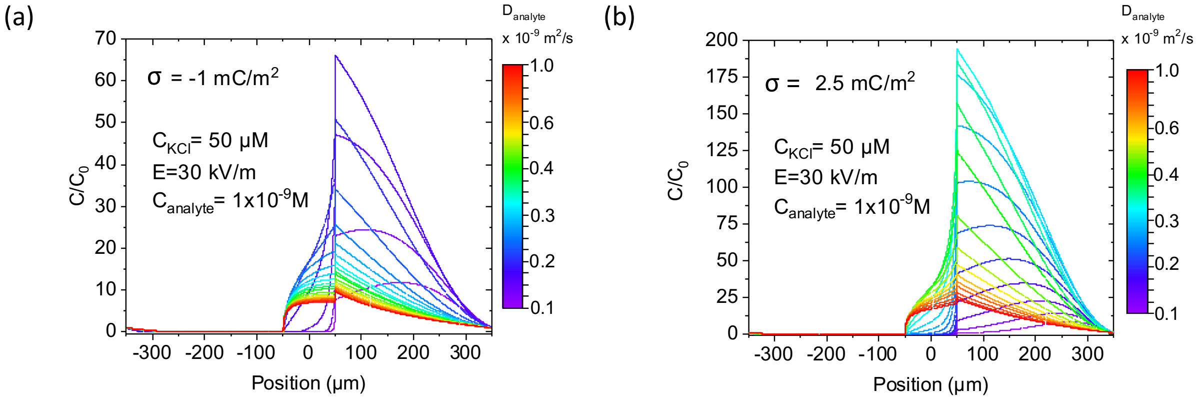

Figure 2.20: Evolution of the normalized concentration profiles with analytes of different diffusivity for two surface charge densities, (a) -1 mC/m^2 and (b) -2.5 mC/m^2. For both figures, the initial bulk BGE concentration is 50 µM, the initial bulk concentration of the analyte is 1x10^{-9} M and the applied electric field is 30 kV/m.

Figure 2.20 presents the evolution of normalized concentration profiles of a dilute analyte being transported through a 100-nm-wide nanochannel with two different surface charge densities (-1 mC/m^2 and -2.5 mC/m^2) for a range of sample mobilities.

In figure 2.20 (a), corresponding to a surface charge density of -1 mC/m^2, most of the analytes with mobilities in the depicted range experience accumulation at the nanochannel outlet in a process previously termed cathodic stacking (CS) [3]. Here, any anionic analyte ions that are able to bypass the electrokinetic exclusion/trapping at the transitioning EDL interface (e.g., via diffusion) are still able to travel through the channel towards the anodic reservoir. Thus, a meaningful concentration of sample ions is still visible in the nanochannel. As the diffusion coefficient of the analyte decreases, the concentration enhancement at the entrance of the nanochannel increases as the sample finds it more difficult to enter and ultimately be transported through the channel. Beyond a critical mobility value (specific to the conditions and extent of ICP observed), the sample is no longer able to migrate through the channel and will instead be driven to a common point of zero net velocity from both sides of the interface. This cathodic focusing (CF) phenomenon provides the highest rate of analyte enrichment when the focusing location coincides with the microchannel-nanochannel interface; however, for lower mobility samples, the electric field gradient associated with the accumulation-depletion zones causes this counter-flow gradient focusing location to shift away from the charge-selective interface into the microchannel, leading to a weaker enhancement effect. For a surface charge density of -2.5 mC/m^2, figure 2.20 (b), predicts maximum interfacial CF for dianionic analytes with a diffusivity around 0.35x10^{-9}m^2/s.

To further investigate the CS and CF mechanisms, we resolve the spatiotemporal propagating ICP dynamics of the BGE and analyte over many temporal orders of magnitude by implementing a logarithmic time discretization. This enables us to start from a condition with equilibrium EDLs and concentration distributions before very rapidly introducing an applied field and observing the evolution of the electrokinetic transport dynamics over an extended period until a steady state is reached.

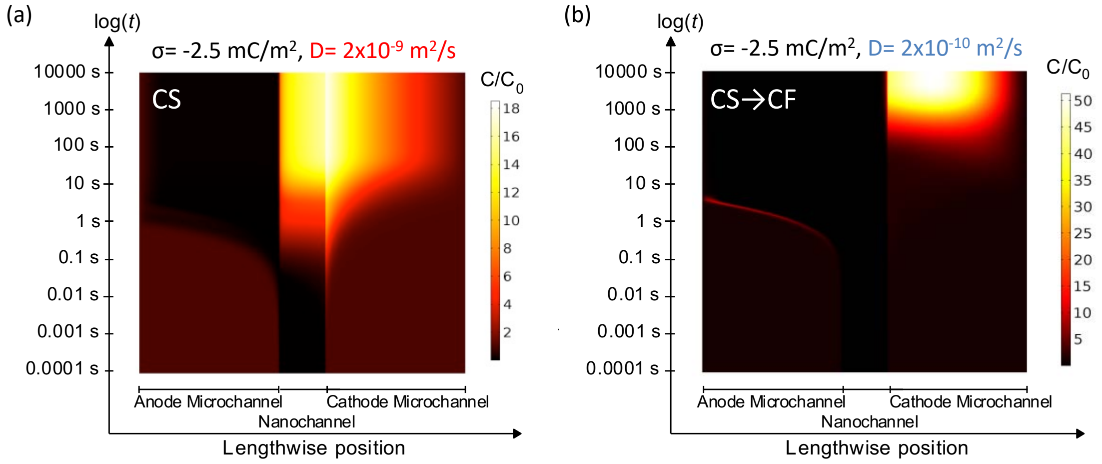

Figure 2.21: The spatiotemporal evolution of the normalized centerline concentration profiles is shown via time-extrusion plots for two analytes with diffusion coefficients of (a) 2x10^{-9}m^2/s and d) 2x10^{-10}m^2/s and a surface charge density of -2.5 mC/m^2. The vertical axis for the time-extrusion plots is logarithmic in time, revealing dynamics of BGE ICP propagation as well as various stacking and focusing analyte enhancement mechanisms occurring over many temporal orders of magnitude.

Figures 2.21 (a) and 2.21 (b) depict a logarithmic time-extrusion of the centerline sample concentration for analytes with diffusivities of 0.2x10^{-9}m^2/s and 2x10^{-9}m^2/s; that is, the profiles are colorized and stacked vertically to create a horizontal position axis and a vertical log(time) axis. As the 2x10^{-9}m^2/s sample essentially has the same diffusivity as the KCl BGE ions [70], the ICP dynamics of these sample ions mirror those of the evolving BGE ion distributions that govern the fluid flow and electric fields. The depletion region is observed to grow linearly in time, in agreement with experimental findings [24] (note again that the plotted time axis is logarithmic), as the depletion front propagates from the channel interface to its ultimate steady state position approximately 250 µm from the nanochannel entrance. The accumulation region also grows linearly in time, though at a slower rate than the fast-moving depletion zone, which generates a large local electric field and subsequently experiences a higher front propagation velocity. The visible charge exclusion of the analyte from the nanochannel at very early times quickly gives way to an increase in concentration as a CS profile develops at the nanochannel outlet and diffusion allows these more mobile ions to overcome the charge exclusion effects to enter and then migrate through the channel.

For a less mobile sample with a diffusivity of $0.2\text{x}10^{-9}\text{m}^2/\text{s}$, figure 2.21 (b) predicts that preconcentration will manifest in both microchannels, though at different time scales. As the BGE concentration distribution evolves due to ICP, the transport of the sample ions will be significantly influenced by the propagating depletion front. Specifically, the large electric field in the ion-depleted zone causes sample ions at the leading edge of the front to migrate at a high electrophoretic velocity. Just ahead of the front (i.e., farther away from the nanochannel), the electric field and subsequent local transport of ions is reduced, causing the faster moving ions behind to stack and increase the local concentration as the depletion zone spatiotemporally propagates. This anodic stacking effect is short-lived, however, and dissipates within 10 seconds as the depletion interface reaches its steady state location close to the microchannel boundary. In contrast to figure 2.21 (a), this lower mobility anionic sample cannot enter the channel on the cathodic side due to the competition between EOF and weaker EP, thus the entire nanochannel remains depleted of sample ions. The focusing interface and subsequent location of maximum concentration for this sample is shifted slightly away from the cathodic microchannel/nanochannel interface, such that the enhancement is purely that of a more conventional focusing phenomenon rather than also being influenced by the electric field associated with the charge-selective transitioning EDL interface.

By analyzing the spatiotemporal dynamics for samples of varying mobility, one can identify useful regimes for preconcentration and tune the design and/or operating conditions of a given system to maximize the enhancement of a given analyte. Figures 2.20 and 2.21 demonstrate that, if a static preconcentration front is desired (e.g., for detection purposes), the greatest level of enrichment will occur when the system is tuned for CF at the microchannel-nanochannel interface.

We have presented four models to study ICP effect of BGE and the preconcentration of analytes inside a micro/nano/microfluidic channel using COMSOL software, that can be summary as below:

- Model I was constructed with short nanochannel and short reservoirs using a very simple mesh formed by triangular elements. Only few concentrations of the BGE solution could be solved because the EDL was not correctly simulated.
- Model II implements two complex meshes integrating rectangular elements along the channels walls to simulate gradients at the EDL. This model was not completely studied but it evidences the importance of imposing correct boundary conditions.
- Model III permitted to simulate long nanochannel and long reservoirs using a manually constructed mesh integrating rectangular elements at the EDL and triangular elements at reservoirs. The steady state study showed characteristic depletion-enrichment profile at the entrance and exit of the nanochannel for Cl^- co-ion at different concentrations and electric fields. However, the study of the role of the surface charge density, the nanochannel width and temporal study of analytes revealed inconsistencies in comparison with theoretical works.
- Finally, Model III B investigates the role of important governing parameters including the BGE concentration, the electric field, the wall surface charge density and the analyte mobility on the ICP dynamics and corresponding preconcentration mechanisms. Our results indicate that stationary stacking and focusing profiles are achievable for anionic analytes of varying mobility, as predicted by 1D simulations [3]. As expected, lower sample mobilities shifted the cathodic preconcentration location away from the nanochannel as the enhancement mechanism transitions from CS to CF at the interface and then weaker CF in the microchannel; the highest preconcentration factor can be observed for CF at the nanochannel EDL interface.

Results from simulations with model III B were submitted to Special Issue of Electrophoresis on Fundamentals in the article “Predicting ion concentration polarization and analyte stacking/focusing at nanofluidic interfaces”. At the moment of the elaboration of this thesis they are in review.

Chapter 3

Experimental Techniques

3.1 Electrophoresis Experimental System

Electropreconcentration experiments are carried out in a glass or h-PDMS/glass chip under the application of an electric field and an external pressure. The experimental bench (figure 3.1) includes an optical arrangement, a microfluidic system and the electronic instrumentation.

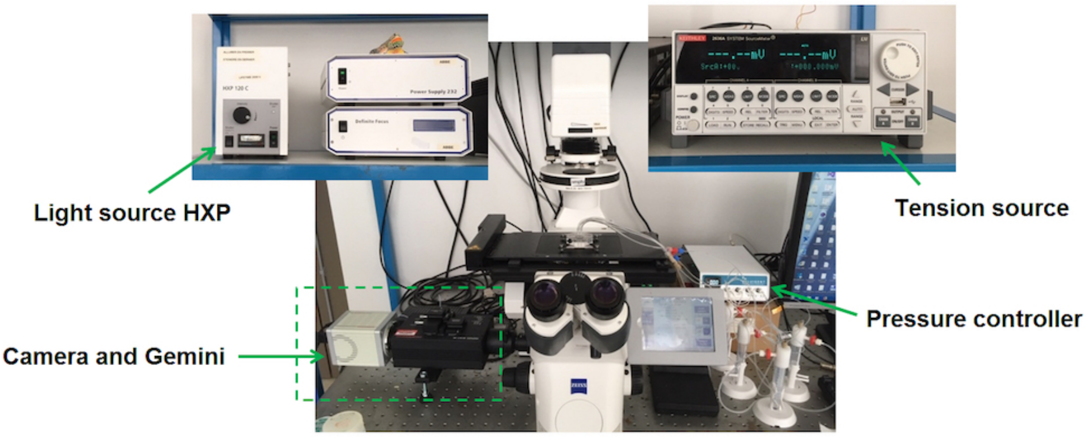

Figure 3.1: View of experimental set-up. In the central photo: the inverted optical microscope (middle), the CMOS camera and Gemini at the left side and the pressure controller at the right. In the upper left photography, the mercury light source (model HXP) and the microscope power supply and on top right the tension source.

The optical arrangement, composed of a CMOS camera (Orca Flash 4.0 LT) joined to an image splitting optics (W-View Gemini) and connected to an inverted optical microscope (Axio Observer Z1, Zeiss), permits detection by fluorescence. Due to the complexity of the optical system, next section describes it in detail.

The microfluidic system (cf. figure 3.2 A and B) incorporates 4 pressure regulated channels directly joined to the h-PDMS/glass chip through fluidics connectors. Each of these connections include a gold cable where electric connections occur. In the first year of my PhD, I worked with glass chips fabricated by the previous PhD student, Mery Ngom [74]. In this case (cf. figure 3.2 A and C), the 4 pressure channels are joined to a PMMA (poly (methyl methacrylate) plastic) block that corresponds to upper part of the chip holder where the fluidic and electric connections occur.

The pressure controller (MFCS-EZ Fluigent) enables the flow actuation of fluid by pressure regulation. A pressure command interface, coded in MATLAB®, manages the pressure controller to activate different operation modes: "Flush" (activation of channel 1 and 3), "Equilibre" (application of the same pressure on all channels), "Pression" (switch on of channels 1 and 2), "Contrepression" (turn on of channels 3 and 4), and the activation of each channel individually. "Flush" and "Equilibre" are mainly used to rinse out the glass chip nano and microchannels and eliminate the air bubbles. "Pression" and "Contrepression" are useful to apply the pressure for the front stabilization.

The electrical system (cf. figure 3.2 A and B) is composed by a sourcemeter (Keithley 2636A) with one ground potential divided in two independent lines connected to reservoirs 1 and 2 of the h-PDMS/glass chip. On the other side, a setpoint voltage is plugged in reservoirs 3 and 4 of the h-PDMS chip. The applied voltage is regulated using one channel of the tension source. For glass chips (cf. figure 3.2 A and C), electric connections are made through the PMMA block. The ground and the setpoint are connected in reservoirs similar as h-PDMS chips. The glass chip is joined to the PMMA block using a PDMS sealant pierced with 4 holes aligned with the reservoirs of the glass chip. The PMMA block has four cavities each one containing a platinum electrode and the liquid is injected into these cavities using a syringe before connecting the tubes.

3.1.1 Description of the optical system

The experiments can be developed in two ways: first, all the equipment is adapted to classical electropreconcentration experiments (Gemini is in bypass mode, that means there are no filters nor dichroic mirror for the detection thus only one image will be given by the camera) or in a second way, where the W-View Gemini is included. This image splitting tool, located between the camera and the microscope, is used to detect and distinguish molecular species with two different emission wavelengths. Gemini's structure can be divided in four blocks:

1. Optical mask: trim the image down to half of its width.
2. Dichroic mirror block: create the pair of simultaneous images separated by wavelength.
3. Emission filter block: each emission filter leads cross short wavelength and long wavelength respectively.
4. Correction lens block: allow to adjust the magnification and focus of images.

Figure 3.3 shows the optical system for detection by fluorescence. The excitation light comes from the mercury lamp and passes through the microscope filters set. This optical block has three filters: (1) excitation filter, (2) dichroic mirror and (3) emission filter. The excitation filter is in our case a bandpass filter (BP) that permits only selected wavelengths from the mercury lamp to pass through on the way toward the sample for its excitation. The dichroic mirror is oriented at 45 ° angle to the path of excitation light. Its function is to reflect light below the

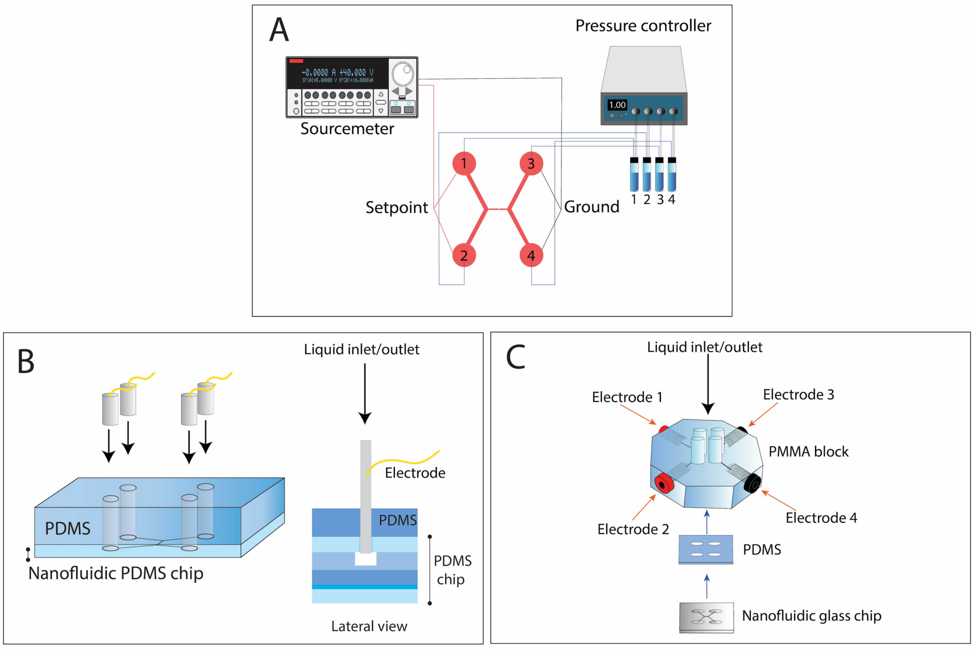

Figure 3.2: A) Scheme of the fluidic connections (from right) and electric connections (from left) of the nanofluidic chip. The setpoint can be a positive or negative voltage. B) Assembly of nanofluidic h-PDMS/glass chip. Four fluidic connectors are introduced in the PDMS layer to inject the liquids. They are adapted with gold cables as electrodes. C) Assembly of nanofluidic glass chip. A PDMS sealant is used to connect the glass chip to the PMMA block, where the fluidic and electric connections are made.

edge wavelength in the excitation band and to transmit light above the edge wavelength in the emission band. We use FT (from German Farb teiler that means color splitter) to refer the dichroic mirror. The emission filter is also in our case a bandpass filter that permits only the wavelengths emitted by the sample to travel and blocks all light outside this band. After the light passes through the microscope filters set, it enters through the different blocks of Gemini to create one pair of images at different wavelength that are detected by the camera. Normally, the top image that we observe using the camera software corresponds to the long wavelength and the bottom image corresponds to the short wavelength.

As we work with fluorescein sodium and ovalbumin marked Texas Red, we use two microscope filters sets adapted for each molecule. For fluorescein sodium the 38 HE filters set (Zeiss) is used and the 31 filters set (Zeiss) is used for ovalbumin. Reader must have in mind that in figure 3.3 the microscope filters set represents 38 HE or 31, depending on the molecule that we study. The optical characteristics of both filter sets are presented in Table 3.1. The 38 HE filters set has an excitation band between 450 nm and 490 nm, a dichroic filter with an edge wavelength of 495 nm and an emission band between 500 nm and 550 nm. The 31 filters set has an excitation band between 550 nm and 580 nm, a dichroic filter with an edge wavelength of 585 nm and an emission band between 590 nm and 650 nm.

For Gemini's emission filters, the short wavelength corresponds to an emission band between 500 nm and 525 nm and the long wavelength has an emission band between 584 nm and 676 nm. The dichroic filter has an edge wavelength of 560 nm.

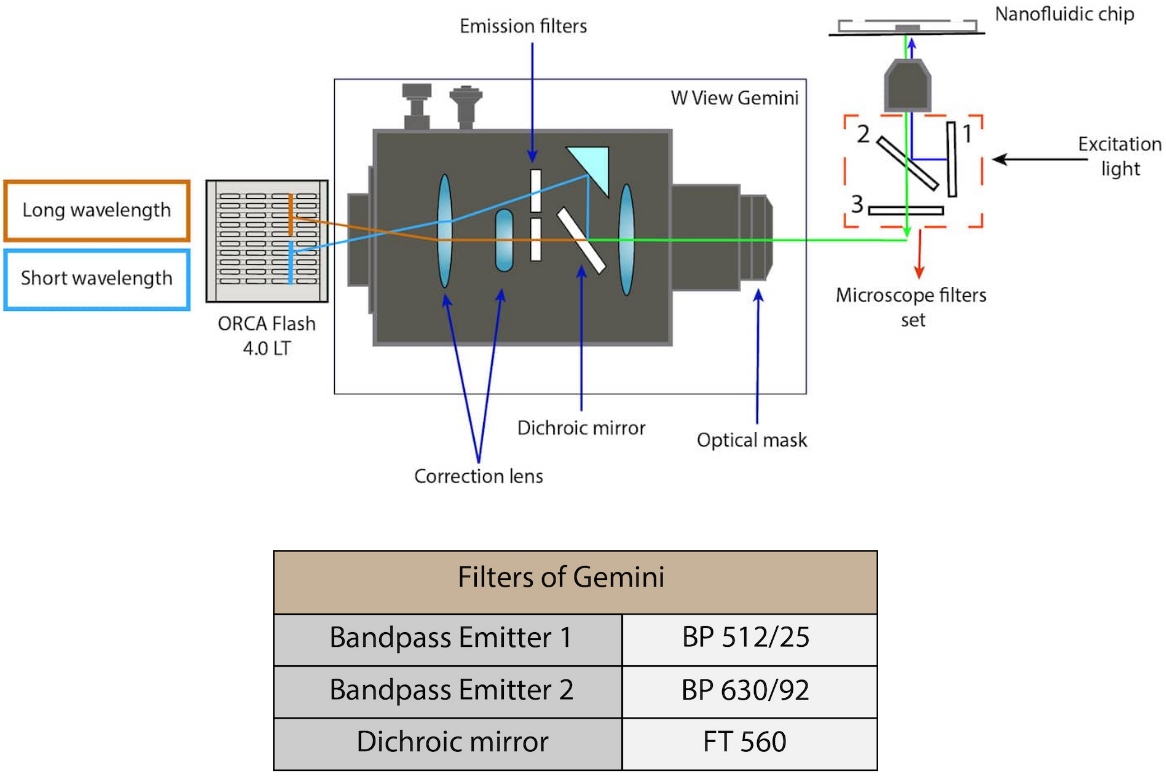

Filters of Gemini	
Bandpass Emitter 1	BP 512/25
Bandpass Emitter 2	BP 630/92
Dichroic mirror	FT 560

Figure 3.3: W View Gemini operation principle and characteristic filters (all in nm) for detection by fluorescence. The excitation light (from the right) enters to the microscope filters set that is composed by the excitation filter (1), dichroic mirror (2) and emission filter (3). Once the sample is excited, the emitted light passes through the different blocks of Gemini until the formation of a pair of images at different wavelengths detected by the camera.

Filters set 38HE		**Filters set 31**	
Excitation	BP 470/40	Excitation	BP 565/30
Dichroic	FT 495	Dichroic	FT 585
Emission	BP 525/50	Emission	BP 620/60

Table 3.1: Microscope filters sets, all units are in nm. For excitation an emission filters, the pair of numbers represent the central wavelength of the bandpass and the bandwidth.

3.1.2 Step-by-step experimental protocol

The initial step consists of positioning the chip to observe it at the microscope. Depending on the material chip, there are two different assemblies. The h-PDMS/glass chip is directly fixed to the microscope chuck via a double-face scotch. The fluidic connections are introduced, and liquid is injected using a syringe. Next, leakages are verified through a 1 bar flush step. On the other hand, the glass chip is aligned with the PMMA block and PDMS sealant. Then, the assembly is attached onto the microscope chuck via the adjustment of four screws to avoid leakage of the liquid. To verify, deionized water is injected at 300 mbar in the four reservoirs with an equilibrium step (the four reservoirs are at the same pressure). For both cases, entrapped air bubbles are removed by flush and equilibrium steps. Figure 3.4 presents the typical pressure controller modes.

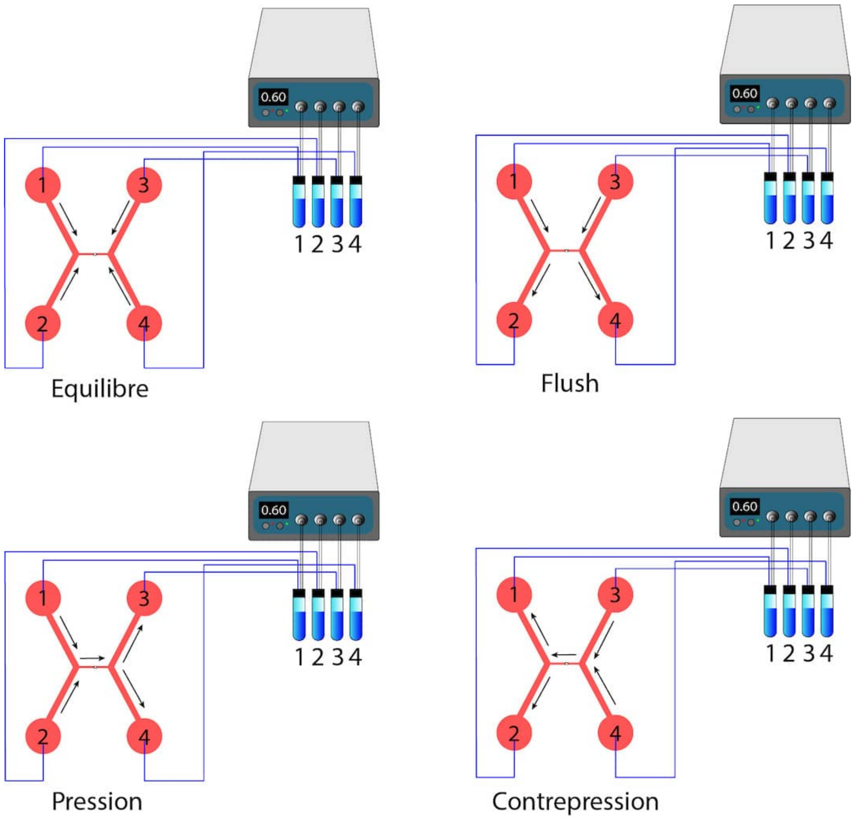

Figure 3.4: Different pressure controller operation modes where the arrows indicate the direction of liquid flow: equilibre=equilibrium (same pressure in all reservoirs), flush=flush (pressure in reservoirs 1 and 3), pression=pressure (pressure in reservoirs 1 and 2) and contrepression=counterpressure (pressure in reservoirs 3 and 4).

Once there are no air bubbles in the channels and tubes, the deionized water is replaced by the buffer solution using the flush mode for 2 hours to ensure that the surface charge is comparable in all chips. Most of the time h-PDMS/glass chips have one or two uses whereas glass chips can be used several times. If glass chips have organic contamination a sequence of rinses is made with sodium hydroxide (NaOH): 10 minutes of NaOH with concentration 1M, 10 minutes of NaOH with concentration 0.1M and a rinse with deionized water for 15 minutes.

At this point, one reference image of the region of interest (ROI) called “Iblack” is taken. This image is used to compare the light intensity before and during the experiment.

Then the analyte of interest can be injected in all reservoirs. Some cycles of pressure, counterpressure, equilibrium and flush are included to ensure the homogeneous distribution of the analyte through the microchannels and nanochannels. Once this is achieved, another image of reference called “Iwhite” is taken. Both “Iblack” and “Iwhite” are described in detail in the data treatment section.

Now it is possible to begin the experiment using the “preconcentrationmod” program. The experiment starts with an electric rinse. 20 V are applied on the chip for 2 minutes, then the buffer solution is renewed for 10 minutes under flush mode and finally equilibrium is applied for

10 minutes. This clean process is used to ensure the same initial state in all the chips and also to improve the electropreconcentration conditions [75].

After cleaning, different voltages and pressures are applied in the chip. The analyte is excited by the mercury lamp and images are taken at regular time intervals. Normally, the camera takes one image every 10 seconds for 1 minute and then one image every minute for 10 minutes, which means 16 images for each pair pressure-voltage. Depending on the number of pair pressure-voltage, the acquisition can take some hours. At the end, all images are analyzed by a treatment MATLAB® program.

Sodium chloride (NaCl) and potassium chloride (KCl) both with a concentration of 10 µM, and phosphate-buffered saline (PBS) x1 solution were used as background electrolyte (BGE) solutions. As model molecules, fluorescein sodium was prepared in NaCl and KCl solutions, respectively, and ovalbumin marked Texas Red was prepared in NaCl. The concentration of all the solutions was 10 µM. For last experiments, the Hepatitis C DNA sequence marked fluorescein was prepared in PBSx1 solution with a concentration of 1 µM.

3.1.3 Description of the electropreconcentration MATLAB® program

The program used for electropreconcentration experiments is composed of a main command interface “preconcentrationmod” that saves the experimental parameters and uses them in a secondary function called “manipsmod”. This secondary function, more complex, handles the application of tension, the application of pressure and the synchronization between the camera and the shutter of reflected light of microscope (it controls the excitation of the molecule by fluorescence) to data acquisition at specific time along the experiment. To avoid photobleaching the molecule is excited few seconds necessary to take each photo so must of the time the shutter of reflected light of microscope remains closed. Additionally, “manipsmod” saves all the information in a specific file to be analyzed later. An initialization function is included in the main program to control the start of the camera, the tension source and the pressure controller.

Figure 3.5 presents the main command interface. There are five sections corresponding at each green rectangle. The “Nettoyage” section corresponds to the clean process of the chip before each acquisition. The “Pression” section includes the experimental pressures in bars and “flux” represents the direction of application of this pressure. The flow options are 0 (no pressure), 1 (pressure mode) or 2 (counterpressure mode). The “caméra” section contains the gain and exposure time of the camera. The “enregistrement” section allows saving the data in a new file. Finally, the “Tension” section includes the experimental voltages and the number of images that are going to be saved.

The Go button launch the acquisition data and the “Déconnexion” button disconnects all the equipment.

As the experimental set-up was never used before for electropreconcentration experiments, the first part of the codification of the MATLAB® program was the interface of different instruments. Simple MATLAB® programs were coded to control individually the sourcemeter, the pressure controller, and the synchronization of the microscope shutter with the mercury lamp for the excitation of the sample. Once the proper functioning of each instrument (correct application of voltage, pressure and excitation for a given time), all was centralized in the com-

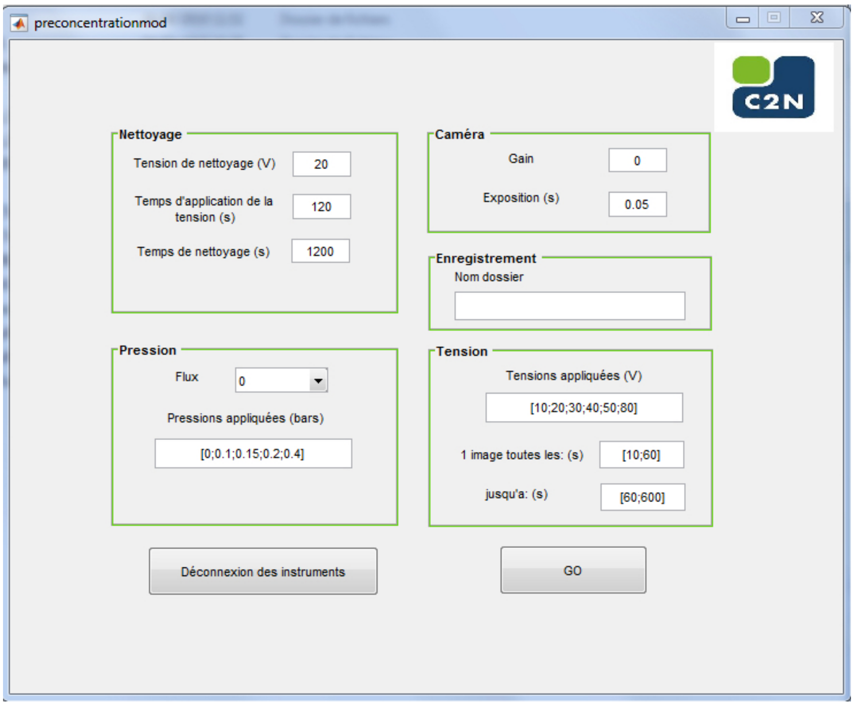

Tension de nettoyage (V): 20
Temps d'application de la tension (s): 120
Temps de nettoyage (s): 1200
Gain: 0
Exposition (s): 0.05
Nom dossier:
Flux: 0
Pressions appliquées (bars): [0;0.1;0.15;0.2;0.4]
Tensions appliquées (V): [10;20;30;40;50;80]
1 image toutes les: (s): [10;60]
jusqu'a: (s): [60;600]

Figure 3.5: Main GUI (graphical user interface) to launch preconcentration program. The user fills all the parameters depending on the experiment.

mand interface. The implementation of the Zeiss microscope SDK (software development kit) on this new command interface, specifically in the "manipsmod" function, allows to properly control the excitation of the sample (by shutter) but also permits the automatization of change of microscope filters set or the change of microscope objectives if necessary.

The camera was the last instrument to be included in the "manipsmod" function, this is because first we found a problem of compatibility with the MATLAB® version and this complicate its interface and then because different exposure times were tested to find the best conditions for the electropreconcentration experiments. It is important that the source of excitation be stable with time and to limit the parasitic light to have clear images.

3.1.4 Data treatment

Once the acquisition of data is done, all images are treated with the "traitementcompletfd" program. This command interface (figure 3.6) facilitates the plot of analyte concentration profiles with time along all the micro/nano/microfluidic channel and save all data to re-plot it if necessary. There are three sections corresponding to each gray rectangle. In the captures section: the name of the file containing the row images to be treated; the number of channels in the chip for treatment; Detection includes an automatic or manual detection through a subprogram that reduces the noise of the row images and allows a better visualization of the channels; figures indicates the option of visualizing all the plots and save them in a new file called Data; and "Canaux très inclines" is used in case of leaning channels with respect to the horizontal axe.

The measurement parameters section is used to identify each row image depending on the voltages and pressures applied in the experiment. To simplify, the parameters used here are the same that those used for the preconcentration program. The total number of images is added in this section and the "Iwhite factor" was always one.

The calibration section contains the slope and the intercept of the linear equation that relates the intensity and concentration of molecules obtained from the calibration curves. These curves are presented in Annex B.2 for the different molecules.

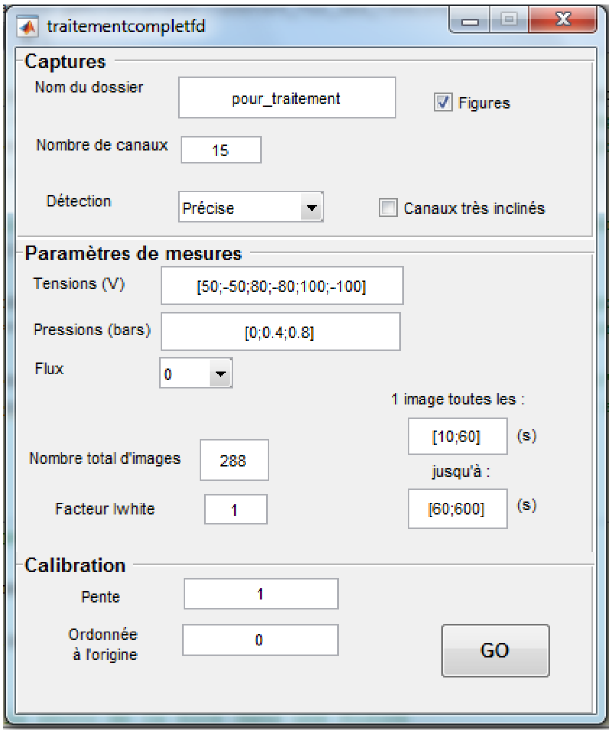

traitementcompletfd

Captures

Nom du dossier: pour_traitement

☑ Figures

Nombre de canaux: 15

Détection: Précise

☐ Canaux très inclinés

Paramètres de mesures

Tensions (V): [50;-50;80;-80;100;-100]

Pressions (bars): [0;0.4;0.8]

Flux: 0

1 image toutes les : [10;60] (s)

jusqu'à : [60;600] (s)

Nombre total d'images: 288

Facteur Iwhite: 1

Calibration

Pente: 1

Ordonnée à l'origine: 0

Figure 3.6: Main GUI (graphical user interface) to launch the treatment program. The user fills all the parameters depending on the sequence of row images to treat. Captures= Captures, Paramètres de measures = Measurement parameters, Calibration= Calibration.

To correctly estimate the local concentration, we must correct the light intensity considering the initial conditions of the experiment, background noise, surrounding light and experimental parameters. Based on previous works [1], the next equation is used:

$$R = \frac{I_{measured}}{I_{reference}} = \frac{I_{row} - I_{black}}{I_{white} - I_{blackw}} \tag{3.1}$$

With:

I_{row}: the intensity inside the channel under the experiment conditions.

I_{black}: the intensity outside the channel under the experiment conditions.

I_{white}: the reference intensity of the analyte with concentration 10 µM, under the experiment conditions but without electric field.

I_{blackw}: the reference intensity of the buffer solution without analyte, under the experiment conditions and without electric field.

The “traitementcompletfd” program collects all parameters used in the electropreconcentration experiment through the command interface and uses two secondary functions called “lirecompletfd” and “traitement_complet” to plot all concentration profiles using the equation (3.1). This program also works with a main folder where row images and references images are saved to be available for treatment.

The “lirecompletfd” function includes a secondary function that reduces the noise and automatically detects the channels when the intensity of images is sufficiently high. If the detection is not correct, the function enables the manual selection of the boundaries of all the channels. The automatic detection or the manual selection is made in the Iwhite image and Iblackw image (reference images), respectively, and the position of each channel is saved. The $I_{reference}$ intensity is calculated trough the subtraction of the mean intensity I_{white} of each channel and the mean intensity I_{blackw}, calculated from all the image since this last one is mainly noise.

The “traitement_complet” function treats each channel individually in the row images for each pair pressure-voltage to obtain the mean intensities I_{black} and I_{row}. The Iblack zone above each channel, in order to correct the potential gradient of intensity present, is automatically selected on the first-row image. Once having $I_{measured}$ for all row images, R (the ratio of intensities) is calculated. We use the linear equation obtained from calibration that relates the concentration to the intensity to find the concentration value. Finally, the concentration profiles are plotted as function of the microchannel x-coordinate for different times. Figure 3.7 shows an example of the different regions of interest (ROI) used for the treatment of one microchannel in a h-PDMS/glass chip and the plot obtained after the treatment.

3.2 UV-Visible spectrophotometry

One of the aims of spectrophotometry measurements is to obtain the characteristic spectra of fluorescein sodium and ovalbumin marked Texas Red. It was of interest to investigate the range of concentration where absorbance and concentration have a linear relation. In addition, the linear relation is investigated for fluorescence and concentration. Even if detection is done by fluorescence, it is important to complete the studies with absorbance measures.

Another aim of spectrophotometry study was to choose the best microscope filters for the optical system thanks to further investigate the exact wavelengths of emission and excitation of the molecules. The utilization of conventional spectrometers is justified by the complexity of develop this kind of measures in a nanofluidic chip. However, to upgrade the set-up and be able to perform such study we recently coupled a miniaturized OceanInsight flame spectrophotometer to the inverted microscope in a second experimental bench at the ICP.

Spectroscopic processes rely on the interactions between electromagnetic radiation and matter. Light interacts with atoms and molecules in discrete ways to produce characteristic absorption and emission profiles. In UV-Visible spectrophotometry, the absorbance or transmittance of species (usually in solution) are studied in wavelengths from 200 to 800 nm most of the time. When a solution absorbs radiation, it attenuates the intensity of the incident radiation for certain wavelengths. The absorption spectrum plots the attenuation of the incident beam according to the wavelength.

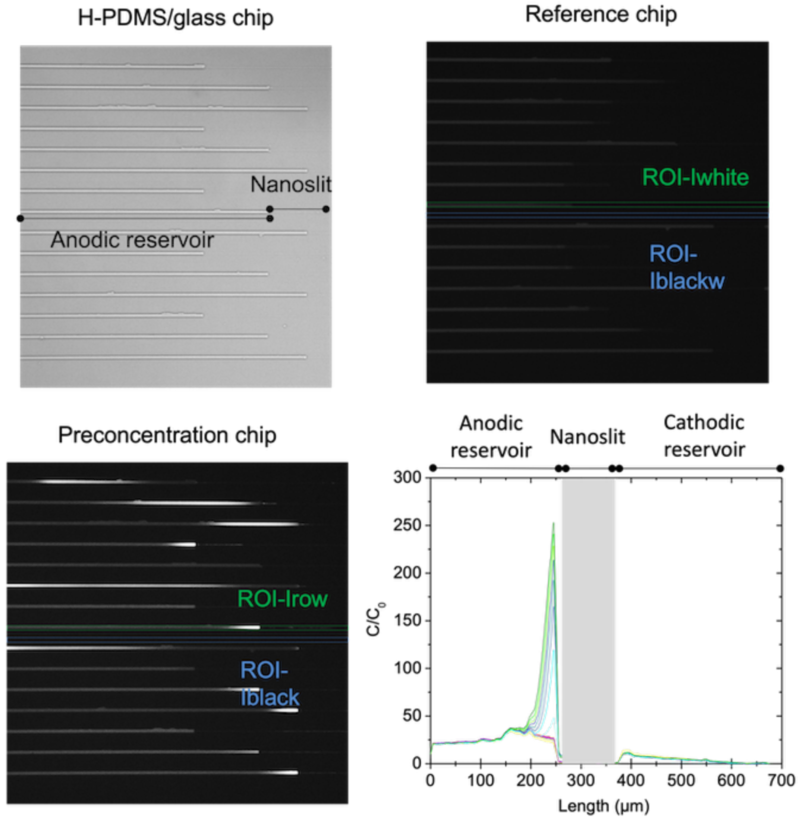

Figure 3.7: On top, a photo of the anodic side of the h-PDMS/glass chip and an image of the reference chip. On bottom, an image of the preconcentration chip where fluorescent spots are visible, and one example of an anodic stacking profile obtained after the MATLAB® treatment.

Absorption is defined as $A = log(\frac{I_0}{I})$ where I_0 is the incident intensity and I is the transmitted intensity.

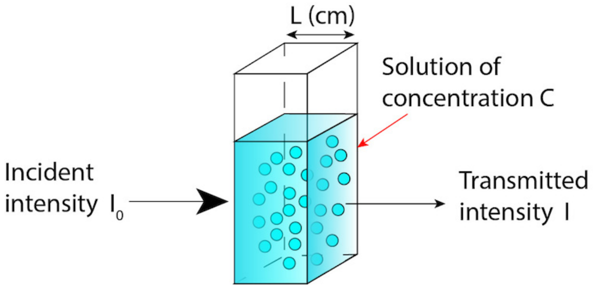

Figure 3.8: Scheme of principle of absorption. The solution of concentration C attenuates the intensity of incident light when it passes through the cuvette with width L.

3.2.1 Experimental description of UV-visible spectrophotometry

All the absorption spectra are recorded on a double-beam Lambda 75 spectrophotometer (Perkin Elmer). It is composed of two polychromatic sources: one of deuterium and the other of tungsten-halogen. Both lamps cover the entire spectrum used in UV-Visible spectrophotometry (200 to

800 nm) and depending on the desired wavelength one or both lamps are used.

Figure 3.9 shows, in a schematic way, the UV-visible spectrophotometer principle. The light passes through an arrangement of mirrors to the grating monochromator and using a filter a monochromatic light is obtained. Then, several mirrors direct the light and separate it into two distinct and equivalent beams. Each beam passes through the reference and sample cuvettes respectively and finally the light arrives on the photonic detector.

Before making a measurement, it is important to do an auto-zero to correct the optics of the system considering the cuvette and the buffer solution. The measurements are done in quartz cells, because of its transparency to the UV radiation, with pathlength of 10 mm from Hellma Analytics.

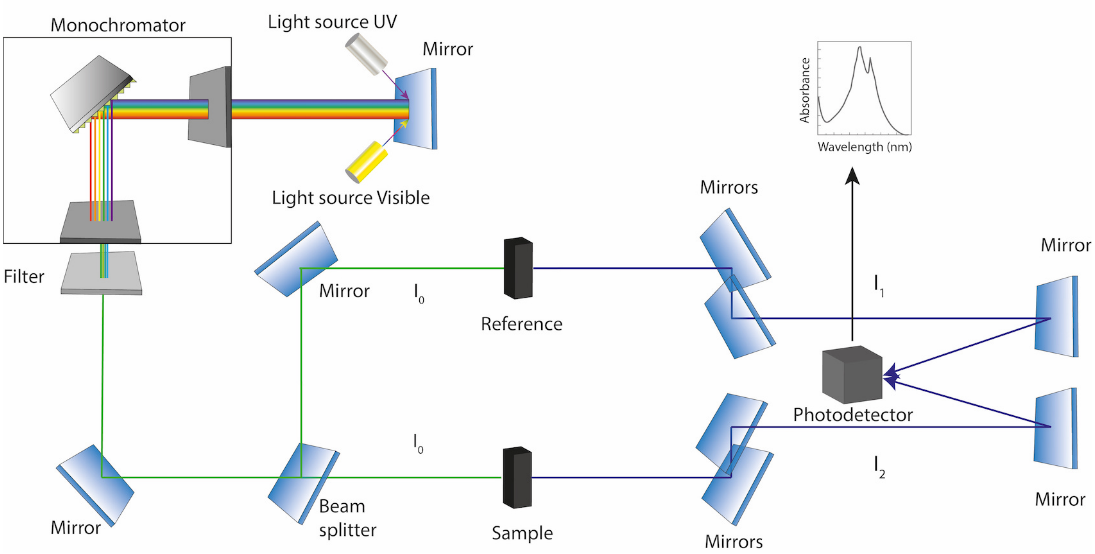

Figure 3.9: Scheme of the principle of a double-beam UV-visible spectrophotometer. I_1 and I_2 represent the transmitted intensity after passing the reference and the sample respectively.

The absorption spectra are collected with the Perkin Elmer software. The quartz cell is filed with 900 µL of each sample and the acquisition starts with the solution with the lowest concentration until the highest concentration. Each sample is analyzed 3 times in an interval of 250 to 800 nm taking as reference the solvent of each sample. Fluorescein and ovalbumin both prepared in NaCl solution with a concentration of 10 µM were analyzed.

3.3 Fluorescence spectroscopy

Aforementioned, the detection in electropreconcentration experiments is made by fluorescence. Therefore, accurate determination of emission fluorescence spectra has a crucial importance.

Fluorescence is a phenomenon of spontaneous light emission that occurs when an electron of a molecule passes from an excited state to a fundamental state after its excitation by light. Fluorescence emission spectroscopy studies the intensity and number of fluorescence photons emitted by a molecule that is excited at a fixed wavelength called excitation wavelength (λ_{exc}).

Fluorescence spectra are presented as the intensity of the fluorescence photons detected according to their emission wavelength (λ_{em}). To study the fluorescence of a molecule it is important that the absorbance on the UV-Visible spectra be of less than 0.1 a.u. It allows us to avoid the no linearity of the relation between C and I because of the parasitic reabsorption phenomena.

3.3.1 Experimental description of fluorescence spectroscopy

All the fluorescence measurements are recorded in a fluorescence spectrometer Fluorolog (Horiba Jobin Yvon). This spectrofluorimeter is composed of a polychromatic source (usually a xenon discharge lamp), grating monochromators and a photo multiplier detector placed in our case at 90° of the sample. In addition, two sets of slits are located before and after each monochromator to change the spectral accuracy of excitation and emission wavelengths (cf. figure 3.10). First, the light is filtered by the grating monochromator that allows a single wavelength to reach the sample. In the sample compartment, the sample responds to the incoming radiation. The resulting radiation is then filtered by the second monochromator that feeds the signal to the detector.

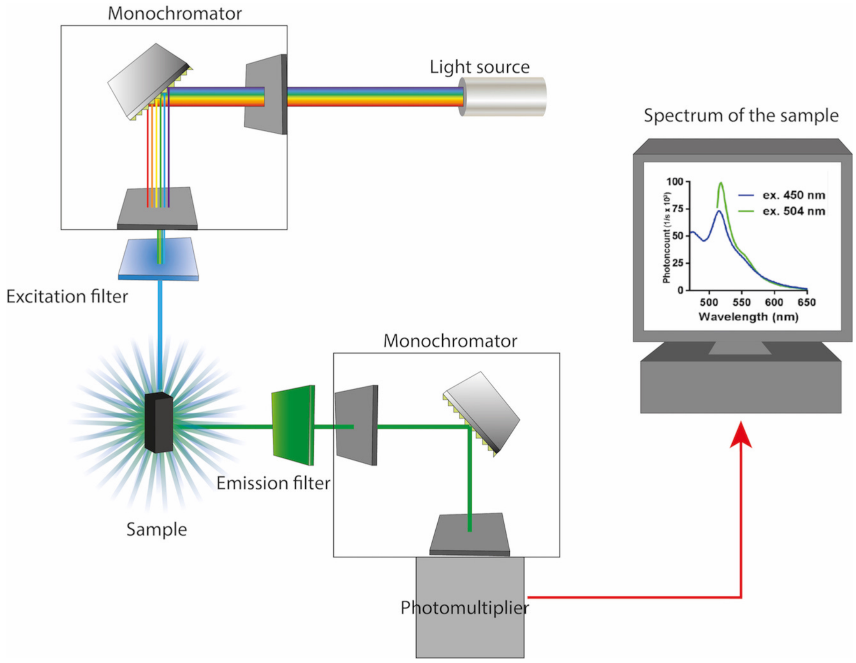

Figure 3.10: Schema of the measure principle of the Fluorolog spectrofluorimeter.

From the UV-visible absorption spectra we chose concentrations of fluorescein with absorbance less than 0.1 a.u. to obtain the fluorescence emission spectra, this to have a linear intensity of fluorescence in function of concentration (to limit parasitic reabsorption through intra-dye excitation-emission that occurs at higher concentration). The quartz cell is filed with 900 µL of each sample (Hellma quartz cell with a 3mm pathlength). Similarly, as absorption spectra, the acquisition starts with the lowest concentration until the highest concentration and 3 rounds of measures are done for each sample. Fluorescein and ovalbumin prepared in a solution NaCl with concentration 10 µM were analyzed.

3.4 Spectrophotometric characterization

3.4.1 Absorbance spectra of fluorescein and ovalbumin

Spectrophotometric measurements are done to study the absorbance and emission spectra of fluorescein sodium (Sigma-Aldrich, F6377) and ovalbumin marked Texas Red (Thermofisher, O23021). These two model molecules are mainly used for electropreconcentration experiments in h-PDMS/glass chips.

Figure 3.11a shows a set of absorbance spectra for fluorescein sodium with five different concentrations in 10 µM NaCl solution in the 250 to 800 nm wavelength region. Two mainly absorbance bands with maximum peaks at 459 nm and 482 nm are in the visible interval. In fact, fluorescein absorbs maximum light at each two wavelengths. The 459 nm peak has no important shift in the position as the concentration increases, we found a variation of two nanometers. That means that this peak is located between 458 nm and 460 nm. On the other hand, the 482 nm peak is more accentuated as the fluorescein sodium is progressively concentrated. We observe a shift between one and five nanometers in the position of the absorption maximum for lowest concentrations (10 µM, 25 µM, 55 µM) and no variation for higher concentrations (75 µM and 100 µM). The fluorescein sodium fabricant reports maximum absorbance peak at 460 nm [76] which agrees with our results.

The calibration curves of figure 3.11b are plotted from each maximum in absorption spectra. Each point corresponds to a maximum absorbance peak from an average wavelength (aforementioned, we got three times the absorbance spectra for each concentration). We use the Beer-Lambert law to trace the straight lines. This equation relates the absorbance of the molecule to its concentration as:

$$A = l\epsilon C \tag{3.2}$$

with A the absorbance, l the pathlength in cm, ϵ the molar absorption coefficient in $\mathrm{M}^{-1}\mathrm{cm}^{-1}$ proper to each molecule and dependent on the wavelength and C the concentration in M.

The slopes of calibration curves give the value of the molar absorption coefficient. According with the fitting line for the 459 nm maximum ($y = 0.0068x - 0.0193$) the molar absorption coefficient is 6803.1 $\mathrm{M}^{-1}\mathrm{cm}^{-1}$. Similarly, from the 482 nm linear fitting ($y = 0.0109x - 0.0994$) the molar absorption coefficient is 10929.6 $\mathrm{M}^{-1}\mathrm{cm}^{-1}$. We obtain good linearity coefficients R^2 of determination for both lines.

Figure 3.12a presents the set of absorbance spectra of ovalbumin marked Texas Red in 10 µM NaCl buffer for five different concentrations at 250-800 nm wavelength. Two main bands with maximum absorbance peak at 556 nm and 594 nm can be seen in the visible interval. Both appear clearly accentuated at higher concentrations and there is no variation in the localization of peaks for all concentrations. The fabricant reports 596 nm [77] as maximum absorbance peak which is in accordance with the experimental results.

The calibration curves for maximum absorbance peaks are plotted in figure 3.12b. Using the Beer-Lambert law (eq. 3.2), ovalbumin linear fitting is more accurate compared to that of the

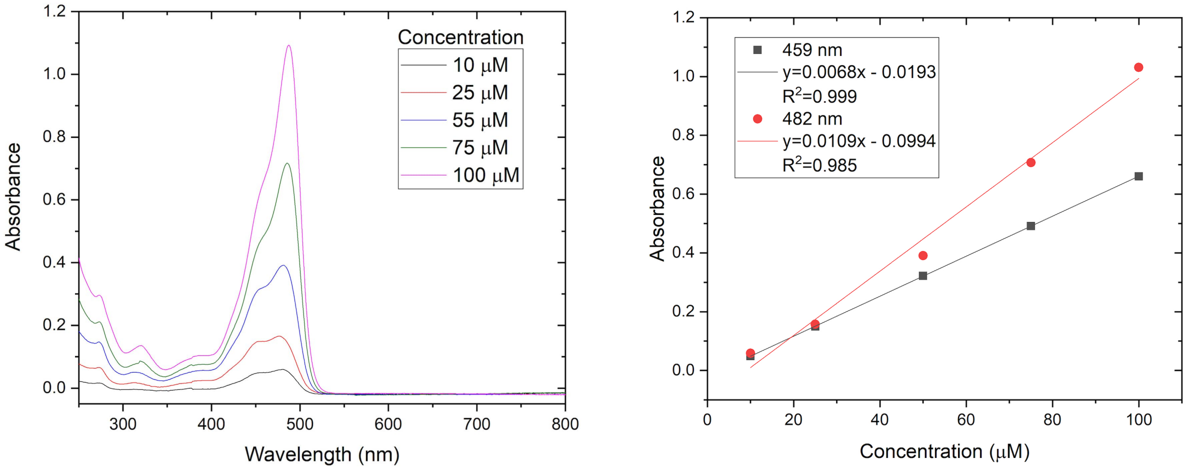

(a) **(b)**

Figure 3.11: (a) Absorption spectra of fluorescein sodium in NaCl wit ionic strength 10 µM for five different concentrations with maximum in absorbance at 459 nm and 482 nm, respectively. (b) Calibration curves in UV visible spectrophotometry of fluorescein sodium at maximum wavelengths.

fluorescein sodium due to the no shifting of peaks for all concentrations. Consequently, fittings have a good coefficient R^2 of determination (0.999) for both lines. The curve slope from the 556 nm peak fitting ($y = 0.0527x - 0.0004$) gives a molar absorption coefficient of 52665.4 $M^{-1}cm^{-1}$. From the 594 nm fitting line ($y = 0.1024x - 0.0012$) the molar absorption coefficient is 102408.4 $M^{-1}cm^{-1}$.

The spectrophotometric results above provide key information for the characterization of both model molecules. Once knowing the wavelength corresponding to a maximum in absorbance, we use it as excitation wavelength to register the fluorescence emission spectra of both molecules. We present these results in the next part.

3.4.2 Emission spectra of fluorescein and ovalbumin

Fluorescence emission spectra of fluorescein sodium in 10 µM NaCl buffer are recorded at low concentrations to minimize the inner filter effect. This problem, common in fluorescence spectroscopy, is related to the attenuation of the excitation beam by highly concentrated samples. While the surface facing the excitation beam fluoresces strongly, the center of the cuvette has lower fluorescence and the detected signal is modified. Indeed, collected absorption spectra show that absorbance at excitation wavelength is less than 0.1 a.u. for concentrations below 10 µM which means that the excitation light intensity along the pathlength is essentially proportional to the concentration. This is the correct situation for quantitative measurements in our nanofluidic chip.

The fluorescein sodium is excited at 482 nm, which is the maximum in absorbance, and the emission spectra is collected in an interval of 488 nm to 661 nm. Figure 3.13a shows that the maximum peak of fluorescence is located at 509 nm. Figure 3.13b presents the corresponding calibration curve. Note that the integrated fluorescence intensity was calculated to have accurate results and not only the maximal fluorescence values are presented, also it explains the change in

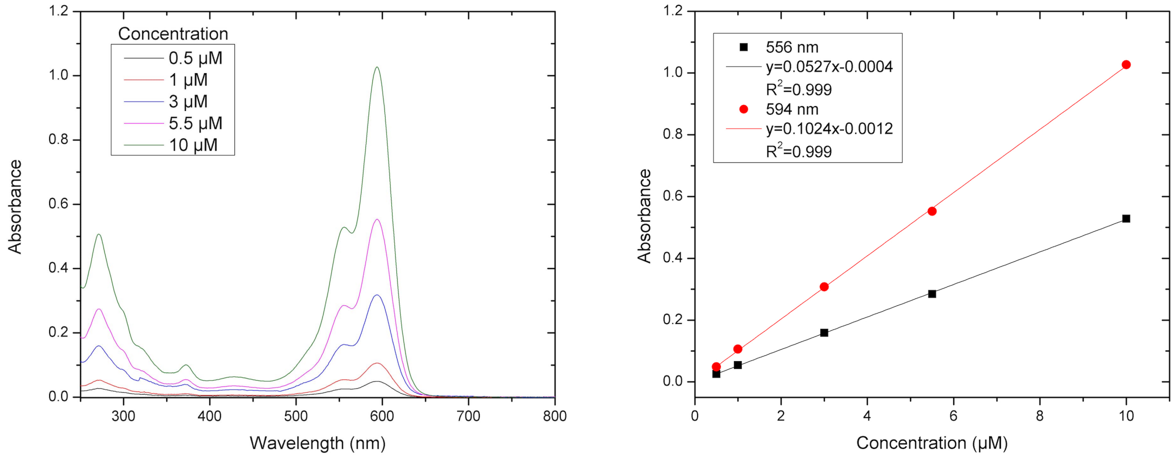

(a) **(b)**

Figure 3.12: (a) Absorption spectra of ovalbumin marked Texas Red molecule in NaCl wit ionic strength 10 µM for five different concentrations. Maximum in absorption are 556 nm and 594 nm in the visible interval. (b) Calibration curves in UV visible spectrophotometry of ovalbumin at maximum wavelengths.

y scale. The integrated fluorescence intensity is not only justified by a more linear relationship between the intensity and the concentration, but it also corresponds to the ROI integration after a bandpass filter in the microfluidic set-up (see above, part 3.1.1).

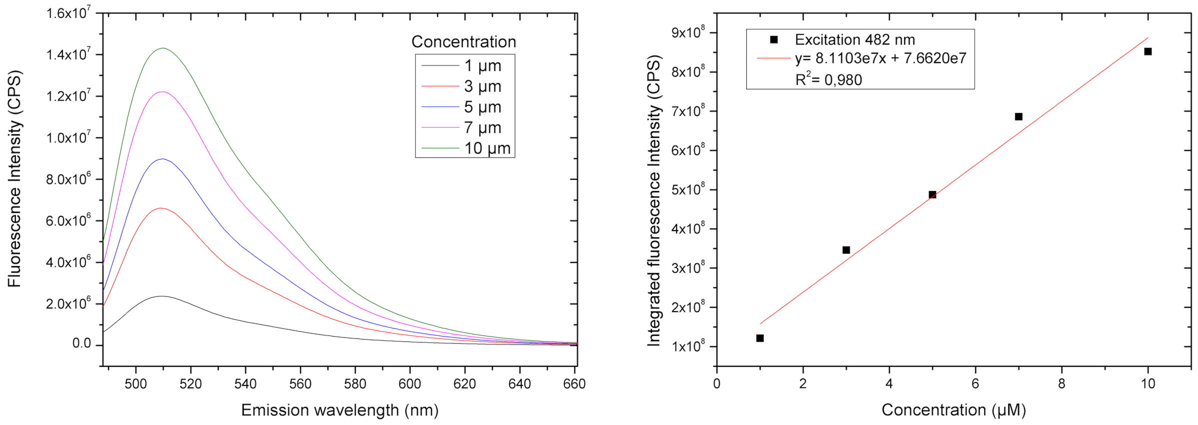

(a) **(b)**

Figure 3.13: (a) Emission spectra of fluorescein sodium in NaCl with ionic strength 10 µM for five different concentrations. The maximum of fluorescence is located at 509 nm. (b) Calibration curve of fluorescein excited at 482 nm.

The emission spectra of fluorescein sodium at higher concentrations between 10 µM and 100 µM is also investigated. In figure 3.14a the maximum peak of fluorescence is located at 512 nm, it presents a shift of 3 nm to longer wavelengths compared to the maximum peak at lower concentrations. However, this maximum is nearly the same as the value reported by the fabricant of 515 nm [76]. In figure 3.14b the calibration curve. This curve is not linear because of reabsorption effects at higher concentrations. A linear behavior is observed for concentrations below 50 µM and then for concentrations above 50 µM a kind of logarithmic behavior is noticed.

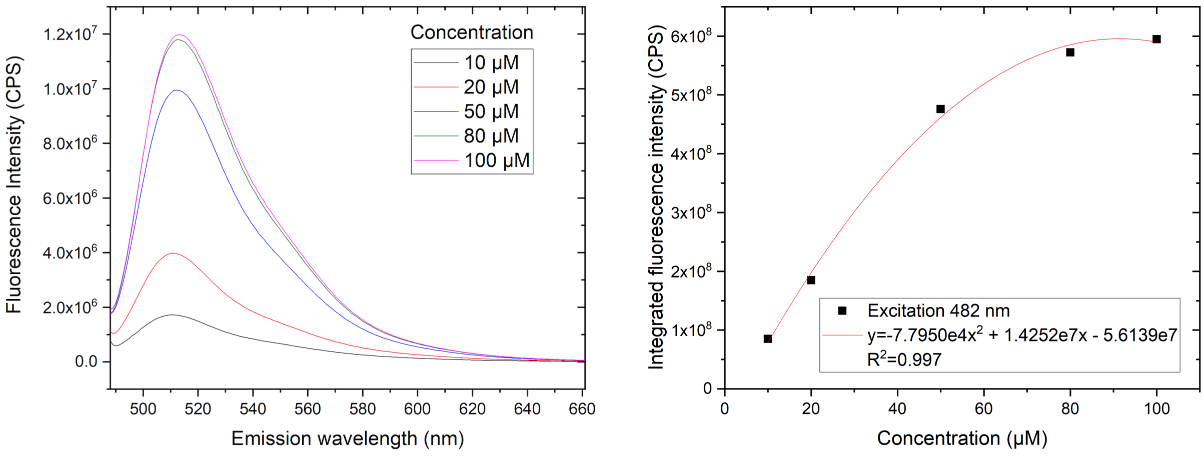

(a) **(b)**

Figure 3.14: (a) Emission spectra of fluorescein sodium in NaCl with ionic strength 10 µM at higher concentrations. Maximum peak of fluorescence is presented at 512 nm. (b) Calibration curve of fluorescein excited at 482 nm.

We found that the best fit for the experimental data is a second order polynomial fitting due to the last two points and this confirms that for these concentrations we can't do quantitative measures.

Figure 3.15a presents the emission spectra of ovalbumin marked Texas Red for concentrations between 0.5 µM and 10 µM. The emission maximum shifts to longer wavelength from 606 nm to 613 nm as the ovalbumin is more concentrated. Fabricant reports a maximal fluorescence at 615 nm [77] which is in accordance with the experimental results. As expected, the calibration curve has not a lineal behavior due to reabsorption effects (figure 3.15b). For concentrations below 3 µM a linear behavior is observed but then for higher concentrations a logarithmic behavior is noticed. A second order polynomial fitting is the best approximation for the experimental data showing that quantitative measures can't be done with concentrations above 3 µM.

To study the excitation and emission as a whole and to provide robust quantitative measurements a 3D scan is carried out for both model molecules. This 3D contour plot, named Excitation Emission Matrix (EEM), illustrates the fluorescence intensity of molecules considering a specific range of excitation and emission wavelengths. For our purposes, we define the range of the excitation and emission corresponding to the optical pathway that is presented in part 3.1.1. In addition, the EEM provides important information for the optimization of the optical system of the microfluidic set-up.

First, we investigate the fluorescein sodium at different concentrations. We take as reference the excitation and emission wavelengths of filter set 09 (Zeiss, BP 450-490, FT 510, LP 515) to construct the EEM. This filter set, used for electropreconcentration experiments before this thesis, has a bandpass filter between 450 nm and 490 nm as excitation filter. To complete it, we have a dichroic mirror with an edge wavelength of 510 nm and a lowpass (LP) filter with an edge wavelength of 515 as emission filter.

Figure 3.16 shows the fluorescence intensity of fluorescein sodium when passing through the excitation and emission wavelengths corresponding to the microscope filters set 09. Parallel

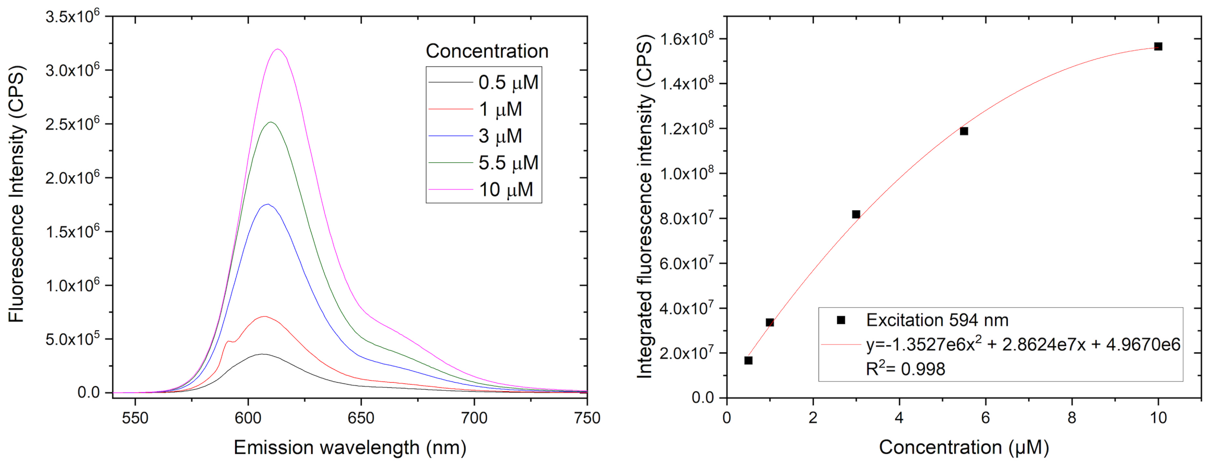

(a) **(b)**

Figure 3.15: (a) Emission spectra of ovalbumin marked Texas Red in NaCl wit ionic strength 10 µM at five different concentrations. Maximum is located from 606 nm for 0.5 µM to 613 nm for 10 µM. (b) Calibration curve of ovalbumin excited at 594 nm.

planes indicate different concentrations and fluorescence intensities increase slightly as concentration rise. The emission maximum located at 509 nm is not included in the 3D plot and only a part of it appears (yellow area in plot). This result highlights that the filters set 09 is not the better choice to study the fluorescein at these concentrations. For optimal fluorescence detection we need that excitation and emission filters be centered on the molecule's absorption and emission peaks. Also, peaks should be narrow in bandwidth and spectrally well separated. Therefore, we change to the 38 H filters set which arranges better to fluorescence characteristics of fluorescein for the experiments.

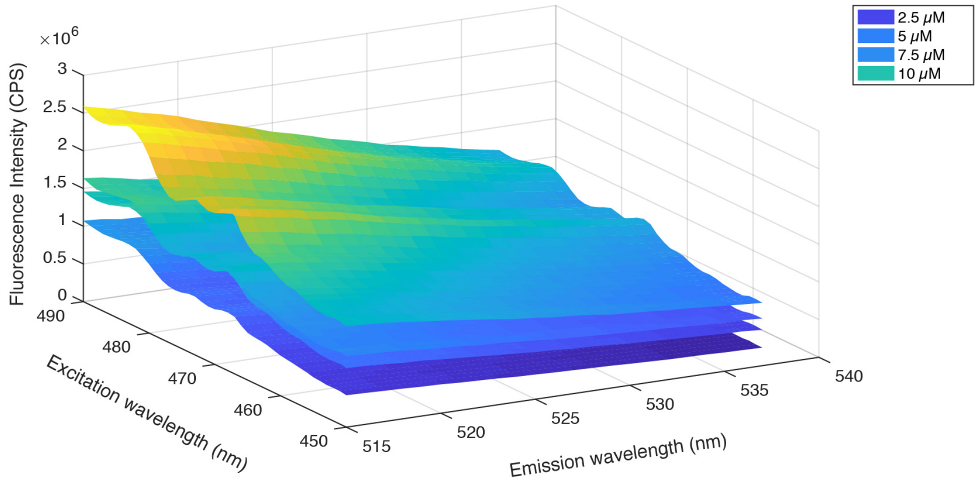

Figure 3.16: EEM of fluorescein at different concentrations. Excitation is made between 450 nm and 490 nm and emission is collected for wavelengths above 515 nm simulating the filters set 09 of Zeiss.

Then, we analyze the ovalbumin marked Texas Red at different concentrations. In figure 3.17, note that the maximum in fluorescence at 609 nm is included in the range of emission wavelengths when considering the excitation and emission wavelengths of filter 31 (Zeiss, BP 565/30, FT 585, BP 620/60). In fact, the filter 31 has a bandpass filter between 550 nm and 580 nm as excitation filter, a dichroic mirror with an edge wavelength of 585 nm and a bandpass filter between 590 nm and 650 nm as emission filter. We see a maximum peak in fluorescence intensity (yellow zone) that increases with the rise of concentration of ovalbumin. This is a good example of an adequate filters set for a molecule.

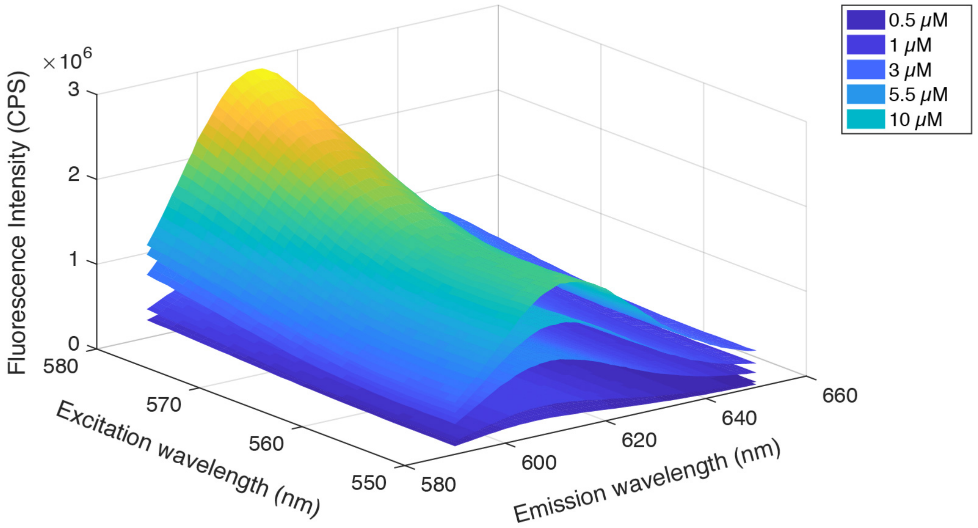

Figure 3.17: EEM of ovalbumin marked Texas Red at different concentrations. Excitation is made between 550 nm and 580 nm and emission is collected for wavelengths between 590 nm and 650 nm simulating the filters set 31 of Zeiss.

To conclude, this chapter presents the spectrophotometric characterization of fluorescein sodium and ovalbumin marked Texas Red to provide robust quantitative measurements in the micro/nanofluidic chips using the microfluidic set-up.

Chapter 4

Experimental results

This chapter will provide a general description of the fabrication process of glass chips. In the first year of my PhD work I carried out electropreconcentration experiments in this kind of chips that were fabricated by Sokhna Mery Ngom, a third-year doctoral student at that time. In a second part, the detailed step-by-step process for the fabrication of Hard-PDMS/glass (h-PDMS/glass) chips is presented, focusing in the optimization of the etching process for the fabrication of the master mold and the surface treatment for unmolding the chips. This new protocol was made by Francois-Damien Delapierre during his postdoctoral research in our group at C2N and I participated in the optimization of the process. Finally, important experimental results are showed using different model molecules.

4.1 Fabrication of glass chips

Figure 4.1 A presents the main steps to fabricate glass chips using Inductively Coupled Plasma - Reactive Ion Etching (ICP-RIE) technique. In figure 4.1 B and C, a photo of the chip integrating eight nanochannels and a tilted SEM photo of one nanochannel. As indicated before, first experiments were made using glass chips, so it is important to introduce the process. In fact, I was not able to continue the fabrication of glass chips because at that moment all the machines in the cleanroom were not available because of the moving of C2N to the new building. In addition, the bonding process is not easy. In general, glass chip fabrication process is long in comparison with that of h-PDMS/glass chips which was the main motivation for changing the process. All details about the fabrication of glass chips are well described in [74] but we can summarize them as below:

1. Deposition of a 1 µm SiO_2 layer on a 500 µm glass substrate.
2. Deposition of a 200 nm aluminum layer on a 1 nm germanium layer to reduce the roughness of the aluminum layer.
3. Deposition of a 500 nm ZEP520A layer as mask for the electron-beam lithography.
4. Electron-beam nano-lithography and development of the ZEP520A resist to generate the nanomotifs.

5. Etching of the aluminiun/germanium layer by ICP-RIE to transfer the nanomotifs.

6. Etching of the SiO_2 layer by ICP-RIE to transfer the same nanomotifs.

7. Finally, the drilling of the reservoirs on the glass cover and the bonding of the chip.

The bonding process is very important in the fabrication of glass chips. Three important aspects must be considered: the cleanliness, the flatness and a good control of micro-roughness of the surfaces that are going to be bonded.

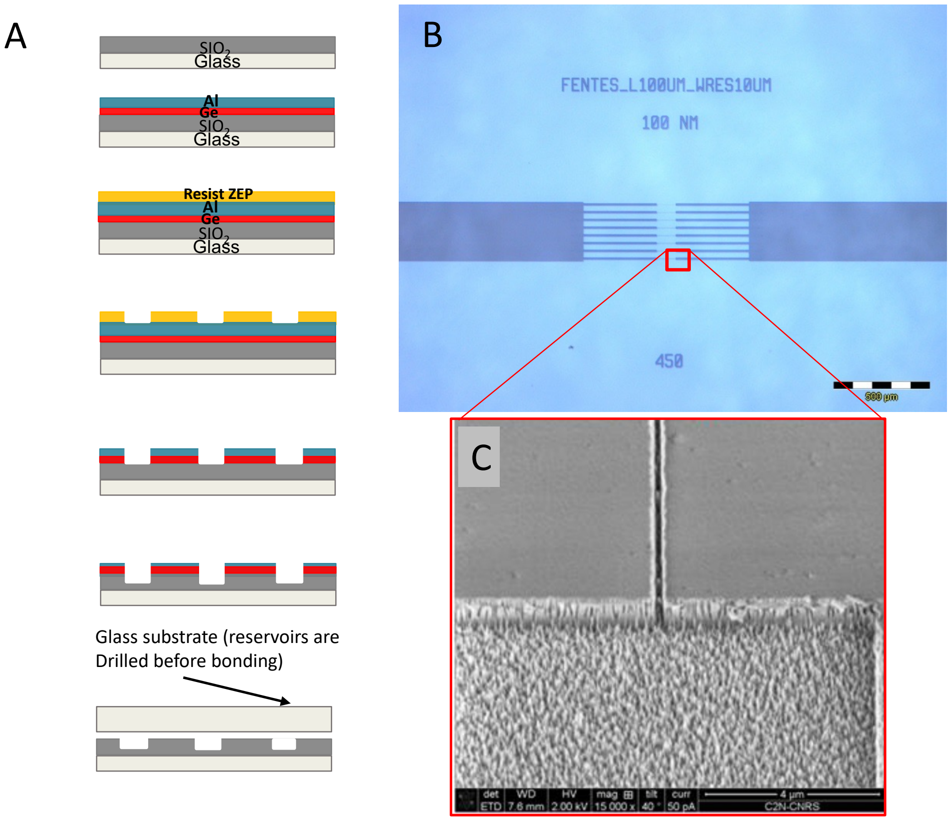

Figure 4.1: A) Main stages to fabricate the glass chips [74]. B) Geometry of the used chips and C) SEM image of the state of one nanochannel after the etching process.

4.2 Fabrication of h-PDMS/glass chips

To fabricate the h-PDMS/glass nanofluidic chips, a silicon master mold produced by electron-beam lithography (EBL) and capacitively coupled plasma reactive ion etching (CCP-RIE) is employed. In this section, we describe the fabrication process of both the silicon master mold and the h-PDMS/glass chips.

4.2.1 Master mold fabrication process

1. A3 Polymethyl methacrylate resist (PMMA) is spin-coated on a 2-inch silicon wafer to obtain a 200 nm-thick layer and followed by a baking at 160 °C.
2. An electron beam lithography is made by Edmond Cambril, followed by the development of the PMMA resist. The wafer is immersed in the developer Methylisobutylketone/Isopropanol (MIBK/IPA, 25/75 in volume) at 20 °C for 60 s, rinsed with IPA for 60 s and dried with a nitrogen gun.
3. After the PMMA development process, a 30 nm-thick layer of chromium is deposited using a Plassys MEB 550 SL e-gun evaporator. This layer is used as etching mask.
4. To remove the chromium in not exposed zones, a lift-off is made using 2-Butanone solution for 10 minutes. In this step we use a syringe with the same solution to assure that all zones are lifted-off.
5. The master mold is then etched in the CCP-RIE Nextral NE100 machine with the “Siliani” program. The silicon is etched using a gas mixture of SF_6 (8 sccm) and CHF_3 (8 sccm) with an etching speed of approximately 84 nm/min and pressure P = 10 mTorr.
6. The remaining metal is then removed with a chromium etchant solution for 10 minutes.
7. Finally, the master mold is functionalized with an optool treatment. This process avoids that PDMS sticks on the master mold and allows the PDMS chip to be unmold without difficulty. It consists first of diluting optool at 1% by volume in the solvent perfluorohexane, then immersing the master mold in this solution for 1 minute and covering the beaker with stretch film. The master mold is then left in a water bath at a temperature between 60 and 65 °C for 1 hour while the grafting takes place. Then, the substrate is rinsed in perfluorohexane solvent for 10 min to remove excess product. Then, the master mold is ready to fabricate the h-PDMS/glass chips.

4.2.2 Master mold: optimization of the fabrication process

To understand the dry etching process (used at nanometer scales) is important to introduce important parameters as the etch rate, the anisotropy and the selectivity.

An etch rate (R) is the ratio of total etched depth (d) by a total etching time (t), defined by:

$$R = \frac{d}{t} \tag{4.1}$$

According to the etch rate as function of the spatial direction, the degree of anisotropy (A) can be defined as follows:

$$A = 1 - \frac{R_L}{R_V} \tag{4.2}$$

where R_L is the lateral etch rate (u/t) and R_V is the vertical etch rate (d/t). For isotropic etching, the etching depth is similar to the undercut distance ($A \approx 0$). In anisotropic etching, another important factor is selectivity (S). Selectivity is defined as the ratio of material removal rates between the target and the masking materials.

$$S = \frac{R_{for\ etched\ material}}{R_{for\ mask\ material}} \tag{4.3}$$

In an ideal process the target material must be removed without degrading the masking material, so a high selectivity is necessary to preserve the etched material.

Reactive ion etching

One of the most common dry etchers systems is the Reactive Ion Etching (RIE). This etching technique uses RF excited plasmas for etching several materials. Source gases are introduced in a chamber leading to chemical reactions that produce plasma species and resulting reactants. Dissociated ions in the plasma are then accelerated towards the sample and the ion bombardment helps the etching reaction. Using this technique, the etched profile is anisotropic and the etch selectivity is reasonably high [78].

One type of RIE consist of using a capacitively coupled plasma (CCP). This plasma is generated between two electrodes while reactive gases are fed into the chamber. The electrodes form parallel plates of a capacitor, a RF power is applied to one of the electrodes while the other is grounded. Then, ions are accelerated from the plasma to the powered electrode, where the sample is situated. The potential difference between the plasma and the powered electrode is known as the bias voltage. The sample then experiences the bias voltage and the bombardment of reactive ions as other species from the plasma causing the etching process.

Numerous RIE processes have been developed to etch silicon. Key etchants for silicon are SF_6, sulfur hexafluoride, which is a clean and nontoxic processing gas, and CHF_3, as passivate gas. The common mask materials for silicon etching include PRs, silicon oxide, and metal films [78].

Optimization of the etching process and unmolding

It is important to mention that first h-PDMS-glass chips were fabricated using a master mold fabricated with a 50 nm-thick nickel layer as etching mask. The silicon mold was etched using the “silifd” protocol (created by François-Damien Delapierre), a gas mixture of SF_6 (5 sccm) and CHF_3 (11 sccm) with an etching speed of 50 nm/min and a pressure P = 5 mTorr. Even if a straight vertical etching was obtained, removing the nickel fluorides after the CCP-RIE process was very hard. Figure 4.2 A and B show examples of a master mold after three hours in a nitric acid solution to try to remove the metal. Nickel remains in most zones of the reservoirs and nanochannels causing a coarse surface. Indeed, the molded h-PDMS/glass chips will replicate this coarse surface creating thinner nanochannels and modifying the preconcentration experiments. In addition, nickel as etching mask favors the micromasking causing grass out of the structure after the etching process. At that time, the postdoctoral research of François-Damien Delapierre finished in the group, so I continue the optimization process.

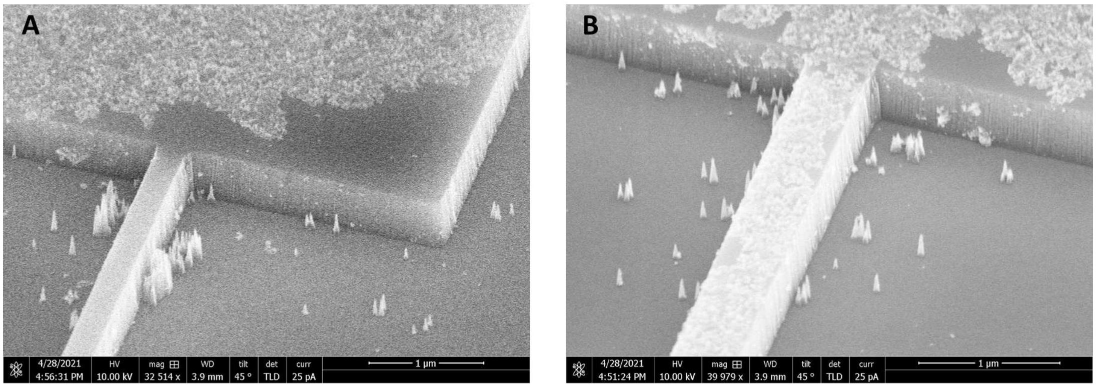

Figure 4.2: SEM images of an etched silicon master mold using nickel as etching mask after three hours in a nitric acid solution to try to remove the remaining metal.

To overcome the problem, other metals were tested as etching mask. 30 nm-thick layers of aluminum and chromium, respectively, were used. After SEM observations, we realize that the aluminum does not withstand the etching process (SF_6, 5 sccm and CHF_3, 11 sccm) for 10 minutes, which was the necessary time to etch at least 500 nm. For this reason, tests only continue using the chromium mask.

Figure 4.3 A, B, C and D present SEM images of nanochannels at four different etching times corresponding to 10 minutes, 12 minutes, 20 minutes and 30 minutes, respectively (using a 30 nm-thick Cr mask). Tests were done to find the maximum etching depth with straight sidewalls of nanochannel and microchannels. At 10 and 12 minutes we observe good etching depth of 500 nm and 510 nm, respectively but with some defects observed at the base of the nanochannels. In a first time, the fact of having this kind of defects seem to be not very important but later we realize that PDMS remains there after unmolding. On the other hand, images at 20 and 30 minutes indicate that the chromium mask was attacked by the etching process, causing a pyramidal form of the nanochannels. Considering the etching depth and the straight sidewalls, unmolding tests were continued with molds fabricated with an etching time of 12 minutes. After the etching process the chromium remained layer was eliminated by a chromium etchant solution for 10 minutes.

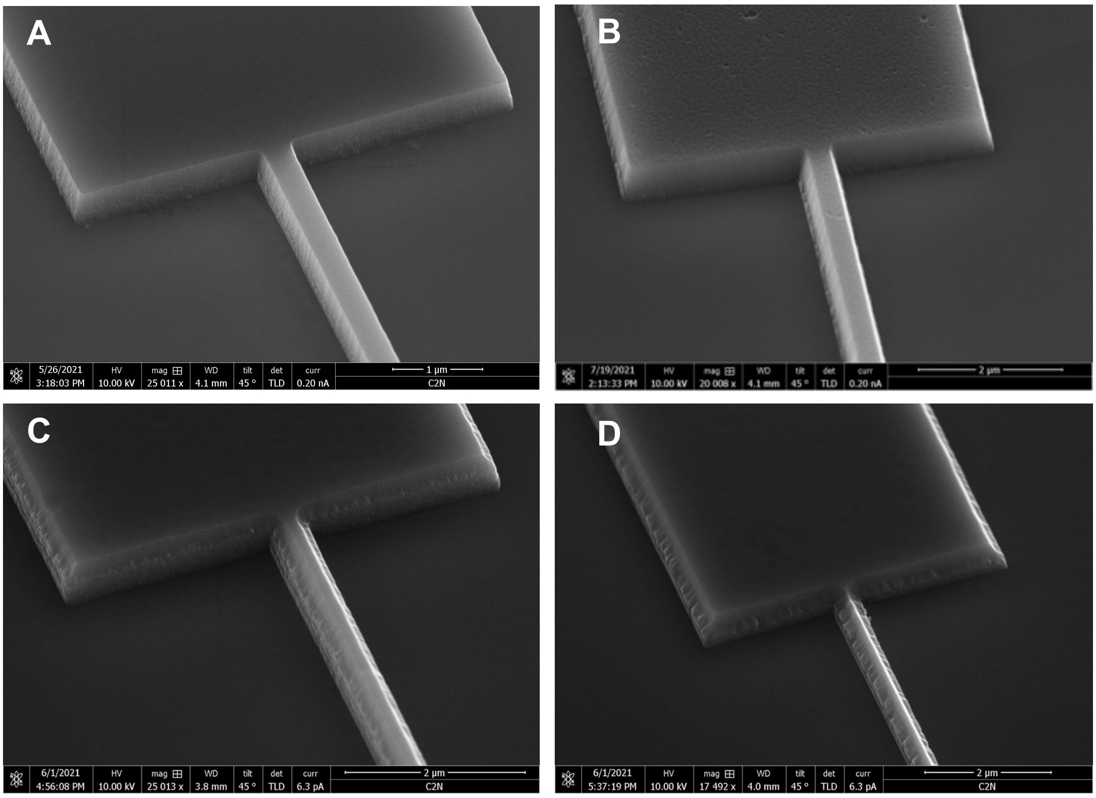

Figure 4.3: SEM images of the silicon master mold using a 30 nm-thick chromium layer as etching mask at different etching times: A) 10 minutes, B) 12 minutes, C) 20 minutes and D) 30 minutes.

Two surface treatments were tested on the silicon mold to avoid sticking of the PDMS and to made easier the unmolding of the chip. The first one consists of a silane layer of trimethylsilylchloride (TMCS) deposed by evaporation process on the mold surface. After a 30 seconds plasma treatment, the mold was put inside a container next to a little beaker containing few drops of liquid TMCS for five minutes. After this process the mold was ready for the tests with PDMS. Simple observations indicate that PDMS remained on the surface of the mold after unmolding. In fact, cleaning the mold is a delicate process to avoid damage of the nanochannels and using TMCS was not working. We then tested the optool process described in previous section in another mold. Even if optool is better anti-adhesive than TMCS, figure 4.4 A and B exhibit that PDMS remains at the sidewalls of the channels. Probably, the significant roughening of the etched sidewalls boosts the adhesion of PDMS, indicating that the etching process need to be changed. Also, we saw that the metallic layer was not always well eliminated affecting the anti-adhesion treatments.

Then, the etching process “Siliani”, presented in the description of the fabrication of master mold, was then used (note the different ratio mixture of SF_6 and CHF_3 (8sccm, 8 sccm)) for 10 minutes. As a result, straight sidewalls were obtained (as see in figure 4.5), compared to the previous etching process. In addition, the metal was easily retired in a chromium etchant solution after the process for 10 minutes. This time the optool treatment was only tested, showing good results when unmolding the chips. First because of straight sidewalls of micro and nanochannels and second because this surface treatment works better without the metallic layer.

It is important to mention that I took over the fabrication of the chips six months before the end of the writing of this manuscript after François-Damien Delapierre left the C2N, so I didn't do enough tests to improve the etching process. For example, I would have liked to do tests using Al/Ge layer as etching mask for silicon with a mixture of SF_6 and CHF_3 (8sccm, 20 sccm) that showed good results during the test of Sokhna Mery Ngom for the fabrication of glass chips [74]. Or maybe I would have liked to use a resist like MaN as etching mask.

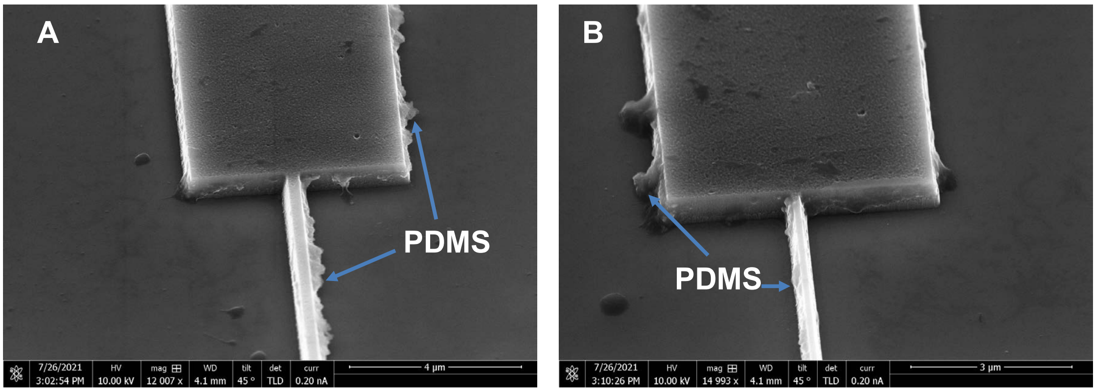

Figure 4.4: SEM images of silicon master mold after the first unmolding of h-PDMS/glass chips indicating that PDMS remains stick at some parts of the walls.

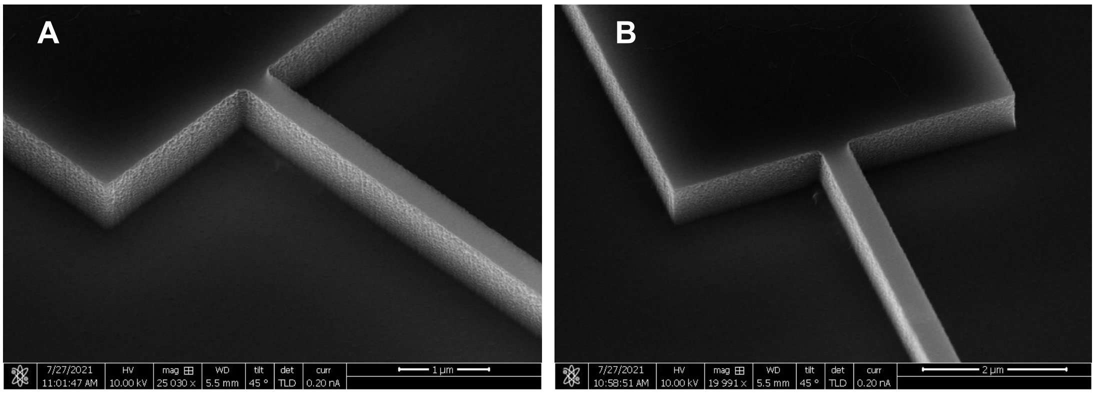

Figure 4.5: SEM images of silicon master mold after 10 minutes etching, with a mixture of gases SF_6 and CHF_3 (8sccm, 8 sccm).

In figure 4.6 A a photo of the 2-inches silicon master mold containing four "H" type motifs. The inset images show the zoom of the central part of one motif that incorporates five nanochannels with different widths varying from 250 nm to 450 nm (figure 4.6 B) and one SEM image of a single nanochannel (figure 4.6 C). Main fabrication steps of master mold are illustrated in figure 4.6 D.

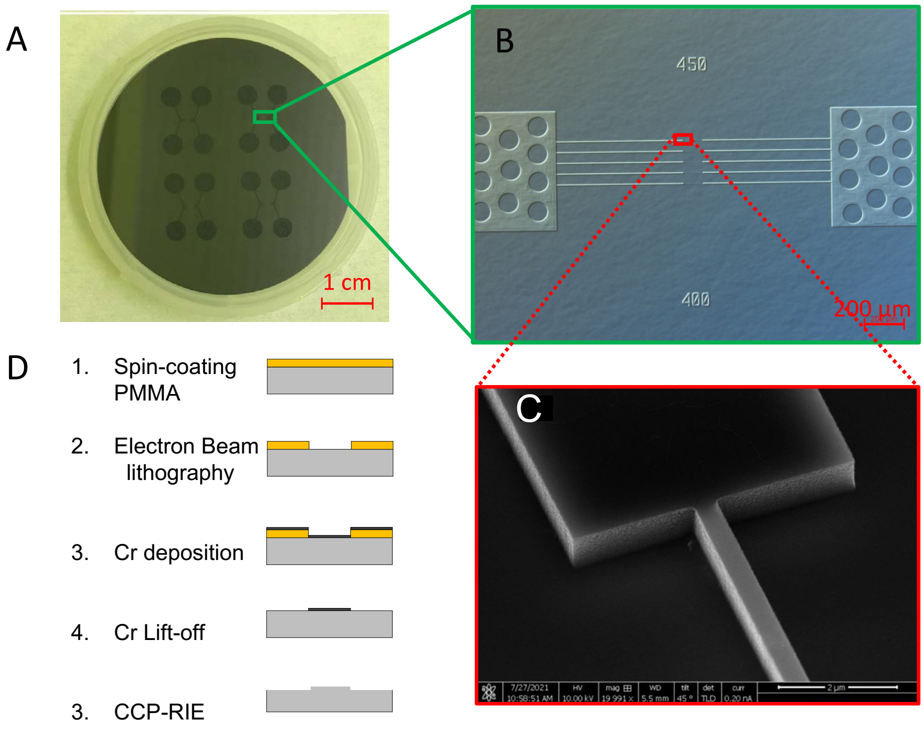

Figure 4.6: (A) Silicon master mold with corresponding zoom of the central part of one chip (B) and a SEM photo of the nanochannel (C). In (D) an illustration of main steps to fabricate the master mold in silicon.

4.2.3 Device fabrication

The fabrication steps of h-PDMS/glass chips are presented in figure 4.7 and described as follows:

1. First, hard-polydimethylsiloxane (h-PDMS) is spin-coated on the master mold with a velocity of 5000 rpm for 30 s. This material improves the quality of nano-scale patterning and avoids nanochannels patterns collapse. Then, PDMS RTV-615 (1:10) is directly spin-coated on the liquid h-PDMS layer. The spin-coating is made with a velocity of 1350 rpm for 30 s followed by a baking at 120 ° C for 5 minutes.

2. Once PDMS cross-linked, the master mold and a 700 µm thick glass slide are activated with a plasma cleaner (Nanonex Ultra-100) for 5 minutes to favor surface adhesion. The glass slide is previously cleaned by a piranha solution (50% H_2SO_4 / 50% H_2O_2) for 2 minutes to eliminate organic residues and serves as first layer of the chip where the micro-nanofluidic pattern is molded.

3. Next, the glass slide is put in contact with the master mold and bonded thanks to a liquid PDMS (1:10) layer (spin-coated before on the master mold with a velocity of 1350 rpm for 30 s). The application of vertical pressure for a few minutes is essential to refine the layer of liquid PDMS until the contact of the glass slide and crosslinked PDMS and to eliminate air bubbles. After that, a baking at 150 ° C for 20 minutes is done.

4. Then, residues of PDMS surrounding the glass slide are cleaned on the master mold

through a simple slipping of the film. This step is essential to avoid contaminations on the chip.

5. In a next step, the glass slide containing the micro-nanochannel pattern is detached from the master mold. Here, the importance of use thick glass slides to avoid breakage in this mechanically violent stage. Cleaning all PDMS residues at the borders of the glass slide is crucial for good bonding of the cover chip.

6. The h-PDMS chip and a glass cover with drilled reservoirs are activated with a plasma cleaner (Nanonex Ultra-100) for 5 minutes and put in contact to bond the PDMS chip. The chip is then baked at 150 ° C for 20 minutes. The glass cover is drilled with tungsten carbide drill bits (Performance Micro Tool) at a speed of 5000 rpm. The glass cover is fixed on a metal plate with paraffin and drilling is carried out in water. Once finished, the paraffin is cleaned by heating the glass cover in soapy water for few minutes and rising first with deionized water, then with acetone and finally with a piranha cleaning (50% H2SO4 / 50% H2O2) for 2 minutes.

7. For the injection of liquid, a block of PDMS (previous drilled with holes slightly smaller in diameter than the cannulas used for liquid injection) is bonded to the chip through an oxygen plasma treatment using the Diener Descum Nano plasma machine for 30 s followed by a baking at 150 ° C for 20 minutes.

8. Finally, fluidic connectors which include the electrodes are introduced into the h-PDMS/glass chip to inject the solutions.

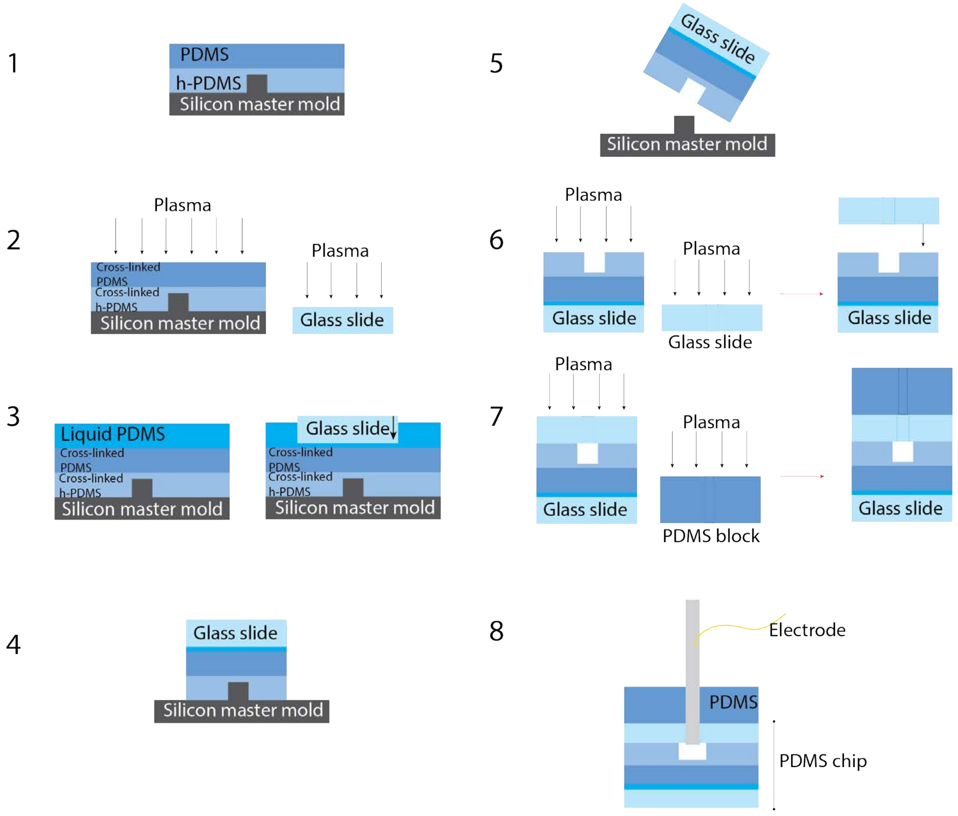

Figure 4.7: Fabrication process of h-PDMS/glass chips.

A top view of a h-PDMS/glass chip is presented in figure 4.8 (right). The upper PDMS layer contains four circular reservoirs to inject the solutions. Deeper, the h-PDMS/glass chip where we observe the microchannels connecting the nanochannels (at the center) to the circular reservoirs. At the left of figure 4.8, a zoom view of the center of the chip where nanochannels are integrated in the chip. Here, we show an example of a chip containing fifteen nanochannels 10 µm to 100 µm long, and 250 nm to 450 nm wide with a height of 1 µm corresponding to figure 1.17 C from the introduction chapter.

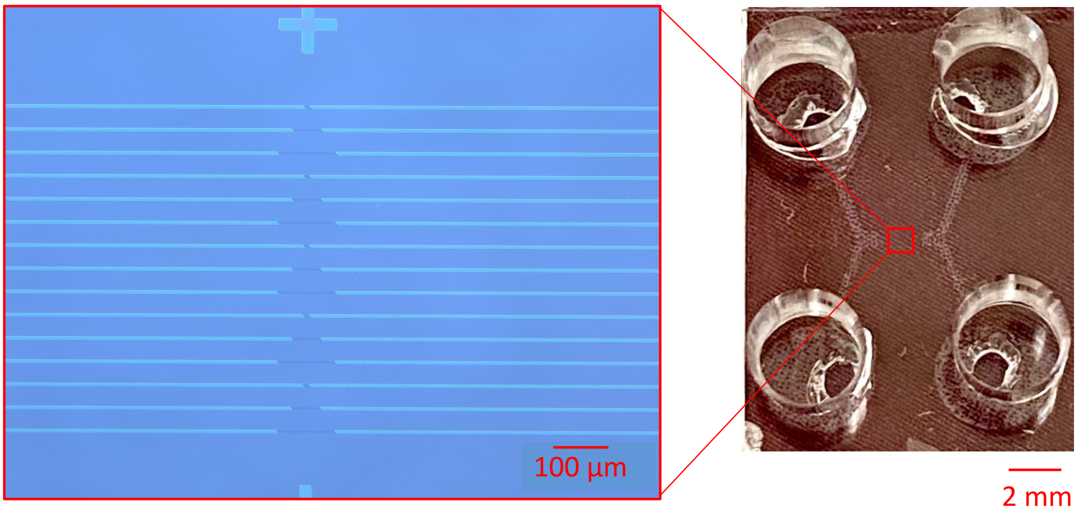

Figure 4.8: Photo of a h-PDMS/glass chip and the respective zoom of the central part.

4.3 Electropreconcentration in 10 µm-long nanochannels

Some electropreconcentration experiments were carried out in chips integrating nanochannels with L_n varying from 10 µm to 100 µm, and widths W_n varying from 250 nm to 450 nm with a height of 1 µm as described in the first part of this work (figure 1.17 C). In this section we focus on the preconcentration inside short nanochannels (10 µm) using NaCl as background electrolyte and fluorescein as model molecule both with concentration 10 µM. Figures 4.9 A and B present the normalized concentration profiles for a 400 nm-wide nanochannel and a 350 nm-wide nanochannel, respectively. The thin gray bar indicates the nanochannel in both graphs and we analyze part of the anodic and the cathodic reservoirs. In figure 4.9 C a preconcentration image of fluorescein indicating the stacking at the exit of the nanochannel in the cathodic reservoir inside a 400 nm-wide nanochannel (in the green rectangle) and the preconcentration far from the exit of the nanochannel in the cathodic reservoir inside a 350 nm-wide nanochannel (in the red rectangle).

Experimental results show that fluorescein concentrates at the cathodic reservoir in short nanochannels of 10 µm long. The 350 nm-wide nanochannel exhibits a cathodic focusing (CF) profile with a maximum rate of preconcentration of 4, whereas the 400 nm-wide nanochannel shows a cathodic stacking (CS) profile at the entrance of the nanochannel with a preconcentration factor of 2.7. This experiment was very important because we show for the first time preconcentration of fluorescein at short and wide nanochannels. In fact, we decided to test this geometry because theoretical simulations at that time showed that it was possible to preconcentrate at these dimensions. The profiles of preconcentration of fluorescein obtained from simulations show a cathodic stacking (CS) profile that increase with time until arrive to a maximum preconcentration factor of 7. It is important to mention that the simulations were done using model III in a non-conservative form.

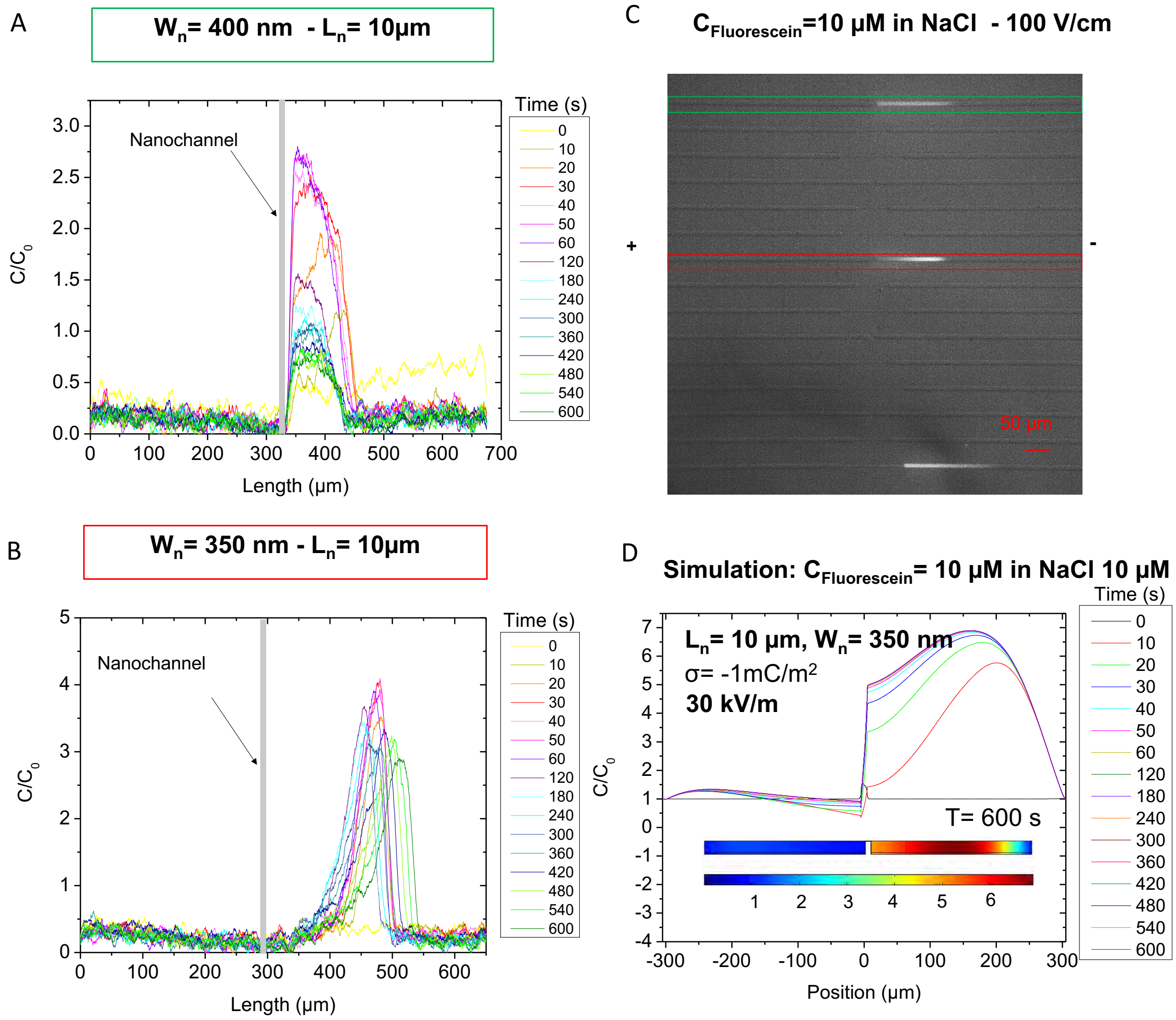

Figure 4.9: Normalized concentration profiles of fluorescein in a (A) 10 µm-long and 350 nm-width and (C) 10 µm-long and 400 nm-width nanochannels and (B) one preconcentration image.

4.4 Fluorescein: role of the surface charge density in electropreconcentration profiles

In this section, electropreconcentration experimental results in glass chip and in h-PDMS/glass chip are presented and discussed in detail. For this experiments, 10 µM fluorescein in 10 µM NaCl solution was used as model molecule since previous experimental results [2] showed stable profiles at low electric field (5 V/cm and 10 V/cm). Let us first analyze glass chip, first experiments were carried out in glass chips integrating eight 100 µm-long nanochannel with different widths varying from 100 nm to 450 nm (see figure 4.1). Here, we analyze a 450 nm-width nanochannel at the cathodic reservoir which produce interesting results.

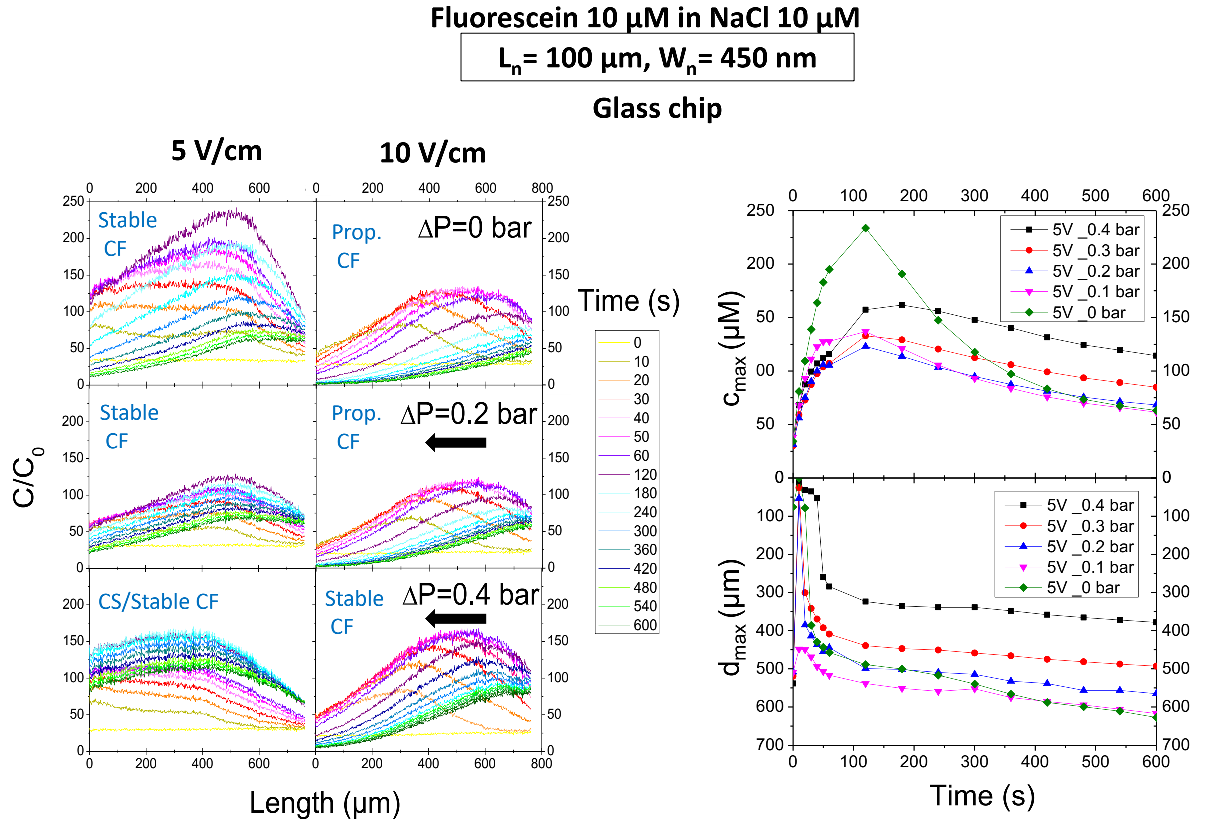

Figure 4.10: (left) Normalized electropreconcentration profiles of fluorescein in NaCl using a glass chip for different pressures and electric fields. (rigth) Evolution of the maximum concentration (c_{max}) and the location of the concentration peak (d_{max}) with time at 5 V/cm.

Figure 4.10 at left shows normalized concentration profiles as function of the distance to the nanochannel in glass chip. In this case we observe the cathode reservoir. In conventional electropreconcentration (ΔP=0 bar, first row), a stable CF profile is observed at low electric field (5 V/cm), in contrast, a propagating CF profile is visible when increasing the electric field up to 10 V/cm. At low electric field we notice a maximum preconcentration factor around 230. The application of a low counter-pressure (ΔP= 0.2 bar and ΔP= 0.4 bar) from the cathode to the anode side permits the stabilization of the preconcentration front. In effect, the propagating CF profile at 10 V/cm and ΔP=0 bar converts to a stable CF profile at ΔP=0.4 bar. As expected, this experiment prove that fluorescein presents a cathodic stacking (CS) or cathodic focusing (CF) profile thanks to its high mobility and it is possible to stabilize the preconcentration front by applying an external counter-pressure.

Figure 4.10 at right presents the evolution of the maximum concentration and the location of the concentration peak as a function of time corresponding to profiles obtained at electric field of 5 V/cm. We observe that with this electric field we don't really need to apply a counter-pressure to stabilize the front. The rate of preconcentration is in the order of $c_{max} = 230$. Other results using glass chips were published as part of an Electrophoresis article [2].

Even if good results were obtained in glass chips, the fabrication process is longer, and we had many problems of unbonded glass covers during the experiments. For this reason, we continue studying electropreconcentration in h-PDMS/glass chips.

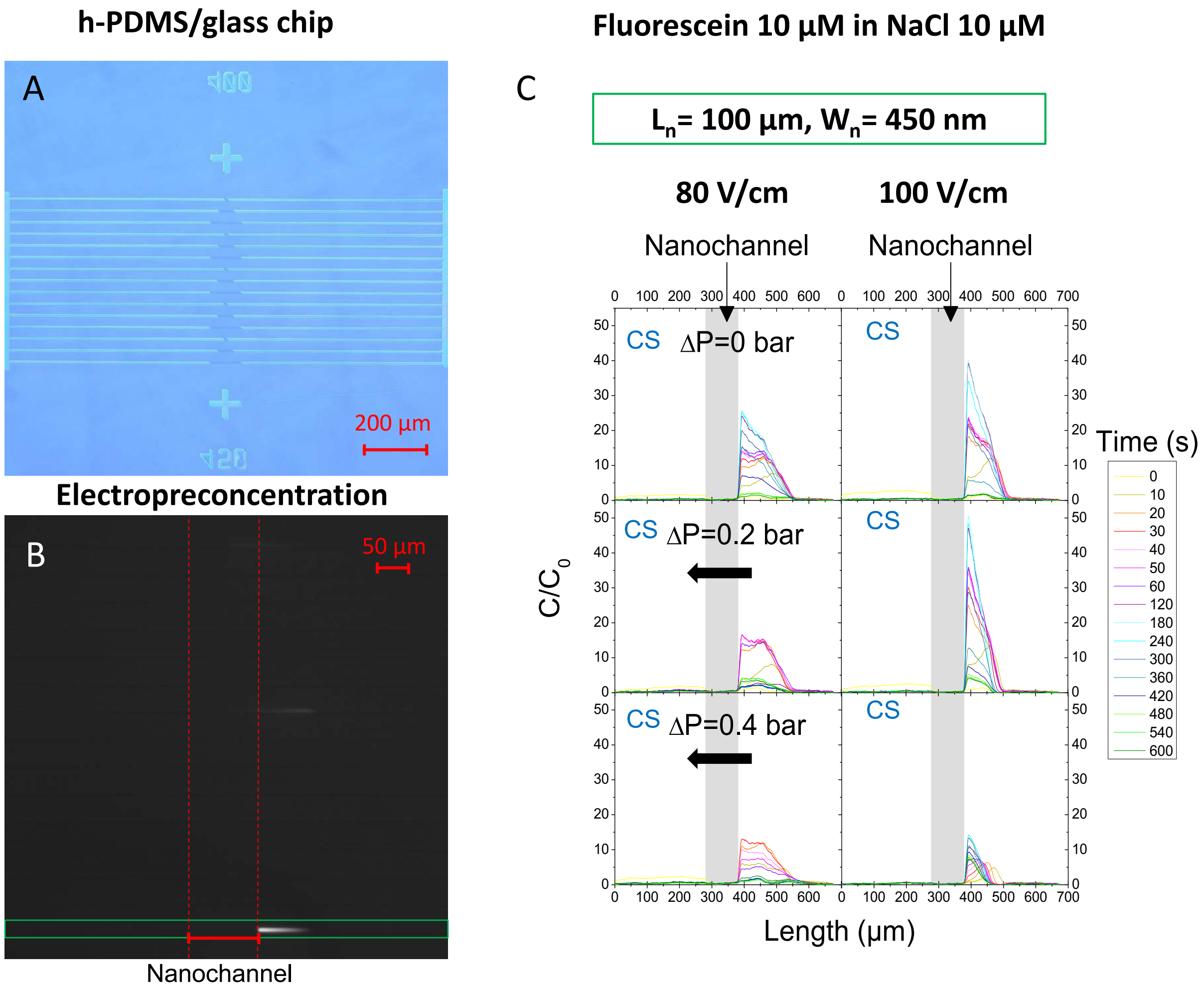

Figure 4.11: A) Image of the h-PDMS/glass chip used for the experiment. B) Preconcentration image of fluorescein after 600 s. C) Normalized electropreconcentration profiles of fluorescein in NaCl using a h-PDMS/glass chip for different pressures and electric fields.

We present then in figure 4.11 preconcentration of 10 µM fluorescein in 10 µM NaCl solution inside h-PDMS/glass chip. In this case the chip that we used integrates fifteen nanochannels with the geometry describe in figure 1.17 C with different length and width (cf. figure 4.11 A). In figure 4.11 B a photo of the preconcentration of the fluorescein during the experiment after 600 s. We observe the preconcentration spot at the last channel corresponding to a 100 µm-long and 450 nm-wide nanochannel (green rectangle) and spots in other channels are not visible. The position of the 100 µm-long nanochannels is indicated by the red vertical dashed lines.

In figure 4.11 C, the nanochannel (indicated as a gray bar) and some parts of the anodic and the cathodic reservoirs are analyzed. Cathodic stacking (CS) profiles are visible in all cases in accordance with theory. As the electric field is increased from 80 V/cm to 100 V/cm the preconcentration factor rises considerably without counter-pressure and applying ΔP= 0.2 bar with values of 40 and 50, respectively. If the counter-pressure is augmented to ΔP= 0.4 the CS profiles reduce their preconcentration factor. In addition, CS profiles seem more extended along the cathodic reservoir at 80 V/cm that those at 100 V/cm.

Electropreconcentration in h-PDMS/glass chips requires higher electric fields (80 V/cm and 100 V/cm) compared with glass chips to preconcentrate the fluorescein. In addition, more the electric field is increased, less the fluorescein propagates along the reservoir in h-PDMS/glass chips. This results also show that higher electropreconcentration rates with low electric field are obtained using glass chips. In effect, as the surface charge density of PDMS material is $\sigma = -1$ mC/m^2, the ICP effect is weaker in comparison with that of the glass material ($\sigma = -2.5$ mC/m^2) disfavoring the preconcentration process.

4.5 Fluorescein: role of the BGE in electropreconcentration profiles

To investigate the role of the electrolyte solution inside h-PDMS/glass chips, two 10 µM fluorescein solutions were prepared; one in a 10 µM NaCl BGE and the other one in a 10 µM KCl BGE. Experiments were performed in h-PDMS/glass chips integrating 100 µm-long nanochannels with different widths varying from 250 nm to 450 nm (see figure 4.12 A and B) and applying an electric field of 100 V/cm. The preconcentration fronts after 60 s can be seen in the figure 4.12 C. The green rectangle indicates the 100 µm-long and 450 nm-wide nanochannel and red vertical dashed lines indicate the position of the five nanochannels.

Figure 4.12 D presents the normalized concentration profiles in a 100 µm long and 450 nm-width nanochannel. Observations are done along the nanochannel which is indicated by the gray bar and some part of the cathodic and anodic reservoirs. Interestingly, preconcentration fronts were seen at the anode reservoir. This was a novelty because previous experiments in the group showed that fluorescein stacks at the cathodic reservoir thanks to its high mobility (3.6x10^{-8} m^{2}V^{-1}s^{-1}). It is important to mention that these experiments were done with a previous 1% bovine serum albumin (BSA) in 1×PBS solution flush for 15 minutes to avoid the adherence of molecules to the walls. The focalization at the anode reservoir can be explained by the change in the surface charge density after using BSA.

The normalized concentration confirms that NaCl as BGE presents higher preconcentration rates in comparison with KCl under the same conditions. Propagating anodic focusing (AF) profiles are observed for classic electropreconcentration (ΔP=0 bar) and applying a counter-pressure (ΔP= 0.2 bar and ΔP= 0.4 bar). In this case applying a counter-pressure from the cathode to the anode was not a good choice because fluorescein propagates to the anode reservoir, then imposing a pressure in the same direction enhances the propagating mode, as seen in the middle and bottom group of profiles. The results confirm the choice of NaCl as BGE.

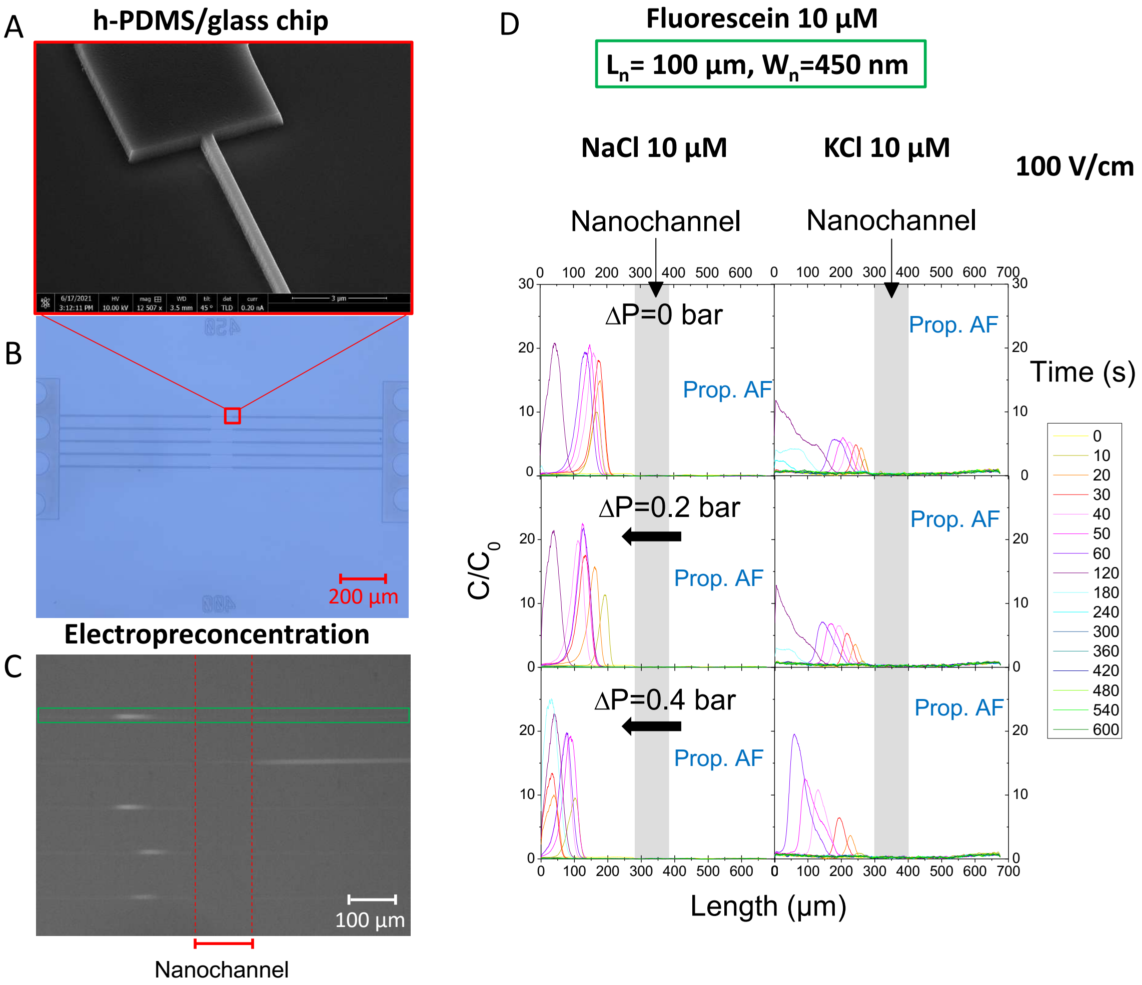

Figure 4.12: A) SEM image of a nanochannel in the master mold used to fabricate the h-PDMS/glass chip (B) used for the experiment. C) Preconcentration image of fluorescein in KCl after 60 s. D) Normalized electropreconcentration profiles of fluorescein in NaCl 10 µM (left side) and in NaCl 10 µM (right side) for different pressures and electric field E= 100 V/cm inside a h-PDMS/glass chips.

4.6 Electropreconcentration of ovalbumin

Ovalbumin marked Texas Red was another molecule of interest. This 45 kD protein is a key reference protein for immunization and biochemical studies, where it serves as an effective carrier and as a stabilizer protein. It can be used in cell culture systems and in the diagnostic industry to stabilize enzymes and hormones that would otherwise lose their functional integrity [79].

For experiments with ovalbumin marked Texas Red 10 µM, we used NaCl as BGE with a concentration of 10 µM. The h-PDMS/glass chip integrates fifteen nanochannels with the configuration explained in figure 1.17 B and presented in figure 4.13 A. In a first part, we focus in two 100 µm-long nanochannels with two different widths, 250 nm and 400 nm. A preconcentration image of ovalbumin after 600 s is showed in figure 4.13 B where we observed different fronts at the entrance of the nanochannels. The 250 nm-wide nanochannel is framed with a purple rectangle and the 400 nm-wide nanochannel is framed with a red rectangle. In this image we indicate the position of 100 µm-long nanochannels with red parallel dashed lines.

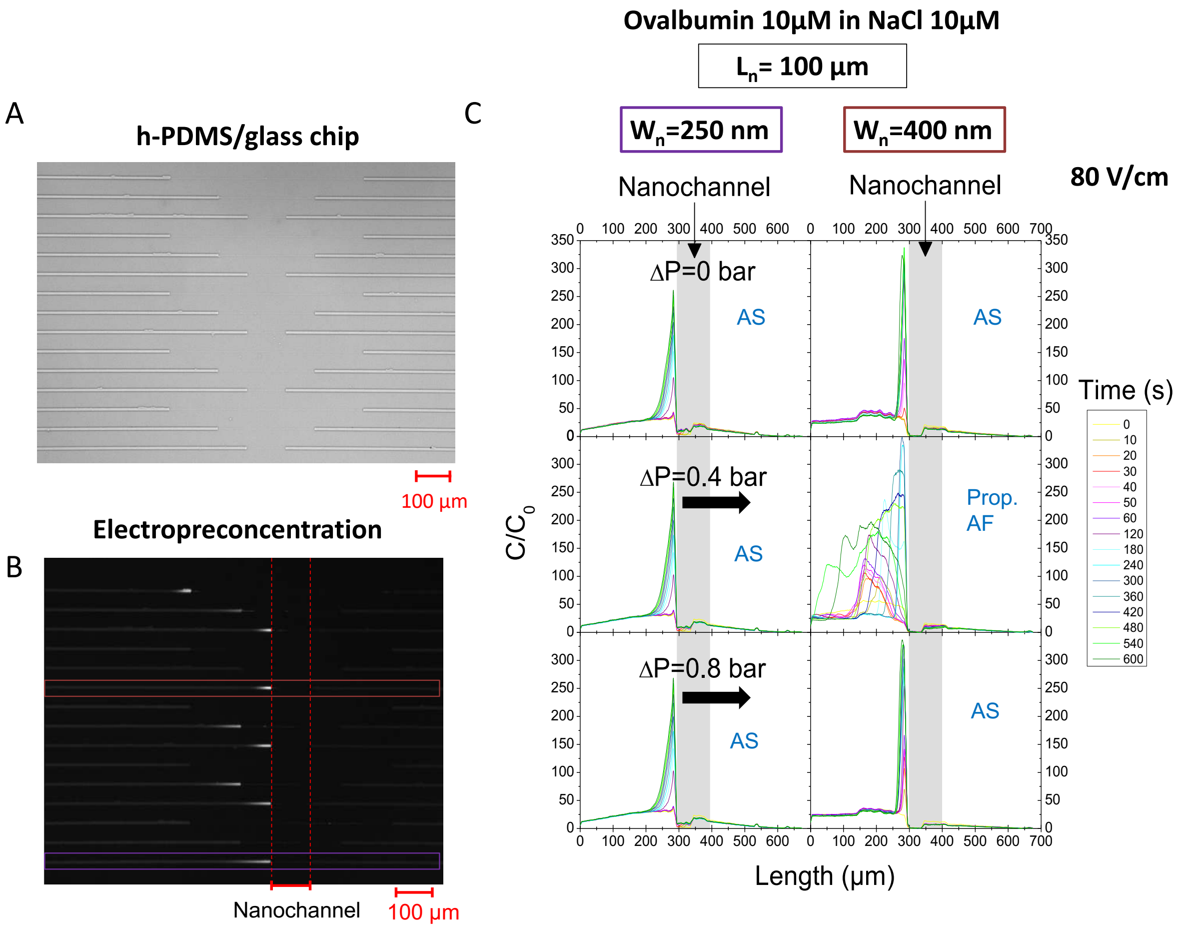

Figure 4.13: A) Image of the h-PDMS/glass chip used for the experiment. B) Preconcentration image of ovalbumin after 600 s. C) Normalized electropreconcentration profiles of ovalbumin in NaCl using a h-PDMS/glass chip for different pressures and electric fields.

Preconcentration inside h-PDMS/glass channels appears at the anode reservoir (at the left of the gray bar) when applying an electric field of 80 V/cm as show in figure 4.13 C. As predicted by the theory and due to the low mobility of ovalbumin ($10^{-9}m^2V^{-1}s^{-1}$ [80]), anodic stacking (AS) profiles appear for a nanochannel of W_n= 250 nm and different pressures from the anode to the cathode side (ΔP=0, ΔP=0.4 and ΔP=0.8). In this case a preconcentration factor above 250 is obtained. If the width of the nanochannel is increased up to 400 nm, anodic stacking (AS) profiles still appear with preconcentration factor above 325. The case of 400 nm and ΔP=0.4 bar seems to be a propagating AF profile but this cannot be assured since the fabrication of the h-PDMS/glass was not optimized at that moment leading to unexpected profiles.

These results confirm that h-PDMS/glass chips require higher electric fields to preconcentrate analytes and thicker channels work for the experiments as theoretical works of Zangle *et al.* [24] indicate.

To continue the study of ovalbumin in NaCl, the preconcentration inside nanochannels with different widths (250 nm, 350 nm and 450 nm) and for two different lengths (100 µm and 250 µm) was analyzed. Figure 4.14 presents normalized profiles for a 100 µm-long nanochannel with an electric field of 80 V/cm, aforementioned, the nanochannel is indicated by the gray bar in all cases so both cathodic and anodic reservoirs are regarded. These results revealed that for classic electropreconcentration (ΔP=0 bar) and considering a nanochannel of 250 nm-width an anodic stacking (AS) profile appears at the entrance of the nanochannel. As the width is increased up to 350 nm and 450 nm, we observe anodic stacking (AF) profiles for classic electropreconcentration (ΔP=0 bar). The 450 nm-width nanochannel shows maximal preconcentration rate around 300. If a high counter-pressure from the cathode to the anode is applied up to ΔP=0.4 bar and ΔP=0.8 bar not important change is observed for a 250 nm-width nanochannel. Contrary, for a 350 nm-width nanochannel the preconcentration factor is lightly reduced obtaining a propagating anodic focusing (AF) at both pressures ΔP=0.4 bar and ΔP=0.8 bar. The 450 nm-wide nanochannel presents a propagating anodic focusing profile at ΔP=0.4 bar but this must be verified because at the time of these experiments, the nano-structuring protocol was not optimal. It is possible that this 400nm nanochannel has a manufacturing defect. The 450 nm-wide nanochannel exhibits an anodic focusing profile at ΔP=0.8 bar, which was obtained from an anodic stacking (AS) profile pushed by the counter-pressure.

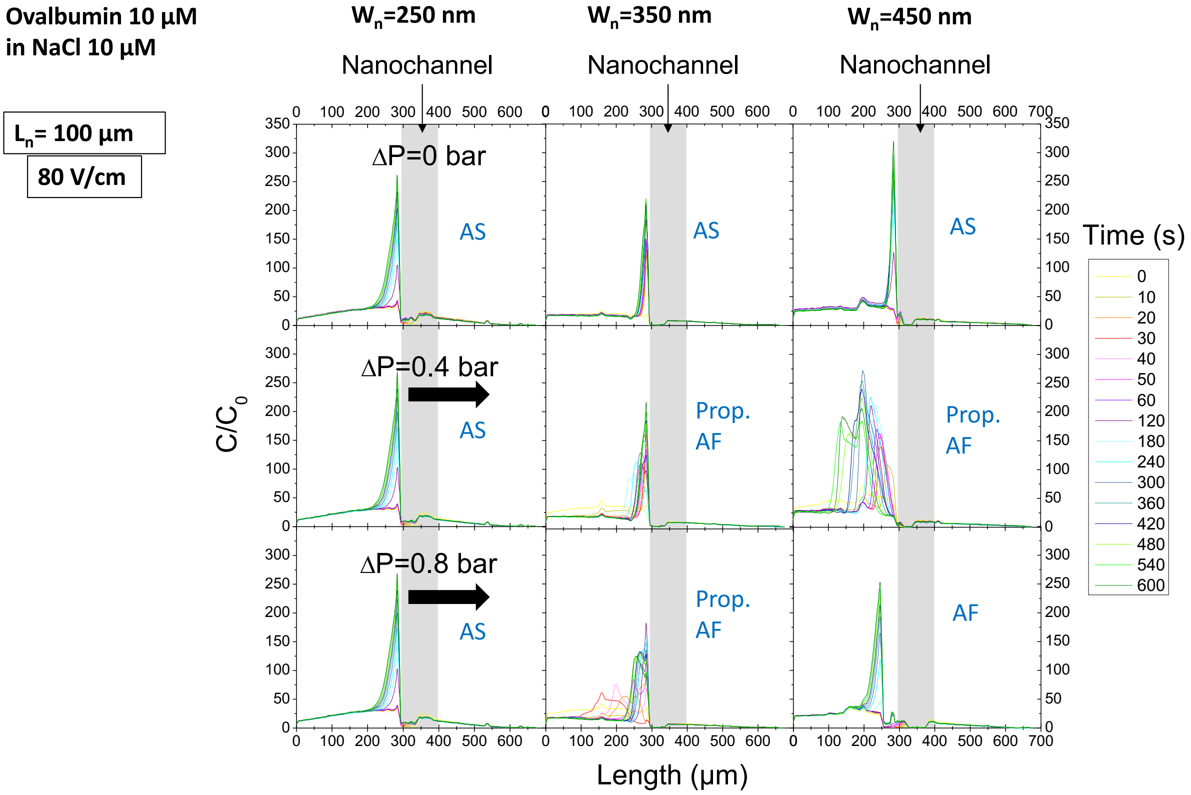

Figure 4.14: Normalized electropreconcentration profiles of ovalbumin in NaCl inside a 100 µm-long nanochannel for different nanochannels widths and different pressures and electric field 80 V/cm.

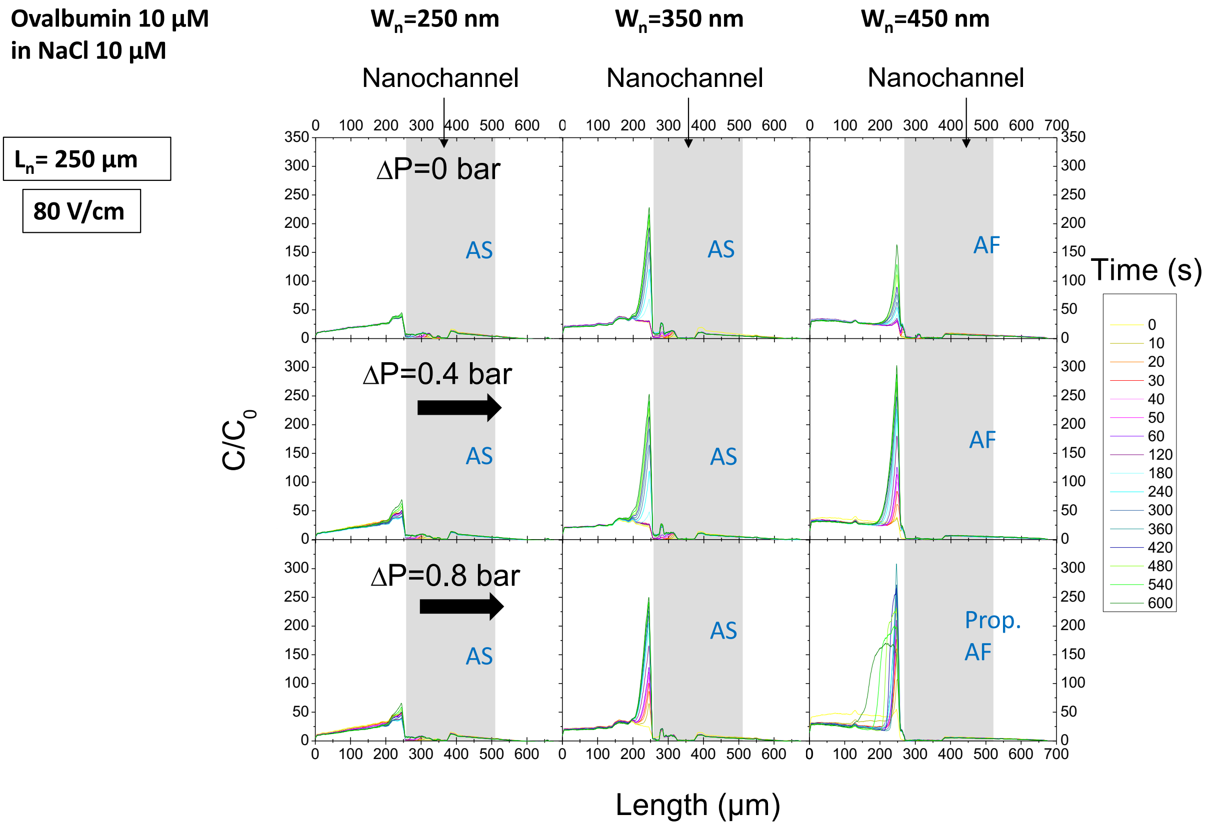

Figure 4.15: Normalized electropreconcentration profiles of ovalbumin in NaCl inside a 250 µm-long nanochannel for different nanochannel widths and different pressures and electric field 80 V/cm.

Now, we analyze a longer nanochannel, under the same conditions. Figure 4.15 depicts normalized profiles for a 250 µm-long nanochannel and applying an electric field of 80 V/cm. As the nanochannel is wider (gray bar), we observe only a few parts of the anodic and cathodic reservoirs, respectively. If we consider the classical preconcentration without external pressure, anodic stacking (AS) profiles are visible for the 250 nm-wide and 350 nm-wide nanochannels, however an anodic focusing (AF) profile appears as the width of the nanochannels is increased to 450 nm. Also, an important reduction of the value of the preconcentration factor is observed in this case. Applying a pressure from the cathode to the anode (ΔP=0.4 bar and ΔP=0.8 bar) in a 250 nm-wide nanochannel and in a 350 nm-wide nanochannel does not change the anodic stacking (AS) profiles significantly. In contrast, we observe an improve of the preconcentration factor up to 300 when applying a counter-pressure of ΔP=0.4 bar. For a 450nm-wide nanochannel and applying a pressure ΔP=0.8 bar we obtain a propagating anodic focusing (AF) profile.

Comparing figures 4.14 and 4.15 we observe that the 250 nm-width nanochannel presents higher preconcentration factors for a 100 µm-long nanochannel. However, for wider nanochannels we have the opposite, preconcentration rates seem to be improved. As a conclusion, our findings appear to be well supported by the theory as ovalbumin is preconcentrated in the anodic reservoir.

4.7 Electropreconcentration of DNA

After working with two model molecules: the fluorescein which stacks or focus at the cathodic reservoir and the ovalbumin which stacks or focus at the anodic reservoir we continue investigating the preconcentration of DNA. We took as reference experiments developed by Han *et al.* [37] which proposed a microfluidic chip integrating ion traps (in Nafion) as ultra-sensitive DNA sensor (concentrations around pM). One of the experiments they developed consist of using Alexa Fluor 647 labeled ssDNA with a background BSA concentration of 50 mg/mL in 2.5× PBS in which they investigated the selective enrichment of nucleic acids (NAs). Figure 4.16 (a) shows the initial state of the device ($\varphi = 0$ V), here, the concentration of BSA was uniform on the left (upstream) and right (downstream) sides of the Nafion membrane. DNA with initial concentration 1 nM was not observable. At zero hydrostatic pressure (figure 4.16 (b)) after the voltage was on for 30 s, both the DNA and BSA were trapped and concentrated at the upstream side of the Nafion membrane. Consequently, BSA was depleted at the downstream side, as indicated by the vanishing of fluorescence at the downstream side. On the other hand, as shown in figure 4.16 (c) under an appropriate hydrostatic pressure (100 Pa), although DNA was still effectively concentrated, BSA was only weakly concentrated. Therefore, DNA could be selectively concentrated by their device [37].

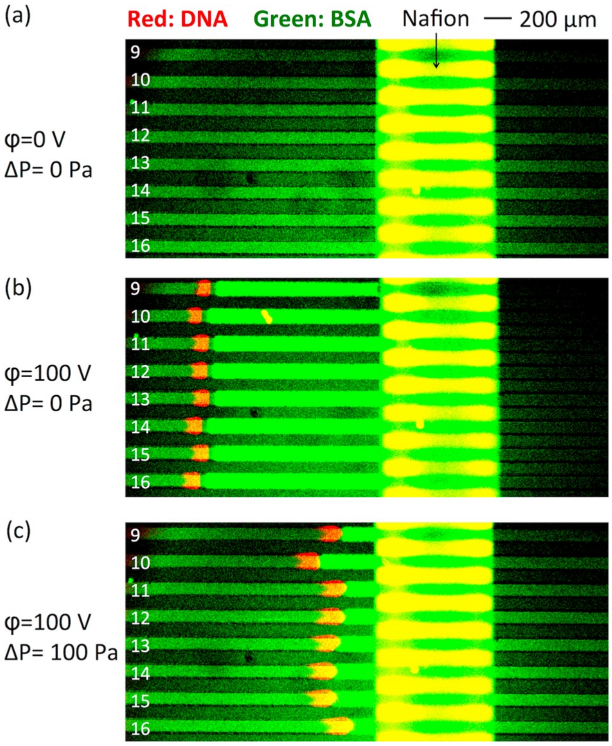

Figure 4.16: Comparison of DNA and BSA concentration behaviors with and without hydrostatic pressure. (a) Initial state of the device ($\varphi = 0$ V). (b) DNA and BSA concentrated near the Nafion at a hydrostatic pressure of zero, resulting in the depletion of BSA downstream. (c) DNA still effectively concentrated under 100 Pa, with significant leakage of BSA downstream indicated by the fact that the BSA fluorescence downstream was as strong as that upstream [37].

The aim of this part of my work, in a first step, was to perform a preconcentration of single-stranded DNAs (ssDNA) labeled Fluorescein 598 of hepatitis C in a buffer solution. Then, to perform a second experiment with unlabeled DNA in the presence of its labeled Alexa Fluor 594 complementary strands, which will fluoresce after hybridization of the two strands inside our h-PDMS/glass chips. Unfortunately, I didn't have the time to complete this experiment and we only tested single-stranded DNA labeled Fluorescein 598.

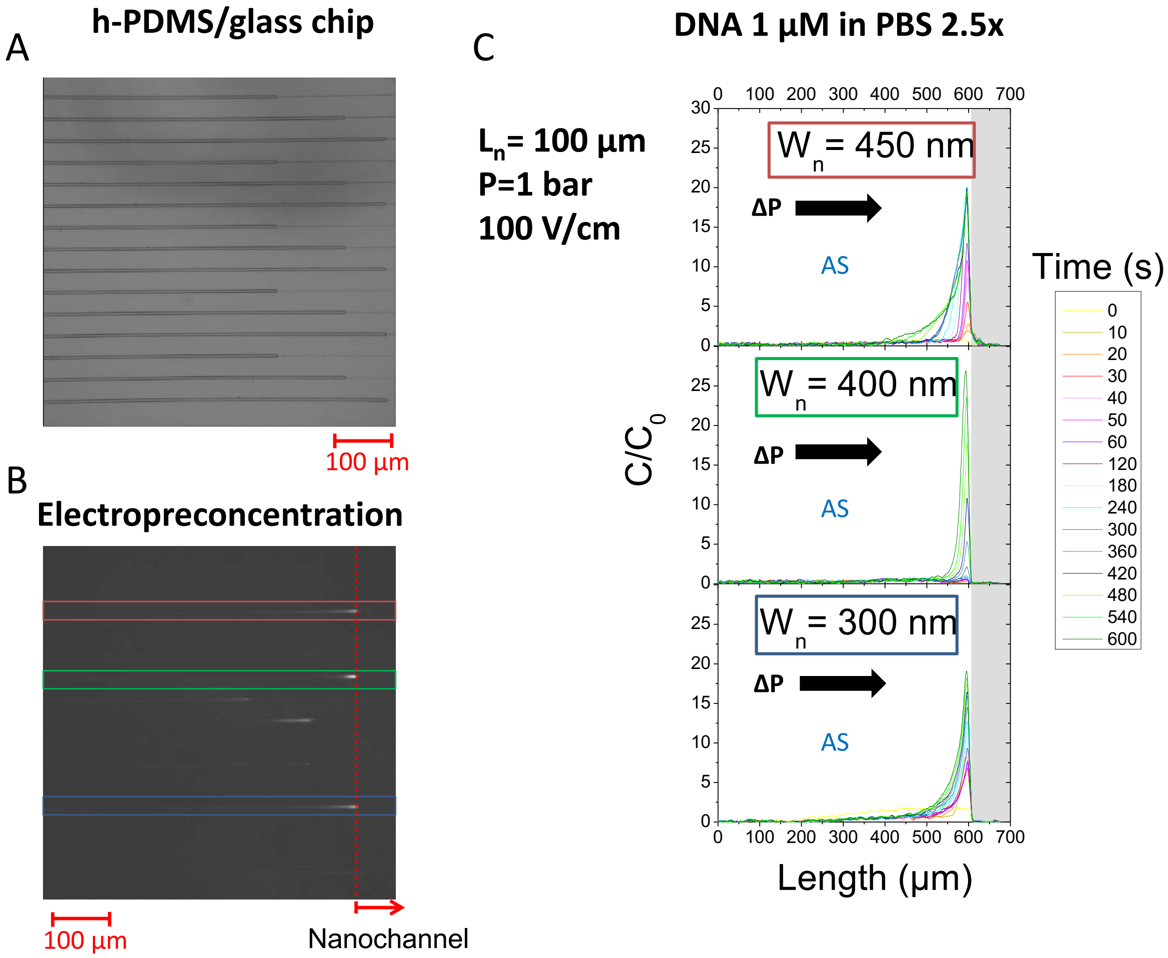

Figure 4.17: A) Image of the h-PDMS/glass chip used for the experiment. B) Preconcentration image of DNA after 600 s. C) Normalized electropreconcentration profiles of DNA 1 µM in a PBS 2.5x solution inside a 100 µm-long nanochannel for different nanochannel widths (300 nm, 400 nm and 450 nm). In all cases we apply a pressure of 1 bar and an electric field 100 V/cm.

Single-stranded DNAs (ssDNA) were synthesized and fluorescently labeled by Eurogentec. We used a 15-base ssDNA (5'- GAT-ACT-TCT-ATC-ACC-3') with the end labeled Fluorescein 598 corresponding to a fragment of hepatitis C DNA. We investigate the electropreconcentration of DNA inside h-PDMS/glass chip integrating fifteen nanochannels with different length and width (figure 4.17 A) described in the first part of this manuscript (figure 1.17 B). A preconcentration photo of DNA with a concentration of 1 µM in a phosphate-buffered saline (PBS) 2.5x solution after 600 s is presented in figure 4.17 B. We analyze in a first part, three 100 µm-long nanochannels with different width, 300 nm (blue rectangle), 400 nm (green rectangle) and 450 nm (red rectangle). The nanochannel is positioned at the right of the image. Note that we only see a part of the nanochannels. The mobility of DNA is around 3x10^{-8}m^{2}V^{-1}s^{-1} [81, 82].

Figure 4.17 C shows normalized preconcentration profiles of DNA for three different widths.

Experiments were carried out applying an external pressure of 1 bar from the anode to the cathode and under an electric field of 100 V/cm. Experiments done by the group of Han showed that ADN is preconcentrated at the anodic reservoir and the front propagates along the reservoir with time, to reduce this propagation, we have chosen to apply the pressure from the anode to the cathode. The nanochannel is placed at the right-side indicated by the gray bar. Anodic stacking (AS) profiles are visible under these conditions. There were no significant differences between the different widths of the nanochannel (300 nm, 400 nm and 450 nm) in terms of the obtained profiles with preconcentration rates above 20.

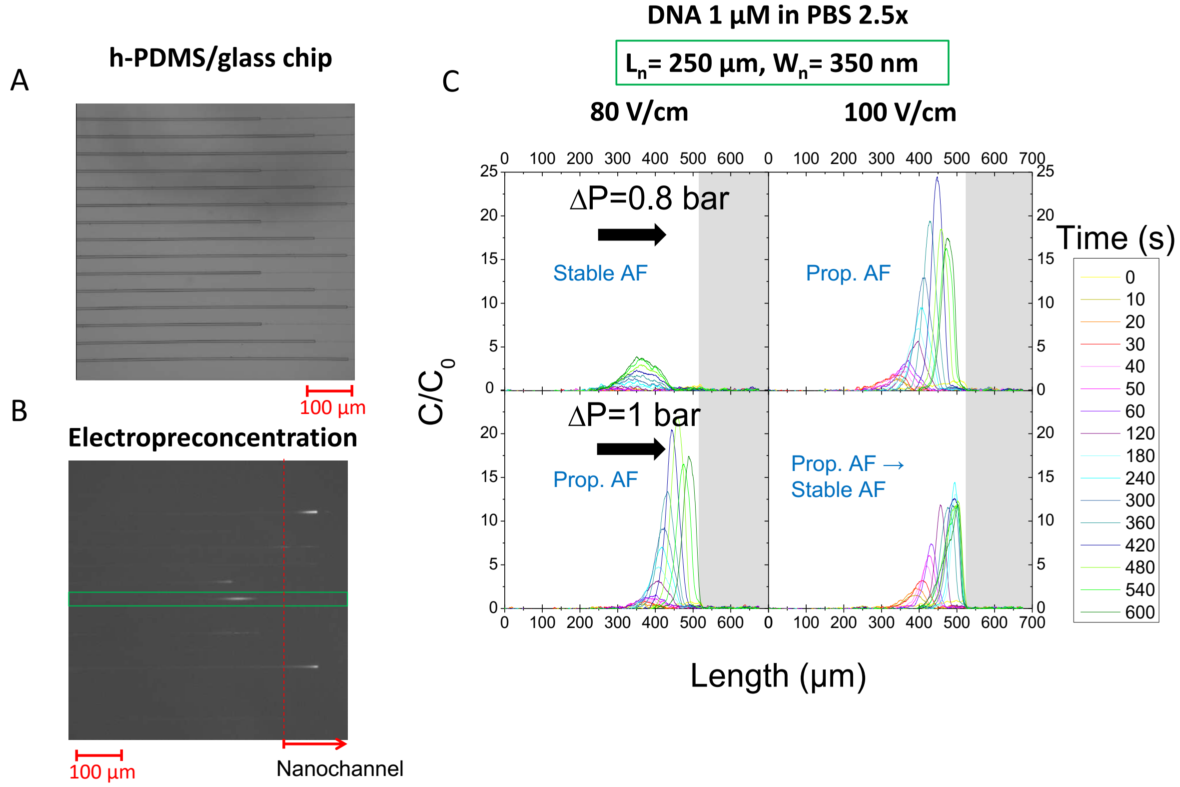

Figure 4.18: A) Image of the h-PDMS/glass chip used for the experiment. B) Preconcentration image of DNA after 60 s. D) Normalized electropreconcentration profiles of DNA in PBS 2.5x inside a 250 µm-long and 350 nm-width nanochannel at two different electric fields and pressures.

Now, in the same experiment, we analyze what happens with the 250 µm-long and 350 nm-width nanochannel. We show in figure 4.18 A the same image of the h-PDMS/glass chip, as these results were obtained at the same time. However, we present a preconcentration photo of DNA after 60 s. As before, the position of the nanochannel is indicated by the red vertical dashed line and the channel of interest is framed with a green rectangle (figure 4.18 B).

Figure 4.18 C presents preconcentration profiles of the 250 µm-long and 350 nm-width nanochannel (position indicated by the gray bar). When we apply an external pressure ΔP=0.8 bar from the anode to the cathode a stable anodic focusing (AF) profile is obtained with a low preconcentration factor of 4. As the electric field is increased up to 100 V/cm, a propagating anodic focusing appears and higher preconcentration factor is obtained towards 20. Analyzing profiles at high external pressure ΔP=1 bar, results in a propagating anodic focusing profile at an electric field of 80 V/cm which is stabilized at high applied voltage 100 V/cm. In effect, this last profile starts with a propagating anodic focusing (AF) and after 120 seconds it remains stable with a preconcentration factor of around 13. Experiments with DNA show that longer nanochannels (250 µm) stabilize the preconcentration fronts compared to shorter nanochannels (100 µm).

To conclude this chapter:

1. A new process for the elaboration of h-PDMS/glass chips was developed and optimized. This process includes the fabrication of a silicon master mold containing vertical nanochannels from which chips are unmolded and then bonded. The master mold is obtained by electronic nanolithography coupled with CCP-RIE etching. The etching process was optimized to obtain straight walls and we included the optool treatment to facilitate the unmolding.
2. We performed electropreconcentration experiments in the h-PDMS/glass chips using model molecules as fluorescein, ovalbumin both in a NaCl solution and DNA in a PBS solution to study the role of the length and the width of the nanochannels. Experimental results confirm that fluorescein concentrates at the cathode reservoir and ovalbumin and DNA at the anode reservoir.
3. We showed that preconcentration inside short nanochannels (10 µm) is possible unless the weak preconcentration rate.

Chapter 5

Conclusions and perspectives

The objective of this thesis was to study the preconcentration of model analytes by ICP effect in a chip that integrates several "vertical" nanochannels to investigate the role of the width and the length of the nanochannel on the location of the focal points.

To better understand this multiparametric phenomenon we developed a 2D COMSOL Multiphysics® numerical model with a parameterized mesh adapted for varying background electrolyte concentrations. We investigated the role of important governing parameters including the BGE concentration, the electric field, the wall surface charge density and the analyte mobility on the ICP dynamics and corresponding preconcentration mechanisms in a microchannel-nanochannel-microchannel system. We first demonstrated the onset and extent of propagating ICP in dilute solution conditions, confirming that both a sufficiently large electric field and a high Dukhin number are necessary conditions in a conventional single-channel configuration for concentration polarization effects to appreciably propagate outwards from the microchannel-nanochannel interfaces.

We illustrated the spatiotemporal evolution of propagating ICP dynamics over disparate time and length scales using a logarithmic time discretization. Our results showed a linear growth in the accumulation and depletion zones over time, in agreement with previous experimental findings [24], and indicate that both transient and stationary stacking and focusing profiles are achievable for anionic analytes of varying mobility, as predicted by 1D simulations [3]. As expected, lower sample mobilities shifted the cathodic preconcentration location away from the nanochannel as the enhancement mechanism transitions from CS to CF at the interface and then weaker CF in the microchannel; the highest preconcentration factor can be observed for CF at the nanochannel EDL interface.

As part of the instrumentation, we adapted and optimized a new experimental bench to develop the electropreconcentration experiments. Through MATLAB® programs we automated the acquisition and treatment of data, facilitating the lunch of experiments and ensuring that all the experiments were done under the same conditions. We did a spectrophotometric characterization of two model molecules: fluorescein and ovalbumin to provide robust quantitative measurements in the micro/nano/microfluidic chips. The characterization included the acquisition of the absorbance and emission spectra for both model molecules at different concentrations.

Experimentally, we implemented a new protocol to fabricate mixed h-PDMS/ glass chips from a silicon master mold elaborated through electron beam lithography of high resolution and a CCP-RIE etching process. By using a gas mixture of SF6 (8 sccm) and CHF3 (8 sccm) we obtained straight channel walls and by adding an optool surface treatment, the unmolding of the chips became easier. Thanks to this protocol we elaborated three designs of chips with different configurations of nanochannels integrating several lengths and widths. We mainly investigated a "pressure assisted" electropreconcentration method for three model analytes, fluorescein, ovalbumin and DNA. For the experiments with fluorescein, we compared glass chips and mixed h-PDMS/ glass chips confirming that preconcentration inside glass channels require low counter-pressure and low electric field for the stabilization of the preconcentration front (stable CF regime) in comparison with h-PDMS/ glass chips. Results with ovalbumin demonstrated that this molecule stacks at the anodic reservoir in most of cases thanks to its low mobility, showing that the length and the width of the nanochannels doesn't have a big impact in the focal point. However, experiments with DNA show that passing from a 100 µm-long nanochannel to a 250 µm-long nanochannel favorize the stabilization of the focal point allowing an anodic focusing preconcentration regime. We also experimentally observed that preconcentration at thick nanochannels (450 nm) gives better results than thin nanochannels (250 nm).

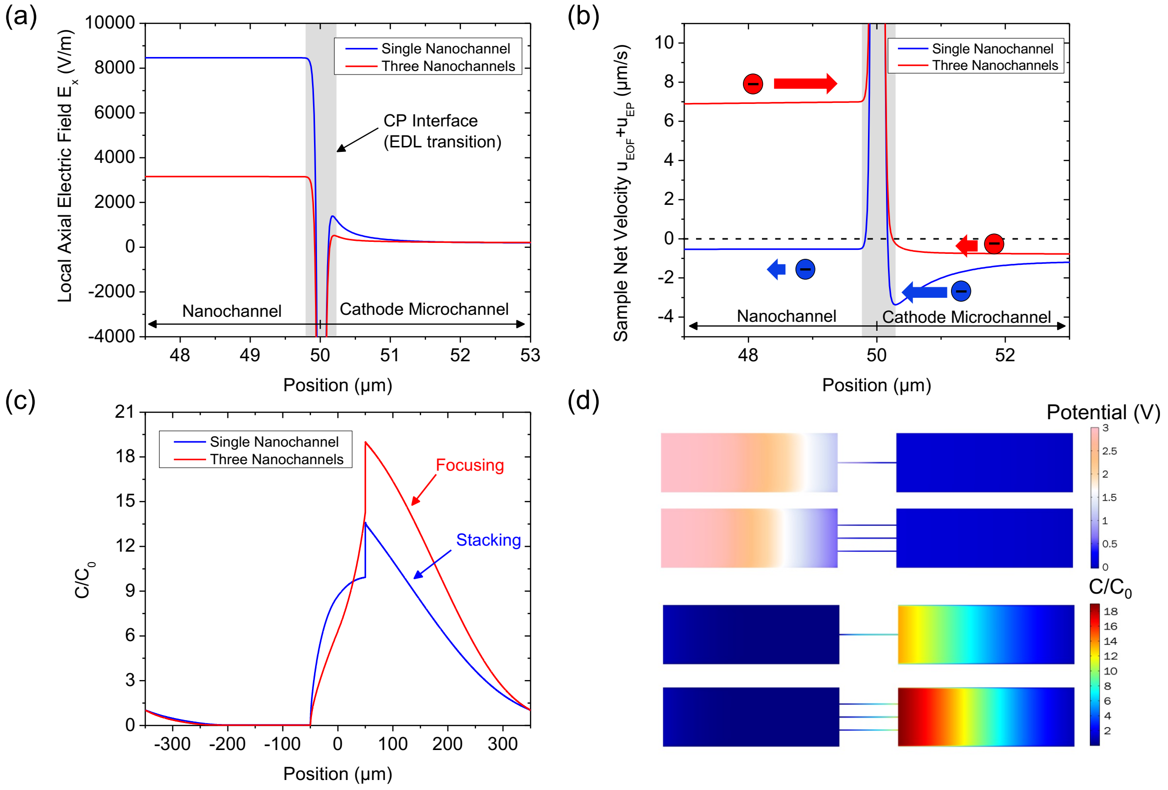

Figure 5.1: ICP for a single nanochannel versus three parallel nanochannels for 50 µM KCl, σ_s = -0.5 mC/m^2, E = 30 kV/m, Wn = 100 nm, and a sample with a diffusivity of 1.33x10^{-}10m^2/s. a) Local electric field and (b) corresponding sample net transport velocity (EOF + EP) near the nanochannel/cathodic microchannel interface for a single nanochannel (blue) and three parallel nanochannels (red). c) Normalized concentration profiles show a transition from a stacking profile with one nanochannel to a focusing profile with three nanochannels due to the change in electric field and ion transport velocity depicted in b). d) 2D depth-averaged concentration and electric potential distributions for one and three nanochannel configurations demonstrate stronger ICP effects and subsequent preconcentration arising from the addition of multiple parallel channels.

As part of the perspectives of this work it could be interesting to continue simulations not only in one nanochannel but in more parallel nanochannels. In our last simulations, we investigated the effect of increasing the interfacial area of the charge-selective microchannel-nanochannel EDL interface by arraying three nanochannels in parallel (cf. figure 5.1). We found that this enhances the overall perm-selectivity of the structure, strengthening ICP effects and improving resulting preconcentration capabilities in certain cases; this is analogous to increasing the pore density in a nanoporous membrane, for example. By changing from a single-channel structure to a three-channel configuration, the electric field in the channel became increasingly nonuniform and further attenuated due to extended depletion zone propagation and more strongly polarized accumulation/depletion profiles. This allows for increased control over the competition between EOF and electrophoretic migration as anionic samples try to enter the nanochannels, and enables the transition from a CS preconcentration mechanism to the more effective CF scheme that allows for higher enrichment factors. Such a multi-channel approach provides added flexibility in the design of ICP systems, particularly in situations where the nanochannel size and/or electrolyte concentration have practical limitations which set a minimum achievable inverse Dukhin number and/or analyte mobility.

In the experimental part, it would be of interest to continue the second experiment with unlabeled DNA in the presence of its labeled Alexa Fluor 594 complementary strand to study the fluoresce after hybridization of the two strands inside our h-PDMS/glass chips. In addition, the preconcentration of a mixture of two analytes will open the possibility to investigate the selectivity of our device.

In the field of biomedical analysis, current macroscopic methods based on chromatography techniques coupled to mass spectrometry remain long and tedious, which may prove detrimental for certain pathologies such as innate errors of metabolism where a fast and early diagnosis is often desired. On-chip analytical methods are therefore very promising, since analysis can be carried out in less than 30 minutes with a microliter of cerebrospinal fluid (CSF). Inborn errors of metabolism (ADEs) are genetic diseases that affect approximately one in five thousand newborns and are transmitted primarily in an autosomal recessive fashion. ADEs result from the mutation of a gene causing a metabolic error resulting in a deficit or a defect in the synthesis of an enzyme. The metabolic disorder caused by this biochemical dysfunction is then accompanied by a progressive neurological disorder requiring immediate management in order to stop or limit the progression of the disease [83, 84]. Substances resulting from cerebral metabolism as well as certain enzymatic cofactors are eliminated in the cerebrospinal fluid (CSF), protected by the blood-brain barrier (BBB). CSF analysis is therefore essential for biological diagnosis, the study of pathophysiological mechanisms as well as the therapeutic monitoring of pathologies affecting the central nervous system (CNS). For example, the determination of neurotransmitters in the CSF is essential for the diagnosis of neurotransmission abnormalities for which the benefit of treatment may be considerable if started early [84]. In collaboration with the Neuro-Pediatrics and Biochemistry Services of the Trousseau Hospital (APHP), the team of Prof. F. Moussa was the first in France to develop the assay of the metabolites of neurotransmitters, pterins and 5 methyl-tetrahydrofolate (5 MTHF) in CSF [85, 86]. The C2N team in collaboration with A. Pallandre and F. Moussa (ICP – Orsay) has started a valorization project to diagnose innate deficits in dopamine and serotonin by assaying their metabolites as well as the enzymatic cofactors, the pterins involved in their biosynthesis, in the CSF thanks to this new nanofluidic chip studied in my PhD. The metabolites derived from the neurotransmitters involved in a very large part of inborn errors of metabolism (ADEs) are dopamine, serotonin and norepinephrine. The half-life of these three neurotransmitters is very short, which is why they are difficult to detect in cerebrospinal fluid. Their production is indirectly measured by the concentrations of their metabolites which are described in the figure below:

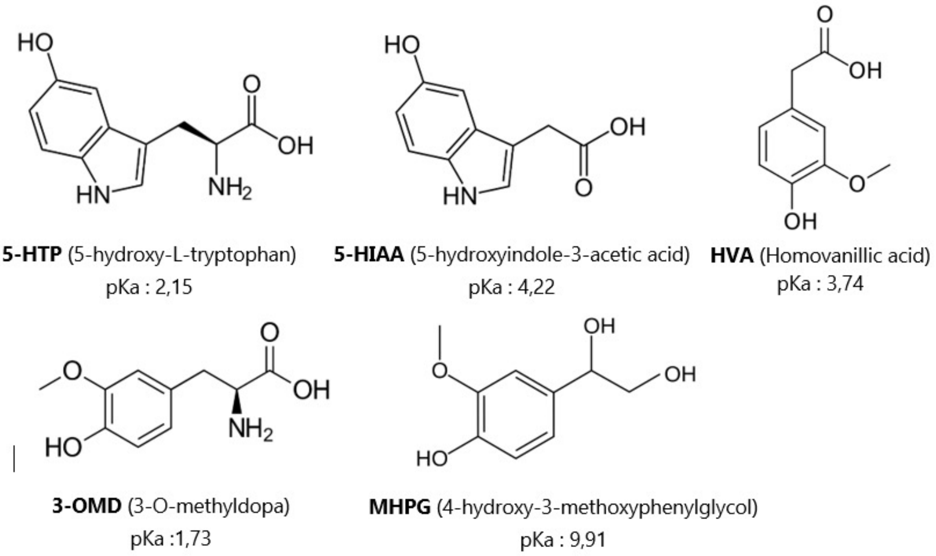

Figure 5.2: Molecular structures and pKa of the five neurotransmitter metabolites studied and involved in numerous ADRs.

The novelty of this approach is based on detection **without pre-labeling of the analytes**. Indeed, the targeted molecules have a chromophore absorbing around 250 to 260 nm, which allows **direct detection in the UV range**. This detection mode simplifies the sample preparation step while improving the robustness of the assay. Preliminary experiments were carried out during a campaign on the DISCO line of the SOLEIL synchrotron in collaboration with Mathieu Refregiers, researcher responsible for the DISCO line, to test UV detection on model CSF solutions containing the 5 metabolites. The purpose of this first synchrotron experiment was to verify that the desired detection limits for diagnosis and therapeutic monitoring were achievable in fluorescence in the UV range ($\lambda_{exc} = 280$ nm) for the five metabolite standards studied. These first tests therefore did not aim to carry out a quantitative analysis of standards but rather very qualitative analyzes, based on the detection of metabolite standards in simple channels in microfluidics. This first run at SOLEIL took place just before confinement in mid-March.

Three different concentrations were chosen to perform the individual analyzes of the five metabolite standards: 1 millimol/liter, 1 µmol/l and 1 nmol/l. The standards were diluted in an aqueous phase of 5 mM ammonium formate pH 7.4 in accordance with the experiments on the reference method in UHPLC-MS. The curve in figure 5.5 (b) is decreasing since the intensity of the synchrotron radiation beam was decreasing before confinement. The carrier must be modeled and then subtracted from the signal. This subtraction ultimately provides the fluorescence signal of the analyte passing through the microchannel. We processed all the measurements for the four molecules analyzed and succeeded in detecting 3 molecules (5-HTP, MHPG, 3-OMD) at a concentration of 1 nM/l. These very promising results with nanomolar detection for three analytes allowed us to submit a project to SOLEIL. This project (Proposal 20200256) was accepted, and 7 beam days were allocated to us for November 2020.

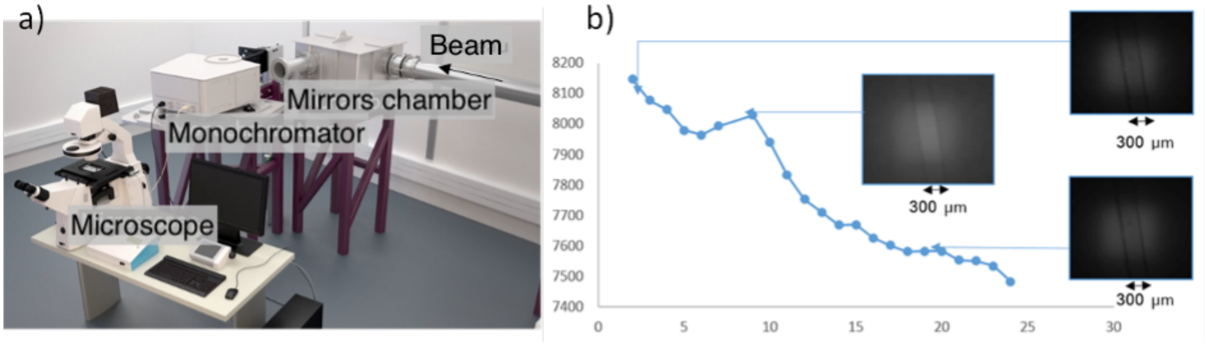

Figure 5.3: a) Experimental station of the DISCO beamline at the SOLEIL Synchrotron for fluorescence analysis and (b) Temporal evolution of the signal intensity during the passage of the 5-HTP analyte without subtraction of the decreasing signal of the synchrotron beam.

During the week working at the DISCO line in November 2020, one nanofluidic chip has been tested. The 5 metabolites were diluted in a 10 µM NaCl solution, with 3 % of methanol (v/v) to exacerbate the fluorescence. The experiments were carried out by exciting the samples around 280 nm and we observed the emitted fluorescence between 327 and 353 nm in an experimental bench similar to that at C2N but using a CCD Camera with UV Coating. First, we studied each metabolite independently applying a difference of potential of 100 V and without applying external pressure during several minutes. In figure 5.4 the distribution of preconcentration fronts for each metabolite.

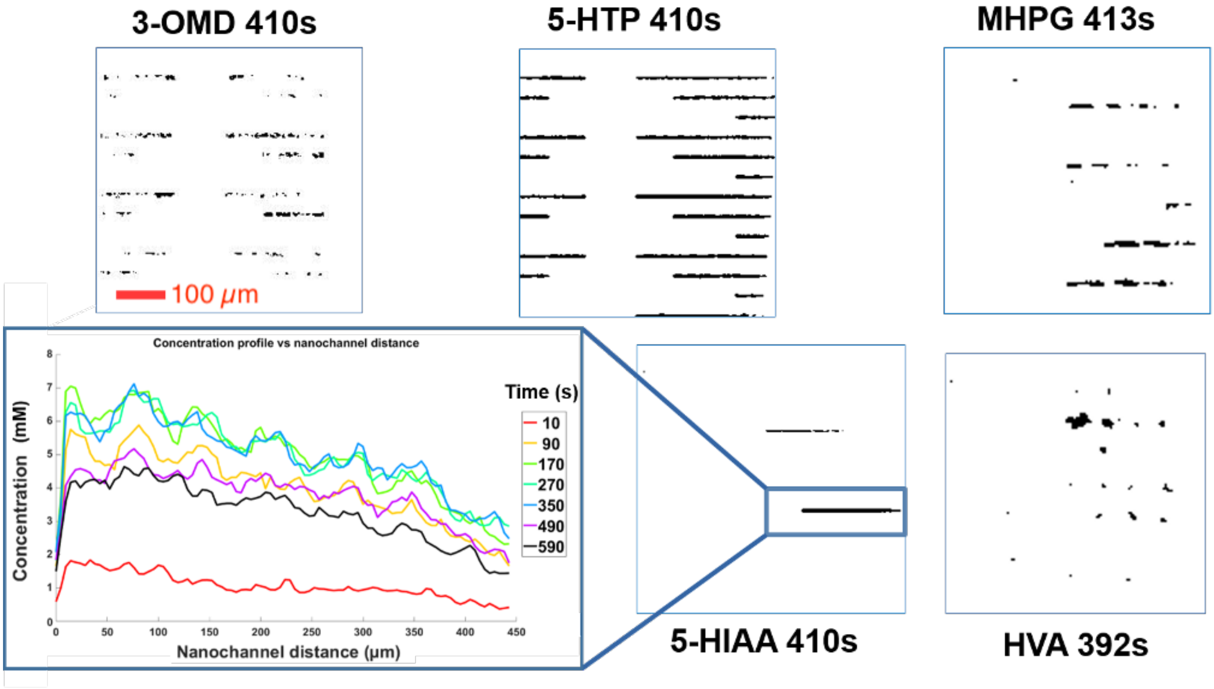

Figure 5.4: Electropreconcentration patterns of the five metabolites, applying a voltage difference of 100 V. At the bottom on left-hand side, the concentration profiles in one of the preconcentration fronts of 5-HIAA at different times.

It is important to mention that the results obtained in figure 5.4 were done in a h-PDMS/glass chip that was fabricated at the time where the protocol of fabrication of the master mold was not optimized, for this reason, it is difficult to interpret these results in detail as we did with other molecules along this work. For example, the 5-HTP metabolite exhibits fluorescent spots along all the microchannels and in both sides of the nanochannels (cathode and anode reservoirs) which seems that all the chip is filled with the metabolite. In addition, we realized that the intensity of the beam during the experiments was not very high, so the detection of metabolites was even more difficult for some metabolites.

In a second part, a real mixture of two metabolites (5-HIAA and 3-OMD) has been done and was compared with the numerical superposition of the preconcentration fronts of 3-OMD and 5-HIAA obtained independently. The numeric and real mixture were hardly distinguishable, but we could find some similarities between both experiments.

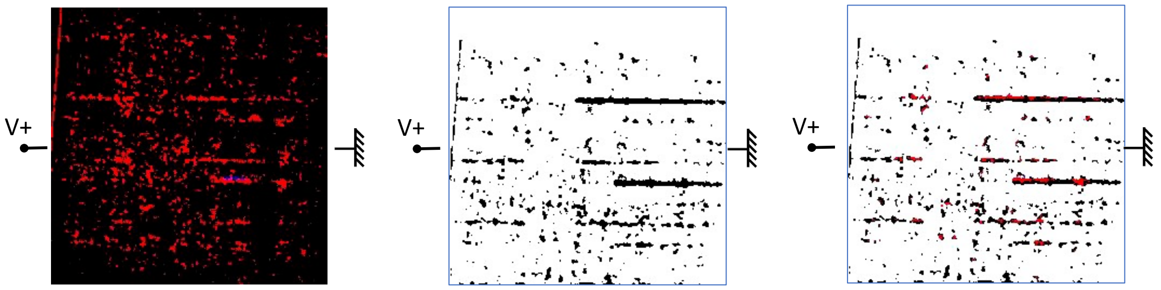

Image 1 : numerical mixture
Red: OMD
Violet: HIAA

Image 2 : real mixture

Image 3 : Superposition of film 1 and 2. Purple is not very visible but is present under the red and the black.

Figure 5.5: (Left) Numerical mixture of preconcentration fronts of 5-HIAA and 3-OMD metabolites. (Middle) Preconcentration fronts of the real mixture of 5-HIAA and 3-OMD metabolites. (Right) Superposition of image 1 and 2.

This project is very promising since the detection of metabolites is done without pre-labeling them by direct detection in the UV range. At the time this manuscript was written, the project was accepted as part of an ANR pre-maturation project.

Appendix A

Modeling tutorial

This tutorial is aimed to explain step-by-step the construction of the preconcentration model using COMSOL v5.6 for a nanochannel with length $L_n = 100\ \mu$m and width $W_n = 100$ nm and reservoirs with length $L_r = 300$ µm and width $W_r = 5$ µm. The surface charge density is set to -1 mC/m^2 and the initial concentration of KCl is 50 µM.

From the File menu, choose New.

- **NEW**
  1. In the **New window**, click **Model Wizard**.
- **MODEL WIZARD**
  1. In the **Model Wizard** window, click **2D**.
  2. In the **Select Physics** tree, select **Fluid Flow** > **Single-Phase Flow** >**Laminar Flow (spf)**.
  3. Click **Add**.
  4. In the **Select Physics** tree, select **AC/DC** > **Electric Fields and Currents** >**Electrostatics (es)**.
  5. Click **Add**.
  6. In the **Select Physics** tree, select **Chemical Species Transport** > **Transport of Dilutes Species (tds)**.
  7. Click **Add**.
  8. In the **Number of species** table, enter 2.
  9. In the **Concentration** table enter the following setting: cp (for positive ions) and cm (for negative ions).
  10. In the **Select Physics** tree, select **Chemical Species Transport** > **Transport of Dilutes Species (tds)**.
  11. Click **Add**.
  12. In the **Number of species** table, enter 1.

13. In the **Concentration** table, enter the following setting: cs (for sample ions)
14. Click **Study**.
15. In the **Select Study** tree, select **General Studies** > **Stationary**.
16. Click **Done**.

- **GLOBAL DEFINITIONS**

  Parameters

  1. On the **Model Builder** window, click **Parameters**.
  2. In the **Settings** window for Parameters, locate the **Parameters** section.
  3. In the table, enter the setting in Table A.1

- **DEFINITIONS**

  1. In the **Model Builder** window, under **Component 1 (comp1)** locate **Definitions**.
  2. On the **Definitions** toolbar, in the **Variables** section choose **Local Variables**.
  3. 3 In the **Settings** window for **Variables** locate the Variables table and enter the setting in Table A.2

- **GEOMETRY 1**

  1. In the **Model Builder window**, under **Component 1 (comp1)** click **Geometry 1**.
  2. In the **Settings** window for Geometry, locate the **Units** section.
  3. From the **Length unit** list, choose μm.

  Rectangle 1 (r1)

  1. On the **Geometry** toolbar, in the **Primitives** section choose **Rectangle**.
  2. In the **Settings** window for Rectangle, locate the **Size and Shape** section.
  3. In the **Width** text field, type Ln.
  4. In the **Height** text field, type Wn.
  5. Locate the **Position** section. In **Base** select **Center**. In the x and y text field, type 0.

  Rectangle 2 (r2)

  1. On the **Geometry** toolbar, in the **Primitives section** choose **Rectangle**.
  2. In the **Settings** window for Rectangle, locate the **Size and Shape** section.
  3. In the **Width** text field, type LR.
  4. In the **Height** text field, type WR.
  5. Locate the **Position** section. In **Base** select **Center**.
  6. Locate the **Position** section. In the x text field, type -Ln/2-LR/2.
  7. Locate the **Position** section. In the y text field, type 0.

  Rectangle 3 (r3)

  1. On the **Geometry** toolbar, in the **Primitives section** choose **Rectangle**.
  2. In the **Settings** window for Rectangle, locate the **Size and Shape** section.

Name	Expression	Value	Description
Ln	100 [μm]	1E-4 m	Length of nanochannel
LR	300 [μm]	3E-4 m	Length of reservoir
Wn	100 [nm]	1E-7 m	Width of nanochannel
WR	5 [μm]	5E-6 m	Width of reservoir
c0	0.05 [mmol/L]	0.05 mol/m^3	Initial concentration of K,Cl
c1	1e-9 [mol/L]	1E-6 mol/m^3	Initial concentration of fluorescein
D1	1.97e-9 [m^2/s]	1.97E-9 m^2/s	Diffusion coefficient of K+
D2	2.01e-9 [m^2/s]	2.01E-9 m^2/s	Diffusion coefficient of Cl-
D3	0.485e-9 [m^2/s]	4.85E-10 m^2/s	Diffusion coefficient of fluorescein
z1	1	1	Charge coefficient K+
z2	-1	-1	Charge coefficient Cl-
z3	-2	-2	Charge coefficient fluorescein
Emax	10 [kV/m]	10000 V/m	Nominal electric field across nanochannel
V0_max	Emax∗Ln	1 V	Intermediate variable for auxiliary sweeps
V0	V0_max	1 V	Applied voltage
P0	0 [Pa]	0 Pa	Pressure
rho_s_max	-1 [mC/m^2]	-0.001 C/m^2	Intermediate variable for auxiliary sweeps
rho_s	rho_s_max	-0.001 C/m^2	Surface charge density
eps_water	80	80	Permittivity
density_water	1000 [kg/m^3]	1000 kg/m^3	Water density
eta	1e-3 [Pa∗s]	0.001 Pa∗s	Dynamic viscosity
num_x	1600	1600	Number of elements along channel length
lambda	sqrt(epsilon∗RT/2∗F^2∗c0)	4.3064E-8 m	Debye length
RT	R_const∗293.15 [K]	2437.4 J/mol	RT thermal energy
epsilon	eps_water∗8.854e-12 [F/m]	7.0832E-10 F/m	Epsilon
F	F_const	96485 C/mol	Faraday constant
DL_width	5∗lambda	2.1532E-7 m	width of EDL wall domains

Table A.1: Parameters for simulations.

Name	Expression	Unit	Description
rhokcl	(cp-cm)∗F_const	C/m^3	Charge density

Table A.2: Variables.

3. In the **Width** text field, type DL_width.
4. In the **Height** text field, type DL_width.
5. Locate the **Position** section. In **Base** select **Corner**.
6. Locate the **Position** section. In the **x** text field, type -LR-Ln/2.

7. Locate the **Position** section. In the **y** text field, type -WR/2.

Rectangle 4 (r4)

1. On the **Geometry** toolbar, in the **Primitives** section choose **Rectangle**.
2. In the **Settings** window for Rectangle, locate the **Size and Shape** section.
3. In the **Width** text field, type DL_width.
4. In the **Height** text field, type DL_width.
5. Locate the **Position** section. In **Base** select **Corner**.
6. Locate the **Position** section. In the **x** text field, type -LR-Ln/2.
7. Locate the **Position** section. In the **y** text field, type WR/2-DL_width.

Rectangle 5 (r5)

1. On the **Geometry** toolbar, in the **Primitives** section choose **Rectangle**.
2. In the **Settings** window for Rectangle, locate the **Size and Shape** section.
3. In the **Width** text field, type DL_width.
4. In the **Height** text field, type DL_width.
5. Locate the **Position** section. In **Base** select **Corner**.
6. Locate the **Position** section. In the **x** text field, type -Ln/2-DL_width.
7. Locate the **Position** section. In the **y** text field, type WR/2-DL_width.

Rectangle 6 (r6)

1. On the **Geometry** toolbar, in the **Primitives** section choose **Rectangle**.
2. In the **Settings** window for Rectangle, locate the **Size and Shape** section.
3. In the **Width** text field, type DL_width.
4. In the **Height** text field, type DL_width.
5. Locate the **Position** section. In **Base** select **Corner.**
6. Locate the **Position** section. In the **x** text field, type -Ln/2-DL_width.
7. Locate the **Position** section. In the **y** text field, type -WR/2.

Rectangle 7 (r7)

1. On the **Geometry** toolbar, in the **Primitives** section choose **Rectangle**.
2. In the **Settings** window for Rectangle, locate the **Size and Shape** section.
3. In the **Width** text field, type LR-2*DL_width.
4. In the **Height** text field, type WR-2*DL_width.
5. Locate the **Position** section. In **Base** select **Corner**.
6. Locate the **Position** section. In the **x** text field, type -LR-Ln/2 + DL_width.
7. Locate the **Position** section. In the **y** text field, type -WR/2 + DL_width.

Rectangle 8 (r8)

1. On the **Geometry** toolbar, in the **Primitives** section choose **Rectangle**.
2. In the **Settings** window for Rectangle, locate the **Size and Shape** section.

3. In the **Width** text field, type DL_width.
4. In the **Height** text field, type Wn.
5. Locate the **Position** section. In **Base** select **Corner**.
6. Locate the **Position** section. In the **x** text field, type -Ln/2 - DL_width.
7. Locate the **Position** section. In the **y** text field, type -0.05.

Mirror 1 (mir1)

1. On the **Geometry** toolbar, in the **Operations section** >**Transforms** choose **Mirror**.
2. In the **Settings** window for Mirror, locate the **Input** section. Click the **Paste Selection** button, and type r2, r3, r4, r5, r6, r7, r8.
3. Select **Keep input objects**.
4. In the **Settings** window for Mirror, locate the **Normal vector to Line Reflection** section. In the **x** text field, type 1.

Rectangle 9 (r9)

1. On the **Geometry** toolbar, in the **Primitives** section choose **Rectangle**.
2. In the **Settings** window for Rectangle, locate the **Size and Shape** section.
3. In the **Width** text field, type 2*LR + Ln.
4. In the **Height** text field, type WR/2.
5. Locate the **Position** section. In **Base** select **Corner**.
6. Locate the **Position** section. In the **x** text field, type -Ln/2 -LR.
7. Locate the **Position** section. In the **y** text field, type -WR/2.

Partition Objects 1 (par1)

1. On the **Geometry** toolbar, in the **Operations section**> **Booleans and Partitions** choose **Partition Objects**.
2. In the **Settings** window for Partition Objects, locate the **Partition Objects** section.
3. In the **Objects to partition** section, click the **Paste Selection** button, and type r1, r2, r3, r4, r5, r6, r7, r8, mir1(1), mir1(2), mir1(3), mir1(4), mir1(5), mir1(6), mir1(7).
4. In the **Tool objects** section, click the **Paste Selection** button, and type r9.

Delete Entities 1 (del1)

1. On the **Geometry** toolbar, in the **Operations section** choose **Delete**.
2. In the **Settings** window for Delete Entities, locate the **Entities or Objects to Delete** section.
3. In the Geometric entity level select **Domain**.
4. In the **Graphics** Window select all the domains above de centerline of the geometry. In the selection part the following domains must appear : par1(1)2, par1(3)1, par1(4)1, par1(6)2, par1(7)2, par1(8)2, par1(9)2, par1(14)2, par1(11)1, par1(12)1, par1(15)2.

Form Composite Domains 1 (cmd1)

1. On the **Geometry** toolbar, in the **Cleanup section** > **Virtual Operations** choose **Form Composite Domains**.

2. In the **Settings** window for Form Composite Domains, locate the **Input** section. Click the **Paste Selection** button, and type 2, 4, 13, 15.
3. Select **Ignore adjacent vertices**.

Form Composite Domains 2 (cmd2)

1. On the **Geometry** toolbar, in the **Cleanup section** > **Virtual Operations** choose **Form Composite Domains**.
2. In the **Settings** window for Form Composite Domains, locate the **Input** section. Click the **Paste Selection** button, and type 1, 3, 11, 13.
3. Select **Ignore adjacent vertices**.
4. Choose **Build All**.

- **MATERIALS**

1. On the **Model Builder** window, click **Materials**.
2. On the **Home** toolbar, in the Materials section, choose **Add Material**.
3. On the **Add material** Column select **Liquids and gases**> **Liquids**>**Water**.
4. In the **Settings** window for Water, locate the **Material Contents** section. Then, type eps_water in the value of relative permittivity, eta in the value of Dynamic viscosity and density_water in the value of density.

- **LAMINAR FLOW**

1. In the **Model Builder** window, under **Component 1 (comp1)** click **Laminar Flow (spf)**.
2. In the **Settings** window for Laminar flow, verify that incompressibility flow is selected.

Fluid Properties 1

1. In the **Model Builder** window, expand the **Component 1 (comp1)**> **Laminar Flow (spf)** node, then click **Fluid Properties 1**.
2. In the **Settings** window for Fluid properties, locate the **Fluid Properties** section.
3. From the ρ list, choose **From material**.
4. From the μ list, choose **From material**.

Initial values 1

1. In the **Model Builder** window, expand the **Component 1 (comp1)**> **Laminar Flow (spf)** node, then click **Initial Values 1**.
2. In the **Settings** window for Initial Values, locate the **Initial Values section**.
3. From the **velocity field**, type 0 in x and 0 in y. (These are the default numbers but verify)
4. From the **pressure**, type 0. (This is the default number but verify)

Symmetry 1

1. On the **Physics** toolbar, click **Boundaries** and choose **Symmetry**.
2. Select boundaries 13, 21, 26, 33 and 39 only.

Open Boundary 1

1. On the **Physics** toolbar, click **Boundaries** and choose **Open Boundary**.
2. Select boundaries 1, 3, 39 and 40 only.

Volume Force 1

1. On the **Physics** toolbar, click **Domains** and choose **Volume Force**.
2. In the **Settings** window for Volume Force, locate the **Domain Selection** section. From the **Selection** list choose **All Domains**.
3. Locate the **Volume Force** section. In the **Volume force** table, enter the following setting: rhokcl*-Vx rhokcl*-Vy

- **ELECTROSTATICS (ES)**

Electric Potential 1

1. On the **Physics** toolbar, click **Boundaries** and choose **Electric Potential**.
2. Select boundary 3 only.
3. In the **Settings** window for Electric Potential, locate the **Electric Potential** section. In the Electric potential text field, type V0.

Electric Potential 2

1. On the **Physics** toolbar, click **Boundaries** and choose **Electric Potential**.
2. Select boundary 32 only.
3. In the **Settings** window for Electric Potential, locate the **Electric Potential** section. In the Electric potential text field, type 0.

Space Charge Density 1

1. On the **Physics** toolbar, click **Domains** and choose **Space Charge Density**.
2. In the **Settings** window for Space Charge Density, locate the **Domain Selection** section. From the **Selection** list, choose **All domains**.
3. Locate the **Space Charge Density** section. From the Space charge density list, choose **User defined**. In the associated text field, type rhokcl.

Surface Charge Density 1

1. On the **Physics** toolbar, click **Boundaries** and choose **Surface Charge Density**.
2. Select boundaries 2, 7, 13, 14, 16 and 18 only.
3. In the **Settings** window for **Surface Charge Density**, locate the **Surface Charge Density** section. In the Surface charge density text field, type rho_s.

- **TRANSPORT OF DILUTED SPECIES (TDS)**

1. In the **Model Builder** window, under **Component 1 (comp1)** click **Transport of Diluted Species (tds)**.
2. In the **Settings** window for Transport of Diluted Species. Locate the **Transport Mechanism** section. Select the **Migration in electric field** check box.
3. In the **Advanced settings** section, select Conservative Form.

Transport Properties 1

1. In the **Model Builder** window, expand the **Component 1 (comp1)> Transport of Diluted Species (tds)** node, then click **Transport Properties 1**.
2. In the **Settings** window for **Transport Properties**, locate the **Convection** section. From the Velocity field list, choose **Velocity field (spf)**.
3. Locate the **Diffusion** section. In the **Diffusion coefficient** text field, type D1 for Dcp and type D2 for Dcm.
4. Locate the **Migration in Electric Field** section. From the **Electric potential** list, choose **Electric potential (es)**. In the Charge number text field, type z1 and z2 for zcp and zcm respectively.

Initial Values 1

1. In the **Model Builder** window, click **Component 1 (comp1)> Transport of Diluted Species (tds)> Initial Values 1**.
2. In the **Settings** window for Initial Values, locate the **Initial Values** section. In the **Concentration** text field, type c0 for both species cp and cm.

Concentration 1

1. On the **Physics** toolbar, click **Boundaries** and choose **Concentration**.
2. Select boundaries 3 and 32 only.
3. In the **Settings** window for **Concentration**, locate the **Concentration** section. Select the **Species cp** check box and type c0 in the associated text field. Then, select the **Species cm** check box and type c0 in the associated text field.

Symmetry 1

1. On the **Physics** toolbar, click **Boundaries** and choose **Symmetry**.
2. In the **Settings** window for **Symmetry**, locate the **Boundary Selection** section. Select boundaries 5, 12, 17, 24 and 30.

- **TRANSPORT OF DILUTED SPECIES 2 (TDS 2)**

1. In the **Model Builder** window, under **Component 1 (comp1)** click **Transport of Diluted Species 2 (tds 2)**.
2. In the **Settings** window for **Transport of Diluted Species 2**. Locate the **Transport Mechanism** section. Select the **Migration in electric field** check box.
3. In the **Advanced settings** section, select Conservative Form.

Transport Properties 1

1. In the **Model Builder** window, expand the **Component 1 (comp1)> Transport of Diluted Species 2 (tds 2)** node, then click **Transport Properties 1**.
2. In the **Settings** window for Transport Properties, locate the **Convection** section. From the **Velocity field** list, choose **Velocity field (spf)**.
3. Locate the **Diffusion** section. In the **Diffusion coefficient** text field, type D3 for Dcs .
4. Locate the **Migration in Electric Field** section. From the **Electric potential** list, choose **Electric potential (es)**. In the **Charge number** text field, type z3 for zcs.

Initial Values 1

1. In the **Model Builder** window, click **Component 1 (comp1)> Transport of Diluted Species 2 (tds 2)> Initial Values 1**.
2. In the **Settings** window for Initial Values, locate the **Initial Values** section. In the **Concentration** text field, type c1 for species cs.

Concentration 1

1. On the **Physics** toolbar, click **Boundaries** and choose **Concentration**.
2. Select boundaries 3 and 32 only.
3. In the **Settings** window for Concentration, locate the **Concentration** section. Select the **Species cs** check box and type c1 in the associated text field.

- **MESH 1**

Mapped 1

1. In the **Model Builder** window, under **Component 1 (comp1)** click **Mesh 1**.
2. On the **Mesh** toolbar, click **Mapped**.
3. In the **Model Builder** window, click **Component 1 (comp1)> Mesh 1>Size**.
4. In the **Settings** window for size, locate the **Element size** section and select **Custom**.
5. Locate the **Element size parameters** section.
6. In the **Maximum element size** text field, type 2.95.
7. In the **Minimum element size** text field, type 0.0132.
8. In the **Settings** window for **Mapped 1**, locate the **Geometric entity level** list and select **Domain**.
9. Select domain 6 (nanoslits).

Distribution 1

1. In the **Model Builder** window, under **Component 1 (comp1)> Mesh 1** right-click **Mapped 1** and select **Distribution**.
2. Select boundaries 15 and 22.
3. In the **Settings** window for **Distribution 1**, locate the **Distribution section**.
4. From the **Distribution type** list, choose **Predefined**.
5. In the **Number of elements** text field, type 60.
6. In the **Element ratio** text field, type 200.

Distribution 2

1. In the **Model Builder** window, under **Component 1 (comp1)> Mesh 1** right-click **Mapped 1** and select **Distribution**.
2. Select boundaries 16 and 17.
3. In the **Settings** window for **Distribution 2**, locate the **Distribution** section.
4. From the **Distribution type** list, choose **Predefined**.
5. In the **Number of elements** text field, type num_x.
6. In the **Element ratio** text field, type 200.

7. Select the **Symmetric distribution** check box.

Mapped 2

1. In the **Model Builder** window, under **Component 1 (comp1)** click **Mesh 1**.
2. On the **Mesh** toolbar, click **Mapped**.
3. In the **Settings** window for **Mapped 2**, locate the **Geometric entity level** list and select **Domain**.
4. Select domains 1, 3, 4, 5, 7, 8, 9 and 10.

Distribution 1

1. In the **Model Builder** window, under **Component 1 (comp1)> Mesh 1** right-click **Mapped 2** and select **Distribution**.
2. Select boundaries 18, 14, 20 and 27.
3. In the **Settings** window for **Distribution 1**, locate the **Distribution** section.
4. From the **Distribution type** list, choose **Predefined**.
5. In the **Number of elements** text field, type 80.
6. In the **Element ratio** text field, type 40.
7. Select the **Symmetric distribution** check box.

Distribution 2

1. In the **Model Builder** window, under **Component 1 (comp1)> Mesh 1** right-click **Mapped 2** and select **Distribution**.
2. Select boundaries 2, 4, 26 and 28.
3. In the **Settings** window for **Distribution 2**, locate the **Distribution** section.
4. From the **Distribution type** list, choose **Predefined**.
5. In the **Number of elements** text field, type 1100.
6. In the **Element ratio** text field, type 5.
7. Select the **Symmetric distribution** check box.

Distribution 3

1. In the **Model Builder** window, under **Component 1 (comp1)> Mesh 1** right-click **Mapped 2** and select **Distribution**.
2. Select boundaries 7, 9, 11 and 12.
3. In the **Settings** window for **Distribution 3**, locate the **Distribution** section.
4. From the **Distribution type** list, choose **Predefined**.
5. In the **Number of elements** text field, type 30.
6. In the **Element ratio** text field, type 40.

Distribution 4

1. In the **Model Builder** window, under **Component 1 (comp1)> Mesh 1** right-click **Mapped 2** and select **Distribution**.
2. Select boundaries 19, 21, 23 and 24.

3. In the **Settings** window for **Distribution 4**, locate the **Distribution** section.
4. From the **Distribution type** list, choose **Predefined**.
5. In the **Number of elements** text field, type 30.
6. In the **Element ratio** text field, type 40.
7. Select the **Reverse direction** check box.

Distribution 5

1. In the **Model Builder** window, under **Component 1 (comp1)**> **Mesh 1** right-click **Mapped 2** and select **Distribution**.
2. Select boundaries 1, 6, 13, 18, 25 and 31.
3. In the **Settings window** for Distribution 5, locate the **Distribution** section.
4. From the **Distribution type** list, choose **Predefined**.
5. In the **Number of elements** text field, type 30.
6. In the **Element ratio** text field, type 40.

Free triangular 1

1. On the **Mesh** toolbar, click **Free triangular**.
2. In the **Settings** window for Free triangular, locate the **Geometric entity level** list and select **Domain**.
3. Select domains 2 and 11.

Size 1

1. In the **Model Builder** window, under **Component 1 (comp1)**> **Mesh 1** right-click **Free triangular** and select **Size 1**.
2. In the **Settings** window for **Size 1**, locate the **Element size** section.
3. Select **custom**.
4. Locate the **Element size parameters** section.
5. Select the **Maximum element size** check box and in the text field, type WR/10.
6. Click **Build all**.

- **STUDY (for electrolyte ions)**

1. In the **Model Builder** window, under **Component 1 (comp1)** click **Study 1**.
2. In the **Settings** window for study 1, type Single-step study in the Label text field.

Step 1: Stationary

1. In the **Model Builder** window, under Single-step study click **Step 1: Stationary**.
2. In the **Settings** window for Stationary click to expand the **Physics and Variables** selection.
3. Clear **solve for Transport of Diluted Species 2 (tds2)**.
4. Click to expand the **Study extensions** section.
5. Select the **Auxiliary sweep** check box.
6. Select **All combinations** in the Sweep type list.

7. Click the **Add**.
8. In the **Parameter name** list select Emax.
9. In the P **arameter value** list enter 0 1000 5000 10000 20000 30000.

Parametric sweep

1. In the **Model Builder** window, under **Component 1 (comp1)** right-click **Single-step study** and select **Parametric Sweep**.
2. In the **Settings window** for parametric sweep, located **study** settings.
3. Click the **Add**.
4. In the **Parameter name** list select C0.
5. In the **Parameter value** list enter 0.05 mol/m^3.
6. Click the **Add**.
7. In the **Parameter name** list select rho_s.
8. In the **Parameter value** list enter -1 mC/m^2.
9. On the **Study** toolbar, click **Compute**.

- **ADD STUDY**

  1. On the **Home** toolbar, click **Add Study** to open the **Add Study** window.
  2. Go to the **Add Study** window.
  3. In the **Studies** section, select **General Studies** and double-click **Time Dependent**.
  4. On the **Home** toolbar, click **Add Study** again to close the Add Study window.

- **STUDY 2 (for sample ions)**

  1. In the **Model Builder** window, under **Component 1 (comp1)** click **Study 2**.
  2. In the **Settings** window for study, type Sample Study in the Label text field.

Step 1: Time dependent

1. In the **Model Builder** window, under **Sample Study** click **Step 1: Time dependent**.
2. In the **Settings** window for Time dependent, locate the **Study Setting** section.
3. Type range (0, 10, 120) in the text field of Output times.
4. Locate the **Physics and variables Selection** section.
5. Deselect **Solve for Laminar flow, Electrostatics and Transport of Diluted Species**.
6. Locate the **Values of Dependent Variables** section.
7. Find the **Values of variables not solved for** subsection. From the **Settings** list, choose **User controlled**.
8. From the **Method** list, choose **Solution**.
9. From the **Study** list, choose **Single-step Study, Stationary**.
10. On the **Study** toolbar, click **Compute**.

User can see the default 2D results in the Results section and line graphs can be easily constructed depending on the parameters to study.

Appendix B

Treatment of data

B.1 Matlab program: noise correction and detection of channels

Noise correction

After entering all the parameters of the experiment (described in the section 3.1.4 of this manuscript), we then use the two white and black images in order to normalize the light intensity in the channels between different experiments using the intensity difference,

$$\Delta I = \frac{\hat{I}_{white} - \hat{I}_{black}}{\alpha_{white}} \tag{B.1}$$

α_{white} being an intensity factor left free for later use ($\alpha_{white} = 1$) and $\hat{I}$ represents the average intensity of the ROI to correct the noise.

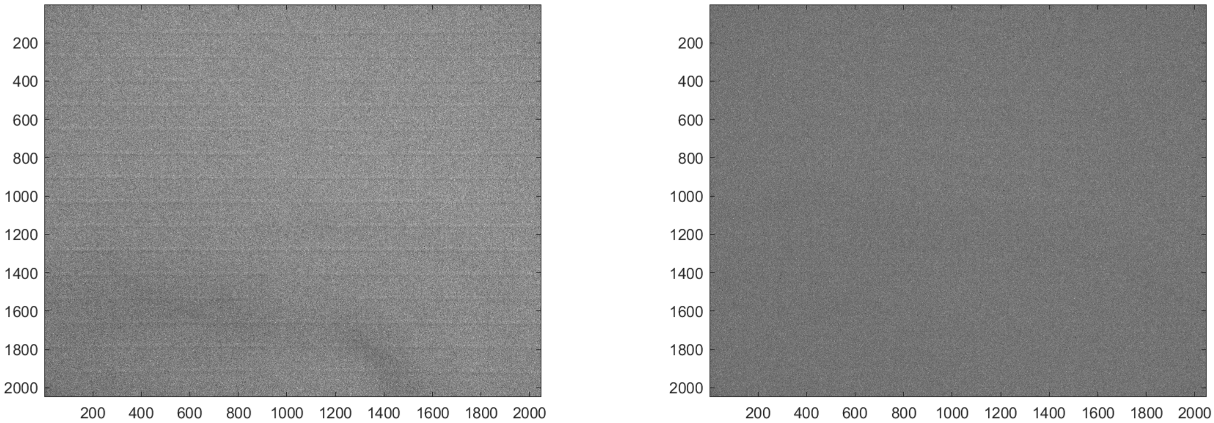

(a) Image of diluted analyte (I_{white}) **(b)** Image of only the BGE (I_{black})

Figure B.1: Images used for normalization of results.

We observed that the average of the ROI of the black image can be confused with the average of the entire image. Indeed the difference is very small (0.15 %) between the average of the ROI and the whole image. The noise is Gaussian and can then be processed by using a Gaussian filter but its high variance implies that the noise will not be completely smoothed.

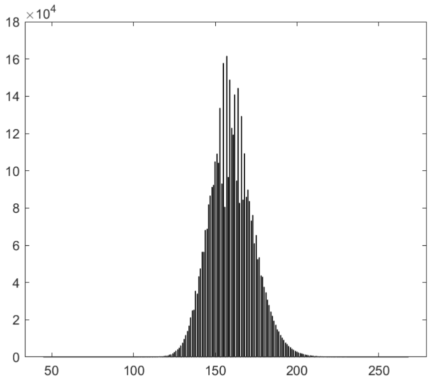

Figure B.2: Histogram of the image to be processed

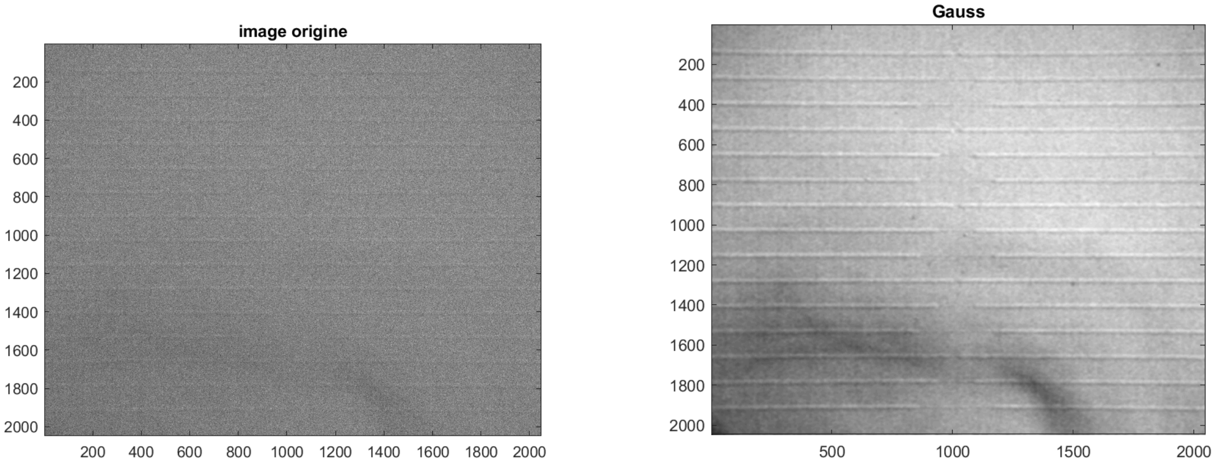

(a) Original image **(b)** Gaussian filter $\sigma = 5$ (very noisy)

Figure B.3: First treatment of images.

We notice a stain on the bottom of the image, this stain came from the microscope which was then cleaned. Thus, a first filter makes it possible to improve visibility. So then we proceeded to the detection of the channels. The first method will be the row detection by the Hough transform and its associated accumulator matrix:

$$\rho = x\ cos(\theta) + y\ sin(\theta) \tag{B.2}$$

Before that, we propose to look for the contours on the y axis using the Sobel filter:

$$Sobel_y = \begin{bmatrix} -1 & -2 & -1 \\ 0 & 0 & 0 \\ 1 & 2 & 1 \end{bmatrix} \tag{B.3}$$

Detection of channels

The image must then be binarized using a threshold. This being very small, a histogram equalization can be applied in order to improve the precision of the thresholding.

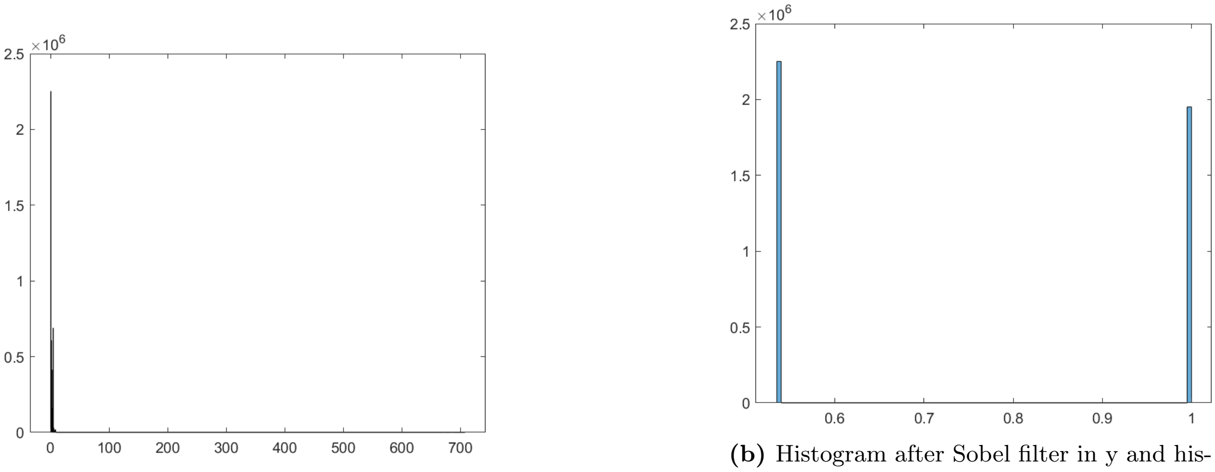

(a) Histogram after Sobel filter in y

(b) Histogram after Sobel filter in y and histogram equalization

Figure B.4: Contour detection

We thus obtain after thresholding the next image:

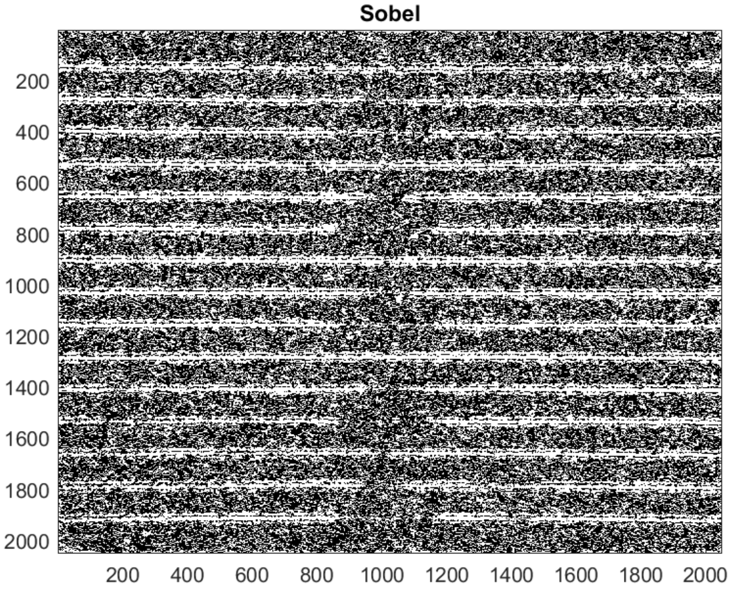

Figure B.5: Contour detection after thresholding

However, there is still a lot of noise. This noise being relatively fine, we can apply an erosion then a dilation of the white pixels to obtain a final binary image :

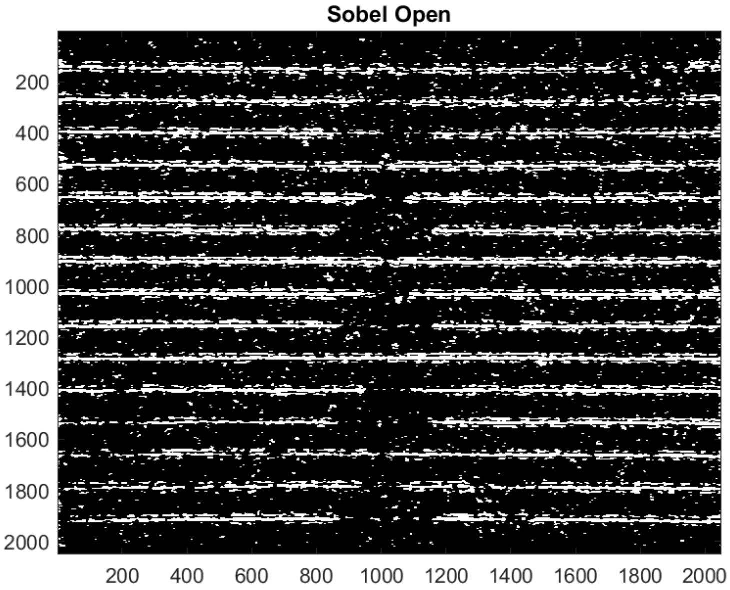

Figure B.6: Contours after dilatation and erosion

The application of the Hough transform is done quickly because the inclination angle θ of the channels is quite close to 0 °. In order to prevent more than 2 lines from being taken for each channel, we apply a minimum distance between two lines. A low quality of the binarized image however makes this minimum distance unnecessary because it may not meet the threshold criterion to consider a line, all the same, an image from a slightly better acquisition makes the solution viable:

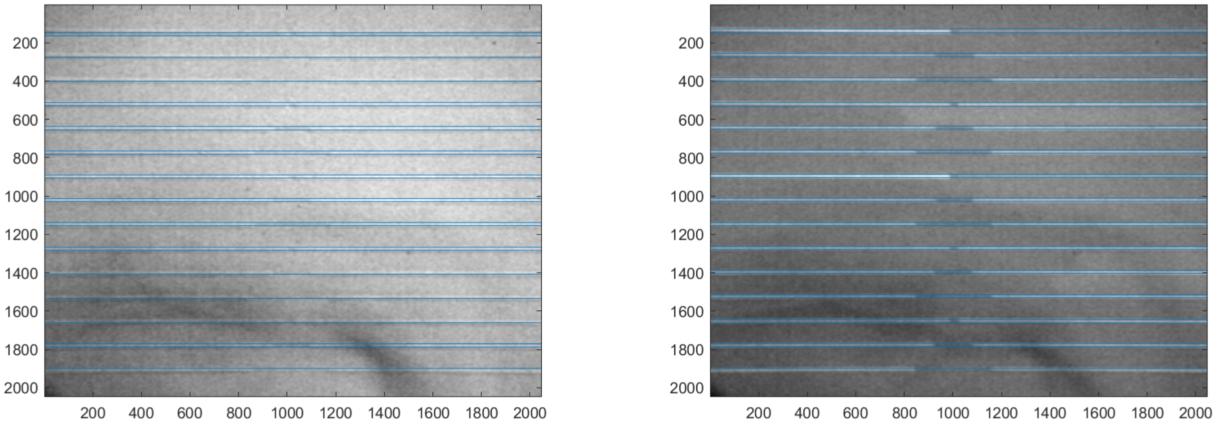

(a) Channel detection with poor quality

(b) Channel detection for slightly better quality

Figure B.7: Channel detection

Another solution would then be to derive the derivative of the accumulators on the y axis and take the largest successive variations (positive then negative) and set up a validity criterion.

Since the contours are detected on the maximum of the accumulators resulting from the Hough transform, this poses a problem when there is a lot of noise present in the image. To work around this problem, the use of a threshold for the number of white pixels on horizontal lines was used.

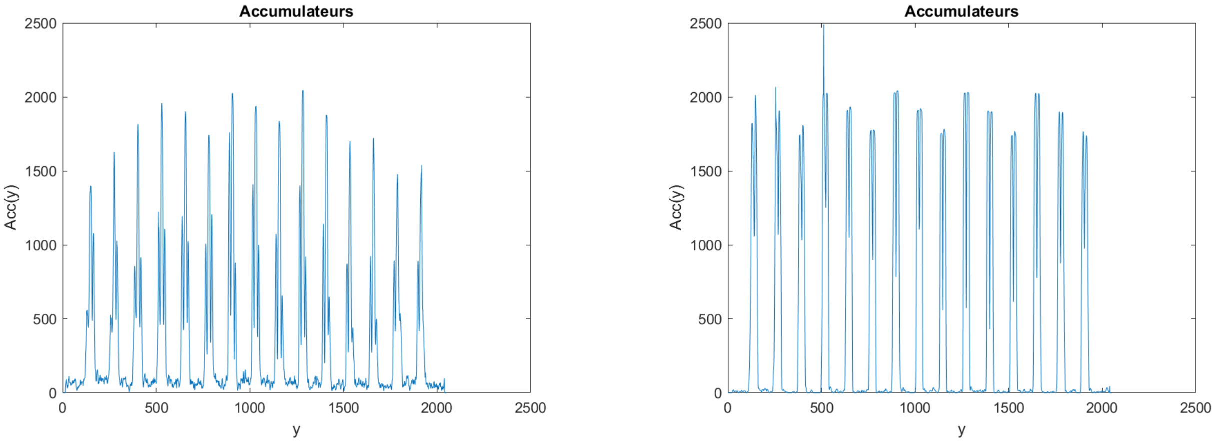

(a) Accumulators for a very noisy image **(b)** Accumulators for a relatively less noisy image

Figure B.8: Accumulators after Hough Transform

For a very noisy image, the figure B.8a accumulators do not have only two peaks or a precise order. We can then decide to encompass the entire channel. So a threshold criterion> 200 makes it possible to find the channels for a noisy image. For a slightly less noisy image, the detection of maxima (2 per channel) allows a more precise detection of the figure B.8b channels. It is still possible to manually select the ends of the channels if the detection program cannot find all the channels (in the case of DNA).

B.2 Calibration

Calibration is essential for the calculation of true concentrations from the corrected fluorescence intensity of an analyte. Here, we present four calibration curves of the different analytes used for this work. By injecting different known concentrations of the analytes in a simple microchannel, the evolution of the corrected intensity as a function of the concentration can be plotted to obtain the calibration curves. Along the calibration and during the preconcentration experiment it is important to keep the same acquisition parameters as the intensity of the fluorescent lamp for excitation of the molecules or the exposition time of the camera.

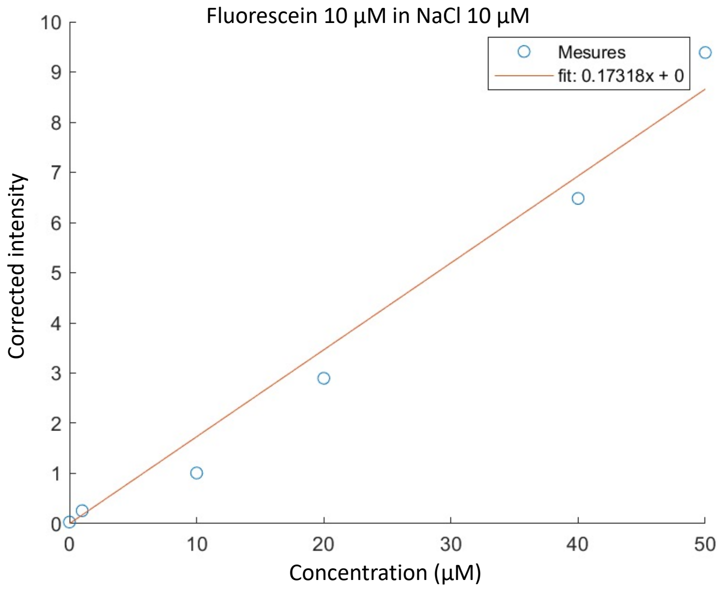

Figure B.9: Calibration curve of fluorescein in NaCl BGE.

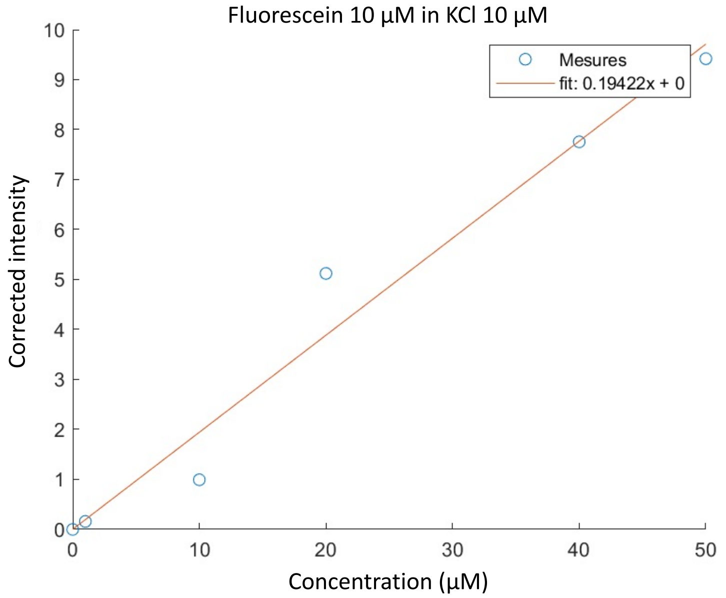

Figure B.10: Calibration curve of fluorescein in KCl BGE.

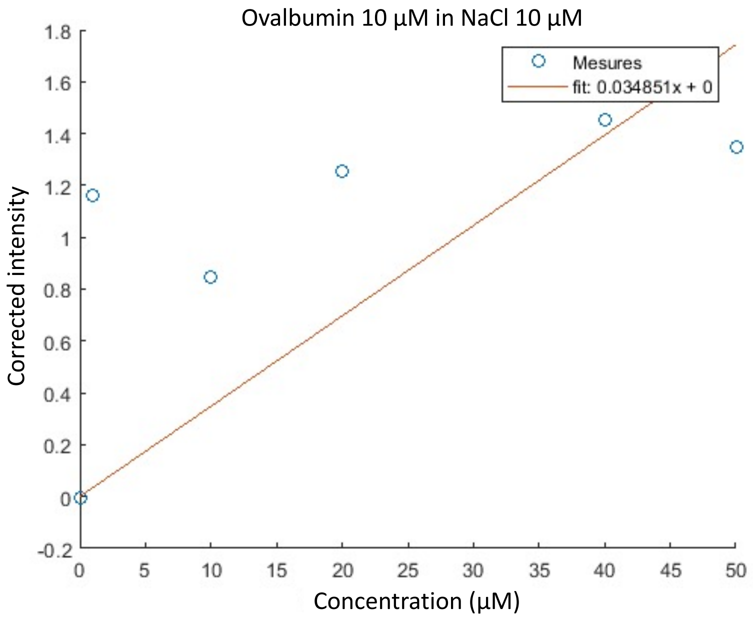

Figure B.11: Calibration curve of ovalbumin in NaCl BGE.

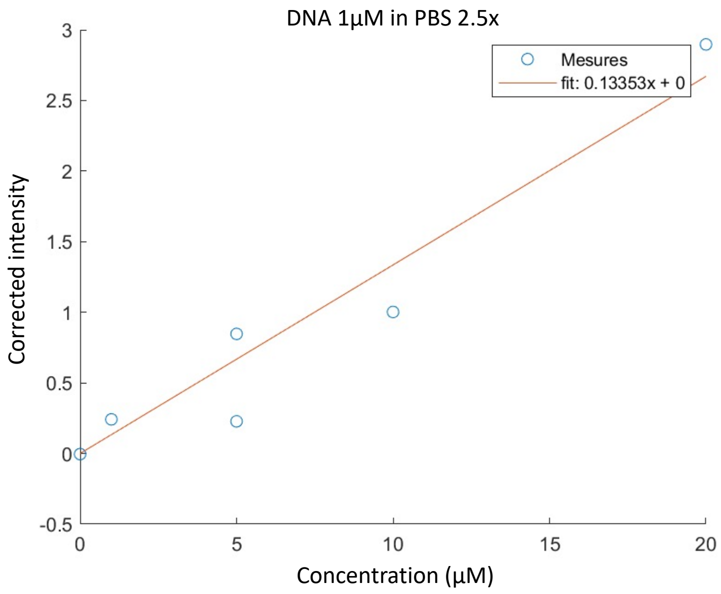

Figure B.12: Calibration curve of DNA in PBS BGE.

References

[1] A. C. Louer. *Préconcentration sélective immunologique en nanofluidique: vers l'identification rapide d'agents du risque biologique.* PhD thesis, Université Paris Sud, 2013.

[2] S. M. Ngom, F. Flores-Galicia, F. D. Delapierre, A. Pallandre, J. Gamby, I. Le Potier, and A. M. Haghiri-Gosnet. Electropreconcentration diagrams to optimize molecular enrichment with low counter pressure in a nanofluidic device. *Electrophoresis*, 41:1617–1626, 2020.

[3] A. Plecis, C. Nanteuil, A. M. Haghiri-Gosnet, and Y. Chen. Electropreconcentration with charge-selective nanochannels. *Anal. Chem.*, 80:9542–9550, 2008.

[4] G. M. Whitesides. The origins and the future of microfluidics. *Nature*, 442:368–373, 2006.

[5] S. C. Terry, J. H. Herman, and J. B. Angell. A gas chromatographic air analyzer fabricated on a silicon wafer. *IEEE Trans. Electron Devices*, 26(12):1880–1886, 1979.

[6] A. Manz, N. Graber, and H. M. Widmer. Miniaturized total chemical analysis systems: A novel concept for chemical sensing. *Sens. Actuator B-Chem.*, 1(1-6):244–248, 1990.

[7] N. Convery and N. Gadegaard. 30 years of microfluidics. *MNE*, 2:79–91, 2019.

[8] M. Napoli, J. C. T. Eijkel, and S. Pennathur. Nanofluidic technology for biomolecule applications: a critical review. *Lab Chip*, 10:957–985, 2010.

[9] L. Bocquet. Nanofluidics coming of age. *Nature Materials*, 19:254–256, 2020.

[10] K. Yamamoto, N. Ota, and Y. Tanaka. Nanofluidic devices and applications for biological analyses. *Anal. Chem.*, 93(1):332–349, 2021.

[11] Z. Zhang, L. Wen, and L. Jiang. Nanofluidics for osmotic energy conversion. *Nature Reviews Materials*, 6:622–639, 2021.

[12] S. Gravelle. *Nanofluidics: a pedagogical introduction.* hal-02375018, 2016.

[13] B. E. Rapp. *Microfluidics: Modelling, Mechanics and Mathematics.* Micro and Nano Technologies, 2017.

[14] L. Bocquet and E. Charlaix. Nanofluidics, from bulk to interfaces. *Chem. Soc. Rev.*, 39(3):1073–1095, 2010.

[15] A. Alizadeh, W.-L. Hsu, M. Wang, and H. Daiguji. Electroosmotic flow: From microfluidics to nanofluidics. *Electrophoresis*, 42:834–868, 2021.

[16] J. A. Davis, R. O. James, and J. O. Leckie. Surface ionization and complexation at the oxide/water interface: I. computation of electrical double layer properties in simple electrolytes. *J. Colloid Interface Sci.*, 63(3):480–499, 1978.

[17] R. B. Schoch, J. Han, and P. Renaud. Transport phenomena in nanofluidics. *RMP*, 80:839–883, 2008.

[18] J. M. Sustarich, B. D. Storey, and S. Pennathur. Field-amplified sample stacking and focusing in nanofluidic channels. *Phys. Fluids*, 22:112003, 2010.

[19] B. Jung, R. Bharadwaj, and J. G. Santiago. Thousandfold signal increase using field-amplified sample stacking for on-chip electrophoresis. *Electrophoresis*, 24:3476–3483, 2003.

[20] R. Bharadwaj and J. G. Santiago. Dynamics of field-amplified sample stacking. *J. Fluid. Mech.*, 543:57–92, 2005.

[21] Q. Pu, J. Yun, H. Temkin, and S. Liu. Ion-enrichment and ion-depletion effect of nanochannel structures. *Nano Lett*, 4:1099–1103, 2004.

[22] S. J. Kim, Y.-A. Song, and J. Han. Nanofluidic concentration devices for biomolecules utilizing ion concentration polarization: theory, fabrication, and applications. *Chem. Soc. Rev.*, 39:912, 2010.

[23] M. Gholinejad, A. J. Moghadam, D.-T. Phan, A. K. Miri, and S. A. M. Shaegh. Design and application of ion concentration polarization for preconcentrating charged analytes. *Phys. Fluids*, 33:051301, 2021.

[24] T. A. Zangle, A. Mani, and J. G. Santiago. Theory and experiments of concentration polarization and ion focusing at microchannel and nanochannel interfaces. *Chem. Soc. Rev.*, 39:1014–1035, 2010.

[25] A. Mani, T. A. Zangle, and J. G. Santiago. On the propagation of concentration polarization from microchannel-nanochannel interfaces part i: Analytical model and characteristic analysis. *Langmuir*, 25:3898–3908, 2009.

[26] C. Wang, Y. Wang, Y. Zhou, Z. Q. Wu, and X.H. Xia. High-performance bioanalysis based on ion concentration polarization of micro-/nanofluidic devices. *Anal. Bioanal. Chem.*, 411:4007–4016, 2019.

[27] B. Berzina and R. K. Anand. Tutorial review: Enrichment and separation of neutral and charged species by ion concentration polarization focusing. *Anal. Chim. Acta*, 1128:149–173, 2020.

[28] B. Jung, R. Bharadwaj, and J. G. Santiago. On-chip millionfold sample stacking using transient isotachophoresis. *Anal. Chem.*, 78:2319–2327, 2006.

[29] H. Cui, K. Horiuchi, P. Dutta, and C. F. Ivory. Multistage isoelectric focusing in a polymeric microfuidic chip. *Anal. Chem.*, 77(24):7878–7886, 2005.

[30] H. Cui, K. Horiuchi, P. Dutta, and C. F. Ivory. Isoelectric focusing in a poly(dimethylsiloxane) microfluidic chip. *Anal. Chem.*, 77(5):1003–1009, 2005.

[31] W. Hsu, D. W. Inglis, M. A. Startsev, E. M. Goldys, M. R. Davidson, and D. J. E. Harvie. Isoelectric focusing in a silica nanofluidic channel: Effects of electromigration and electroosmosis. *Anal. Chem.*, 86(17):8711–8718, 2014.

[32] W. L. Hsu, D. J. E. Harvie, M. R. Davidson, H. Jeong, E. M. Goldys, and D. W. Inglis. Concentration gradient focusing and separation in a silica nanofluidic channel with a non-uniform electroosmotic flow. *Lab Chip*, 14(18):3539–3549, 2014.

[33] A. Plecis, R. B. Schoch, and P. Renaud. Ionic transport phenomena in nanofluidics: Experimental and theoretical study of the exclusion-enrichment effect on a chip. *Nano Lett.*, 5(6):1147–1155, 2005.

[34] T. A. Zangle, A. Mani, and J. G. Santiago. On the propagation of concentration polarization from microchannel-nanochannel interfaces part ii: Numerical and experimental study. *Langmuir*, 25:3909–3916, 2009.

[35] J. Gamby, F.D. Delapierre, A. Pallandre, B. Tribollet, C. Deslouis, and A-M. Haghiri-Gosnet. Dielectric properties of a single nanochannel investigated by high-frequency impedance spectroscopy. *Electrochem. commun.*, 66:5–9, 2016.

[36] D. Hlushkou, R. Dhopeshwarkar, R. M. Crook, and U. Tallarek. The influence of membrane ion-permselectivity on electrokinetic concentration enrichment in membrane-based preconcentration units. *Lab Chip*, 8:1153–1162, 2008.

[37] W. Ouyang, Z. Li, and J. Han. Pressure-modulated selective electrokinetic trapping for direct enrichment, purification and detection of nucleic acids in human serum. *Anal. Chem.*, 90:11366–11375, 2018.

[38] A. Plecis. *Etude et controle de la charge de surface dans les dispositifs micro/nanofluidiques: nouveaux outils pour les sciences separatives.* PhD thesis, Université Paris-Sud 11, 2008.

[39] Y. Wang, K. Pant, Z. Chen, G. Wang, W. F. Diffey, P. Ashley, and S. Sundaram. Numerical analysis of electrokinetic transport in micro-nanofluidic interconnect preconcentrator in hydrodynamic flow. *Microfluid Nanofluid*, 7:683–696, 2009.

[40] W. Han and X. Chen. Nano-electrokinetic ion enrichment in a micro-nanofluidic preconcentrator with nanochannel's cantor fractal wall structure. *Appl. Nanosci.*, 10:95–105, 2020.

[41] W. Han and X. Chen. A novel design of nanochannel structure in a micro–nanofluidic preconcentrator for electrokinetic ion enrichment. *J Braz. Soc. Mech. Sci. Eng.*, 42:49, 2020.

[42] W. Liu, Y. Zhou, and P. Shi. Electrokinetic ion transport at micro–nanochannel interfaces: applications for desalination and micromixing. *Appl. Nanosci.*, 10:751–766, 2020.

[43] L. Gong, Z. Li, and J. Han. Numerical simulation of continuous extraction of highly concentrated li+ from high mg2+/li+ ratio brines in an ion concentration polarization-based microfluidic system. *Sep. Purif. Technol.*, 217:174–182, 2019.

[44] P. Dubsky, S. Das, A. van den Berg, and J. C. T. Eijkel. Concentration polarization in nanochannel dna electrophoresis. In *MicroTAS*, pages 212–214, 2011.

[45] Z. Li, W. Liu, Y. Zhu, X. Lu, Y. Gu, and J. Han. Accurate multi-physics numerical analysis of particle preconcentration based on ion concentration polarization. *Int. J. Appl. Mech.*, 9(8):1750107, 2017.

[46] M. Gholinejad, A. J. Moghadam, S. A. M. Shaegh, and A. K. Miri. Multifactorial analysis of ion concentration polarization for microfluidic preconcentrating applications using response surface method. *Phys. Fluids*, 32:072012, 2020.

[47] J. Y. Wang and Q. Hou. Effect of nanochannel geometry on electrokinetic ion transport in a micro-nanofluidic system. *AIP Advances*, 9:125213, 2019.

[48] S. Movahed and D. Li. Electrokinetic transport through nanochannels. *Electrophoresis*, 32:1259–1267, 2011.

[49] Y.C. Wang, A. L. Stevens, and J. Han. Million-fold preconcentration of proteins and peptides by nanofluidic filter. *Anal. Chem.*, 77:4293–4299, 2005.

[50] S. M. Kim, M. A. Burns, and E. F. Hasselbrink. Electrokinetic protein preconcentration using a simple glass/poly(dimethylsiloxane) microfluidic chip. *Anal. Chem.*, 78:4779–4785, 2006.

[51] P. Mao and J. Han. Fabrication, and characterization of 20nm planar nanofluidic channels by glass–glass and glass–silicon bonding. *Lab Chip*, 5(8):837–844, 2005.

[52] P. Mao and J. Han. Massively-parallel ultra-high-aspect-ratio nanochannels as mesoporous membranes. *Lab Chip*, 9(4):586–591, 2009.

[53] A. C. Louër, A. Plecis, A. Pallandre, J. C. Galas, A. Estevez-Torres, and A.M. Haghiri-Gosnet. Pressure-assisted selective preconcentration in a straight nanochannel. *Anal. Chem.*, 85(16):7948–7956, 2013.

[54] P. S. Chung, Y. J. Fan, H. J. Sheend, and W. C.Tian. Real-time dual-loop electric current measurement for label-free nanofluidic preconcentration chip. *Lab Chip*, 15:319–330, 2015.

[55] J. H. Lee, Y. A. Song, and J. Han. Multiplexed proteomic sample preconcentration device using surface-patterned ion-selective membrane. *Lab Chip*, 8(4):596–601, 2008.

[56] S. J. Kim and J. Han. Self-sealed vertical polymeric nanoporous-junctions for high-throughput nanofluidic applications. *Anal. Chem.*, 80(9):3507–3511, 2008.

[57] J. Y. Wang, Z. Xu, Y. K. Li, C. Liu J. S. Liu, L. Chen, L. Q. Du, , and L. D. Wang. Nanopore density effect of polyacrylamide gel plug on electrokinetic ion enrichment in a micro-nanofluidic chip. *Appl. Phys. Lett.*, 103:043103, 2013.

[58] S. Hong, R. Kwak, and W. Kim. Paper-based flow fractionation system applicable to preconcentration and field-flow separation. *Anal. Chem.*, 88(3):1682–1687, 2016.

[59] M. Zhiyue, Y. Xichen, R. Li, Y. Yang, F. Huicheng, and S. Peng. Recent advances in paper-based preconcentrators by utilizing ion concentration polarization. *Electrophoresis*, 42:1340–1351, 2021.

[60] E. Choi, K. Kwon, S.J. Lee, D. Kim, and J. Park. In-situ self-assembled colloidal crystals within microchannels using one step stamping for direct seawater desalination by ion concentration polarization. *IEEE MEMS*, 59:1213–1215, 2012.

[61] E. Choi, K. Kwon, D. Kim, and J. Park. An electrokinetic study on tunable 3d nanochannel networks constructed by spatially controlled nanoparticle assembly. *Lab Chip*, 15(2):512–523, 2015.

[62] S.Y. Son, S. Lee, H. Lee, and S. J. Kim. Engineered nanofluidic preconcentration devices by ion concentration polarization. *BioChip J.*, 10:251–261, 2016.

[63] L. F. Cheow, S. H. Ko, S. J. Kim, K. H. Kang, and J. Han. Increasing the sensitivity of enzyme-linked immunosorbent assay using multiplexed electrokinetic concentrator. *Anal. Chem.*, 82:3383–3388, 2010.

[64] S. H. Ko, Y. A. Song, S. J. Kim, M. Kim J. Han, and K. H. Kang. Nanofluidic preconcentration device in a straight microchannel using ion concentration polarization. *Lab Chip*, 12:4472–4482, 2012.

[65] S. H. Ko, S. J. Kim, L. F. Cheow, L. D. Li, K. H. Kang, and J. Han. Massively parallel concentration device for multiplexed immunoassays. *Lab Chip*, 11(1351-1358), 2011.

[66] W. Ouyang and J. Han. Universal amplification-free molecular diagnostics by billion-fold hierarchical nanofluidic concentration. *Proc Natl Acad Sci U S A*, 116(33):16240–16249, 2019.

[67] D. C. Martins, V. Chu, and J. P. Conde. The effect of the surface functionalization and the electrolyte concentration on the electrical conductance of silica nanochannels. *Biomicrofluidics*, 7(3):034111., 2013.

[68] COMSOL Multiphysics® v. 5.6. COMSOL AB. *The coefficient Form PDE.* Stockholm, Sweden, 2020.

[69] COMSOL Multiphysics® v. 5.6. COMSOL AB. *The CDF Module User's Guide.* Stockholm, Sweden, 2020.

[70] A. Eden, C. McCallum, B. D. Storey, S. Pennathur, and C. D. Meinhar. Analyte preconcentration in nanofluidic channels with nonuniform zeta potential. *Phys. Rev. Fluids*, 2:124203, 2017.

[71] F. Schlegel. Modeling electroosmotic flow and the electrical double layer. https://www.comsol.com/blogs/modeling-electroosmotic-flow-electrical-double-layer/, October 2013.

[72] C. Hughes, L. H. Yeh, and S. Qian. Field effect modulation of surface charge property and electroosmotic flow in a nanochannel: Stern layer effect. *J. Phys. Chem. C*, 117:9322–9331, 2013.

[73] D. Milanova, R. D. Chambers, S. S. Bahga, and J. G. Santiago. Electrophoretic mobility measurements of fluorescent dyes using on-chip capillary electrophoresis. *Electrophoresis*, 32(22):3286–3294, 2011.

[74] S. M. Ngom. *Dispositifs nanofluidiques á électro-préconcentration sélective.* PhD thesis, Université Paris-Saclay, 2019.

[75] C. Nanteuil. *Etude du transport ionique a travers un nanocanal fluidique : vers l'électropréconcentration sélective.* PhD thesis, Paris 11, 2010.

[76] Merck. Fluorescein sodium salt. https://www.sigmaaldrich.com/catalog/product/sial/f6377, July 2021.

[77] Thermofisher. Ovalbumin conjugates. https://www.thermofisher.com/document-connect/document-connect.html?url=httpsJuly 2021.

[78] S. Prakash and J. Yeom. *Nanofluidics and Microfluidics: Systems and Applications.* William Andrew, 2014.

[79] Bioseutica®. Ovalbumin. https://www.bioseutica.com/products/ovalbumin.

[80] S.-H. Chang and S.-J. Kim. Studies on the paper electrophoresis, i on the mobility of egg albumin(ovalbumin). *J. Korean Chem. Soc*, 4(1):1–6, 1957.

[81] N. C. Stellwagen and E. Stellwagen. Effect of the matrix on dna electrophoretic mobility. *J Chromatogr A.*, 1216(10):1917–1929, 2009.

[82] N. C. Stellwagen, C. Gelfi, and P. G. Righetti. The free solution mobility of dna. *Biopolymers*, 42(6):687–703, 1997.

[83] D. Doummar and F. Moussa. Pathologies des amines biogènes, ptérines et folates : quand y penser? *Neurologies*, 13(125):76–80, 2010.

[84] F. Moussa, J. F. Benoist, E. Thioulouse, M.-C. Berthe, and R. Couderc. Spectrométrie de masse et maladies métaboliques héréditaires. *Revue Francophone des Laboratoires*, 437:65–72, 2011.

[85] S. Leu-Semenescu, I. Arnulf, C. Decaix, F. Moussa, F. Clot, C. Boniol, Y. Touitou, R. Levy, M. Vidailhet, and E. Roze. Sleep and rhythm consequences of a genetically induced loss of serotonin. *Sleep*, 33(3):307–314, 2010.

[86] M.-A. Spitz, M.-A. Nguyen, H. Ogier, S. Roche, N. Garcia, E. Roze, D. Gras, L. De Pontual, B. Heron, M. Milh, B. Chabrol, A. Cano, N. Bahi-Buisson, I. Desguerre, P. De Lonlay, L. Lion-François, H. Testard, L. Damaj, S. Napuri, M. Barth, A. Küster, F. Rivier, S. Fournier-Favre, L. Christa, F. Moussa, J.-F. Benoist, C. Ottolenghi, C. Vianey-Saban, C. Corne, and A. Roubertie. Déficit en décarboxylase des acides amines aromatiques (aadc) chez dix patients français : particularités phénotypiques. *Archives de pédiatrie*, 20(4):426, 2013.

[87] D. Chen, J.-T. Kim, L. P. Chamorrob, and A. T. Timperman. Exceeding ohmic scaling by more than one order of magnitude with a 3d ion concentration polarization system. *Lab Chip*, 21(16):3094–3104, 2021.

[88] Z. Almutairi, C. L. Rena, and L. Simonc. Evaluation of polydimethylsiloxane (pdms) surface modification approaches for microfluidic applications. *Colloids Surf.*, 415:406–412, 2012.

List of publications

Articles

1. S. M. Ngom, F. Flores-Galicia, F. D. Delapierre, A. Pallandre, J. Gamby, I. Le Potier, and A. M. Haghiri-Gosnet, "Electropreconcentration diagrams to optimize molecular enrichment with low counter pressure in a nanofluidic device", Electrophoresis, 41,1617-1626, 2020. https://doi.org/10.1002/elps.202000117
2. F. Flores-Galicia, A. Eden, A. Pallandre, S. Pennathur and A. M. Haghiri-Gosnet, "Predicting ion concentration polarization and analyte stacking/focusing at nanofluidic interfaces" submitted to Special Issue of Electrophoresis on Fundamentals 2021.

Poster of conference

1. F. Flores-Galicia, F. D. Delapierre, A. Pallandre and A. M. Haghiri-Gosnet, Predicting ion concentration polarization in short nanochannel, µTAS 2021.

Oral of conference

1. F. Flores-Galicia, F. D. Delapierre, A. Pallandre and A. M. Haghiri-Gosnet, Predicting ion concentration polarization in short nanochannel, GDR Toulouse 2021.

université
PARIS-SACLAY

ÉCOLE DOCTORALE
Physique et ingénierie :
électrons, photons,
sciences du vivant (EOBE)

Titre: Electropréconcentration dans des dispositifs nanofluidiques : prédire et démontrer expérimentalement les régimes focalisants

Mots clés: Nanofluidique, Transport électrocinétique, Simulations COMSOL 2D, Nanofabrication

Résumé: La détection d'analytes faiblement concentrés dans des échantillons complexes est un domaine des plus complexes en bioanalyse. L'électropréconcentration basée sur l'effet de polarisation de concentration ionique (ICP) à l'intérieur de dispositifs nanofluidiques apparaît comme une méthode prometteuse pour concentrer et détecter simultanément des biomolécules. L'ICP est induite à travers des nanocanaux qui jouent le rôle de filtre à perméabilité sélective d'ions entre les microcanaux et entraînent des zones d'enrichissement et d'appauvrissement avec une conductivité élevée et faible en entrée ou sortie, du nanocanal, zone où un analyte peut s'empiler et donc se concentrer.

Dans ce contexte, l'objectif de mon travail de thèse est d'étudier la préconcentration d'analytes modèles dans des puces h-PDMS/verre incorporant plusieurs nanocanaux verticaux. Je présente des simulations numériques 2D d'électrophorèse d'électrolytes de fond (BGE) et d'espèces ioniques à l'intérieur d'une structure micro/nano/fluidique à l'aide du logiciel COMSOL Multiphysics®. Ces modèles permettent d'étudier d'abord l'effet ICP du BGE puis la préconcentration des analytes. Les simulations numériques prédisent les régimes d'empilement cathodique (CS) et de focalisation cathodique (CF) d'analytes anioniques aux interfaces nanofluidiques. Dans le cadre de mon travail expérimental, j'ai étudié le rôle de la longueur et de la largeur des nanocanaux pour trois molécules modèles, la fluorescéine, l'ovalbumine et l'ADN de l'hépatite C. La fluorescéine est préconcentrée/focalisée au niveau du réservoir cathodique grâce à sa grande mobilité et l'ovalbumine et l'ADN se localisent au niveau du réservoir anodique grâce à leur mobilité plus faible.

Title: Electropreconcentration in nanofluidic devices: predict and experimentally demonstrate stacking/focusing regimes

Keywords: Nanofluidics, Electrokinetic transport, 2D COMSOL Simulations, Nanofabrication

Abstract: Detection of low concentrated analytes in complex samples is one of the most interesting challenges in bioanalysis. Electropreconcentration based on ion concentration polarization (ICP) effect inside nanofluidic devices appears as an interesting alternative to simultaneously concentrate and detect biomolecules. ICP is induced across nanochannels that play the role of ion-selective filter between microchannels and results in enrichment and depletion zones with high and low conductivity media on opposite sides of the nanochannel where an analyte can focus and therefore concentrate.

In this context, the aim of my PhD work is to study preconcentration of chosen analytes in h-PDMS/glass chips incorporating multiple vertical nanochannels. I present 2D numerical simulations of electrophoresis of background electrolyte (BGE) and ionic species inside a micro/nano/fluidic structure using COMSOL Multiphysics® software. These models permits to study first the ICP effect of BGE and then the preconcentration of the analytes. Numerical simulations predict the cathodic stacking (CS) and cathodic focusing (CF) regimes of anionic analytes at nanofluidic interfaces. As part of my experimental work, I studied the role of nanochannel length and width for three model molecules, fluorescein, ovalbumin and hepatitis C DNA. Fluorescein is stacked/focused at the cathode reservoir thanks to its high mobility and the ovalbumin and DNA are preconcentrated at the anode reservoir thanks to their lower mobility.

Maison du doctorat de l'Université Paris-Saclay
2^{eme} étage aile ouest, Ecole normale supérieure Paris-Saclay
4 avenue des Sciences,
91190 Gif sur Yvette, France